

Copyright

by

Ying Tian

2007

**The Dissertation Committee for Ying Tian Certifies that this is the approved version  
of the following dissertation:**

**BEHAVIOR AND MODELING OF REINFORCED CONCRETE  
SLAB-COLUMN CONNECTIONS**

**Committee:**

---

James O. Jirsa, Supervisor

---

Oguzhan Bayrak

---

Eric B. Becker

---

John L. Tassoulas

---

Sharon L. Wood

**Behavior and Modeling of Reinforced Concrete Slab-Column  
Connections**

**by**

**Ying Tian, B.S.; M.S.**

**Dissertation**

Presented to the Faculty of the Graduate School of

The University of Texas at Austin

in Partial Fulfillment

of the Requirements

for the Degree of

**Doctor of Philosophy**

**The University of Texas at Austin**

**May 2007**

**To my family**

## **Acknowledgements**

I would like to express my sincere gratitude to Dr. James O. Jirsa, my dissertation supervisor. His technical guidance was crucial for my PhD research and his moral encouragement allowed me to get through an anguishing period for my family. Gratitude is extended to Dr. Oguzhan Bayrak, Dr. John L. Tassoulas, Dr. Sharon L. Wood, and Dr. Eric B. Becker for their advice and serving on my dissertation committee. Appreciation is also expressed to Dr. Jaime Argudo and Dr. Widiyanto who have collaborated with me for the experimental investigations.

I would like to thank my wife, Quan Wang, and my parents, Aiyun Yao and Weihua Tian, for their love and support for my pursuing excellence throughout the years.

The financial support from the National Science Foundation under grant numbers CMS 0301632 and CMS 0301395 and the assistance of Stacy Bartoletti, James R. Cagley, Larry D. Olson, and Loring A. Wyllie who served on technical advisory panel are gratefully acknowledged.

**Ying Tian**

**May 2007**

# **Behavior and Modeling of Reinforced Concrete Slab-Column Connections**

Publication No. \_\_\_\_\_

Ying Tian

The University of Texas at Austin, 2007

Supervisor: James O. Jirsa

Experimental results of five large-scale isolated slab-column connections subjected to three types of loading histories are presented. The subassemblies represented typical flat-plate construction designed prior to the 1980's that had low slab reinforcement ratios and discontinuous bottom reinforcement at the column. The specimens failed in punching after extensive slab flexural yielding occurred. The damage induced by simulated seismic loading to a prescribed drift level (1.25%) did not reduce the connection punching capacity under gravity loading. The post-earthquake connection stiffness was significantly reduced. The flexural reinforcement ratio had a significant effect on connection strength and stiffness.

Test data for interior flat-plate slab-column connections subjected to concentric gravity load and combined gravity and lateral loads were collected. The connection strength was evaluated using ACI code design equations. From test data, equations for connection gravity load capacity as a function of concrete strength, slab reinforcement

ratio and yield strength, and the ratio of column size to slab effective depth were developed.

Based on a beam analogy concept, a 2D nonlinear model for interior slab-column connections was developed for use in pushover analyses of flat-plate structures. The slab lateral resistance from flexure and shear acting on the connection was modeled by an equivalent beam element and the resistance from torsion by a rotational spring element. The parameters defining connection lateral stiffness were calibrated from the tests presented in this study and were validated using experimental data reported in other studies.

## Table of Contents

List of Tables .....	xiii
List of Figures .....	xv
Chapter 1 Introduction .....	1
1.1 Description of Flat-Plate Structure .....	1
1.2 Statement of Problem .....	3
1.3 Research Scope and Objectives .....	3
1.4 Previous Research and Code Design Requirements .....	5
1.4.1 Interior Slab-Column Connections Subjected to Concentric Gravity Load .....	5
1.4.1.1 Experimental Research .....	5
1.4.1.2 Mechanical Modeling .....	13
1.4.1.3 Code Requirements for Two-Way Shear .....	16
1.4.2 Interior Slab-Column Connections Subjected to Lateral Loading .....	20
1.4.2.1 Experimental Research .....	20
1.4.2.2 Analysis and Design Methods .....	25
Chapter 2 Design of Experimental Program .....	31
2.1 General .....	31
2.2 Description of Prototype Structure .....	31
2.3 Overall Test Objectives and Procedures .....	34
2.4 Finite Element Analysis .....	37
2.4.1 Element Type .....	37
2.4.2 Material Modeling .....	38
2.4.2.1 Concrete .....	38
2.4.2.2 Steel .....	43
2.4.3 Geometry, Boundary Conditions, and Loads for FEM Analyses .....	44
2.4.3.1 Continuous Structure Simulating Prototype Structure .....	44

2.4.3.2 Isolated Connection Simulating Laboratory Testing .....	46
2.4.4 FEM Analysis Results.....	48
2.4.4.1 Gravity Loading .....	48
2.4.4.2 Combined Loading.....	50
2.5 Details of Test Setup and Loading Apparatus .....	55
2.5.1 Combined Loading.....	55
2.5.2 Gravity Loading .....	58
2.6 Description of Test Specimens .....	60
2.6.1 Specimen Dimension and Nomination .....	60
2.6.2 Reinforcement Arrangement.....	61
2.6.3 Specimen Construction and Material Properties.....	63
2.7 Instrumentation and Data Collection .....	66
2.7.1 Load .....	66
2.7.2 Displacement.....	67
2.7.3 Strain .....	68
2.8 Specimen Transfer and Placement in Test Setup.....	69
Chapter 3 Experimental Results of Slab-Column Connections under Combined Lateral and Gravity Loading.....	71
3.1 General.....	71
3.2 Loading History .....	71
3.3 Global Response .....	73
3.3.1 Overall Load-Drift Response.....	73
3.3.2 Connection Stiffness Degradation .....	77
3.3.2.1 Lateral Stiffness Degradation .....	77
3.3.2.2 Connection Stiffness Degradation after Damage.....	79
3.4 Observed Damage and Failure Pattern .....	83
3.4.1 Specimen LG0.5 .....	84
3.4.2 Specimen LG1.0 .....	86
3.4.3 Specimen L0.5 .....	88
3.5 Steel Strain.....	90
3.5.1 Top Steel Strain of Specimen L0.5 .....	90

3.5.2 Top Steel Strain of Specimen LG1.0 .....	93
3.5.3 Bottom Steel Strain of Specimens L0.5, LG0.5, and LG1.0 .....	96
3.6 Summary of Tests Results .....	96
3.7 Failure Mechanism and Discussion .....	97
3.8 Summary .....	101
Chapter 4 Experimental Results of Gravity Load-Carrying Capacity of Slab- Column Connections with and without Earthquake Damage .....	104
4.1 General .....	104
4.2 Gravity Loading Response of Specimens G0.5 and G1.0 .....	105
4.2.1 Load-Deflection Relationship .....	105
4.2.2 Cracking Pattern and Failure .....	107
4.2.2.1 Specimen G0.5 .....	107
4.2.2.2 Specimen G1.0 .....	110
4.2.3 Strain Distribution .....	112
4.2.3.1 Steel Strains .....	112
4.2.3.2 Concrete Strains .....	116
4.3 Punching Strength of Earthquake-Damaged Connections .....	118
4.4 Behavior of Lightly-Reinforced Slab-Column Connections .....	120
4.4.1 Summary of Response of Lightly-Reinforced Slab-Column Connections .....	120
4.4.2 Failure Mechanism of Lightly-Reinforced Slab-Column Connections .....	121
4.4.2.1 Local Deformation Capacity of the Slab .....	121
4.4.2.2 Internal Forces at the Inclined Crack .....	123
Chapter 5 Shear Strength of Slab-Column Connections under Concentric Gravity Loading .....	129
5.1 General .....	129
5.2 Using Code Equations to Estimate Connection Shear Strength .....	130
5.3 Evaluation of Punching Strength Based on Test Data .....	133
5.3.1 Effects of Concrete and Flexural Reinforcement .....	134
5.3.1.1 Data Analysis Procedures .....	134
5.3.1.2 Analysis Results .....	135

5.3.2 Critical Section Location .....	138
5.3.3 Effects of $c/d$ -Ratio .....	140
5.3.4 Formulation of Connection Punching Strength .....	141
5.3.5 Reinforcement Concentration .....	143
5.3.6 Use of Proposed Equation for Connection Shear Strength.....	144
<b>Chapter 6 A Model for Behavior of Interior Slab-Column Connections</b>	
Transferring Gravity Shear and Unbalanced Moment.....	145
6.1 General.....	145
6.2 Connection Strength.....	146
6.2.1 ACI Building Code Procedures .....	146
6.2.2 Beam Analogy Approach.....	151
6.2.2.1 Unbalanced Moment Resisted by Flexure at Bending Faces .....	153
6.2.2.2 Unbalanced Moment Resisted by Shear at Bending Faces .....	154
6.2.2.3 Unbalanced Moment Resisted by Torsion at Side Faces .....	155
6.3 Analysis and Slab-Column Frames.....	162
6.3.1 General Model .....	162
6.3.2 Model for Beam Element.....	166
6.3.2.1 Moment Provided by Flexure, $M_1$ and $M_2$ .....	166
6.3.2.2 Moment Provided by Shear, $M_{v1}$ and $M_{v2}$ .....	167
6.3.2.3 Combined Resistance from Flexure and Shear .....	168
6.3.3 Model for Torsion .....	171
6.3.4 Summary of Nonlinear Modeling .....	172
6.3.5 Calibration of Stiffness Parameters, $I^*$ , $\gamma_{y,T}$ , and $K$ .....	173
6.3.5.1 Equivalent Frame Models of Specimens .....	173
6.3.5.2 Joint Rotation at Torsional Yielding, $\gamma_{y,T}$ .....	175
6.3.5.3 Equivalent Moment of Inertia, $I^*$ , and Positive Bending Stiffness Parameter, $K$ .....	176
6.3.5.4 Response of Specimens L0.5 and LG1.0 Based on Proposed Model .....	180
6.3.6 Summary of Analysis Procedures.....	181

6.3.7 Verification for the Suggested Analytical Model .....	184
6.3.7.1 Description of Tests for Verification .....	184
6.3.7.2 Nonlinear Analyses and Results .....	186
Chapter 7 Conclusions .....	189
7.1 Conclusions .....	189
7.2 Suggestions .....	191
Appendix A Crack Pattern of Specimen L0.5 .....	193
Appendix B Failure Pattern of Specimens LG0.5 and LG1.0 .....	195
Appendix C Database for Evaluating Punching Strength of Interior Slab-Column Connections .....	198
Appendix D Notation .....	201
References .....	204
Vitae .....	210

## List of Tables

Table 1.1:	Required Slab Thickness for An Example Slab-Column Connection	18
Table 2.1:	Summary of Parameters for Modeling Concrete	43
Table 2.2:	Summary of Specimens	61
Table 2.3:	Compressive Strength of Concrete	65
Table 2.4:	Tensile Properties of Reinforcement in Slabs	65
Table 3.1:	Experimental Results for Specimens Subjected to Combined Loading	97
Table 3.2:	Influence of Loading History on Lateral Deformation Capacity	100
Table 4.1:	Summary of Test Results of Specimens G0.5 and G1.0	107
Table 4.2:	Summary of Test Results of Specimens LG0.5 and LG1.0	118
Table 4.3:	Slab Maximum Local Deformation (G0.5, LG0.5, and L0.5)	122
Table 4.4:	Contribution of Compressive Reinforcement to Punching Strength	125
Table 5.1:	Average and Standard Deviation of Calculated Connection Strength	133
Table 5.2:	Effects of Concrete Strength on Connection Punching Strength	136
Table 5.3:	Effects of Slab Tensile Reinforcement on Connection Punching Strength	137
Table 5.4:	Data Grouping for Determination of Critical Section	139
Table 5.5:	Determination of Critical Section Location	139
Table 5.6:	Effective Area of Banded Reinforcement	144
Table 6.1:	Properties of Specimens Subjected to Combined Loading	149

Table 6.2:	Unbalanced Moment and Failure Mode Based on ACI 318-05 Procedures.....	150
Table 6.3:	Properties of Specimens for Determining $T_0$ .....	157
Table 6.4:	Calculated Connection Strength Based on Suggested Beam Analogy .....	160
Table 6.5:	Data for Calibrating Stiffness Parameters.....	175
Table 6.6:	Calibration of Equivalent Moment of Inertia.....	177
Table 6.7:	Properties of Specimens for Examining Suggested Model.....	185

## List of Figures

Figure 1.1: Flat-plate structure .....	1
Figure 1.2: Partial collapse of a flat-plate structure .....	2
Figure 1.3: Punching test schemes for isolated slab-column connections .....	5
Figure 1.4: Crack patterns and failure surfaces of continuous slab under simulated gravity loading (Gardner and Shao, 1996) .....	10
Figure 1.5: Effects of flexural reinforcement on the behavior of slab-column connections under concentric gravity loading (Criswell, 1974) .....	12
Figure 1.6: Kinnunen and Nylander's model (1960).....	14
Figure 1.7: Truss model (Alexander and Simmonds, 1986) .....	15
Figure 1.8: Critical section location .....	20
Figure 1.9: Test schemes for slab-column connections subjected to combined gravity and lateral loads .....	21
Figure 1.10: Eccentric shear stress model .....	26
Figure 1.11: Beam analogy.....	28
Figure 1.12: Nonlinear model for interior slab-column connections suggested by Akiyama and Hawkins (1984) .....	29
Figure 2.1: Prototype structure .....	32
Figure 2.2: Reinforcement arrangement around the prototype interior connection .....	33
Figure 2.3: Overall testing schemes .....	35
Figure 2.4: 8-Node quadratic shell element with reduced integration in FEM analyses .....	37
Figure 2.5: Concrete yield and failure surfaces in the $p$ - $q$ plane.....	39

Figure 2.6: Modeling of tension stiffening for concrete.....	39
Figure 2.7: Uniaxial response of concrete.....	41
Figure 2.8: Response of concrete under multiaxial stress state.....	41
Figure 2.9: Comparison of FEM prediction to test result.....	42
Figure 2.10: Illustration of the structures analyzed by inelastic finite element analyses.....	44
Figure 2.11: Geometry of continuous structure and isolated connection for FEM analyses.....	45
Figure 2.12: SM2 (gravity loading).....	49
Figure 2.13: SM1 (gravity loading).....	49
Figure 2.14: Deflection shape and vertical deflection (gravity loading).....	50
Figure 2.15: SM2.....	52
Figure 2.16: SM1.....	52
Figure 2.17: SM2 (0.5% rotation).....	53
Figure 2.18: SM1 (0.5% rotation).....	53
Figure 2.19: Deflection shape and vertical deflection (combined loading).....	54
Figure 2.20: Test setup for combined loading.....	56
Figure 2.21: 3-D view of the test setup for combined loading.....	57
Figure 2.22: Test setup for gravity loading.....	59
Figure 2.23: 3-D view of the test setup for gravity loading.....	60
Figure 2.24: Reinforcement details of Specimens L0.5, LG0.5, and G0.5.....	62
Figure 2.25: Reinforcement details of Specimens LG1.0 and G1.0.....	62
Figure 2.26: Reinforcement layout along slab depth.....	63
Figure 2.27: Column reinforcement details.....	63
Figure 2.28: Steel cages and slab forms (Specimen LG1.0).....	64

Figure 2.29: Stress-strain curves for reinforcement .....	66
Figure 2.30: Location of load cells and LVDTs.....	67
Figure 2.31: Typical steel strain gauge location.....	68
Figure 2.32: Preparation for specimen lifting.....	69
Figure 2.33: Placement of specimen in test setup .....	70
Figure 3.1: Lateral Displacement Routine for L0.5 .....	72
Figure 3.2: Lateral Displacement Routine for LG0.5 and LG1.0 .....	72
Figure 3.3: Pinching effect under cyclic loading (Specimen LG0.5).....	74
Figure 3.4: Lateral load versus drift response of Specimen L0.5.....	74
Figure 3.5: Lateral load versus drift response of Specimen LG0.5.....	75
Figure 3.6: Lateral load versus drift response of Specimen LG1.0.....	75
Figure 3.7: Comparison of response envelope curves.....	76
Figure 3.8: Definition of secant and tangential stiffness.....	77
Figure 3.9: Secant stiffness degradation.....	78
Figure 3.10: Tangential stiffness degradation .....	79
Figure 3.11: Vertical deflection versus lateral drift.....	80
Figure 3.12: Stiffness degradation ratio versus lateral drift .....	81
Figure 3.13: Crack types on slab upper surface .....	83
Figure 3.14: Top cracking pattern of Specimen LG0.5.....	84
Figure 3.15: Bottom cracking pattern of Specimen LG0.5 .....	86
Figure 3.16: Top cracking pattern of Specimen LG1.0.....	87
Figure 3.17: Bottom cracking pattern of Specimen LG1.0 .....	88
Figure 3.18: Damage around column at 2% lateral drift (Specimen L0.5) .....	89
Figure 3.19: Failure pattern of Specimen L0.5.....	89
Figure 3.20: Close view of failure pattern of Specimen L0.5 .....	90

Figure 3.21: Top reinforcement strain of Specimen L0.5 (along transverse direction).....	91
Figure 3.22: Top reinforcement strain of Specimen L0.5 (along longitudinal direction).....	92
Figure 3.23: Top reinforcement strain of Specimen LG1.0 (along transverse direction).....	94
Figure 3.24: Top reinforcement strain of Specimen LG1.0 (along longitudinal direction).....	95
Figure 3.25: Strain of bottom reinforcement for three specimens.....	96
Figure 3.26: Failure surface of Specimen L0.5 .....	98
Figure 3.27: Failed joint area of Specimen L0.5 .....	98
Figure 3.28: Failure initiation and propagation under combined loading.....	99
Figure 3.29: Overall behavior of slab-column connections under combined loading.....	102
Figure 4.1: Load-deflection curves for Specimens G0.5 and G1.0.....	105
Figure 4.2: Cracking pattern and failure of Specimen G0.5.....	108
Figure 4.3: Punching surface of Specimen G0.5 .....	109
Figure 4.4: Cracking and failure patterns of Specimen G1.0.....	111
Figure 4.5: Punching surface of Specimen G1.0.....	111
Figure 4.6: Two yield-line mechanisms for isolated slab-column connections .....	112
Figure 4.7: Measured steel strains of Specimen G0.5 .....	113
Figure 4.8: Measured steel strains of Specimen G1.0.....	114
Figure 4.9: Location of strain gauges T1 and T2 in Specimen G1.0.....	115
Figure 4.10: Localized bending due to slab rotation .....	116

Figure 4.11: Concrete strain of G1.0 .....	117
Figure 4.12: Load-deflection curves for Specimens LG0.5 and G0.5.....	119
Figure 4.13: Load-deflection curves for Specimens LG1.0 and G1.0.....	119
Figure 4.14: Orientation of the inclined cracks .....	120
Figure 4.15: Illustration of connection local deformation.....	122
Figure 4.16: Internal forces acting on the slab-column joint.....	123
Figure 4.17: Concrete splitting due to dowel action.....	126
Figure 5.1: Range of parameters in database (84 tests).....	130
Figure 5.2: Comparison between measured and calculated strength (ACI 318-05).....	131
Figure 5.3: Comparison between measured and calculated strength (CEB-FIP MC90).....	132
Figure 5.4: Critical section for calculating punching strength .....	133
Figure 5.5: Effect of $c/d$ -ratio on connection strength (52 tests).....	140
Figure 5.6: Comparison of measured strength and calculated strength based on the proposed formulation (Equations 5.11 and 5.11a).....	142
Figure 5.7: Comparison of measured strength and calculated strength based on the proposed formulation (Equations 5.14 and 5.14a).....	143
Figure 6.1: ACI 318-05 design approach for connections transferring unbalanced moment and gravity shear.....	147
Figure 6.2: Internal forces acting on the critical sections.....	152
Figure 6.3: Test scheme for determining $T_0$ (Kano and Yoshizaki, 1979).....	156
Figure 6.4: Test setups for lateral loading without applying gravity load.....	156
Figure 6.5: Effective area of calculating torsion capacity $T_0$ .....	158

Figure 6.6: Comparison of calculated strength using beam analogy and ACI approach for 28 specimens ( $\rho < 1.5\%$ , $V_g/V_c \leq 0.40$ ).....	161
Figure 6.7: 2D model of interior slab-column connections.....	163
Figure 6.8: Beam element with plastic hinges.....	164
Figure 6.9: Modeling of joint region (eliminating effects of equilibrium-restrained shear).....	165
Figure 6.10: Joint rotation and plastic hinge rotation.....	166
Figure 6.11: Inelastic models for unbalanced moment resisted by flexure .....	167
Figure 6.12: Inelastic models for unbalanced moment resisted by shear.....	168
Figure 6.13: Inelastic models for combined lateral resistance from flexure and shear .....	169
Figure 6.14: Modeling of plastic hinge properties .....	170
Figure 6.15: Inelastic modeling for torsion .....	171
Figure 6.16: Gravity load effect on connection inelastic behavior .....	172
Figure 6.17: Equivalent beam model for test specimens (lateral loading).....	174
Figure 6.18: Characteristic points used to calibrate stiffness parameters .....	176
Figure 6.19: Comparison of analytical and experimental results (L0.5 and LG1.0).....	180
Figure 6.20: 2D frame model and input data for strength and stiffness parameters .....	181
Figure 6.21: Test setups of the Specimens used for verifying the proposed model.....	185
Figure 6.22: Comparison of analytical and experimental results (Specimens H-5 and H-10) .....	187

Figure 6.23: Comparison of analytical and experimental results (Specimens 1 and 3).....	188
Figure 6.24: Comparison of analytical and experimental results (Specimen C-02).....	188
Figure A.1: Top cracking pattern of Specimen L0.5.....	193
Figure A.2: Bottom cracking pattern of Specimen L0.5 .....	194
Figure B.1: Failure pattern of Specimen LG0.5.....	195
Figure B.2: Failure surface of Specimen LG0.5 .....	196
Figure B.3: Failure pattern of Specimen LG1.0.....	196
Figure B.4: Failure surface of Specimen LG1.0 .....	197

# Chapter 1

## Introduction

### 1.1 DESCRIPTION OF FLAT-PLATE STRUCTURE

A flat-plate structure, as shown in Figure 1.1, consists of a slab with uniform thickness supported on the columns with no beams or drop panels. Conventionally reinforced flat-plate systems are generally used for lightly loaded structures such as residential or office buildings with relatively short spans, typically less than 24 feet. For longer spans or heavier loads, flat-slabs system with shear capitals or drop panels would be more feasible.

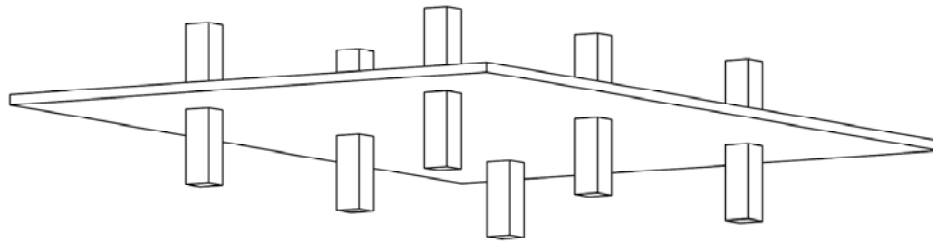


Figure 1.1: Flat-plate structure.

Flat-plates have been widely used due to the reduced construction cost associated with the simple formwork and simple arrangement of flexural reinforcement. An additional advantage of a flat-plate is reduced building story heights that result in more usable space in a building for a given or limited height.

In spite of the above advantages, several drawbacks of flat-plate exist. First, such a structure is prone to slab punching failure that takes place locally at the column due to

highly concentrated shear and slab bending. Such failure must be avoided since the gravity loads initially carried by the connection that fails in punching would be transferred to other supports. The gravity load redistribution may cause subsequent punching failure at adjacent connections, leading to large scale collapse of the floor and even catastrophic progressive collapse of the building. Figure 1.2 shows the collapse of a 16-story residential building that occurred in Boston in 1971. The collapse was triggered by punching failure initiated at a slab-column connection at the roof level and propagated to all floors (King and Delatte, 2004).

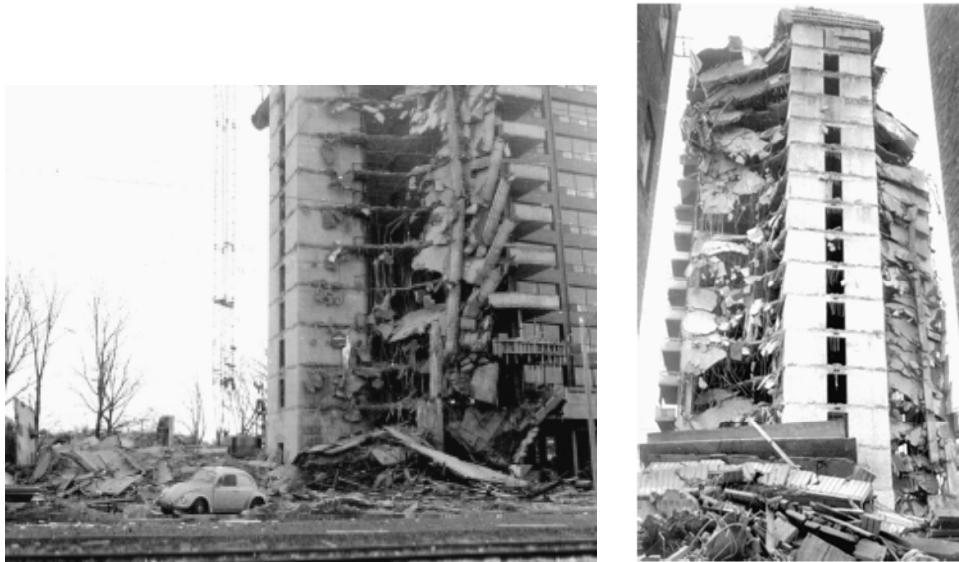


Figure 1.2: Partial collapse of a flat-plate structure (reproduced from the paper by King and Delatte, 2004).

When a slab-column connection carries both gravity load and unbalanced moment induced by wind or seismic load, significant shear and bending moment are concentrated at one side of the column where punching failure may occur. Collapse of several flat-plate buildings during the 1985 Mexico City earthquake has been reported by Ghali and Megally (2000).

Second, flat-plate structures are inherently flexible. Under service level gravity loads, the slab may exhibit extensive cracking around the column that reduces the slab-column connection stiffness and may result in unacceptable slab deflection.

## **1.2 STATEMENT OF PROBLEM**

Despite research progress and code improvements, several concerns emerged from evaluation of existing flat-plate structures. First, any change in building function may require the structure to carry more gravity load than that considered in the original design. Guidelines for realistically evaluating the gravity load-carrying capacity of the existing flat-plates are needed.

Second, seismic loads may significantly damage the slab-column connections. Given that concrete must provide a major portion of the shear resistance at a connection, post-earthquake gravity load-carrying capacity becomes a major concern.

Third, many existing flat-plates located in the seismic regions were designed without any seismic consideration. There is little experimental data regarding the behavior of non-ductile slab-column connections under seismic loading.

Fourth, there is a lack of simple but relatively accurate analytical tools for modeling the nonlinear behavior of a slab-column connection subjected to lateral loading.

## **1.3 RESEARCH SCOPE AND OBJECTIVES**

The study presented herein composes part of the two research projects sponsored by the National Science Foundation. The experiments involved were used for research on: (1) the structural evaluation of existing slab-column connections, (2) the application of non-destructive testing techniques in assessing the degree of damage of slab-column connections (Argudo, 2006), and (3) the investigation of various connection rehabilitation and repair techniques (Widianto, 2006).

The research presented herein focuses on the behavior and modeling of interior slab-column connections of the existing flat-plate structures subjected to various loading conditions. Only connections constructed with normal-weight concrete and supported on square columns without any slab shear reinforcement were considered.

The objectives of this research were to:

- Investigate the failure mechanism of interior slab-column connections subjected to (1) concentric gravity loading and (2) combined gravity and lateral cyclic loading.
- Investigate the gravity load-carrying capacity of slab-column connections with and without earthquake damage.
- Develop a nonlinear behavioral model capable of predicting the lateral strength and stiffness characteristics of slab-column connections subjected to combined gravity and lateral cyclic loads.

Combined experimental and analytical research was conducted to accomplish the above goals. Five slab-column connection subassemblies were tested under different loading and boundary conditions at the Ferguson Structural Engineering Laboratory at the University of Texas. The insight gained through the test program facilitated the development of an analytical model.

#### **1.4 PREVIOUS RESEARCH AND CODE DESIGN REQUIREMENTS**

Two categories of research and design requirements for the interior slab-column connections of a flat-plate structure are summarized in this section: (1) connection punching strength under gravity load only, and (2) behavior and modeling of a connection subjected to combined gravity and lateral loading.

## 1.4.1 Interior Slab-column Connections Subjected to Concentric Gravity Loading

### 1.4.1.1 Experimental Research

Experimental investigation of slab-column connections under concentric gravity loading started as early as 1913, when footing test results were published by Talbot (1913). Since then considerable experimental research has been conducted on isolated specimens with a focus on the two-way shear capacity of slab-column connections.

Figure 1.3(a) shows a widely used test scheme where the slab was supported along its four edges with the corners free to lift up and was loaded through the center column stub. In most early tests, no column stub extended beyond the slab tension surface.

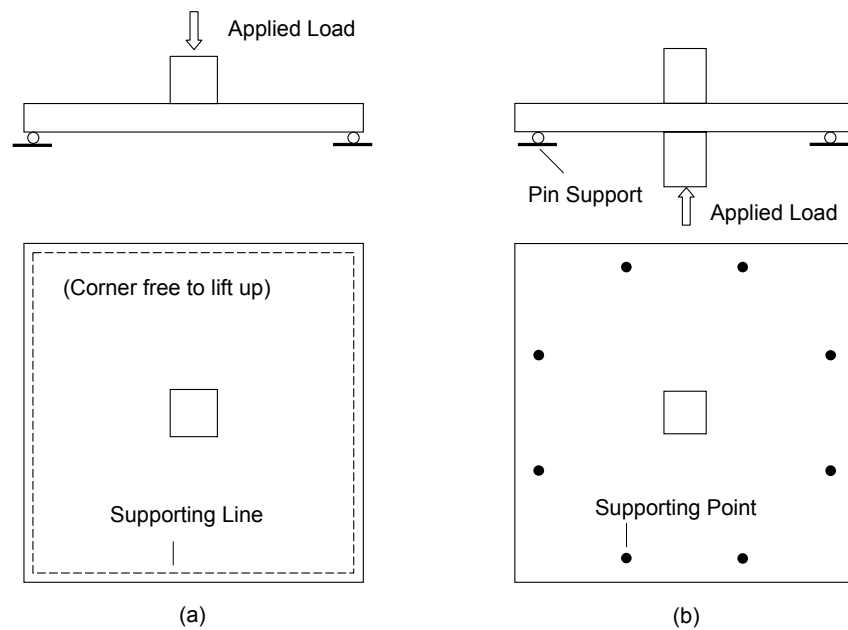


Figure 1.3: Punching test schemes for isolated slab-column connections.

Figure 1.3(b) shows the test setup used recently by Alexander and Simmonds (1992), Ospina et. al. (2003), and McHarg et. al. (2000). In the isolated connection tests,

the supporting lines or points were intended to simulate the contraflexure points in a prototype structure that were assumed to be located at a distance of 20% of the span length from the columns.

Representative experimental studies of slabs supported on square columns and the associated findings are selected and briefly described as follows.

***Elstner and Hognestad (1956)***

Elstner and Hognestad (1956) reported 30 tests of slabs without shear reinforcement. Twenty-five 6-ft. square and 6-in. thick slabs were tested using the setup shown in Figure 1.3(a). Major variables included concrete compressive strength (2000 to 7300 psi), tension reinforcement ratio (0.55 to 3.7%), layout of reinforcement (with or without reinforcement concentration around the column), and column size (10 in. and 14 in.).

The final failure of all specimens involved the punching of the slab around the column. For highly-reinforced slabs, brittle shear failure occurred at small center deflection. However, yielding in tension bars was identified in most slabs including those having a slab reinforcement ratio as high as 2.5%. Three slabs with low tension reinforcement ratios (0.5% and 0.55%) developed overall yielding, beyond which the slab center deflection increased remarkably to about 1 in. when a punching failure occurred. No concrete crushing at failure was reported regardless of the amount of slab tension reinforcement.

Based on the test findings, Elstner and Hognestad concluded that: (1) shear and flexure must be treated as a combined loading problem for a slab, not as two separate cases; (2) connection shearing strength is a function of concrete strength as well as other variables; (3) concentrating 50% of the tension reinforcement (for slabs with overall

reinforcement ratio 2.47%) directly over the column did not increase the shearing strength; (4) for slabs with low reinforcement ratios, the measured capacity was 10 to 20% higher than the strength predicted by the yield-line theory.

$V_n$ , the ultimate strength for slabs that failed in shear, was suggested using an explicit equation as

$$V_n = \frac{7}{8} b d f_c' \left( \frac{333}{f_c'} + \frac{0.046}{\phi_o} \right) \quad (1.1)$$

where  $b$  is the column circumference,  $d$  the slab effective depth,  $f_c'$  the concrete cylinder compressive strength (in *psi*), and  $\phi_o$  the ratio of  $V_n$  to the capacity determined from the yield-line theory,  $V_{flex}$ . Equation (1.1) can be rearranged to solve for  $V_n$ .

### ***Moe (1961)***

Moe tested 12 specimens without the presence of either shear reinforcement or holes adjacent to the column to investigate shear failure mechanisms under pure gravity loading. The slabs had the same geometry as those tested by Elstner and Hognestad (1956), except that the column size was 12-in. or 6-in. for some specimens. Main variables included reinforcement ratio and tensile reinforcement concentration around the column.

In the tests, inclined cracks usually started from bending cracks, developed as early as 50% of the ultimate load, and extended rapidly to the neutral axis. Subsequently, the inclined cracking extended gradually toward the slab compressive region without introducing immediate punching failure. In many cases, the compression zone that remained intact was fairly shallow when the ultimate load was reached. The characteristics of punching shear failure after extensive flexural yielding was quite different from that of a beam without web reinforcement.

Moe found two-way shear strength of slabs and footings to be a function of the slab flexural strength. Moreover, concentration of flexural reinforcement in narrow bands across the column did not increase the shearing strength. However, such concentration increased the slab stiffness as well as the load at first yielding. The above findings confirmed the test observations by Elstner and Hognestad (1956). Moe also stated that the shear force developed in the tension bars crossing the inclined cracks, termed as dowel action, and the extensional force in the slab plane, referred to as membrane action, could be neglected. He further concluded that the shear has to be carried entirely by the concrete compression zone at the inclined cracks.

With the shearing strength of the concrete assumed to be proportional to  $\sqrt{f'_c}$ , Moe expressed the shear capacity of a slab-column connection as

$$V_n = bd\sqrt{f'_c} \left[ A \left( 1 - C \frac{r}{d} \right) - B\phi_o \right] \quad (1.2)$$

where  $r$  is the column size;  $A$ ,  $B$ , and  $C$  are constants; and the other variables are defined as in Equation 1.1.

Based on the test data of 106 footings and 37 slabs that failed in shear ( $\phi_o < 1$ ), the three constants  $A$ ,  $B$ , and  $C$  in Equation 1.2 were determined and the ultimate shearing strength was formulated as

$$V_n = \left( bd\sqrt{f'_c} \right) \left[ \frac{15 \left( 1 - 0.075 \frac{r}{d} \right)}{1 + 5.25 \frac{bd\sqrt{f'_c}}{P_{flex}}} \right] \quad (1.3)$$

It must be noted that, for the slabs where punching failure was a secondary phenomenon ( $\phi_o < 1$ ), the above equation did not apply.

***Marzouk and Hussein (1991)***

Marzouk and Hussein (1991) reported tests of 17 slabs with varying concrete strength (4350 to 11600 psi), slab thickness (3.5 to 5.9 in.), tension reinforcement ratios (0.64 to 2.37%), and column sizes (5.9 to 11.8 in.).

Major conclusions derived from this investigation included: (1) punching failure of high strength concrete slabs can be classified into two modes, “flexure-punching” and “punching shear” failure. Flexural-punching occurred in the slabs with relatively low reinforcement ratio; (2) as reinforcement ratio increased, slab stiffness increased and deformation capacity decreased; (3) Equation 1.3 suggested by Moe overestimated the shear capacity of a high-strength concrete slab; (4) relating connection shear strength to the square root of concrete strength resulted in an overestimation of the effect of concrete strength.

***Alexander and Simmonds (1992)***

Using a test setup shown in Figure 1.3(b), Alexander and Simmonds (1992) conducted tests on specimens with a 96-in. square and 6.1-in. thick slab supported on a 7.87-in by 7.87-in. (cross section) column. The investigation focused on the effects of concrete clear cover of the tension flexural reinforcement, bar spacing at the column (effect of reinforcement concentration), and slab boundary conditions.

Three specimens with identical slab geometry and material properties but with different effective depths (therefore different thicknesses of concrete cover) achieved nearly the same loading capacity, indicating that connection punching strength may not be proportional to the slab effective depth. The thickness of concrete cover that resists the doweling effects of slab tensile bars could be equally important for connection punching strength. Based on the bar force profiles, it was claimed that several specimens with

reinforcement concentration at the column failed due to loss of anchorage. The observation convinced the researchers that the failure of specimens with highly-banded reinforcement reported by Elstner and Hognestad (1956) and Moe (1961) was actually an anchorage failure rather than a shear failure.

In addition, the ultimate strength was enhanced by the rotational restraint applied at the slab edges, indicating the significance of test boundary conditions.

***Gardner and Shao (1996)***

Very few tests of continuous flat-plate specimens exist. Gardner and Shao (1996) tested a four-panel specimen with 108-in.-span in each direction, as shown in Figure 1.4. The 5.5-in. thick slab had a 0.79% top reinforcement ratio in the column strip and the size of interior column was 10-in. square. The gravity load acting on the prototype structure was simulated in the test by 40 concentrated vertical loads distributed uniformly over the slab surface.

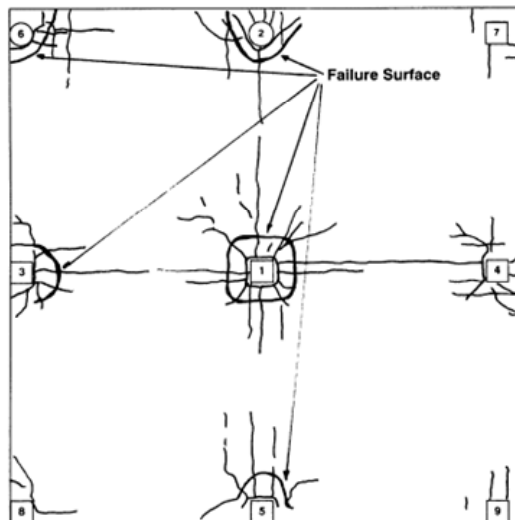


Figure 1.4: Crack patterns and failure surfaces of continuous slab under simulated gravity loading (Gardner and Shao, 1996).

Slab steel yielding, accompanied with significantly wide cracks, developed at the interior column due to the concentrated negative bending. The crack patterns are shown in Figure 1.4. Based on the test observations, it was concluded that: (1) the interior connection was more prone to punching failure than the edge and corner connections; (2) an isolated punching test can represent the behavior of interior slab-column connections in a continuous slab system; (3) punching shear was a “flexural shear” instead of a pure shear phenomenon and a “strut-and-tie” model could be more valid than the shear perimeter (critical section) method to describe the connection strength.

### ***Summary of Experimental Observations***

Punching failure that resulted in an instant loss of gravity load-carrying capacity was observed in all reported slab-column connections. However, punching may not be a shear problem if the overall connection behavior is examined.

The characteristic behavior of slab-column connections under gravity load can be illustrated by Figure 1.5, taken from a study by Criswell (1974). Apart from concrete strength, slab flexural reinforcement had a significant effect on both connection strength and failure mode. Generally, as the tensile reinforcement ratio  $\rho$  decreased, the behavior was more ductile, however, with reduced connection strength. Moe (1961) defined shear failure as one that was mainly caused by transverse forces and took place before the flexural capacity was reached. Flexural capacity was measured by  $V_{flex}$ , the gravity shear at the formation of yield-line mechanism. If the ratio of ultimate load,  $V_u$  to  $V_{flex}$  was less than unity, the failure was classified as a shear failure. Otherwise, the failure was treated as a flexural failure. Thus, a lightly-reinforced slab-column connection would fail predominantly in flexure with punching a secondary phenomenon.

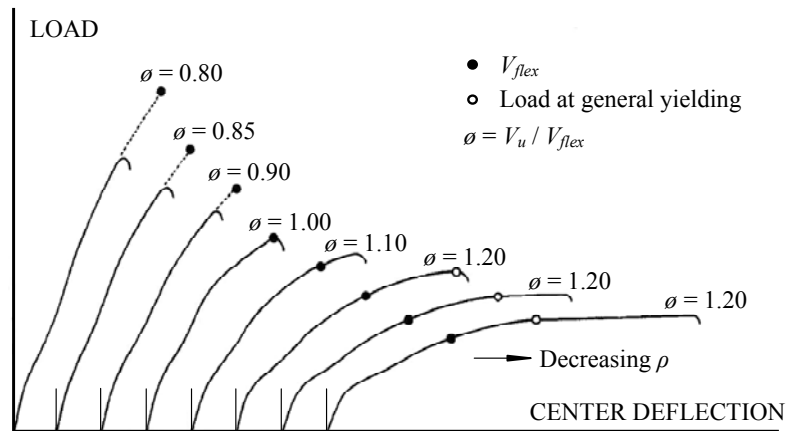


Figure 1.5: Effects of flexural reinforcement on the behavior of slab-column connections under concentric gravity loading (Criswell, 1974).

Note that the behavior of a slab-column connection cannot be compared to that of a beam without transverse reinforcement. For connections that failed in shear, the diagonal tension cracks were usually generated in the early loading stage but remained stable. For connections controlled by flexure, inclined cracking resulted in significant connection deformation but concrete crushing could not be observed in the compression zone in a test.

From experimental investigations, shear capacity of a connection was a function of the following variables:

- (1) The ratio of column size to slab depth,  $c/d$ . Based on the test data, Moe (1961) concluded that the shear strength decreased as the  $c/d$  ratio increased.
- (2) Size effect. The tests conducted by Bazant and Cao (1987) on circular slabs with varying slab thickness demonstrated that the average shear stress at the critical section at peak load decreased as the slab thickness increased.
- (3) Boundary condition. The rotational restraints applied on the slab boundaries had a beneficial effect on the slab punching capacity.

- (4) Span to depth ratio. Lovrovich and McLean (1990) examined the effects of the ratio of slab span to effective depth. Test results indicated that connection shear strength increased with a decrease in the shear span ratio. However, such effect tended to vanish as the shear span ratio became larger than 3, as in a typical slab-column connection.

#### ***1.4.1.2 Mechanical Modeling***

Kinnunen and Nylander (1960) and Alexander and Simmons (1986) developed two different types of mechanical models that can describe the connection punching mechanism and predict the ultimate strength.

##### ***Kinnunen and Nylander's Model (1960)***

Kinnunen and Nylander (1960) suggested a model based on the tests of circular slabs centrally supported on the circular columns and loaded at the slab edges. As shown in Figure 1.6, the idealized model consisted of a central truncated cone enclosed by the inclined cracks and slab segments. The slab segments were separated by radial cracks extending in the slab plane from the center to the edge and supported by an imaginary compressed conical shell located between the column and the inclined crack tip. Each slab segment, assumed to be rigid, rotates around an axis located at the crack tip (denoted as CR in Figure 1.6) under vertical loading. The slab internal forces depended on the rotation angle,  $\psi$ , and material properties. Failure was assumed to occur when the circumferential concrete strain at slab bottom surface underneath the conical shell reaches a critical value that was assumed to be a function of the ratio of column size to the slab effective depth and was calibrated from the test data. The ultimate load was determined from equilibrium as well as the failure criteria described above.

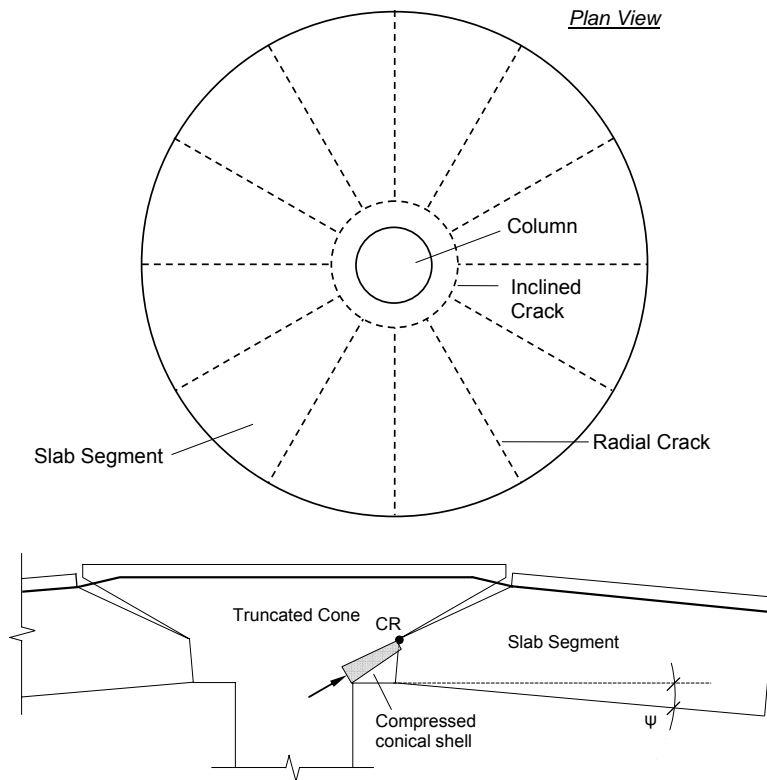


Figure 1.6: Kinnunen and Nylander's model (1960).

The suggested model yielded good agreement with the test results. Because the ultimate load could be predicted regardless of the connection behavior being dominated by flexure or shear, the model provided a continuous transition between the two failure modes. Another prominent capability of this model was the prediction of connection deformation. Although an iterative analytical procedure is required, the model is suitable for computer analysis. A simplified version of the model was proposed by Nylander and Kinnunen (1976).

#### ***Alexander and Simmonds's Truss Model (1986)***

Alexander and Simmonds (1986) suggested a space truss model composed of steel tension ties and concrete compression struts (shaded area in Figure 1.7) inclined at

an angle  $\alpha$  to the slab plane. The fundamental assumptions made for this model included: (1) the steel bars at the vicinity of column function as tension ties and yield before failure; (2) punching occurs when the concrete cover spalls due to a vertical component of the compression strut at the intersection of compression struts and tension ties.

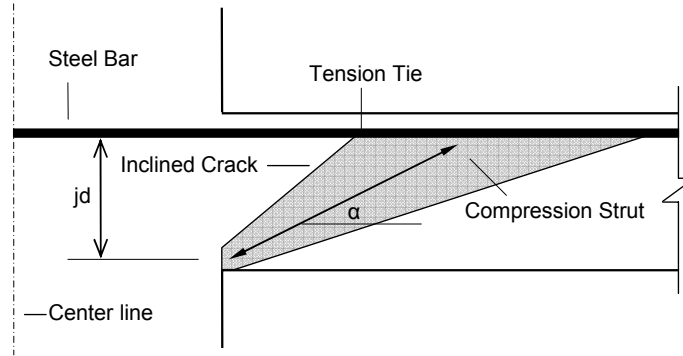


Figure 1.7: Truss model (Alexander and Simmonds, 1986).

The inclined angle,  $\alpha$ , was assumed to be a function of several variables including tension bar spacing, concrete strength, bar area and yield strength, column size, and slab effective depth. Although a straight-line compression strut was initially suggested (Figure 1.7), Alexander and Simmonds (1992) later concluded that a curved compression strut with varying  $\alpha$  along the slab depth was more consistent with the test data.

An alternative approach, as expressed by Equation 1.4, was developed for predicting the punching capacity of a slab supported on the square column and equally reinforced in two orthogonal directions.

$$V_n = 8\sqrt{M_s w_{ACI}} \quad (1.4)$$

where  $M_s$  is the sum of negative moment capacity at column and the midspan positive moment capacity evaluated in a slab strip of width  $c$ , and  $w_{ACI}$  is the one-way shear capacity per unit width of the strip, defined as  $w_{ACI} = 2d\sqrt{f'_c}$ .

Equation 1.4 correlated the connection punching strength with the slab flexural capacity and provided a lower-bound estimation of the connection capacity.

#### ***1.4.1.3 Code Requirements for Two-way Shear***

Most code provisions regarding the two-way shear design of a slab-column connection use the critical section (control perimeter) approach. According to this method, the nominal shear stress due to gravity load is determined at an assumed vertical critical section around the column. The shear stress should be limited to a nominal shear strength usually assumed to be a function of concrete strength and geometric parameters. Although such a method lacks physical reality, it is simple and leads to reasonable estimates if properly formulated (Regan and Braestrup, 1985).

Different codes define considerably different critical section locations and hence different associated nominal shear strength. Also, the ways in which parameters affecting the connection punching strength are considered are significantly different.

The evolution of shear design requirements of slab-column connections in ACI code is reviewed. Current code requirements in ACI 318-05 and CEB-FIP MC90, two representative building codes, are discussed.

#### ***ACI 318 Code Evolution***

The working stress method was used to design flat-plate structures before the ultimate strength design approach was adopted in ACI 318-63.

In ACI 318-51, the shearing stress was calculated at the critical section specified at a distance equal to the slab thickness minus 1.5 in. from the column face. The nominal shear stress, determined from Equation 1.5, was required to be limited to: (1)  $0.03 f_c'$  (psi), if at least 50% of total tensile reinforcement in the column strip passes directly over

the column; (2)  $0.025 f_c'$  (psi), if 25% or less of the tensile bars in the column strip passed directly over the column; (3) linear interpolation of those stress limitations, if the percentage ratios were between 25% and 50%.

$$v = \frac{V}{bj(h-1.5)} \quad (1.5)$$

where  $v$  is the nominal shear stress,  $b$  the critical section perimeter,  $V$  the service level gravity shear transferred from the slab to the column,  $h$  the slab thickness,  $j$  the ratio of distance between centroids of compression and tension zone to the slab effective depth.

In ACI 318-56, the critical section was defined at a distance  $d$  beyond the column face and the nominal shear stress was calculated using Equation 1.6. The allowable shearing stress was the same as in ACI 318-51 except that limiting values of 100 psi and 85 psi were also applied for cases (1) and (2), respectively.

$$v = \frac{V}{bjd} \quad (1.6)$$

Working stress and ultimate strength design approaches coexisted in ACI 318-63. The two-way shear design recommended in ACI 318-63 was based on an investigation by joint ACI-ASCE Committee 326 (1962) that simplified Equation 1.3 and a design equation was derived from a conservative fit to data from tests that failed in shear ( $V_u > V_{flex}$ ). Thus, it is evident that Moe's definition of connection failure modes was inherent in ACI code provisions. The assumed critical section was changed to be located at a distance  $0.5d$  from the column periphery and the shear strength was correlated with  $\sqrt{f_c'}$ . For the working stress design method, it was required that the nominal shear stress under service gravity load, calculated from Equation 1.7, should not exceed  $2\sqrt{f_c'}$  (psi).

$$v = \frac{V}{b_o d} \quad (1.7)$$

where  $b_o$  is the perimeter of the critical section.

For the ultimate strength design approach, factored gravity load,  $V_u$ , was determined using a load combination factor of 1.5 for the dead load and 1.8 for the live load. The nominal shear stress, calculated from Equation 1.8, was limited to  $4\phi\sqrt{f'_c}$ , where  $\phi$  is the strength reduction factor equal to 0.85.

$$v_u = \frac{V_u}{b_o d} \quad (1.8)$$

In ACI 318-71, the working stress design method was eliminated. The shear design of a slab-column connection using ultimate strength design was the same as in ACI 318-63 except that the load combination factor was reduced to 1.4 for the dead load and 1.7 for the live load (if only these two types of load were considered). Since then, the rules for connection two-way shear design have changed little.

It is noted that the working stress approach usually yielded a more conservative shear design. Consider an interior slab-column connection having a 20-ft span in each direction, column size of 21 in. by 21 in., specified concrete compressive strength of 3000 psi, live load of 50 psf, and partition load of 20 psf. Assuming  $d = 0.85h$ , and  $j = 0.95$ , the slab thickness required by shear design following the different editions of the ACI 318 is shown in Table 1.1.

Table 1.1: Required Slab Thickness for An Example Slab-Column Connection

Design Approach	Working Stress					Ultimate Strength	
ACI Code Edition	318-51 Case (a)	318-51 Case (b)	318-56 Case (a)	318-56 Case (b)	318-63	318-63	318-71
Required $h$ (in)	10.2	8.6	11.5	9.2	8.9	7.4	6.8

### **ACI 318-05**

ACI 318-05 requires that  $v_u$ , the nominal shear stress at an interior slab-column connection calculated from Equation 1.8, should satisfy

$$v_u \leq \phi 4 \sqrt{f_c'} \quad (1.9)$$

$$v_u \leq \phi \left( 2 + \frac{4}{\beta_c} \right) \sqrt{f_c'} \quad (1.10)$$

$$v_u \leq \phi \left( \frac{40d}{b_o} + 2 \right) \sqrt{f_c'} \quad (1.11)$$

where  $\phi = 0.85$  and  $\beta_c$  is the length ratio of long side to short side of the column.

Equation 1.10 was used for connections with rectangular columns. Equation 1.11 was introduced since tests indicated that shear strength decreases as the ratio  $b_o/d$  increases. However, this equation is not effective unless  $b_o/d$  is larger than 20. Thus, for interior connections with square columns of typical size and without shear capitals or drop panels, the shear design is governed by Equation 1.9.

### **CEB-FIP MC90**

CEB-FIP MC90 (1991), the model code for concrete structures prepared by the Comité Euro-International du Béton (CEB) and Fédération International de la Précontrainte (FIP), defined the control perimeter as shown in Figure 1.8 (a) to be the minimum length taken  $2d$  from the column surface. Figure 1.8 (b) shows as a comparison the critical section defined in ACI 318-05. The two-way shear design is prescribed in CEB-FIP MC90 as

$$\frac{V_u}{ud} \leq v_c = 0.18 \xi (100 \rho f_{ck})^{1/3} / \gamma_c \quad (\text{in N-mm units}) \quad (1.12)$$

where  $u = 2(c_1 + c_2 + 2\pi d)$ ,  $\xi = 1 + (200/d)^{1/2}$  (the size effect term);  $f_{ck}$  = the cylinder concrete compressive strength;  $\gamma_c = 1.5$ , the partial safety factor;  $\rho$  = slab tensile reinforcement ratio evaluated in a width equal to the side dimension of the column plus  $3d$  to either side of it.

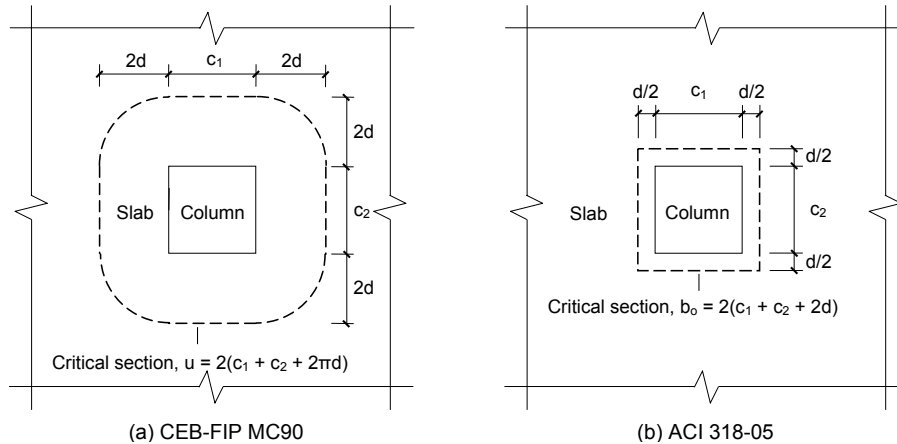


Figure 1.8: Critical section location: (a) CEB-FIP MC90, and (b) ACI 318-05.

## 1.4.2 Interior Slab-Column Connections Subjected to Lateral Loading

### 1.4.2.1 Experimental Research

It was not until the 1970's that the behavior of flat-plates under seismic type loading became the subject of research. However, compared with the experimental studies on slab-column connections under pure gravity load, test data regarding connections subjected to combined gravity and lateral loads is relatively meager.

Typical test schemes are shown in Figure 1.9. Due to the constraints on specimen size, most tests were carried out on the isolated slab-column connections. Setup A was used in the early tests. The gravity load was first simulated by slab self-weight as well as the additional weight applied on the slab surface and then the seismic effect was

simulated by applying a cyclic load at the slab edges. For the test schemes B and C, two slab edges were supported on the struts that functioned as rollers. The lateral movement of the column lower end was restrained while cyclic loading was applied at the top of the column. Gravity load was simulated by placing extra weight on the slab in scheme B or by vertically applying an upward load through the column in scheme C.

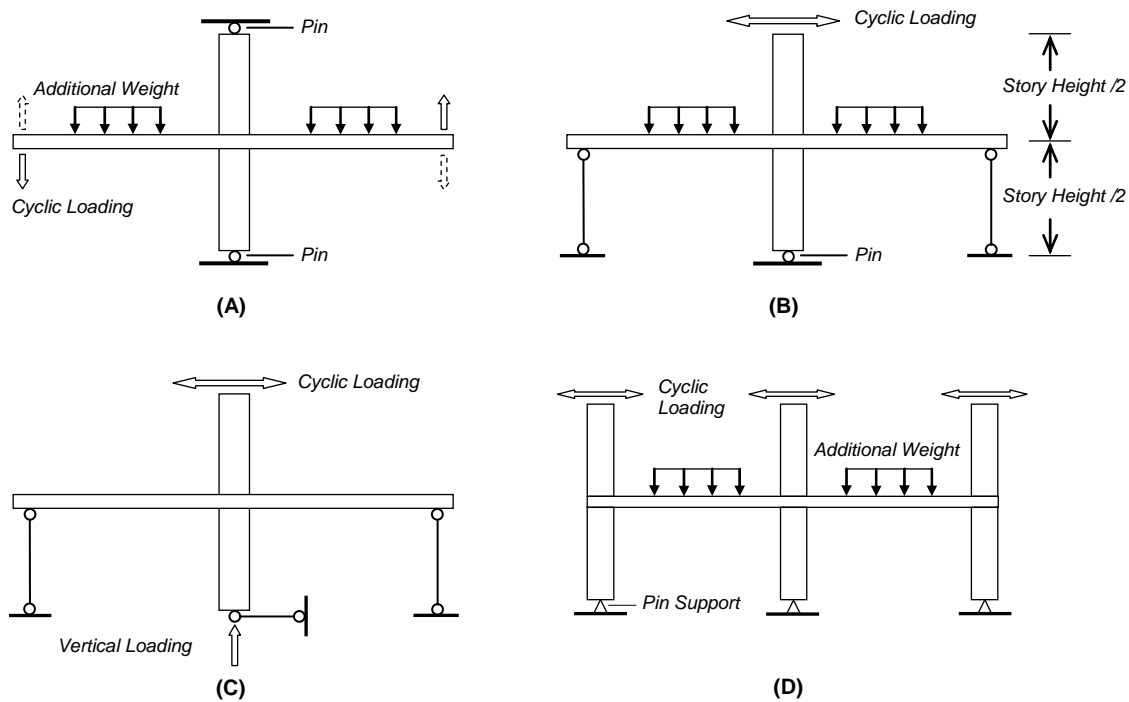


Figure 1.9: Test schemes for slab-column connections subjected to combined gravity and lateral loads.

Tests on continuous flat-plates usually involved a structure with two to three bays in the lateral loading direction, as illustrated by scheme D in Figure 1.9. The behavior of both exterior and interior slab-column connections can be investigated in such tests.

Slab top reinforcement ratio around the column and the gravity load level applied on the specimens were generally the main variables investigated. The gravity load level

was often measured by a gravity shear ratio defined as  $V_g/V_c$ , the ratio of gravity shear transferred from the slab to the column to the nominal two-way shear strength based on Equation 1.9 (without using a  $\phi$  factor).

Major findings from the tests on interior slab-column connections without shear reinforcement are summarized as follows.

***Hawkins, Mitchell, and Sheu (1974)***

Using test setup A shown in Figure 1.9 and cyclic loading (controlled by load), Hawkins, Mitchell, and Sheu (1974) tested four isolated slab-column connections with slab tensile reinforcement ratios ranging from 0.6% to 1.3% and gravity shear ratios,  $V_g/V_c$ , from 0.34 to 0.45.

The specimens experienced significant stiffness degradation at the following characteristic stages: (1) concrete cracking at the slab-column interface, (2) first yielding of the slab top bars passing through the column, and (3) yielding of the bottom bars passing through the column and the top bars situated within a width of approximately  $c+2h$  centered on the column. It was claimed that (1) connection lateral strength could be dominated by first yielding of flexural reinforcement, and (2) the connection lateral deformation beyond concrete cracking was caused by bond slip of the slab tensile reinforcement at the column, which initiated a slab rigid body motion relative to the column.

***Ghali, Elmasri, and Dilger (1976)***

Ghali, Elmasri, and Dilger (1976) reported six isolated slab-column connections subjected to monotonic lateral loading. High speed lateral loads were applied on three specimens and static lateral loads on the others. The top reinforcement ratio of these specimens ranged from 0.5 to 1.5% and the  $V_g/V_c$ -ratio was around 0.30.

Although all statically loaded specimens failed in a punching failure mode, the specimen with a top reinforcement ratio of 0.5% reached significant lateral deformations after general yielding was achieved. Tests indicated that, as reinforcement ratio increased, the connection lateral strength also increased but with reduced lateral deformation capacity.

The connections subjected to high speed lateral loading reached both higher moment-carrying capacity and higher energy adsorption capacity, indicating loading rate had an effect on connection behavior.

#### ***Morrison, Hirasawa, and Sozen (1983)***

Morrison, Hirasawa, and Sozen (1983) reported five tests of isolated specimen with relatively large size columns. The reinforcement ratio ranged from 0.7 to 1.4% and  $V_g/V_c$ -ratio from 0 to 0.16.

All specimens failed by punching during lateral loading. However, such failure appeared to be secondary since the connections were able to develop general yielding in the lateral load-drift response envelopes and a joint rotation exceeding 0.04 rad. was reached at failure. Both connection lateral stiffness and strength were reduced by the presence of gravity load, but reduction in strength was not proportional to the gravity load level and the effect of low gravity load on connection lateral behavior was not significant.

#### ***Pan and Moehle (1992)***

Since the 1980's, lateral deformation capacity became the primary research focus of slab-column connections. Pan and Moehle (1992) tested four 3/5-scale isolated connections using the test setup B shown in Figure 1.9. Major variables included gravity load level and lateral loading history. Two specimens were subjected to a uniaxial cyclic

lateral load combined with different gravity loads ( $V_g/V_c = 0.22$  and  $0.35$ ) acting on the slab. For the two other specimens, lateral load with increasing displacement magnitude was applied bi-axially by alternating the loading directions along two principal axes.

Tests indicated that both increased gravity load level and biaxial lateral loading reduced the lateral stiffness, strength, and deformation capacity of slab-column connections. The continuous bottom bars passing through the column effectively suspended the slab after punching failure and were therefore suggested to be used in a flat-plate structure for preventing a progressive collapse.

#### ***Durrani, Du, and Luo (1995)***

Using test scheme D shown in Figure 1.9, Durrani, Du, and Luo (1995) tested four continuous slab specimens with varying gravity loads applied on the slab. The behavior of lightly-reinforced flat-plate structures designed prior to the 1971 ACI building code and featuring discontinuous bottom reinforcing bars at the columns was investigated.

It was found that gravity load affected the connection behavior including failure mode, lateral stiffness, and lateral strength. Two specimens with low gravity load were dominated by flexure and exhibited a drift capacity larger than 4%. Two other specimens with higher gravity load failed in punching after general yielding was evident or nearly reached. The specimen with a gravity load as high as  $V_g/V_c = 0.37$  was able to sustain a lateral drift of 2%.

The exterior connections were observed to lose stiffness much faster than the interior connection. Consequently, more gravity load was distributed to the interior connection, making it more prone to punching failure.

### ***Connection Deformation Capacity***

Even if other structural components, such as shear walls or perimeter moment frames, are used as the primary system to resist lateral loads, slab-column connections should have sufficient rotational capacity to avoid a punching failure so that the gravity load-carrying capacity can be maintained under seismic excitations. Therefore, deformation capacity is of particular concern for slab-column connections subjected to lateral loads.

As described previously, test data strongly indicated the trend of connection deformation capacity being reduced by the increased gravity load. The connection deformation capacity, generally expressed as the inter-story drift ratio, was empirically formulated by Pan and Moehle (1989), Megally and Ghali (2000), Durrani, Du, and Luo (1995), Hueste and Wight (1999), and Robertson and Johnson (2006). It is noted that the ratio of  $V_g/V_c$  has been hitherto formulated as the only variable affecting the connection deformation capacity.

In ACI 318-05, the effect of gravity load on drift capacity of a flat-plate structure was recognized and the following percentage drift limitations were recommended:

$$Drift(\%) = \begin{cases} 3.5 - 5 \frac{V_g}{V_c} & \frac{V_g}{\phi V_c} \leq 0.60 \\ 0.5 & \frac{V_g}{\phi V_c} > 0.60 \end{cases} \quad (\phi = 0.75) \quad (1.13)$$

#### ***1.4.2.2 Analysis and Design Methods***

##### ***ACI Code Approach for Shear Design***

The ACI shear design approach for an interior slab-column connection resisting an unbalanced moment, defined as the moment transferred between the slab and the

column, is based primarily on work by Hanson and Hanson (1968). It is assumed that a fraction,  $\gamma_f$ , of the factored unbalanced moment,  $M_u$ , is resisted by flexure, where  $\gamma_f$  is defined as

$$\gamma_f = \frac{1}{1 + \frac{2}{3} \sqrt{\frac{b_1}{b_2}}} \quad (1.14)$$

and  $b_1$  and  $b_2$  are the width of the critical section measured in the direction parallel and perpendicular to the lateral load, respectively.

The flexural reinforcement used to resist  $\gamma_f M_u$ , in addition to the reinforcement required by the factored gravity load, should be placed in a width of  $c_2 + 3h$  centered on the column. Another portion of the unbalanced moment not resisted by flexure,  $\gamma_v M_u = (1 - \gamma_f) M_u$ , is assumed to be carried by a so-called eccentric shear stress, a linear variation of concrete shear stress around the same critical section as defined for pure gravity loading. The shear stress due to  $\gamma_v M_u$  is then superimposed with the gravity-induced shear. The resulting eccentric shear stress distribution is shown in Figure 1.10 and maximum shear stress is given by Equation 1.15.

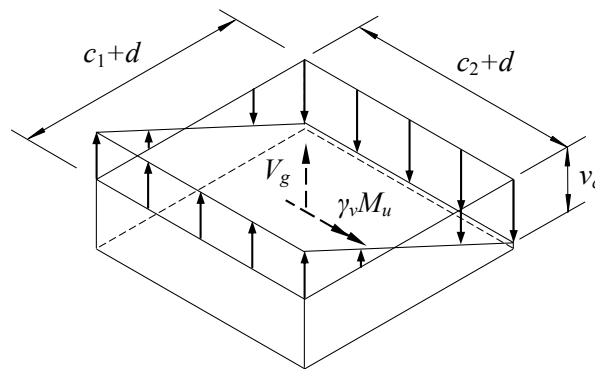


Figure 1.10: Eccentric shear stress model.

$$v_u = \frac{V_g}{A_c} + \frac{\gamma_v M_u \left( \frac{c_1 + d}{2} \right)}{J_c} \quad (1.15)$$

where  $A_c$  is the critical section area;  $V_g$  is the gravity shear; and  $J_c$  is a property of the section analogous to a polar moment of inertia and expressed as

$$J_c = \frac{d(c_1 + d)^3}{6} + \frac{(c_1 + d)d^3}{6} + \frac{d(c_2 + d)(c_1 + d)^2}{2} \quad (1.16)$$

where  $c_1$  and  $c_2$  are the column size in the direction transverse and parallel to the unbalanced moment vector, respectively. The maximum stress,  $v_u$ , should not exceed the concrete shear strength defined as the minimum value determined from Equations 1.9 through 1.11.

### ***Beam Analogy***

A beam analogy can be used to formulate the connection lateral strength by describing all the forces acting on an assumed perimeter surrounding the connection, often taken for convenience as the code-prescribed critical section for shear.

As shown in Figure 1.11, under the unbalanced moment  $M_u$  and gravity load  $V_g$ , shear and bending moment act on the critical section faces AD and BC, while shear, bending moment, and torsion act on the faces AB and CD. Equilibrium requires

$$M_u = M_{DA} + M_{BC} + T_{AB} + T_{CD} + (V_{AD} + V_{BC}) \left( \frac{c_1 + d}{2} \right) \quad (1.17)$$

$$V_g = V_{AB} - V_{BC} + V_{CD} + V_{DA} \quad (1.18)$$

Although rational, the beam analogy approach is generally difficult to apply in a connection design because multiple failure modes associated with various actions must be considered.

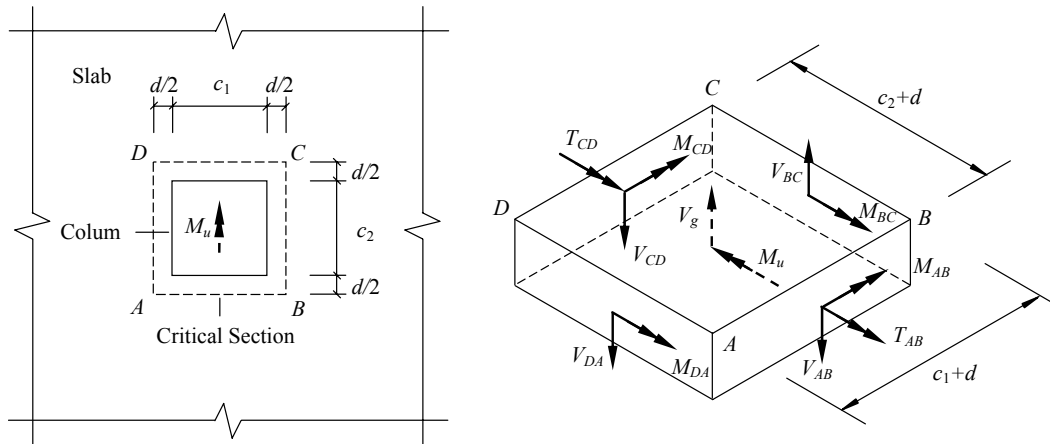


Figure 1.11: Beam analogy.

***Akiyama and Hawkins's Model (1984)***

Akiyama and Hawkins (1984) developed an analytical model, as shown in Figure 1.12, for nonlinear dynamic analyses of flat-plate structures using the beam analogy concept. Slab nonlinearity was assumed to be concentrated around the column and was modeled by means of flexural elements, torsional elements, and bond-slip elements. Rigid connecting bars were used to impose deformation compatibility among the flexural element, torsional elements and the elastic slab. Three characteristic loading stages including cracking, yielding, and ultimate strength were defined for the torsional and flexural elements.

Data of some tests conducted at the University of Washington (Hawkins, Mitchell, and Sheu, 1974) were used to calibrate crucial parameters of the model, while other tests in the same experimental investigation were used to evaluate the suggested model. Fair agreement was achieved between the experimental results and the predictions from the suggested model. The model was also used to analyze the dynamic response of Holiday Inn, Orion Avenue, that experienced the 1971 San Fernando Earthquake. Again, reasonable agreement was found between measured and predicted dynamic response.

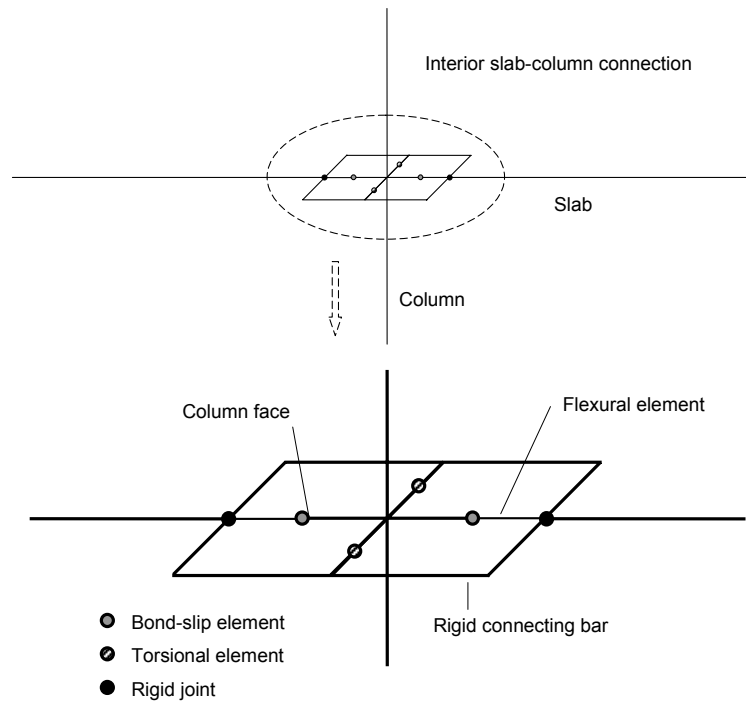


Figure 1.12: Nonlinear model for interior slab-column connections suggested by Akiyama and Hawkins (1984).

### ***Hueste and Wight's Model (1999)***

Hueste and Wight (1999) proposed a 2D nonlinear frame model for slab-column connections that focused mainly on predicting connection punching failure and post-punching behavior of a flat-plate structure.

A conventional beam element consisting of an elastic line element, two nonlinear rotational springs, and two rigid end zones was used to model the slab. The slab flexural strength was taken as 1.25 times the yield strength evaluated from the full slab width. Stiffness characteristics of the cracked slab were simulated using  $0.5I_g$  ( $I_g$  is the moment of inertia for the full gross slab section) as the moment of inertia for the elastic line element. The elastic stiffness of the rotational spring was related to  $2/3I_g$  for negative bending and  $1/3I_g$  for positive bending for interior slab-column connections. One critical

parameter related to the connection deformation capacity was  $\theta_{cr}$ , defined as the spring rotation at which punching failure occurs. The model requires a pushover analysis up to certain inter-story drift levels without consideration for punching failure. Based on a user-specified relationship between drift capacity and gravity shear,  $\theta_{cr}$  can be determined from the pushover analysis and then incorporated into the hysteretic model developed by Al-Haddad and Wight (1986) and Raffaele and Wight (1992) for reinforced concrete members. The post-punching behavior was simulated by modifying the member-end rigidity to account for the loss of rotational stiffness caused by punching.

The proposed model was used for a nonlinear dynamic analysis of a four story RC flat-slab building (with shear capitals) that suffered punching damage at interior slab-column connections during the 1994 Northridge earthquake. The punching damage was predicted after the earthquake using the suggested model.

## **Chapter 2**

### **Design of Experimental Program**

#### **2.1 GENERAL**

In this chapter, the design and construction of a series of isolated slab-column connections simulating the behavior of an interior connection in continuous flat-plate structures subjected to gravity and combined gravity and lateral loadings is presented. The prototype structure is described first. Then the overall test scheme is presented. Inelastic analyses using the finite element method (FEM) are conducted to facilitate the determination of testing boundary conditions that provided information for detailed design of the test setups. The details of the specimens including reinforcement layout, material properties, and fabrication procedures are described. The instrumentation of these specimens for testing is discussed.

#### **2.2 DESCRIPTION OF PROTOTYPE STRUCTURE**

The prototype structure is a multistory office building located in a high seismic region. With a 12 ft story height, four bays in the short direction and five bays in the long direction, this structure consists of a flat-plate floor system combined with exterior perimeter frames. A partial structure that represents the lower story and contains the interior slab-column connection to be investigated is cut from the prototype building by two horizontal planes passing through mid-height of the columns and illustrated in Figure 2.1 (without showing the perimeter frames). The 9 in. thick reinforced concrete slab is

supported on 24 in. by 24 in. square columns without shear capitals or drop panels and spans 21 ft. measured from column center to center in each direction.

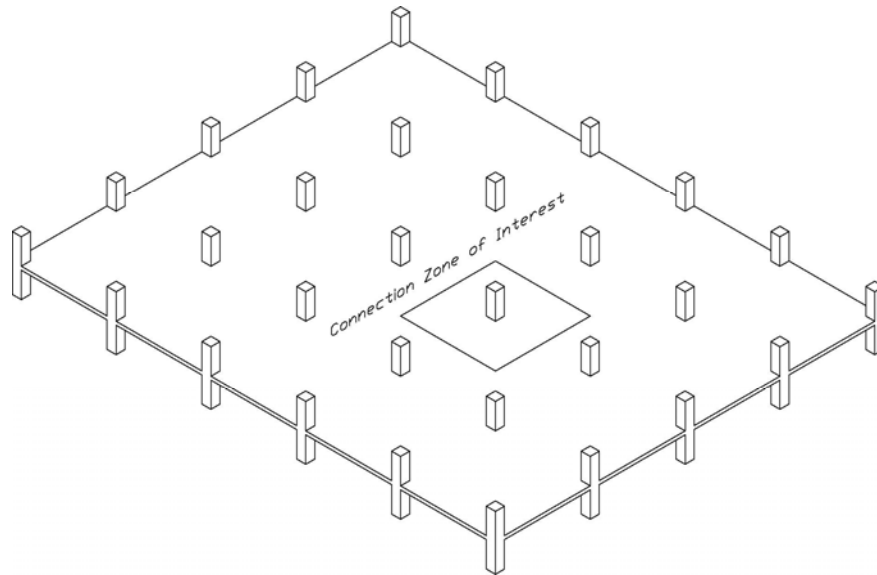


Figure 2.1: Prototype structure.

It was assumed that the perimeter frames were designed to provide lateral seismic resistance, whereas the slab-column framing was designed to carry only gravity loads. The service gravity load included a 112.5 psf self-weight of the slab, 20 psf additional dead load accounting for the weight of floor finishes and partition walls, and 50 psf superimposed live load. It was also assumed that only 25% of the live load, in addition to the dead loads, was acting on the floor in the event of earthquake. The slab was constructed using Grade 60 reinforcement and concrete with a specified 4000 psi compressive strength.

The sectional design of slab flexural resistance followed the *Direct Design Method* provided by the building code ACI 318-71. It is noted that the bottom reinforcing bars at the column extended 9 in. into the column face but were not continuous.

Moreover, the detailing requirements for reinforcement in ACI 318-71 were also followed in determining the bar spacing, the cutoff location for top reinforcement outside the interior support, and the minimum length of bottom reinforcement. Figure 2.2 shows the resulting reinforcement arrangement around an interior slab-column connection, the zone enclosed by lines at mid-span as shown in Figure 2.1. The clear concrete cover was 3/4 inch for both top and bottom bars.

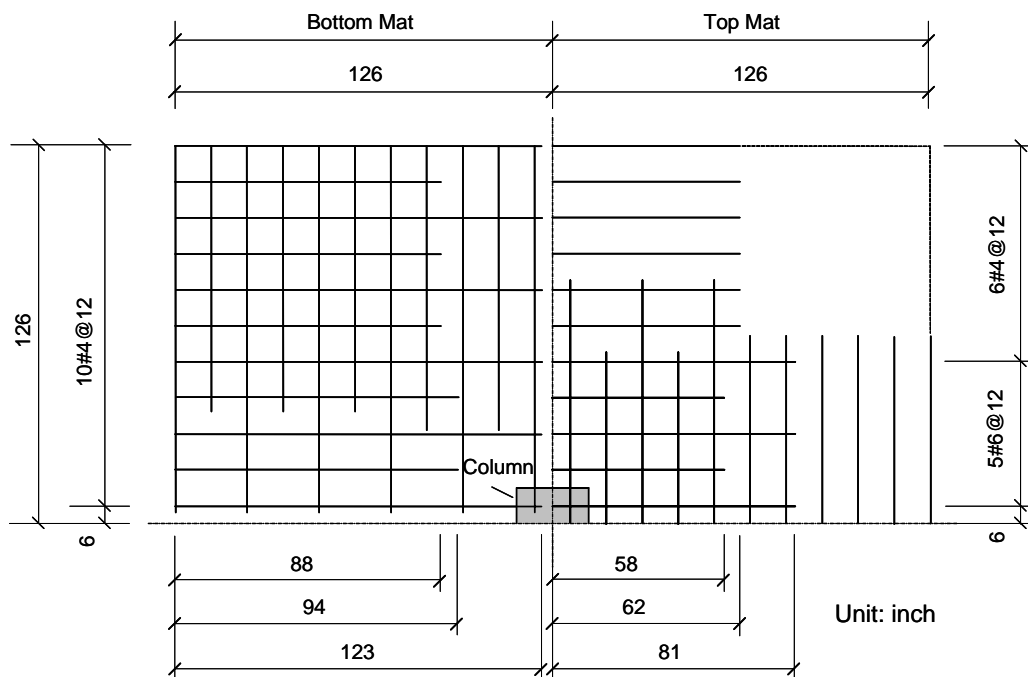


Figure 2.2: Reinforcement arrangement around the prototype interior connection.

With the given slab thickness and specified concrete strength, the connection two-way shear strength as defined by the code was well above the design gravity shear transferred from the slab to the column. In addition, the reinforcement layout described above gives a 0.5% reinforcement ratio for top bars in the column strip, defined by a

width of half the span centered on the column, and 0.25% for top bars in the middle strip, defined as the region outside the column strip.

### **2.3 OVERALL TEST OBJECTIVES AND PROCEDURES**

The behavior of the interior slab-column connection shown in Figure 2.1 under the following three types of loading condition was experimentally investigated in this study.

- Pure vertical loading to failure (no lateral load) to investigate the connection gravity load carrying capacity;
- Constant gravity loading combined with cyclic lateral loading until failure to study the connection strength, stiffness degradation, and deformation capacity in the event of earthquake;
- Constant gravity loading combined with cyclic lateral loading until a predetermined lateral deformation was reached to produce damage in slab, but without complete failure. The connections were then loaded vertically to investigate the gravity load capacity of earthquake-damaged interior connections.

Two major testing variables were investigated: (1) lateral deformation level and (2) reinforcement ratio. The deformation level can be related to the degree of seismic damage, which could produce negative effects on the subsequent gravity load carrying capacity; the amount of reinforcement may influence the connection behavior under both gravity loading and combined loading and was therefore also studied.

Research by Bazant and Cao (1987) described the size effect on slab punching shear strength, i.e., the nominal shear stress at failure decreases as the slab thickness increases. In addition, Abrams (1987) pointed out that one-quarter should be the lowest scaling limit for testing flexural behavior of beams such that their strength and stiffness

characteristics can be preserved. Thus, to ensure the applicability of experimental results to practical applications, the slab thickness of specimens tested in this study was determined as 6 in., representing a 2/3-scale of the prototype. It is noted that the geometry of the prototype structure was chosen based on this thickness as well as typical spans of existing flat-plate construction and constraints imposed by laboratory geometry and space, such as the tie-down locations on the strong floor. In fact, the slab thickness in the prototype structure, 9 in., was larger than the minimum thickness required by ACI 318-71 for both shear strength and deflection serviceability.

Because of size and cost constraints, a series of isolated slab-column connections scaled down by a factor of 2/3 from the middle interior slab-column connection shown in Figure 2.1 were tested. These isolated specimens were intended to simulate the behavior of interior connections of the continuous prototype structure under the three types of loading conditions described previously.

A schematic of the test setup used to study the gravity load-carrying capacity of connections with and without seismic damage is shown in Figure 2.3(a), where the vertical struts supporting the slab were symmetrically arranged around the column.

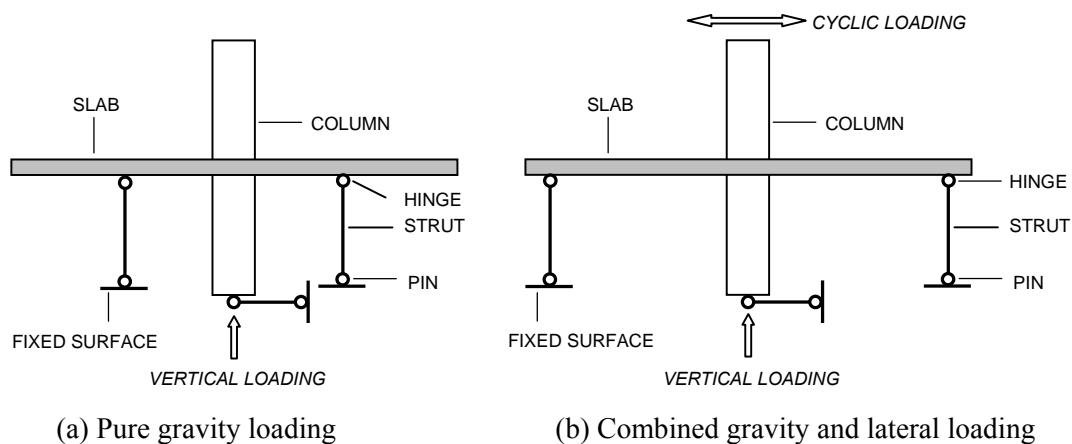


Figure 2.3: Overall testing schemes.

Under combined gravity and lateral loading, a testing scheme shown in Figure 2.3 (b) was employed. The vertical load was applied first to simulate the gravity load effects on a continuous structure. Then cyclic lateral loading was applied on the top of the column while the previous applied vertical load was maintained at a constant level. The choices of test boundary conditions were affected by the following considerations.

First, under the service level gravity load, according to the elastic theory of plates (Timoshenko and Woinowsky-Krieger, 1959), the flexural moment at the column face in the prototype structure would be as high as half of the slab yield moment. This implies that gravity loading effects should be taken into account in designing the test setup. Even though the test setup shown in Figure 2.3(a) is suitable for gravity loading, it is not acceptable for lateral loading because it would introduce unrealistically high bending moments around the column. The testing scheme was determined as shown in Figure 2.3(b), where the struts were symmetrically arranged around the column but at a larger distance from the column than that used for pure gravity loading.

Second, using the second test scheme discussed above, the bending moment around column during the first loading stage, gravity loading, would be higher than that of the continuous structure. The situation could be improved by stacking or hanging additional weight on the slab at certain locations determined from analysis and, meanwhile, connecting the struts with the slab only at its two edges perpendicular to the lateral loading direction. Although this approach can reduce the negative bending at the column resulting from a concentrated vertical load applied through the column, it was not implemented in this study because both non-destructive testing and visual inspection of damage during lateral loading were planned. There was no conventional way to load the slab without obstructing large area of the slab surface for visual inspection and non-destructive testing.

## 2.4 FINITE ELEMENT ANALYSIS

Since most connection damage and failure were anticipated in the slab at the vicinity of column, it was expected that under pure gravity loading and combined loading the isolated connection without scaling and the continuous structure should provide similar internal moment distributions at the column. This goal was achieved by determining the layout of the vertical struts in the test schemes shown in Figures 2.3 (a) and (b) from inelastic finite element analyses. Although cyclic lateral loads would be applied in the tests, the boundary conditions for combined loading were determined based on the analyses of structures subjected to gravity and monotonic lateral loading.

The general-purpose finite element analysis software, ABAQUS, was used to analyze the continuous structure and isolated slab-column connection. The element type, material modeling, geometry and loading of the analytical model, and the analysis results are presented in this section.

### 2.4.1 Element Type

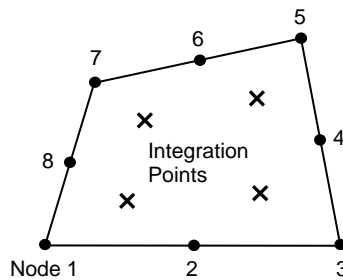


Figure 2.4: 8-Node quadratic shell element with reduced integration in FEM analyses.

Because the ratio of slab thickness to span was as low as  $1/28$ , a shell element was used to model the reinforced concrete slab. The 8-node quadratic shell element with reduced integration and six active degrees of freedom at each node, S8R, as shown in

Figure 2.4, was applied to both isolated and continuous assemblies. In addition, seven Simpson integration points were used along the shell thickness.

## **2.4.2 Material Modeling**

### **2.4.2.1 Concrete**

The concrete smeared cracking model, applicable to both plain and reinforced concrete subjected to essentially monotonic straining at low confining pressures, was used to simulate cracking and post-cracking behavior of concrete. This model is suitable for a variety of element types including truss, shell, and solid. On the basis of maintaining a continuous displacement field, this model employs the concept of oriented damaged elasticity, smeared cracking, to describe the inelastic tensile behavior of concrete. The model does not track individual “macro” cracks; rather, calculations are performed independently at each integration point of an element and the cracking effects are simulated by modifying the stress and material stiffness associated with the integration points.

Cracking is assumed to occur when the stress reaches the “crack detection surface” shown in Figure 2.5 and defined according to uniaxial tensile strength, the equivalent pressure stress,  $p$ , and the Mises equivalent deviatoric stress,  $q$ . Upon the detection of a crack, its orientation is stored for the following calculations. The subsequent cracking at the same point is restricted to being orthogonal to the direction of the first crack. The post-cracking behavior for direct straining across cracks is modeled by tension stiffening that defines the strain-softening behavior of cracked concrete. Cracks are irrecoverable and affect the calculations by using the damaged elasticity model in the sense that, although the cracks are allowed to close, the cracking effects remain for the following calculations.

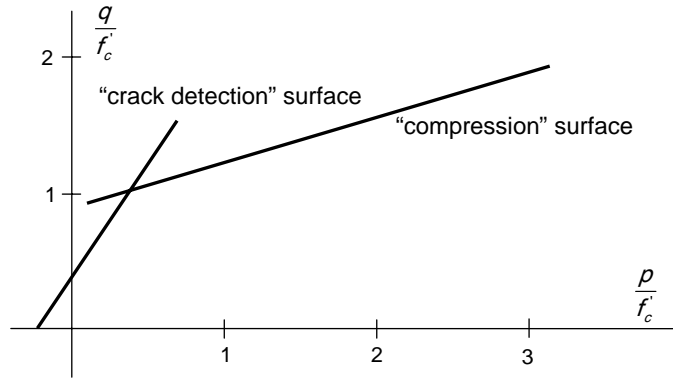


Figure 2.5: Concrete yield and failure surfaces in the  $p$ - $q$  plane.

Tension stiffening used in this study took the form of a linear post-failure stress-strain relationship shown in Figure 2.6, where  $\sigma_t^u$  denotes the uniaxial tensile strength of concrete,  $E_0$  Young's modulus of concrete, and  $\varepsilon_u$  the tensile strain at which stress is reduced to zero ( $\varepsilon_u$  must be estimated). Generally, too low a value of  $\varepsilon_u$  causes unstable behavior in the overall response of the model. Therefore, a strain of 0.002 was used for  $\varepsilon_u$  in this study to obtain converged numerical solutions.

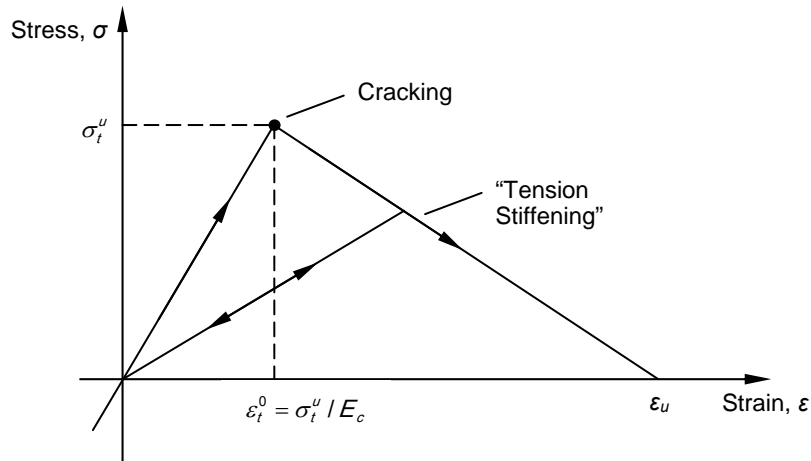


Figure 2.6: Modeling of tension stiffening for concrete.

Another influence of cracking is diminishing concrete shear stiffness. This effect can be simulated by the shear retention, through which the reduction in shear modulus invoked by concrete cracking can be specified as a function of the opening strain across the crack. The reduced shear modulus influences behavior mainly when a previously opened crack is closed and normal stress across a crack becomes compressive. However, shear retention was not adopted in this study because monotonic loads were applied in the analyses and it was found that introducing shear retention into the model had little effect on either global response in terms of slab vertical deflection or local response such as the internal moment at the vicinity of column.

When loaded in compression, concrete initially exhibits elastic response. As the stress is increased, some irrecoverable inelastic straining occurs and the material softens. The inelastic behavior of concrete under compression is described by a “compression” yield surface shown previously in Figure 2.5. Plastic straining is modeled by an elastic-plastic theory using a simple yield surface written in terms of the first and second stress invariants,  $p$  and  $q$ . Moreover, associated flow and isotropic hardening are used in this model.

The tensile and compressive responses of concrete incorporated in the modeling described above are illustrated in Figure 2.7 and Figure 2.8 for concrete under uniaxial and multiaxial stress states.

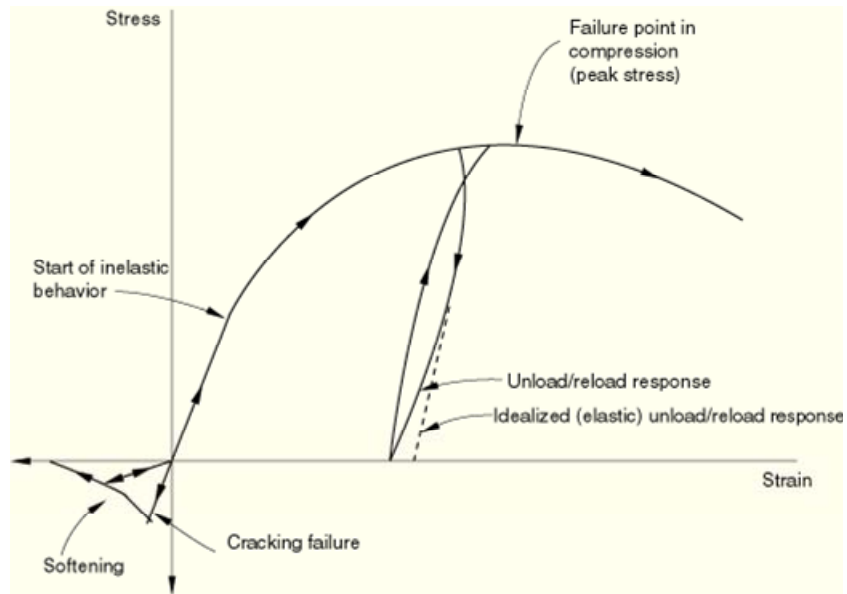


Figure 2.7: Uniaxial response of concrete (reproduced from ABAQUS documents).

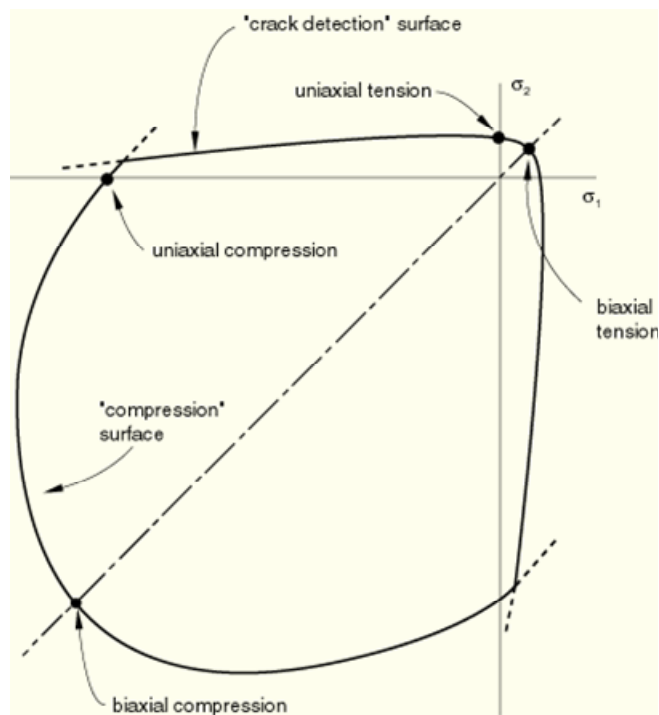


Figure 2.8: Response of concrete under multiaxial stress state (reproduced from ABAQUS documents).

Smearred concrete cracking was incorporated into the shell element by Chen and Marzouk (1993) to analytically study the gravity loading capacities of high-strength concrete slabs tested by Marzouk and Hussein (1991). These square slabs, with a 120 mm thickness and 1500 mm span, were simply supported along their four edges and loaded axially through the column stub during the testing (Figure 1.3(a)). The strength predicted using ABAQUS/FEM analysis for lightly-reinforced slabs was in good agreement with the experimental results. However, as illustrated in Figure 2.9, there was a large discrepancy at initial load-deflection response between analytical and experimental results. The shell element appeared to be too stiff to describe the elastic behavior of slabs before significant concrete cracking and steel yielding occurred. Thus, in addition to using reduced integration in this study, the Young's modulus of concrete,  $E_c$ , was decreased by 50% from that determined from  $E_c = 57000\sqrt{f'_c}$  to further reduce the shell stiffness in the FEM model.

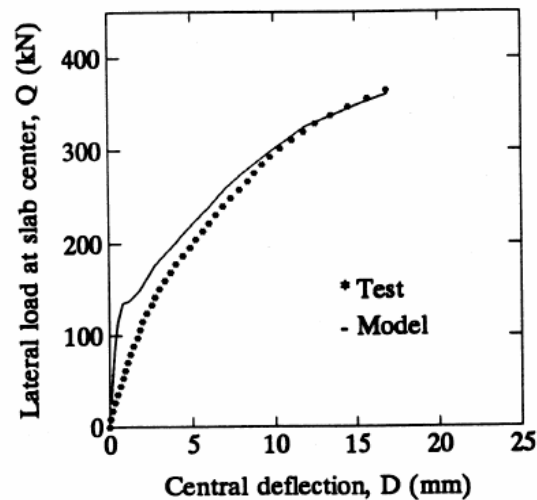


Figure 2.9: Comparison of FEM prediction to test result (reproduced from the paper by Chen and Marzouk, Specimen HS5).

The parameters for modeling concrete in FEM analyses are listed in Tables 2.1.

Table 2.1: Summary of Parameters for Modeling Concrete

Young's modulus	1.8x10 <sup>6</sup> psi	Plastic strain at failure	0.0015
Poisson's ratio	0.15	Ratio of uniaxial tension to compression failure stress	0.10
Yield stress for uniaxial compression	3000 psi	Ratio of biaxial to uniaxial compression failure stress	1.16
Failure stress for uniaxial compression	4000 psi	Strain at zero stress for tension stiffening	0.002

#### 2.4.2.2 Steel

The slab flexural reinforcement was modeled by a rebar layer. Through this option, the equivalent “smeared” orthotropic steel layers were generated according to the actual bar area, spacing, orientation, and location along the slab depth. Each rebar layer embedded in the concrete shell element was positioned parallel to the mid-surface of the shell element and was treated as a one-dimensional strain theory element.

The inelastic behavior of steel in ABAQUS is described by metal plasticity models. The interaction between rebar and concrete, such as bond slip and dowel action, can be simulated by modifying the parameters associated with concrete tension stiffening. However, no such attempt was made in this study due to lack of test data to calibrate relevant parameters.

Totally four layers of reinforcement, two in each principle direction, were used in this study to model the top and bottom mats of rebar. The modeling parameters for steel were determined from material properties and reinforcement layout in the prototype structure. Although some small areas of the prototype structure did not have top reinforcement, as shown in Figure 2.2, all concrete shell elements were reinforced with top rebar layers to ensure convergence.

## 2.4.3 Geometry, Boundary Conditions, and Loads for FEM Analyses

### 2.4.3.1 Continuous Structure Simulating Prototype Structure

As shown in Figure 2.10, the analyzed portion of the prototype structure was bounded by two slab center lines AA' and BB' and contains the interior slab-column connection to be investigated. Appropriate boundary conditions reflecting the conditions in the prototype were applied at lines AA' and BB'. The columns were omitted from the analytical model, but the intersection zones of column and slab, termed as joints in the following discussions, were modeled to be rigid by assigning a large Young's modulus. The geometry of this continuous structure used in FEM analyses is shown in Figure 2.11.

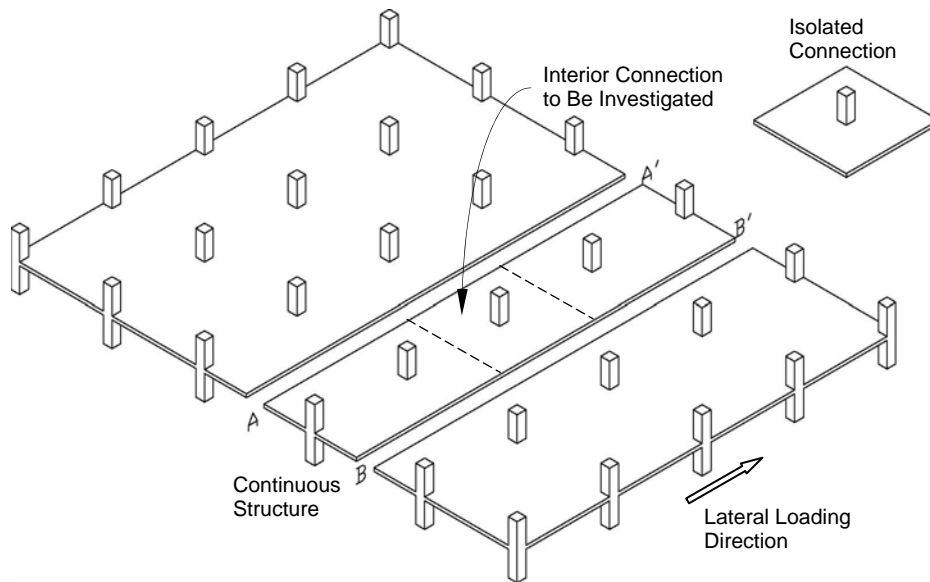


Figure 2.10: Illustration of the structures analyzed by inelastic finite element analyses.

The FEM analyses contained two phases for the continuous strip structure: (1) gravity loading only and (2) combined gravity and lateral loading.

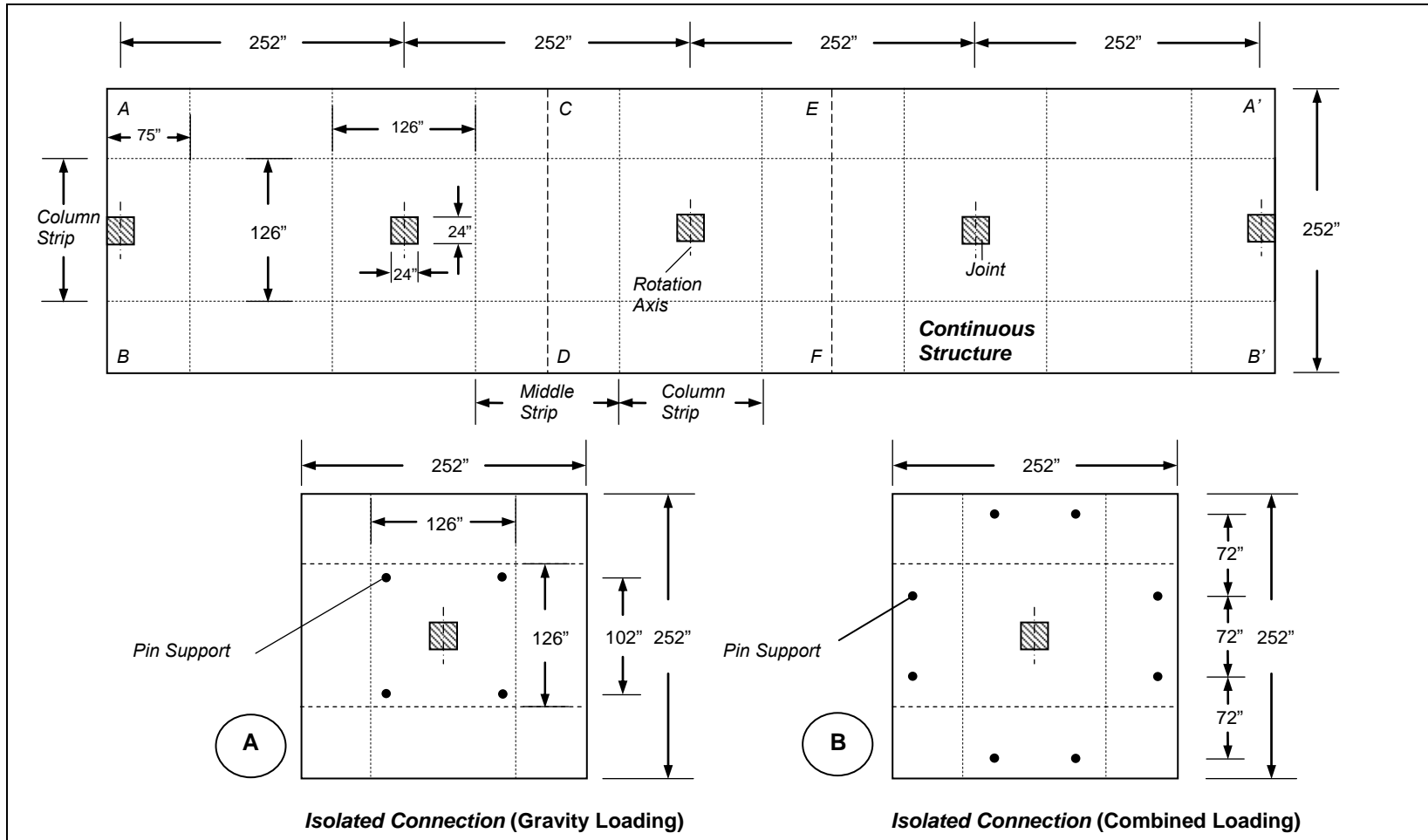


Figure 2.11: Geometry of continuous structure and isolated connection for FEM analyses.

For gravity loading, any rotational or translational displacement at element nodes in the joint areas was prohibited. In addition, boundary conditions along lines AA' and BB' were as follows: (1) rotation about these lines and about an axis perpendicular to the slab plane was restrained, and (2) no in-plane translational displacement in the direction normal to these lines was allowed. A uniformly distributed vertical load with a magnitude of 145 psf was applied on the slab top surface to simulate the gravity loads acting on the prototype structure including slab self-weight, superimposed dead load, and 25% design live load.

For combined loading, the vertical loads on the slab surface and the boundary conditions on lines AA' and BB' were identical to those for gravity loading. However, an equal amount of rotation about an axis passing through the joint center and perpendicular to the lateral loading direction was imposed on each joint to simulate the connection lateral deformation. Meanwhile, no translational displacement was allowed at the joint center.

#### ***2.4.3.2 Isolated Connection Simulating Laboratory Testing***

When the isolated connection was analyzed, the column was omitted from modeling and the joint was modeled to be sufficiently stiff, as was done for the continuous structure. A structure equivalent to the single connection shown in Figure 2.3 but simplified for FEM analysis was attained by substituting the vertical links with pins and the lateral load, if any, was simulated by specifying a joint rotation.

Analysis was first conducted on single connection (A), shown in Figure 2.11, under pure gravity loading. An upward concentrated load of 63.4 kips was applied at the joint. The load was equal to the total gravity shear transferred from the slab to the middle interior joint in the analysis of the continuous structure. The slab self-weight of the isolated connection was not considered because the effects of self-weight become

insignificant as the magnitude of the concentrated load increased during the laboratory tests. The pins were arranged at the slab diagonal lines and their locations were determined by trial-and-error until the moment distribution around the joint was similar to that of the continuous structure. The pins were allowed to rotate but the translational displacement was restrained. The nodes of shell elements in the joint area were allowed to move only in a direction normal to the slab plane. The pin locations shown in Figure 2.11 were determined from analysis and were used for design of the test setup for pure gravity loading.

Analysis was also conducted on the isolated slab-column connection (B) under combined gravity and lateral loads. The option of pin location, however, was restrained by the laboratory condition. The pin positions shown in Figure 2.11 for combined loading (after using a 2/3 scaling factor) correspond to the tie-down locations on the lab strong floor, where the bottom pins in Figure 2.3(b) would be anchored. Analysis was carried out to verify the appropriateness of these pin positions. The analysis included two steps, gravity loading followed by the lateral loading. During the first step, the boundary conditions were applied on the slab in the same manner as in the gravity loading analysis for the isolated connection. Meanwhile, a 112.5 psf uniformly distributed vertical load, simulating the slab self-weight, was applied downwards on the slab top surface and a 63.4 kips concentrated load, same amount as in gravity loading analysis, was applied at the joint center. The surface load was less than that applied on the continuous structure since neither superimposed dead load nor live load would be applied on the slab in the tests. In the second step of analysis, the vertical loads that had been applied in the previous loading stage were maintained and a rotation about the joint axis normal to the lateral loading direction was imposed at the joint center to simulate the lateral loading.

#### **2.4.4 FEM Analysis Results**

The analysis results for the isolated connection and for the region in the continuous structure corresponding to the isolated connection (area CDFE in Figure 2.11) are compared and presented in this section. Attention was mainly given to the moment distribution around the joint where the bending moment was concentrated. The vertical slab deflection derived from analyses is also shown on the deformed shapes.

In the analysis results to be presented, SM2 and SM1 denote the moment per unit length about two orthogonal in-plane axes 2, and 1 in the local coordinate system (1 and 2 denote an axis parallel and normal to the long direction of the continuous slab, respectively). The vector notations of these variables are shown together with the analysis results. The slab upward vertical deflection was designated by U2.

##### ***2.4.4.1 Gravity loading***

By means of symmetry, Figures 2.12 and 2.13 present the moment distribution under gravity loading for the interior connection of the continuous structure and for the isolated connection supported on four pins that were located at the chosen positions as shown in Figure 2.11 (A, for pure gravity loading). It can be seen that an approximately equal maximum bending moment around the joint was achieved in these two structures with different support conditions.

The slab vertical deflection due to gravity loading is shown in Figure 2.14 (a) for the continuous structure and (b) for the isolated connection.

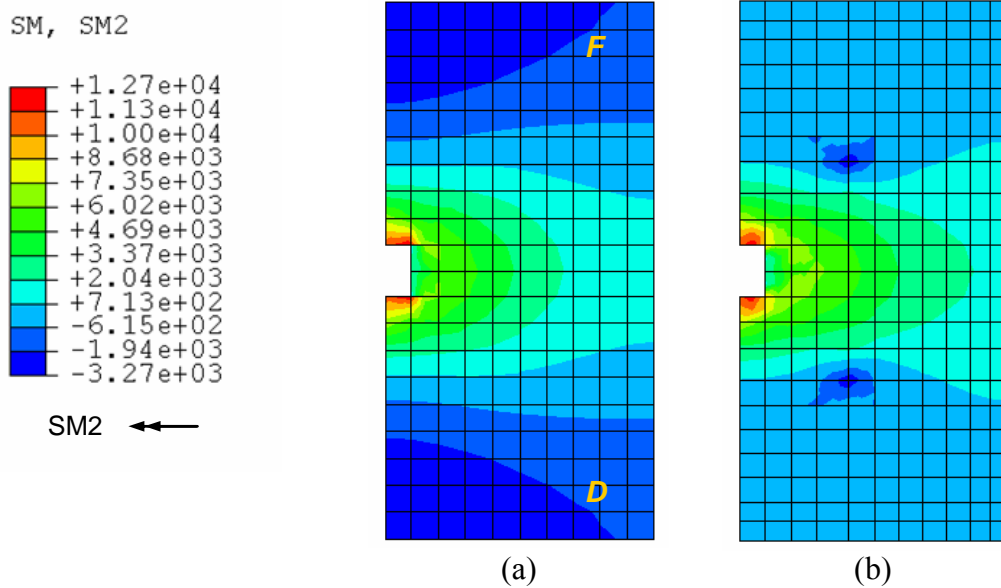


Figure 2.12: SM2 (gravity loading, unit: lb-in): (a) Prototype (Max = 12700, Min = -3270); and (b) Isolated connection (Max = 12100, Min = -3090).

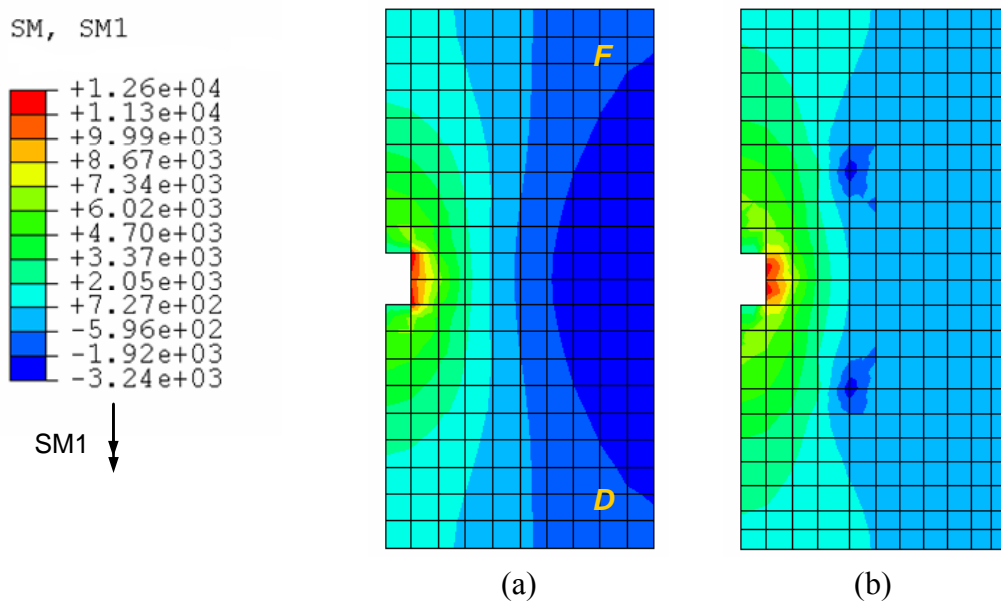
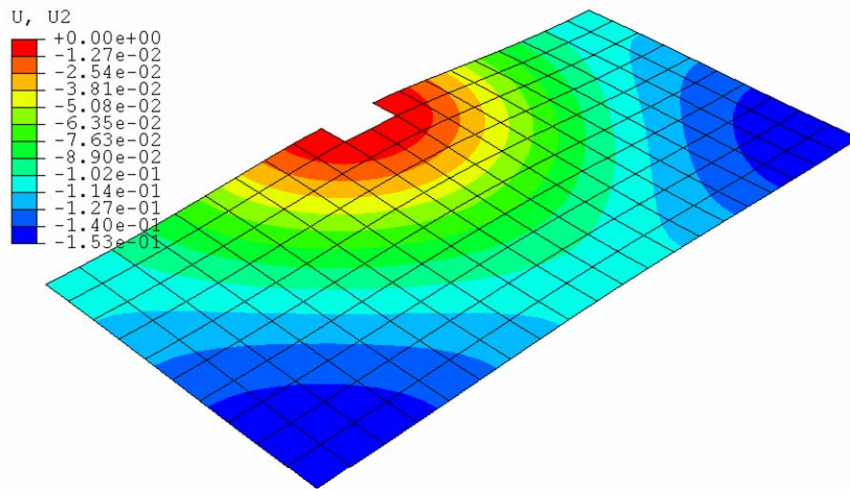
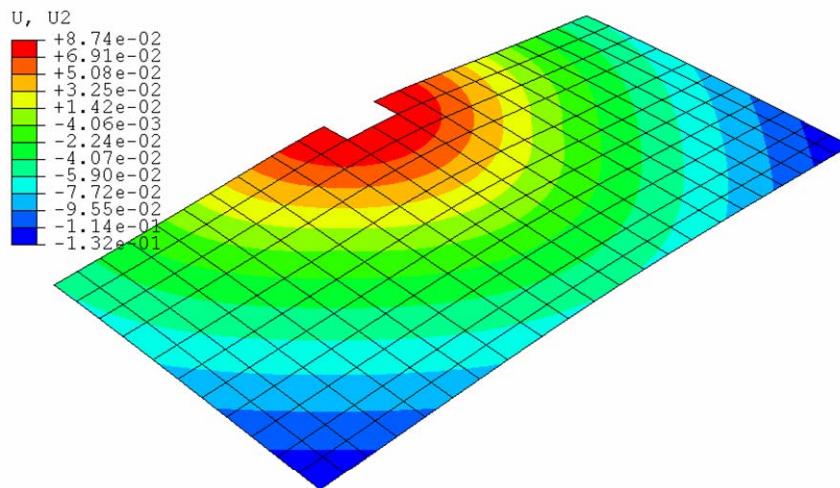


Figure 2.13: SM1 (gravity loading, unit: lb-in): (a) Prototype (Max = 12600, Min = -3240); and (b) Isolated connection (Max = 12100, Min = -3090).



(a) Continuous structure



(b) Isolated connection

Figure 2.14: Deflection shape and vertical deflection (gravity loading, unit: in).

#### 2.4.4.2 Combined Loading

For combined gravity and lateral loading, gravity load was first applied on the continuous structure and the isolated connection B. Because the isolated connection B

was supported on pins with a larger distance from the joint than that used for the isolated connection A (Figure 2.11), the maximum moment around column in the isolated connection is around 20 percent larger than that in the continuous structure, as shown in Figures 2.15 and 2.16.

Following the gravity loading, lateral load was applied. It was found that the maximum applicable joint rotation was about 0.6% radians, beyond which the analyses on both structures could not converge. The divergence was likely caused by (1) the loss of local stiffness that resulted from reinforcement yielding at one side of joint where negative bending due to gravity loading and lateral loading were added, or (2) the inelasticity at the two sides of the joint that resist torsion.

Comparison of the moment distribution between the continuous structure and the isolated connection B was made at a joint rotation of 0.5% radians. At this rotation, significant reinforcement yielding occurred in the analysis. The results of SM1 and SM2 are shown in Figures 2.17 and 2.18, respectively. It can be seen that the negative bending moment around the column in single connection B is close to that in the continuous structure. Therefore, the pin positions in the FEM analysis for the isolated connection B were used for detailing the test setup discussed in the next section.

It is noted that the moment, SM2, derived from FEM analyses was higher than the ultimate flexural capacity calculated from a classic concrete beam approach, where the tensile strength of concrete is completely ignored. It was found that the high value of moment in the analyses could not be reduced by using smaller mesh size or by using more integration points along the slab depth. Thus, such a phenomenon could be partly attributed to constitutive relations, especially tension stiffening, used for concrete in the modeling.

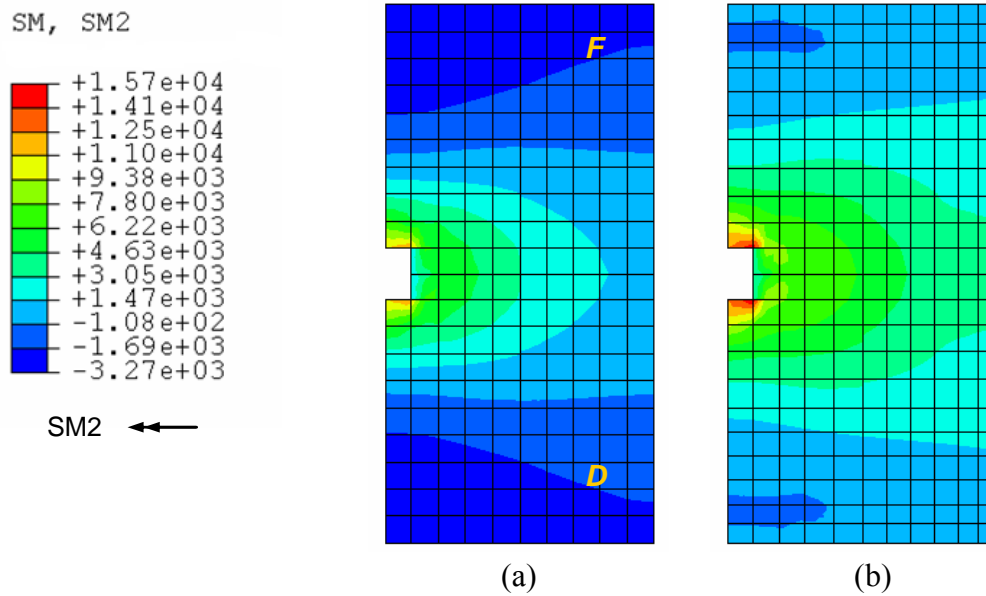


Figure 2.15: SM2 (Gravity loading, unit: lb-in): (a) Prototype (Max = 12700, Min = -3270); and (b) Isolated connection (Max = 15700, Min = -405).

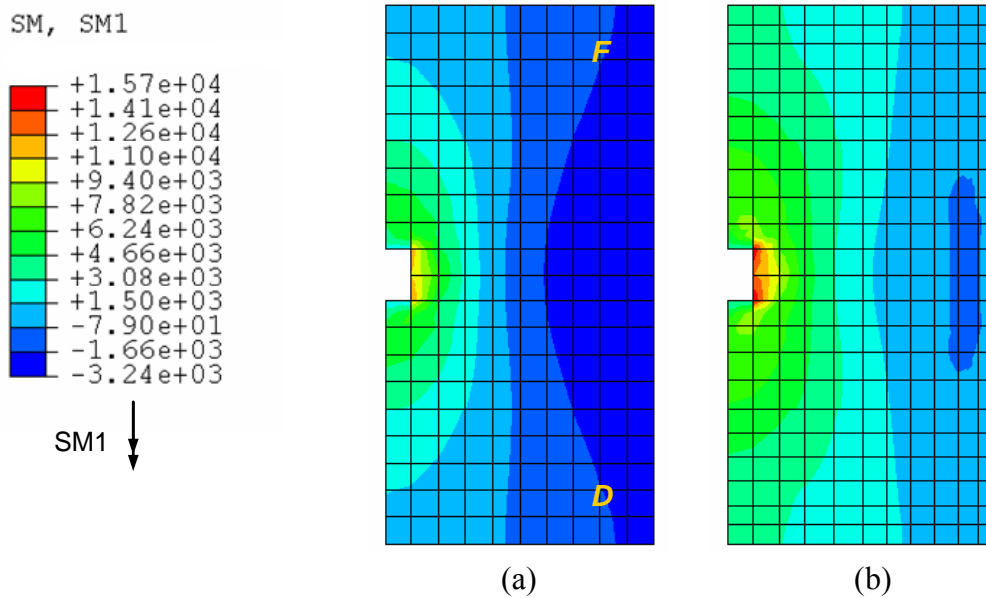


Figure 2.16: SM1 (Gravity loading, unit: lb-in): (a) Prototype (Max = 12600, Min = -3240); and (b) Isolated connection (Max = 15700, Min = -405).

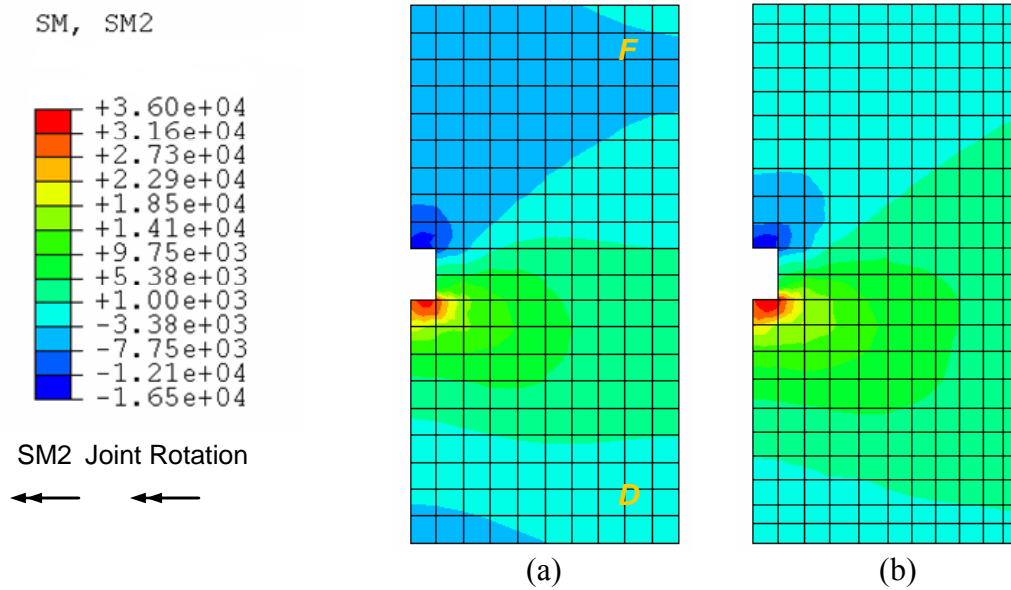


Figure 2.17: SM2 (0.5% rotation, unit: lb-in): (a) Prototype (Max = 34000, Min = -16400); and (b) Isolated connection (Max = 36000, Min = -16500).

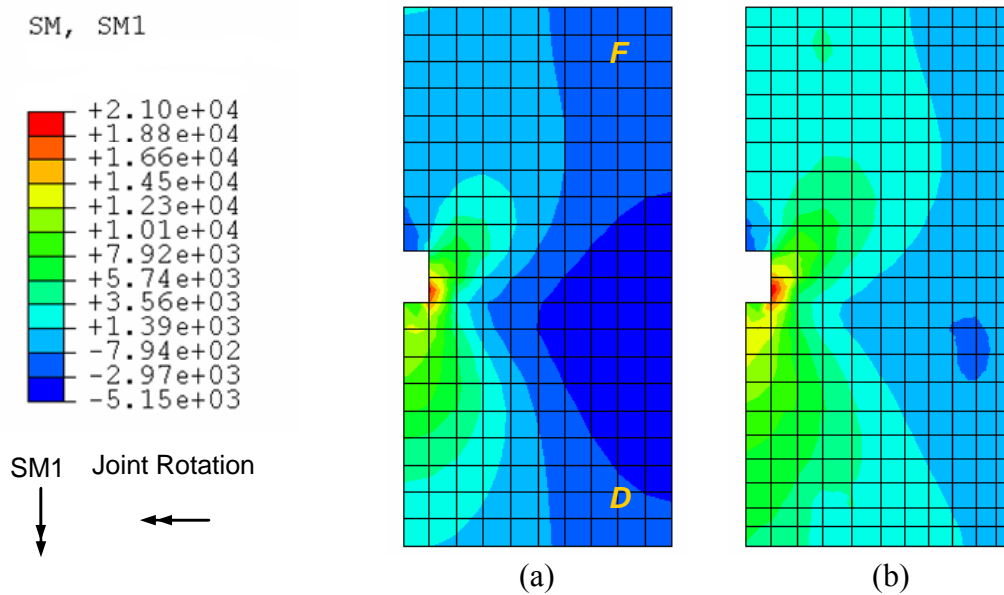
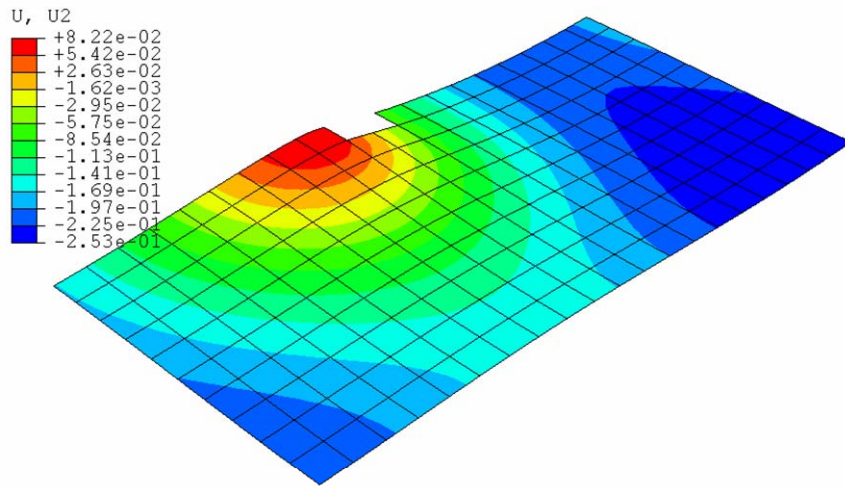
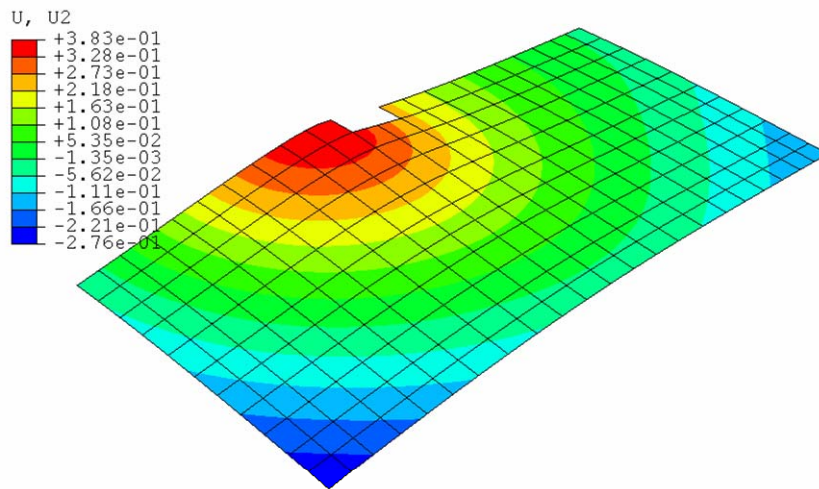


Figure 2.18: SM1 (0.5% rotation, unit: lb-in): (a) Prototype (Max = 19500, Min = -5150); and (b) Isolated connection (Max = 21000, Min = -2040).

The vertical deflection under gravity loading combined with a joint rotation of 0.5% radians is shown in Figure 2.19(a) for the continuous structure and (b) for the single connection.



(a) Continuous structure



(b) Isolated connection

Figure 2.19: Deflection shape and vertical deflection (combined loading, unit: in).

## **2.5 DETAILS OF TEST SETUP AND LOADING APPARATUS**

### **2.5.1 Combined Loading**

Based on the inelastic finite element analyses described previously, the testing setup for 2/3-scale isolated slab-column specimens subjected to combined loading was designed as shown in Figure 2.20.

Eight vertical struts with clevises at each end were symmetrically distributed around the column to restrain slab vertical displacement. The lower clevises sitting on the steel tube spacers were anchored to the strong floor by high-strength bolts. Considering the unevenness of the slab bottom surface and the floor and imperfectness in the length of struts as well as spacers, each upper clevis was connected to the slab by four high-strength bolts and two steel plates clamping the slabs. In this way, the overall length of these vertical connecting components was adjustable. In addition, to minimize the second order effect during lateral loading, the length of vertical struts was designed such that the distance between the pin axes of the clevis of each strut was close to the effective height of the lower column (48 in.) measured from the centroid of the slab-column intersection to the clevis installed underneath the column.

A horizontal strut was used to laterally restrain the lower end of the column and transfer the horizontal reaction to the reaction wall. The left end of this strut was connected with the column by one clevis and the right end with the reaction wall by another clevis. Two torsional struts, parallel to the slab plane and pin-connected to the reaction wall and the slab, were used to prevent the specimen from rotating about the vertical axis of column.

The design of the above-mentioned connection components such as struts, clevises, and bolts considered not only the strength but also the stiffness such that their deformation could be negligible in the tests.



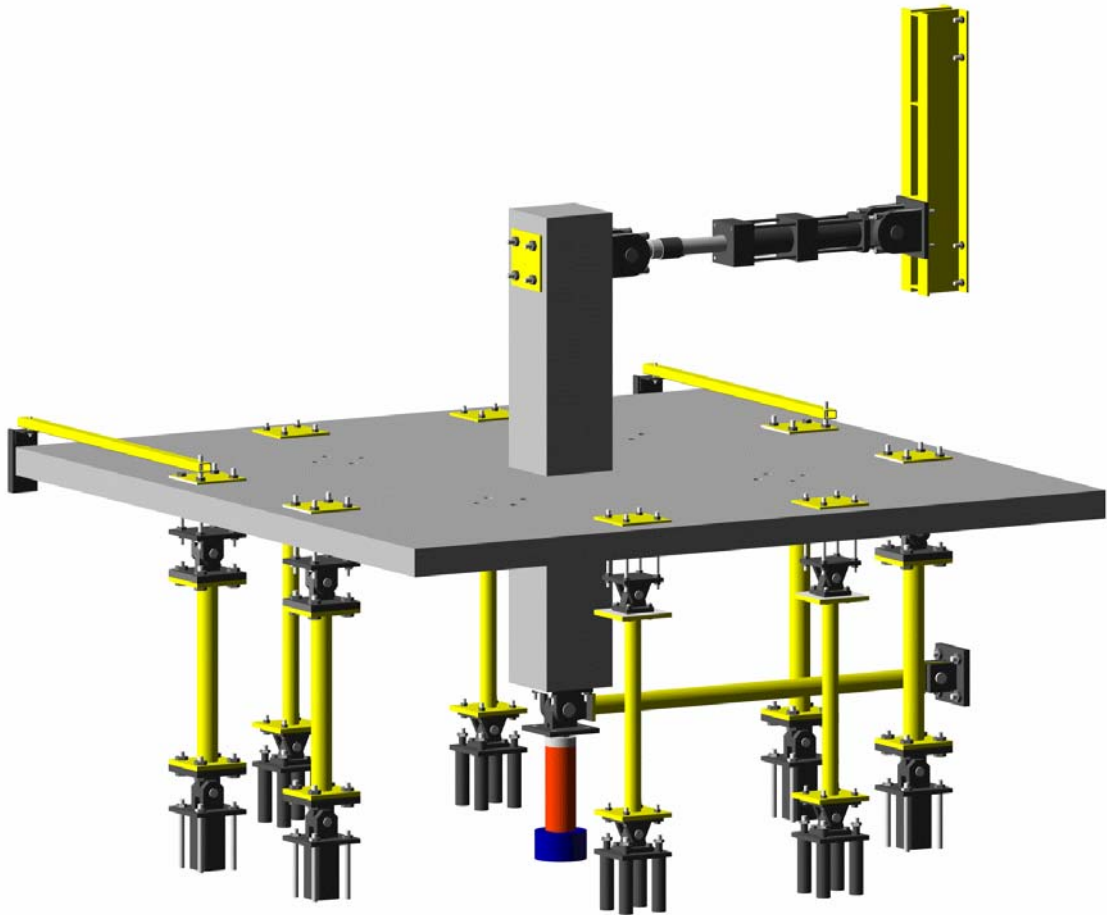


Figure 2.21: 3-D view of the test setup for combined loading.

A 3-D view of the test setup for combined loading is shown in Figure 2.21.

The loading apparatus included a vertical hydraulic jack and a closed-loop servo-controlled hydraulic actuator. The target gravity load was applied through the vertical jack that had a compressive loading capacity of 220 kips and a stroke of 13 inches.

The lateral cyclic deformations were simulated by applying quasi-static cyclic displacement to desired drift levels at the top column through the actuator. The actuator was installed horizontally and connected with the column top end and with a vertical beam mounted on the reaction wall. As shown in Figure 2.20, the vertical distance

between the actuator and connection joint center was 48 in. Thus, the two clevises connected to column top and bottom ends defined a 96 in. effective column height. The loading and stroke capacities of the actuator were 55 kips and  $\pm 5$  inches.

The vertical load was intended to be maintained at a constant level during lateral loading. The vertical load was monitored using a data acquisition system and the pump was manually operated to keep the oil pressure to the vertical jack constant as the slab deflected vertically.

The details of loading history for the combined loading are provided in Chapter 3.

### **2.5.2 Gravity Loading**

The test setup shown in Figure 2.22 was designed for testing the specimens subjected to pure gravity load. The slab was loaded monotonically through the same vertical jack used during the combined loading. The actuator braced the specimens as gravity load was applied.

Four struts were used to transfer tensile reaction force to the strong floor. To minimize the restraint to the slab flexural deformation, the rotational axis of each clevis on the struts was oriented as shown in Figure 2.22. The clevises at the lower end of vertical struts were installed on four beams anchored on the strong floor. A number of stiffeners were welded to each beam to minimize the flange local deformation.

The 3-D view of the test setup for pure gravity loading is shown in Figure 2.23. It is noted that, when the gravity load-carrying capacity of earthquake-damaged specimens was tested, they were first loaded using the test setup shown in Figure 2.21 to introduce damage in the slab and then loaded to failure using the test setup discussed in this section (Figure 2.23).

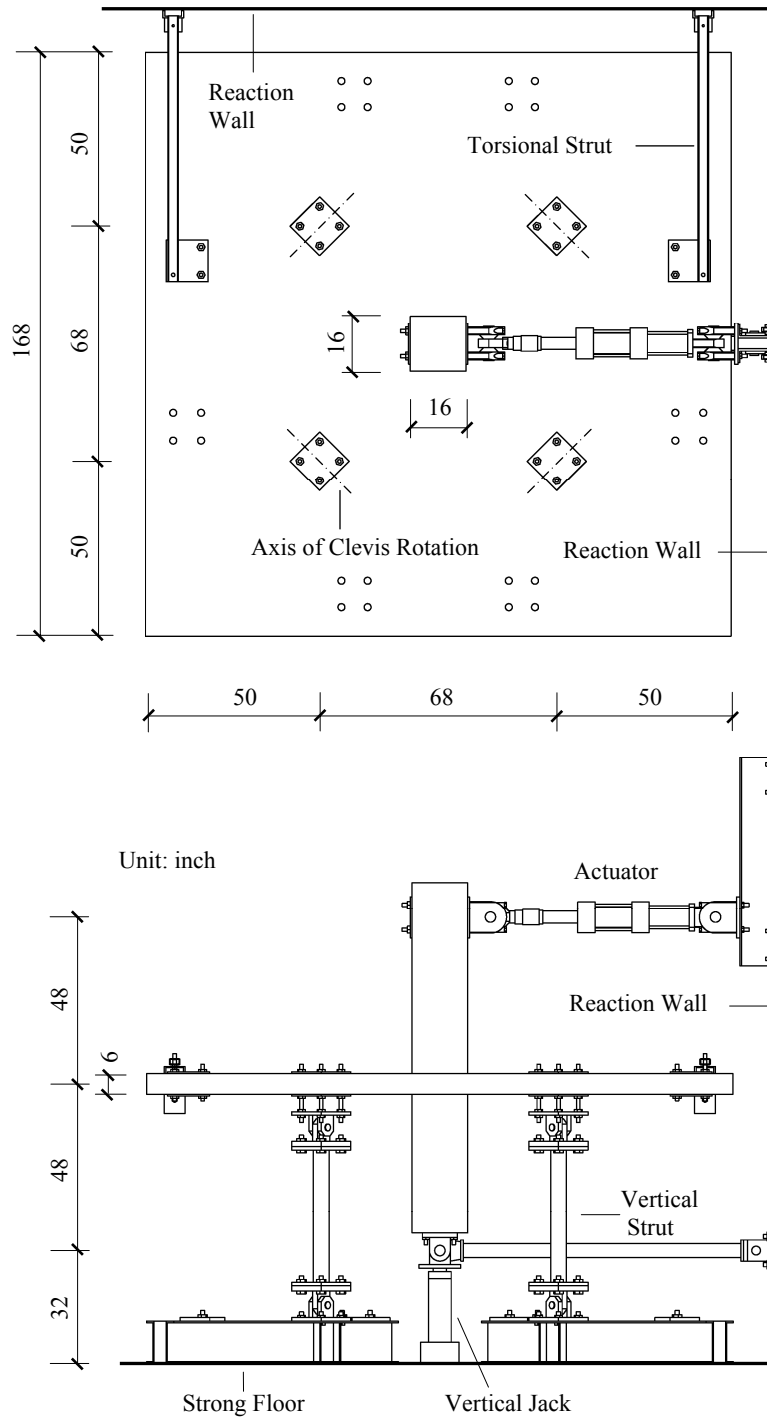


Figure 2.22: Test setup for gravity loading.

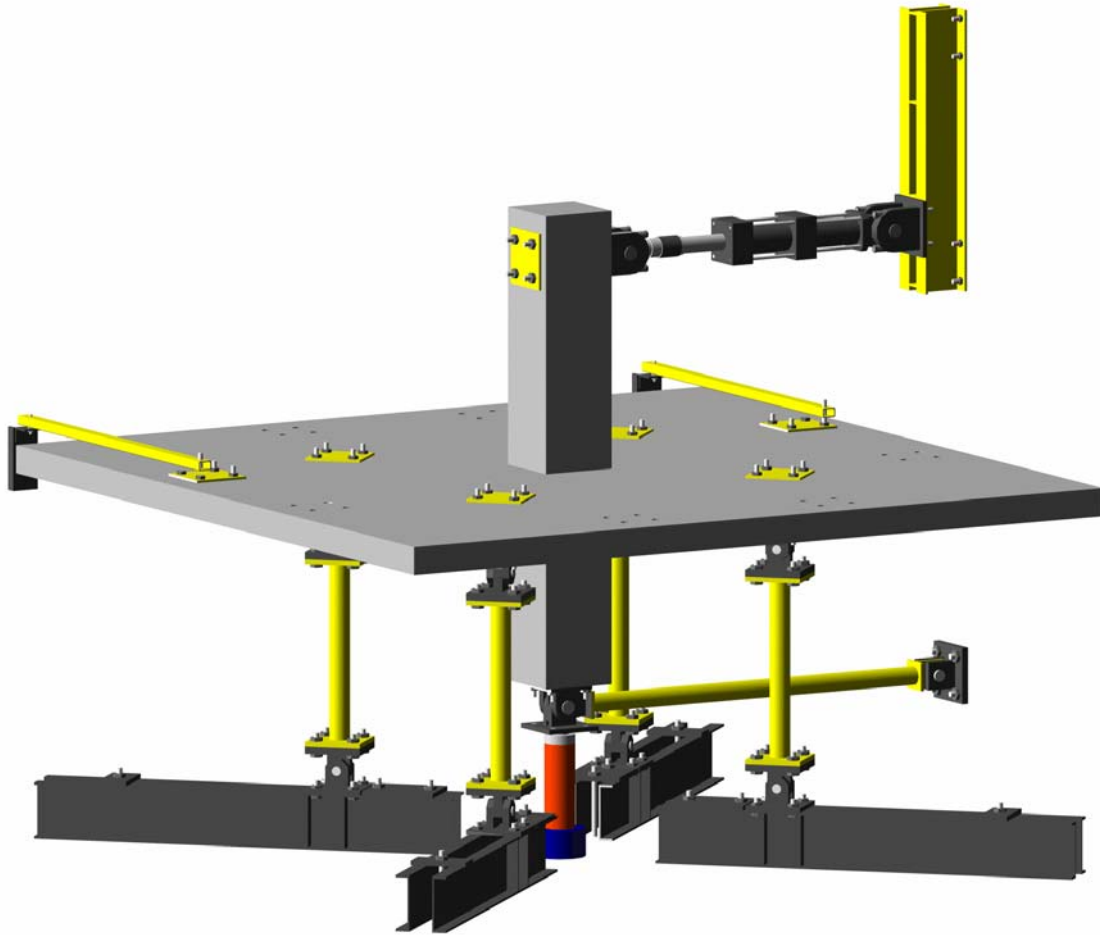


Figure 2.23: 3-D view of the test setup for gravity loading.

## 2.6 DESCRIPTION OF TEST SPECIMENS

### 2.6.1 Specimen Dimension and Nomination

Five specimens, representing a  $2/3$ -scale model of the interior slab-column connection shown by the enclosed area CDFE in Figure 2.11, were constructed and tested to failure. Each specimen consisted of a slab measuring 14 ft. square and 6 in. thick and a 16 in. square column in the slab center extending 55 in. beyond the slab top surface and 40 in. beyond the bottom surface.

To facilitate discussion, the designation of the specimens consisted of letter(s) indicating the loading conditions (discussed in Section 2.3) followed by a number showing the percentage top reinforcement ratio within a slab width  $c+3h$  centered on the column. A summary of the notation for the specimens tested is shown in Table 2.2.

Table 2.2: Summary of Specimens

Specimen	Loading History	Top Reinf. Ratio in $c+3h$ (%)	Test Setup Used
L0.5	Combined loading	0.5	Figure 2.21
LG0.5	(1) Combined loading; (2) Gravity loading	0.5	(1) Figure 2.21; (2) Figure 2.23
LG1.0	(1) Combined loading; (2) Gravity loading	1.0	(1) Figure 2.21; (2) Figure 2.23
G0.5	Gravity Loading	0.5	Figure 2.23
G1.0	Gravity Loading	1.0	Figure 2.23

### 2.6.2 Reinforcement Arrangement

The reinforcement details of Specimens L0.5, LG0.5, and G0.5, determined with a 2/3 scaling factor from the reinforcement layout of prototype connection (Figure 2.2), are shown in Figure 2.24.

To investigate the effects of reinforcement ratio, the spacing of top bars within  $c+3h$  region was reduced by half in Specimens LG1.0 and G1.0, leading to a 1.0% top reinforcement ratio in this area. The amount and layout of the bars in other areas were kept to be identical to those in Specimens L0.5, LG0.5, and G0.5. Figure 2.25 shows the bar details of Specimens LG1.0 and G1.0.

All specimens had a 0.5 in. clear concrete cover for both top and bottom reinforcement. The arrangement of slab reinforcement along slab depth is shown in Figure 2.26, where the bars parallel to the loading direction were located at the outermost layer measured from the slab depth center.

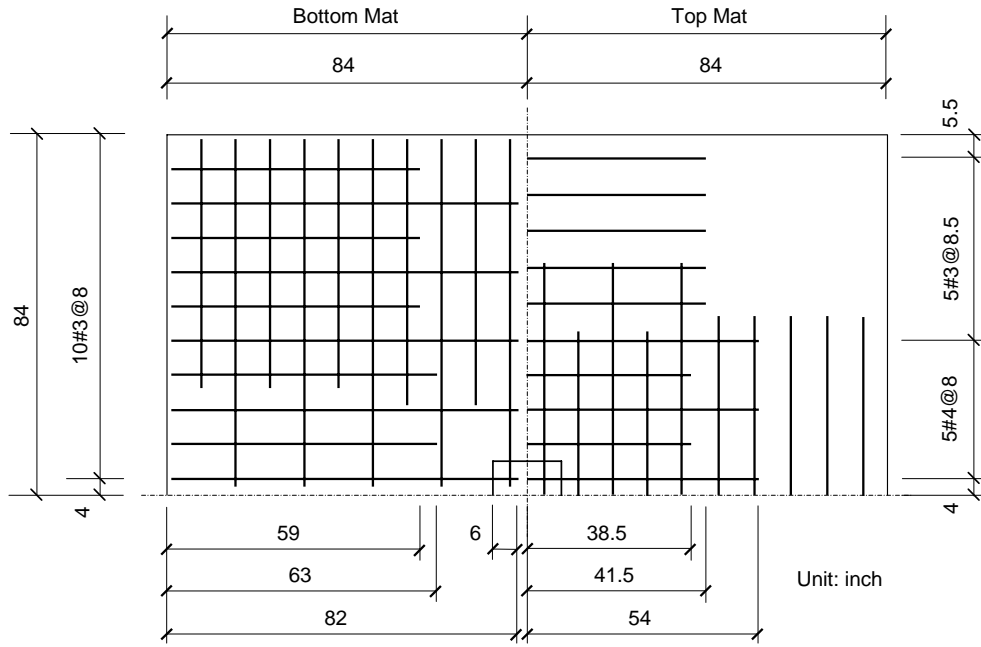


Figure 2.24: Reinforcement details of Specimens L0.5, LG0.5, and G0.5.

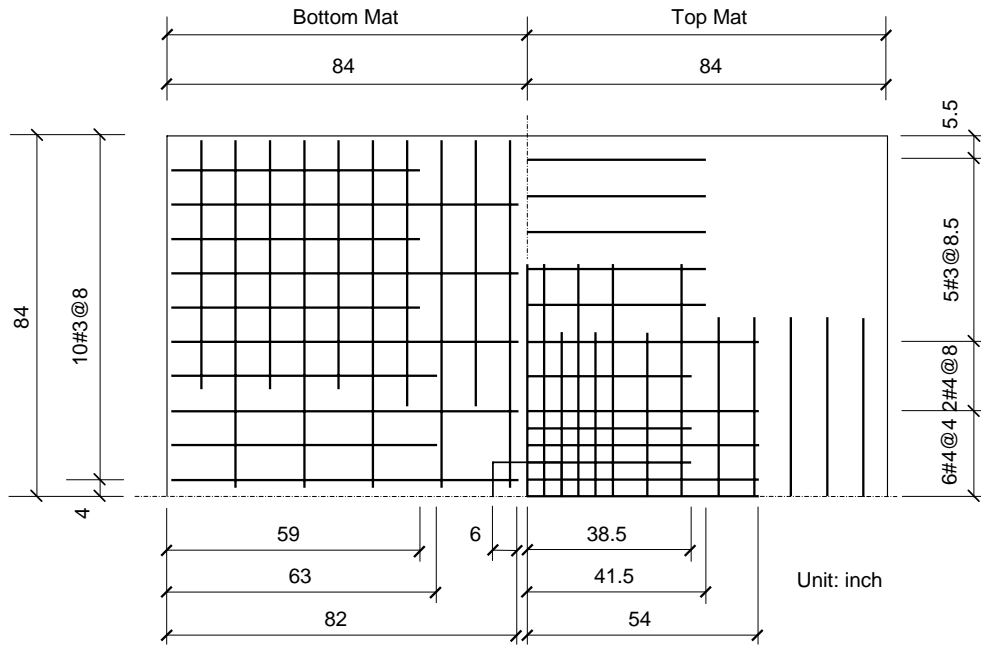


Figure 2.25: Reinforcement details of Specimens LG1.0 and G1.0.

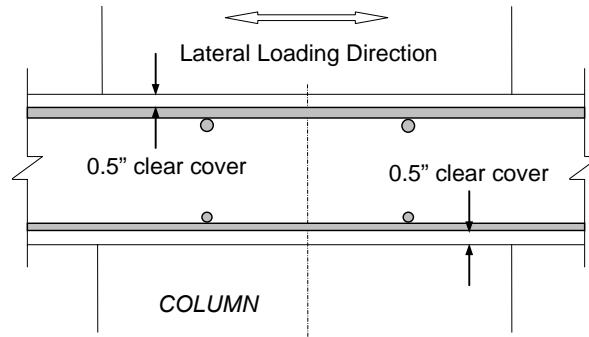


Figure 2.26: Reinforcement layout along slab depth.

The columns were heavily reinforced such that they behaved elastically and their deformation was negligible during tests. The column cross section is shown in Figure 2.27, where the clear cover of the column longitudinal reinforcement was 1 in. (2/3 of the 1.5" cover in the prototype).

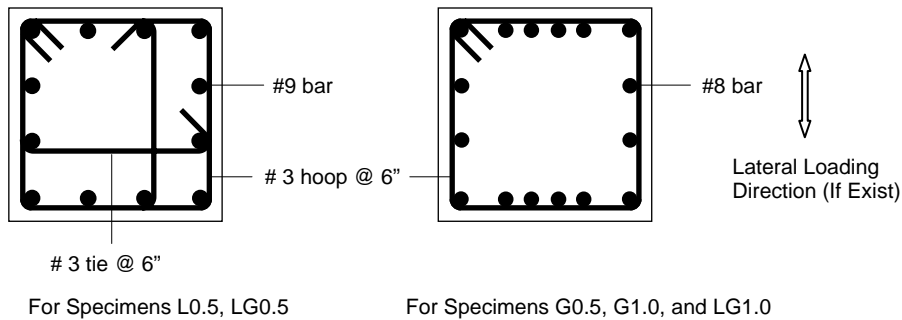


Figure 2.27: Column reinforcement details.

### 2.6.3 Specimen Construction and Material Properties

The slab bottom bars were placed on 0.5-in.-high plastic chairs. The top mat within the column strip rested on 4.5-in.-high steel chairs, most of which were placed away from the column to eliminate any beneficial effect on the specimen capacity. The top bars of middle strip were installed on chairs with 4.75 in. height. Forty-eight slab holes were provided by two inch diameter PVC pipes installed and secured at selected

positions. These holes were used for passing the high-strength rods used to attach the struts to the slab. The steel mats and cages as well as the slab forms for Specimen LG1.0 are shown in Figure 2.28.



Figure 2.28: Steel cages and slab forms (Specimen LG1.0).

The specimens were constructed with ready-mixed normal-weight concrete with specified properties of a 3/8 inch maximum aggregate size, 4 inch minimum slump, and 4000 psi compressive strength. Two concrete placements were needed for each specimen: one for the lower column and the slab and another for the upper column. After the first concrete casting, the specimen was cured by covering the slab with wet burlap and plastic sheet for at least six days. Then the remaining portion of the specimen, the top column, was cast after the joint area was cleaned and roughened to ensure the quality of construction joint.

A number of 6 by 12 inch standard concrete cylinders were cast from each batch of concrete. Testing was initiated no less than one month after the second concrete casting. Three cylinders for the slab and, if the lateral loading was applied, three for the upper column were tested at the start of each loading stage for every specimen. The average measured concrete compressive strength is given in Table 2.3.

Table 2.3: Compressive Strength of Concrete

Specimen	Testing Time	$f_c'$ (psi) (slab and lower column)	$f_c'$ (psi) (upper column)
L0.5	Beginning of combined loading	3710	3390
LG0.5	(1) Beginning of combined loading	4820	3580
	(2) Beginning of gravity loading	4860	—
LG1.0	(1) Beginning of combined loading	4000	3440
	(2) Beginning of gravity loading	3930	—
G0.5	Beginning of gravity loading	4545	—
G1.0	Beginning of gravity loading	4060	—

Grade 60 deformed bars were used for the slabs. The stress-strain curves derived from tensile coupon tests for the bars from the same heat are shown in Figure 2.29. The steel properties for each specimen are summarized in Table 2.4. The yield strength was derived at a strain of 0.002 if a well-defined yield plateau was absent.

Table 2.4: Tensile Properties of Reinforcement in Slabs

Specimen	No. 3 bars		No.4 bars	
	Yield strength $f_y$ (ksi)	Ultimate Strength $f_u$ (ksi)	Yield strength $f_y$ (ksi)	Ultimate Strength $f_u$ (ksi)
L0.5	64	92	68	90
LG0.5	67	104	66	107
LG1.0, G0.5, G1.0	59	89	61	95

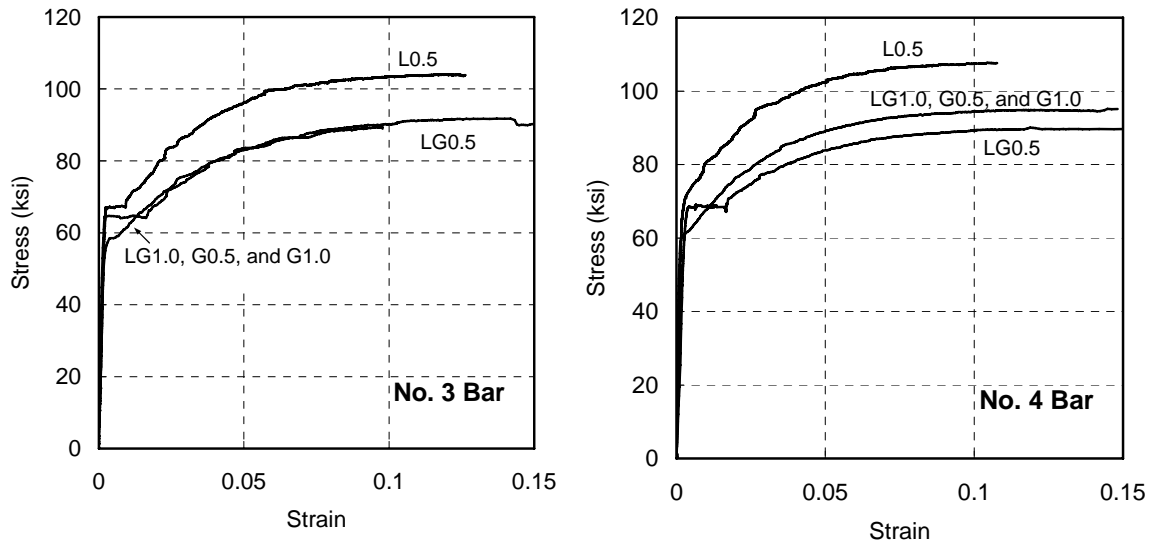


Figure 2.29: Stress-strain curves for reinforcement.

## 2.7 INSTRUMENTATION AND DATA COLLECTION

Each specimen was instrumented to provide detailed information regarding the connection behavior throughout the entire loading history. Input from instrumentation was transferred first to a data scanner and then to the data acquisition system, where the data was converted to engineering terms, used for monitoring the test, and stored for evaluation and interpretation. Measurements involved load, displacement, and strains.

### 2.7.1 Load

The vertical load applied through the jack was measured by a load cell and a pressure transducer. The load cell, as shown in Figures 2.30, was located underneath the jack and rested on the strong floor. The transducer, used as a backup for measuring the vertical load, was connected to the pump.

The horizontal load applied on the top column during the combined loading was measured from a built-in load cell in the actuator.

## 2.7.2 Displacement

Column lateral displacement was determined from the actuator stroke that was measured by a built-in linear voltage displacement transducer (LVDT). Another LVDT shown in Figure 2.30 was installed to measure the vertical displacement of the column bottom surface. To avoid the effect of column rotation on measurement during lateral loading, the measuring point was located at the column vertical centerline. Based on the measurement from this LVDT, vertical deflection of the slab was indirectly acquired because of the negligible column axial deformation induced by vertical load.

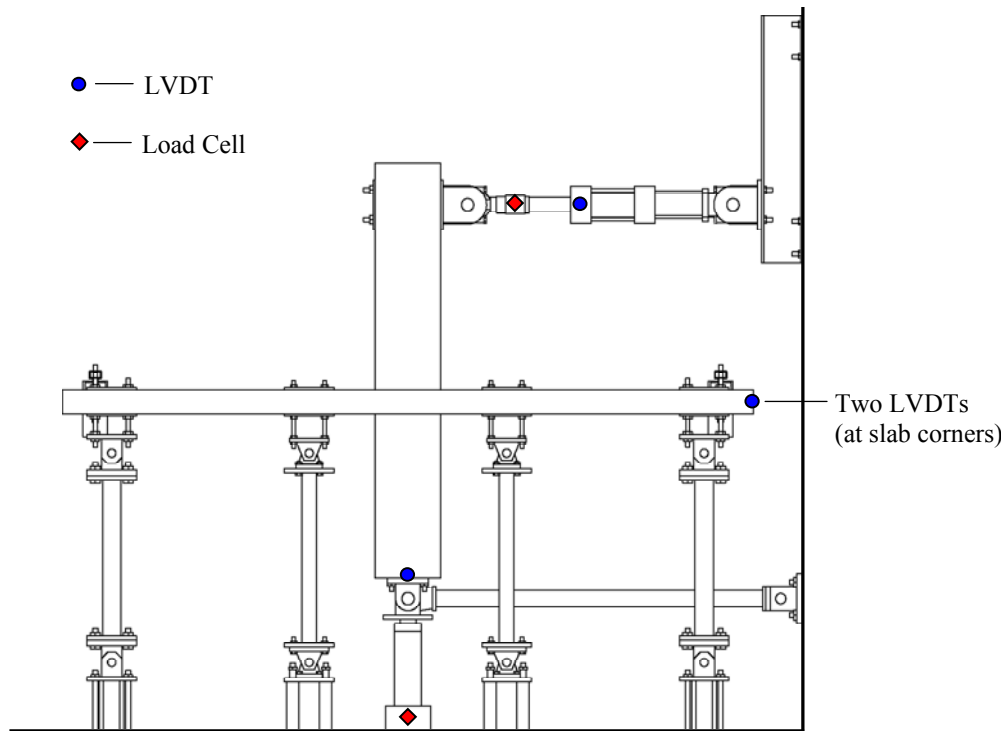


Figure 2.30: Location of load cells and LVDTs.

During lateral loading, as shown in Figure 2.30, two LVDTs were installed at the slab corners along an edge perpendicular to the lateral loading to measure the slab lateral displacement. Such measurement had two functions. First, since no relative displacement

between those two points was observed, the torsional stability of the specimens was verified. Second, the recorded lateral displacement was almost exactly half of that measured from the actuator at the top column, indicating that column lateral deformation was substantially small. Thus, lateral drift ratio, defined as the ratio of column top displacement to the effective column height (96 in.), can be approximated as the slab-column joint rotation relative to its original position.

### 2.7.3 Strain

Electrical resistance strain gauges were attached to the flexural reinforcement at selected locations of the slabs to provide information regarding internal force distribution and redistribution. The number of such gauges ranged from 28 to 50 depending on the testing specimen and loading history. The typical locations of steel strain gauges in one quadrant of the slab, which was most heavily gauged, are shown in Figure 2.31.

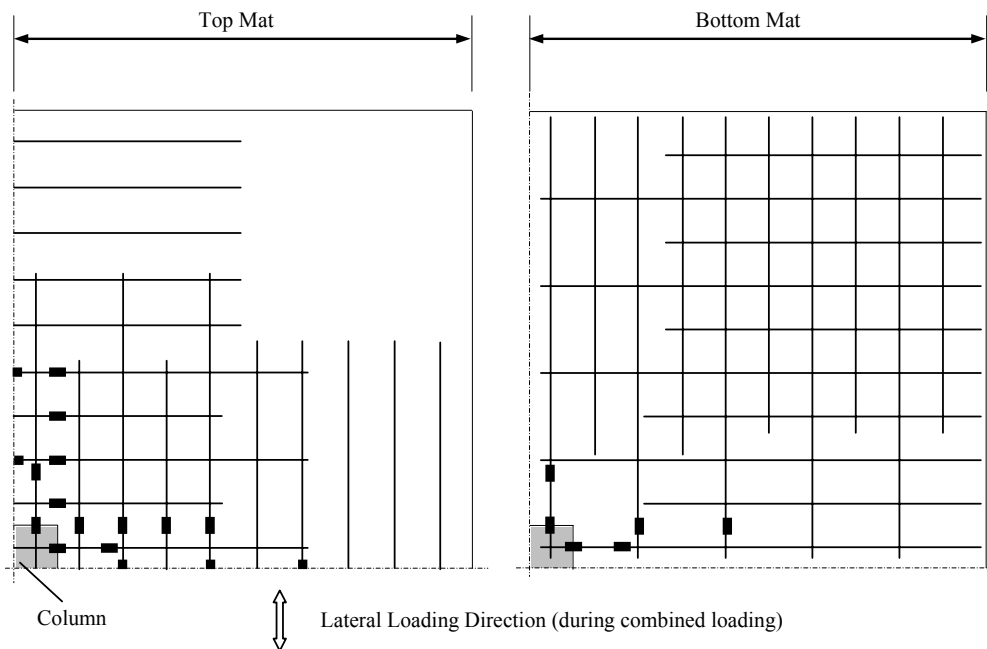


Figure 2.31: Typical steel strain gauge location.

Strain gauges were also mounted at the slab bottom surface near the column for Specimen G1.0. These gauges were oriented in a tangential direction (parallel to the column face) and radial direction (perpendicular to the column face) at each side of column.

## 2.8 SPECIMEN TRANSFER AND PLACEMENT IN TEST SETUP

Before the specimens were lifted and assembled on the test setup, steel chains were used to support the slab corners from the top column, as shown in Figure 2.32. This was done to prevent the damage due to the slab self-weight during lifting.



Figure 2.32: Preparation for specimen lifting.

After the specimens were lifted from the formwork, they were placed on temporary shoring, as shown in Figure 2.33. Then the struts, clevises, and actuator were connected. Special care was taken to avoid introducing load to the specimens during the

assembling process. The temporary shoring was disassembled once vertical loads were applied to the specimens through the vertical jack.



Figure 2.33: Placement of specimen in test setup.

## Chapter 3

### Experimental Results of Slab-Column Connections under Combined Lateral and Gravity Loading

#### 3.1 GENERAL

Experimental results of three test assemblies L0.5, LG0.5 and LG1.0 subjected to combined lateral and gravity loading are presented in terms of damage pattern, load-deformation characteristics, stiffness degradation, and recorded reinforcement strain. Although the primary goal of testing Specimens LG0.5 and LG1.0 was to investigate the gravity load-carrying capacity of earthquake-damaged connections, the test data recorded during the first loading stage, combined lateral and gravity loading, provided data regarding the effect of reinforcement ratio on the connection behavior.

#### 3.2 LOADING HISTORY

The loads applied on the specimens included an upward vertical load on the column simulating gravity load effects and lateral deformation reversals with increasing amplitudes simulating seismic effects. Prior to lateral loading for Specimen L0.5, a vertical load of 26.4 kips was applied. Subtracting 2.9 kips for the weight of the column and the loading apparatus attached to the column, the applied vertical load resulted in a gravity shear of  $V_g = 23.5$  kips on the critical section around the column. The gravity shear on the critical section was intended to simulate dead load plus 25% of the design live load acting on the floors of the prototype structure. The corresponding gravity shear ratio,  $V_g/V_c$ , was 0.23, where  $V_c$  is the two-way shear strength based on ACI 318-05 provisions. Following gravity loading, L0.5 was subjected to lateral deformation

reversals shown in Figure 3.1. In order to observe the specimen behavior in the elastic range, a small amplitude lateral deformation was first applied to L0.5 to produce a drift ratio of 0.25%. Then the drift level was gradually increased to 0.5%, 0.75%, 1.0%, 1.5%, 1.75%, 2%, and 2.5% until the connection failure. For each drift level, three reversed cycles were applied through the servo-controlled actuator.

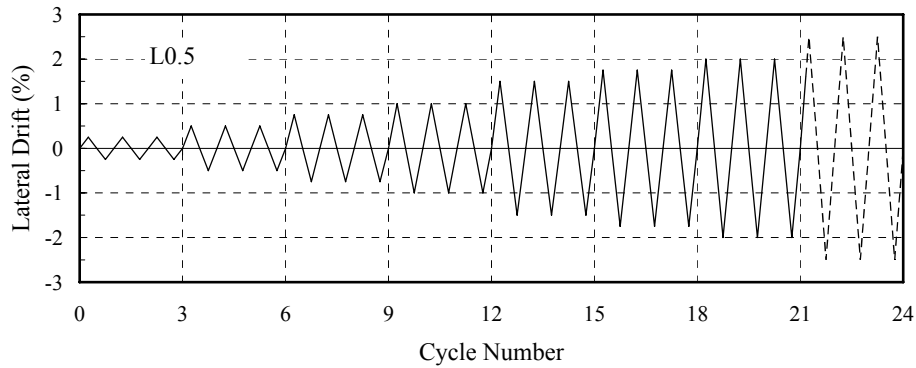


Figure 3.1: Lateral Displacement Routine for L0.5.

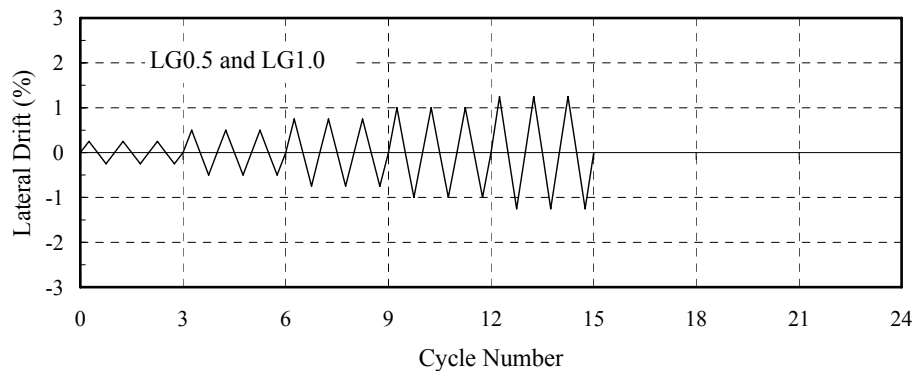


Figure 3.2: Lateral Displacement Routine for LG0.5 and LG1.0.

Two test phases were used for Specimens LG0.5 and LG1.0. First, they were subjected to combined loading using the test setup shown in Figure 2.21. The same gravity shear ratio used for L0.5,  $V_g/V_c = 0.23$ , was applied to LG0.5 and LG1.0 to

determine the initial vertical load. The corresponding gravity shear was 26.8 kips for LG0.5 and 24.1 kips for LG1.0. Based on the test observation from Specimen L0.5, lateral loading for LG0.5 and LG1.0 was terminated after cycling to 1.25% drift, as shown in Figure 3.2, to avoid a connection failure. During the second test phase, the test setup shown in Figure 2.23 was used and the damaged specimens due to lateral loading were vertically loaded to failure.

Lateral loading for L0.5, LG0.5, and LG1.0 was paused several times at peak drift or zero lateral load for each drift level to allow nondestructive testing to determine the connection damage condition, inspecting testing system, marking slab cracks, and photographing crack patterns (Argudo, 2006). Hence, no attempt was made to maintain a specific lateral loading rate.

### **3.3 GLOBAL RESPONSE**

#### **3.3.1 Overall Load-Drift Response**

The overall behavior of the specimens is described by means of lateral load-drift response. The sign convention for lateral drift shown in Figure 2.20 was followed in the discussions.

After reaching 0.5% drift, the hysteretic loops in all specimens exhibited pinching, indicating strength and stiffness degradation as well as low energy dissipation capacity. Figure 3.3 shows as an example the pinching effect observed in Specimen L0.5. Such characteristic behavior was typical of slab-column connections under large lateral deformation reversals reported in the literature.

The complete lateral load-drift response and the response envelopes are plotted together for Specimens L0.5, LG0.5, and LG1.0 in Figures 3.4 through 3.6.

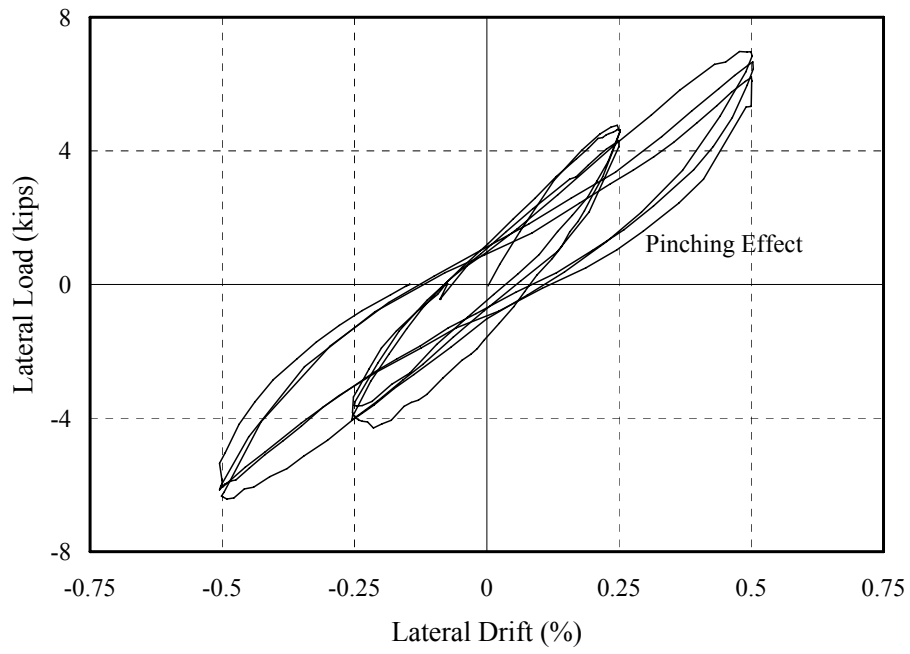


Figure 3.3: Pinching effect under cyclic loading (Specimen LG0.5).

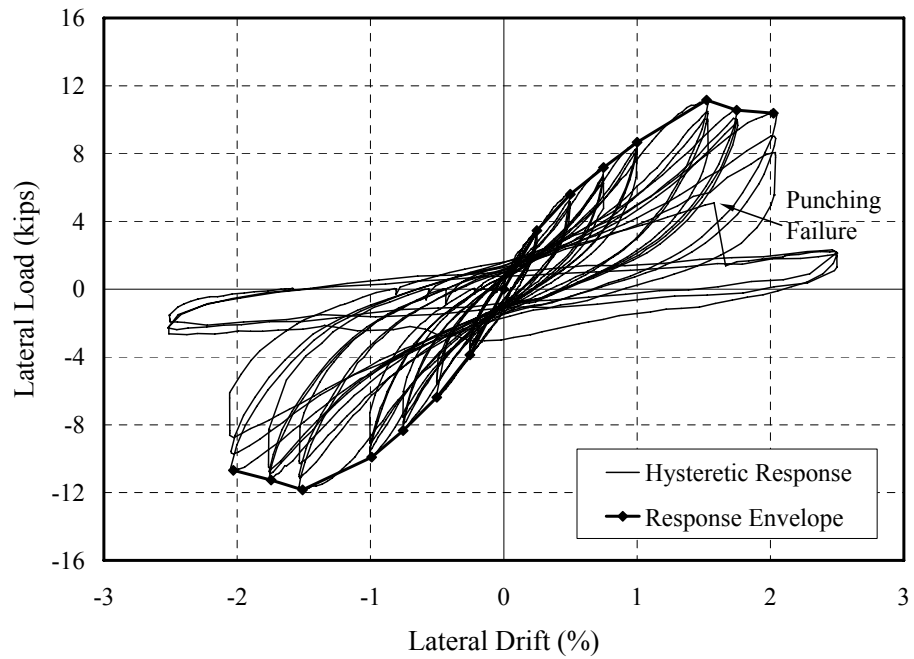


Figure 3.4: Lateral load versus drift response of Specimen L0.5.

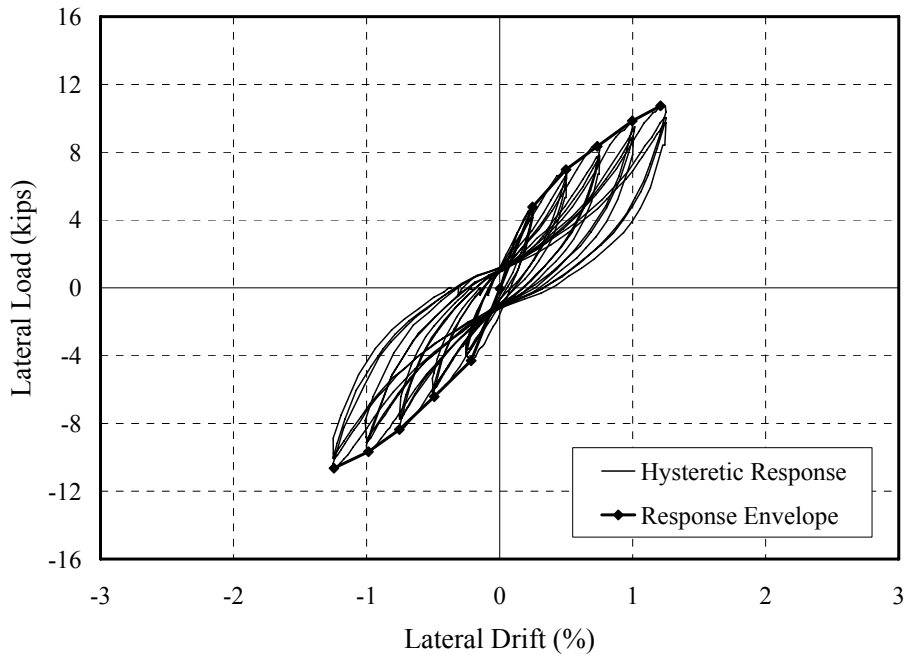


Figure 3.5: Lateral load versus drift response of Specimen LG0.5.

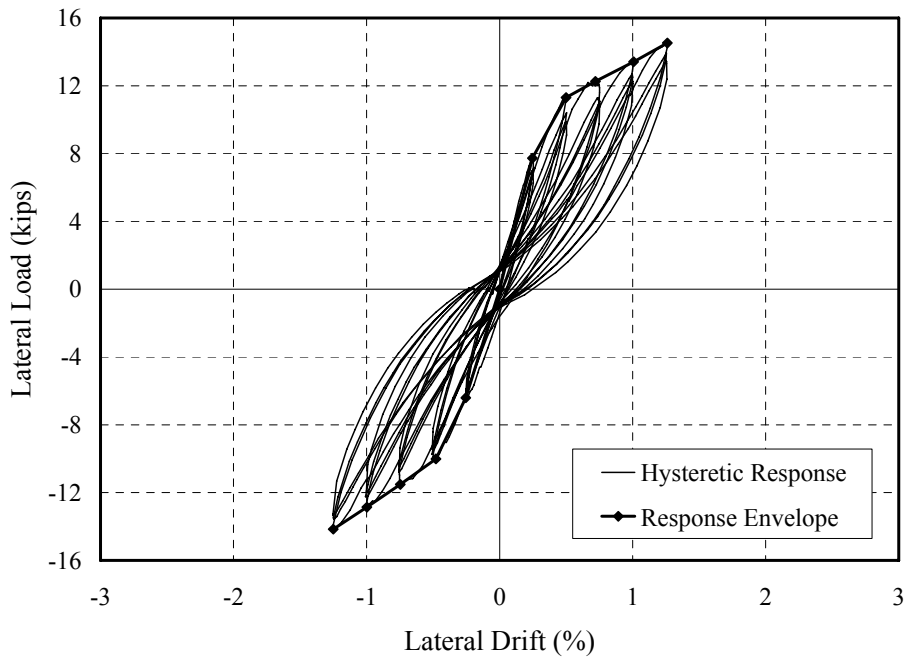


Figure 3.6: Lateral load versus drift response of Specimen LG1.0.

The peak lateral load attained in L0.5 was 11.4 kips at +1.5% drift and 11.8 kips at -1.5% drift. After that the connection withstood an additional 0.5% drift while ninety percent of the lateral load carrying capacity was maintained.

After completion of cycles at 2.0% drift, the failure of L0.5 occurred at a drift of 1.6% when cycles to 2.5% drift were attempted. A brittle failure was evident in the sudden drop of both lateral and vertical loads. Based on Equation (1.13) and the applied gravity load level ( $V_g/V_c = 0.23$ ), L0.5 should sustain a drift of 2%, a value equal to the observed connection drift capacity.

The response envelope curves for the three specimens are shown in Figure 3.7. Although L0.5 had slightly lower lateral stiffness in the positive loading direction than LG0.5, the backbone curves of these specimens at the negative lateral direction were nearly identical until 1.25% drift when lateral loading for LG0.5 was terminated.

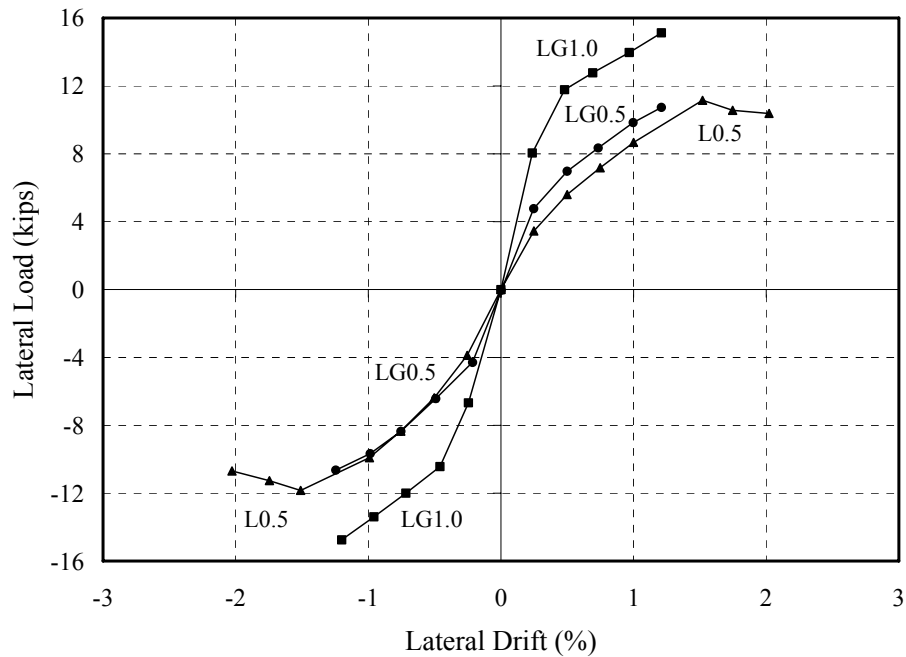


Figure 3.7: Comparison of response envelope curves.

### 3.3.2 Connection Stiffness Degradation

#### 3.3.2.1 Lateral Stiffness Degradation

Due to the highly indeterminate nature of a slab-column connection and the ability of slab systems to redistribute forces from highly stressed to less stressed sections, the specimens subjected to combined loading experienced gradual lateral stiffness degradation. The lateral stiffness can be expressed as secant or tangential rotational stiffness of the response envelopes. As shown in Figure 3.8, the secant stiffness at lateral drift level  $i$  was defined as the ratio of unbalanced moment to the joint rotation. The tangent stiffness at  $i$  was defined as the ratio of incremental moment to incremental joint rotation between  $i$  and the succeeding drift level  $i+1$ . The unbalanced moment was determined from the measured lateral load and effective column height.

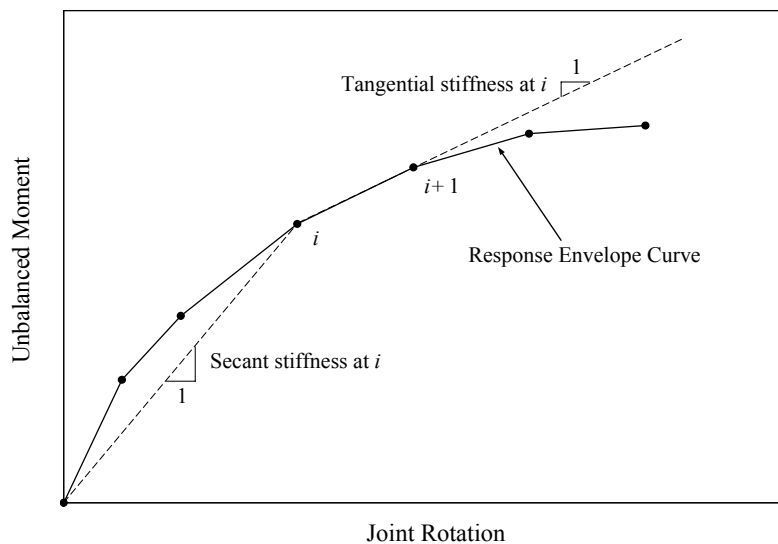


Figure 3.8: Definition of secant and tangential stiffness.

Figure 3.9 shows the secant stiffness of L0.5, LG0.5, and LG1.0, defined as the ratio of unbalanced moment to the connection lateral drift measured toward the reaction wall during the first cycle at various drift levels. Under lateral deformation reversals,

considerable stiffness loss was evident due to concrete cracking and reinforcement yielding near the column. When 1% drift was reached, the secant stiffness was only about 50% to 60% of the initial value. Thus, it can be inferred that, without the presence of stiffer structural elements such as shear walls, substantial inter-story deflections will occur in a flat-plate structure under severe earthquake.

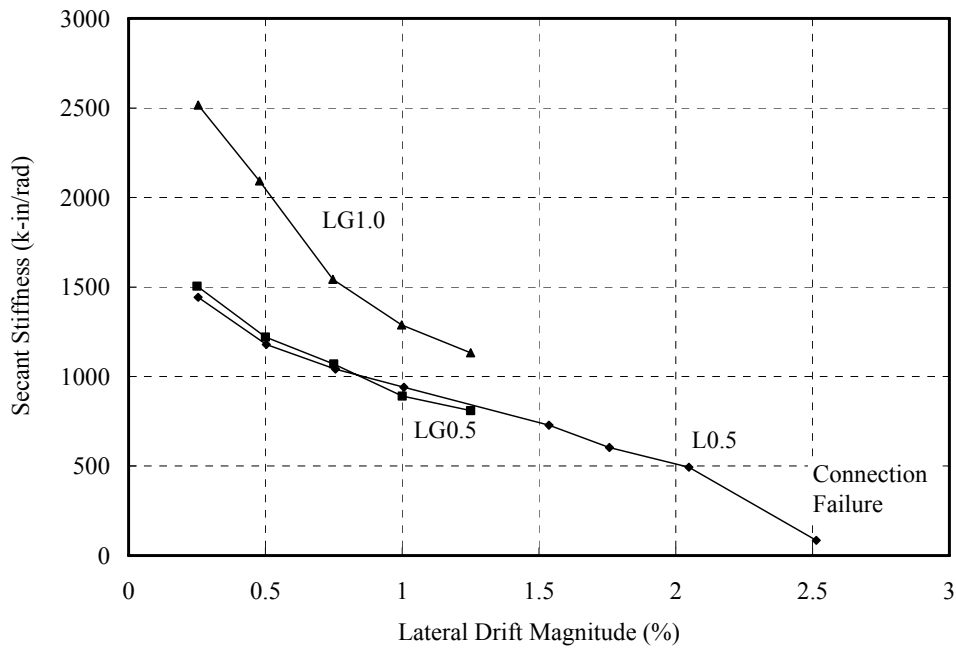


Figure 3.9: Secant stiffness degradation.

In Figure 3.10, the tangential stiffness of the three specimens is plotted. The difference in lateral stiffness of LG0.5 and LG1.0 indicates the significant effect of reinforcement ratio on connection stiffness. As shown in Figure 3.10, the initial stiffness (at zero lateral drift) of LG0.5 was only sixty percent of LG1.0, where the reinforcement ratio within a width  $c+3h$  centered on the column was twice that of L0.5. Prior to reaching 0.75% drift, the stiffness of LG1.0 degraded at a higher rate than LG0.5, as can be seen in Figures 3.9 and 3.10.

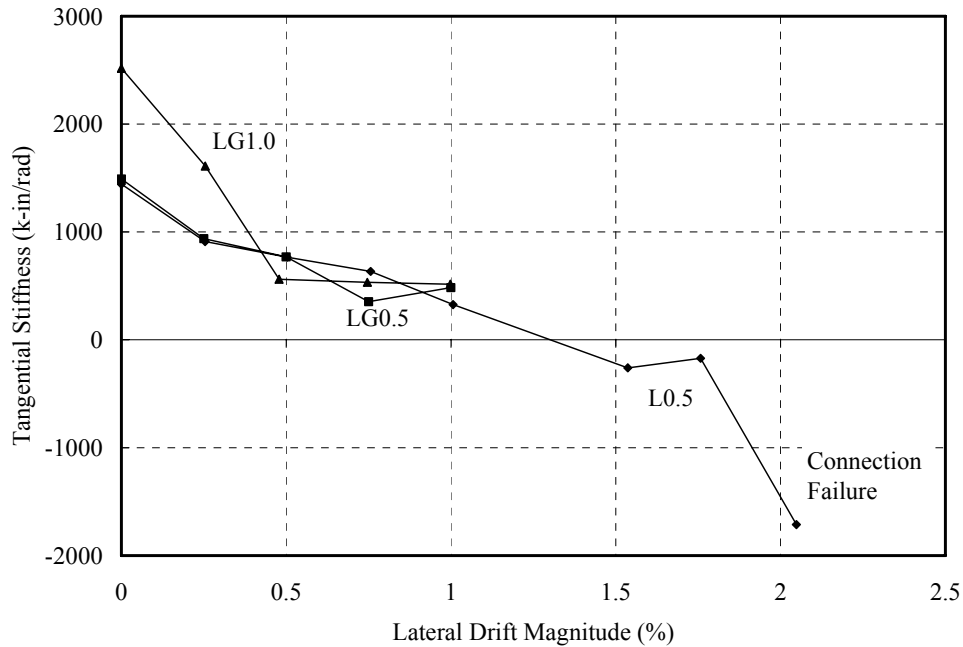


Figure 3.10: Tangential stiffness degradation.

In addition, the tangential stiffness degradation stopped at 0.5% drift in LG1.0. As will be discussed later, the top bars around column had already yielded under negative bending when 0.5% drift was reached. After this lateral drift level, the tangential stiffness of LG1.0 remained constant, suggesting that no further reinforcement yielding occurred and the connection behaved linearly in terms of the overall response.

### 3.3.2.2 Connection Stiffness Degradation after Damage

The stiffness degradation can also be illustrated by the increased slab vertical deflection as the damage that resulted from lateral cycling accumulated. The slab center deflection, measured when the lateral load for a drift level was completely released, as a function of that lateral drift level is plotted in Figure 3.11. This figure clearly indicates the increased slab vertical deflection under an approximately constant gravity load as the connection was subjected to increased amplitude of lateral deformation. In addition, the

deflection of LG1.0 was always much smaller than that of LG0.5, showing again the effect of reinforcement ratio on connection stiffness.

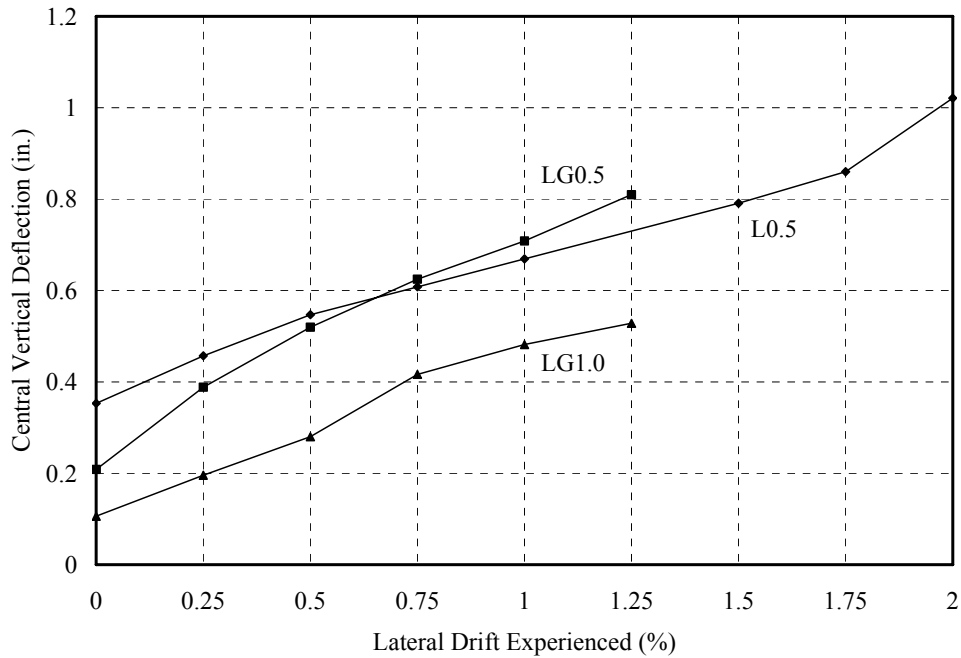


Figure 3.11: Vertical deflection versus lateral drift.

The primary objective of testing Specimens LG0.5 and LG1.0 was to investigate the gravity load-carrying capacity of an interior slab-column connection damaged by certain level of lateral deformation imposed by an earthquake. For a flat-plate structure in the field, however, the connection lateral drift that was caused by an earthquake is not likely to be known. In order to extend the conclusion derived from this study to field application, it is of particular interest to correlate quantifiable damage with the maximum drift that the connection has possibly experienced. A stiffness degradation ratio defined as the ratio of vertical deflections of the connection with and without seismic damage was calculated. The relationship between the stiffness degradation ratio and lateral drift for LG0.5 and LG1.0 is presented in Figure 3.12.

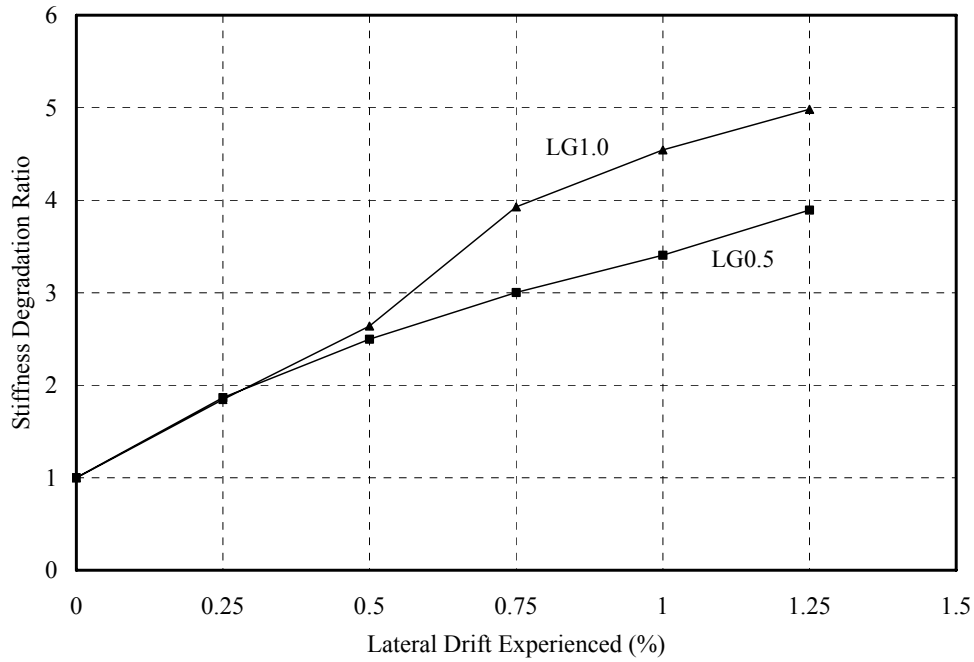


Figure 3.12: Stiffness degradation ratio versus lateral drift.

Figure 3.12 suggests an approach to extend test results to field applications since the stiffness declination ratio appears to be a function of the lateral drift as well as the reinforcement ratio. The following discussion briefly illustrates the relevant procedures:

- (1) The vertical deflection of a specimen due to gravity shear,  $V_g$ , before and after applying the lateral load was defined as  $\Delta_0$  and  $\Delta$ , respectively;  $K_0$  and  $K$  were defined as the secant stiffness of connection associated with  $\Delta_0$  and  $\Delta$ . These variables have the following relationships:

$$\Delta = \frac{V_g}{K} \quad (3.1)$$

$$\Delta_0 = \frac{V_g}{K_0} \quad (3.2)$$

- (2) Based on Figure 3.12, it was assumed that

$$\frac{\Delta}{\Delta_0} = f(DR, \rho) \quad (3.3)$$

where  $DR$  denotes the drift ratio the connection has experienced;  $f(DR, \rho)$  is a function of  $DR$  and reinforcement ratio  $\rho$  and its specific expression should be generalized from the tests.

(3) Combining Equations (3.1) through (3.3) gives

$$\frac{K_0}{K} = f(DR, \rho) \quad (3.3)$$

(4) It was assumed that the same gravity load was applied on the structure before and after earthquake and, under a specific lateral drift, the field structure experienced the same degree of stiffness degradation as that for an isolated specimen in the laboratory test. Thus,

$$\frac{\Delta^*}{\Delta_0^*} = f(DR, \rho) \quad (3.4)$$

where  $\Delta_0^*$  and  $\Delta^*$  are slab vertical deflections at the same location in a field structure before and after an earthquake.

It must be noted that both  $\Delta_0^*$  and  $\Delta^*$  in Equation 3.4 are the short-term slab deflections without any consideration for the time effects because the tests, from which  $f(DR, \rho)$  can be determined, were carried out in a short period.  $\Delta_0^*$  can be estimated from analysis.  $\Delta^*$  can be determined from the slab deflection or from the deflection of non-structural components such as the ceiling. However, such measurement may include time effects (beyond the scope of this study) that should be removed when determining  $\Delta^*$ . Due to concrete creep associated with crack spreading, the vertical deflection of a slab with a 0.5% top reinforcement ratio at the age of five years or more is about 60% higher than the initial deflection.

It is noted that the test boundary conditions for L0.5, LG0.5, and LG1.0 under combined loading were not suitable for estimating the slab deflection due to gravity load for a continuous flat-plate structure. Nonetheless, using the stiffness degradation ratio bypasses the boundary condition effects and makes the application of laboratory test results to field evaluation possible.

### 3.4 OBSERVED DAMAGE AND FAILURE PATTERN

Four types of cracks shown in Figure 3.13 were generated on the slab top surface: (1) peripheral cracks around the column, (2) torsional cracks at column sides, (3) diagonal cracks radiating from the column to the slab boundaries, and (4) radial cracks along the flexural reinforcement.

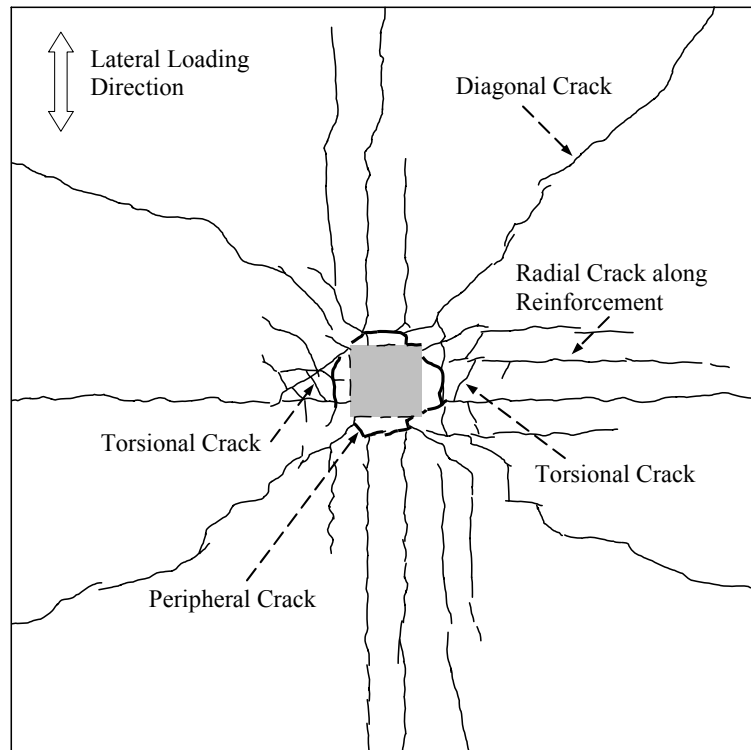


Figure 3.13: Crack types on slab upper surface.

### 3.4.1 Specimen LG0.5

The cracking patterns in Specimen LG0.5 at various drift levels are shown in Figure 3.14 and discussed in detail.

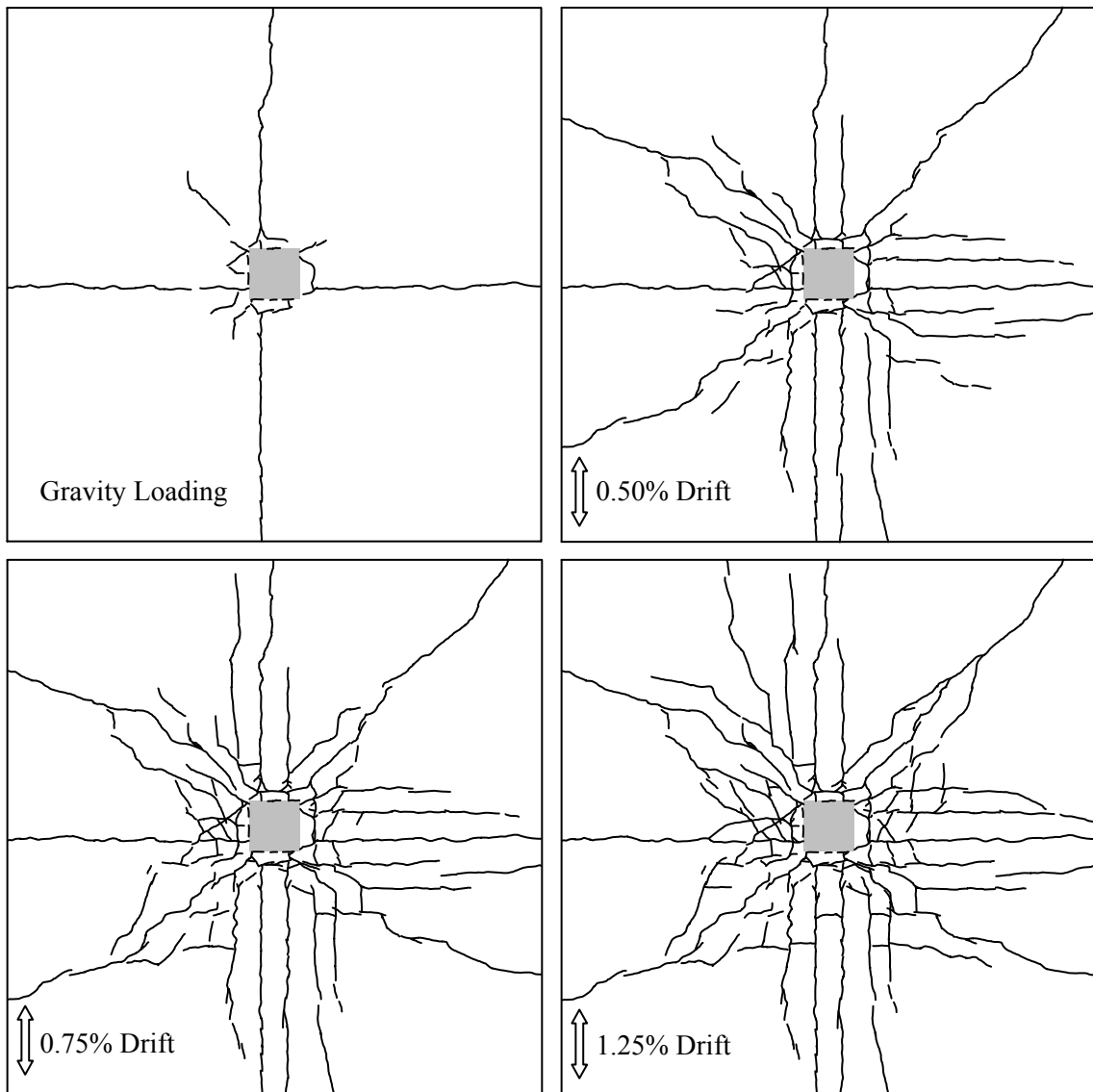


Figure 3.14: Top cracking pattern of Specimen LG0.5.

After applying gravity load, peripheral cracks appeared in LG0.5 on the slab upper surface around the column due to the highly concentrated negative bending. Such cracking generally was not developed at the column faces but above the flexural reinforcement closest to the column. The peripheral cracks were always the most pronounced cracks in terms of crack depth and width during the entire loading process and outlined the final punching surface. Gravity loading also caused the radial cracks along the top bars that extended outwards from the column to the slab boundaries. Because these cracks were oriented along two orthogonal principle directions, it is believed that such cracking occurred immediately after the formation of peripheral cracks that caused the negative bending moment redistribution in the slab.

The emergence of peripheral and radial cracks due to gravity loading modified the slab stiffness characteristics such that, upon the application of lateral load, diagonal cracking took place. Because no top flexural reinforcement existed in the slab corner area (Figure 2.24), once the diagonal cracks that initially appeared in the column vicinity extended beyond the top reinforced area, they quickly reached the slab corners, where the crack depth was measured as high as four inches. Meanwhile, lateral loading generated more radial cracks and caused the existing such cracks to spread outwards along reinforcement lines. Flexural cracking occurred along the column faces but remained as secondary damage compared with the peripheral cracking.

After the connection experienced a 0.5% lateral drift, a torsional crack in the slab oriented around forty-five degrees to the lateral loading direction took place at one side of the column. After completion of cycles to 0.75% drift, visible flexural cracks emerged at the interface of column and slab bottom surface, as shown in Figure 3.15.

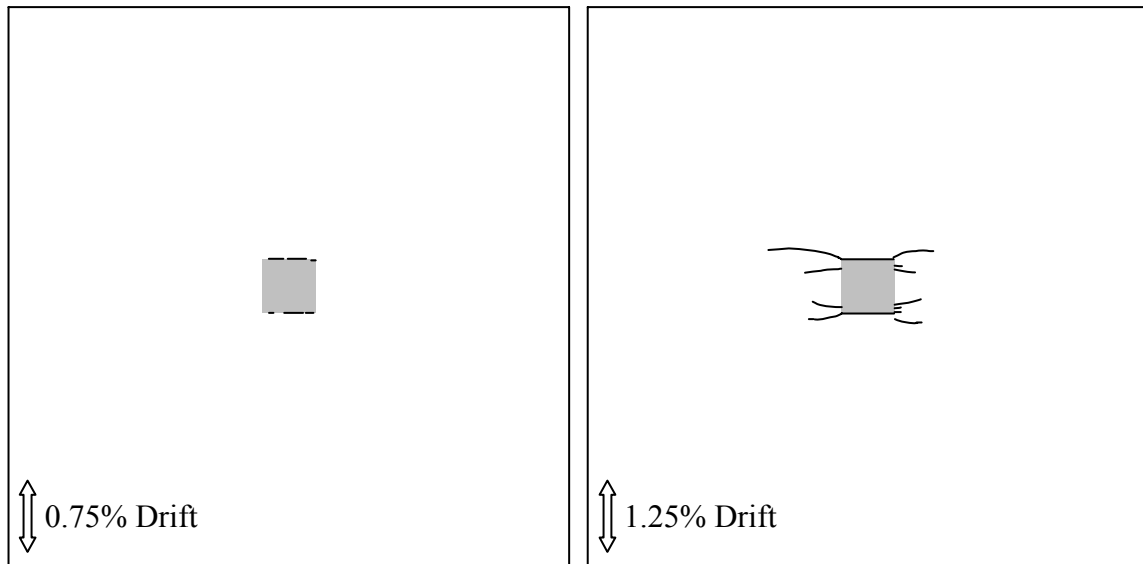


Figure 3.15: Bottom cracking pattern of Specimen LG0.5.

Upon the completion of cycles to 1% drift, top cracking was well established. It was observed that the torsional cracks were limited to an area approximately  $5d$  (25 in.) outside each column face parallel to the loading direction. After 1% drift, no new cracks were noted on the slab top surface. Lateral loading slightly extended the existing cracks and caused slab bottom cracking. After 1.25% drift was reached, significant torsional cracks appeared in the slab lower face and bottom flexural cracks extended beyond the slab-column interface.

### 3.4.2 Specimen LG1.0

Specimen LG1.0 developed cracking patterns similar to LG0.5 except that: (1) no visible cracking was identified due to the gravity loading, but cracks formed immediately after applying the lateral load; (2) cracks were developed more symmetrically on the slab top surface; and (3) cracks were narrower but denser than in Specimen LG0.5. The cracking patterns of this specimen at various drift levels are shown in Figures 3.16 for top cracking and 3.17 for bottom cracking.

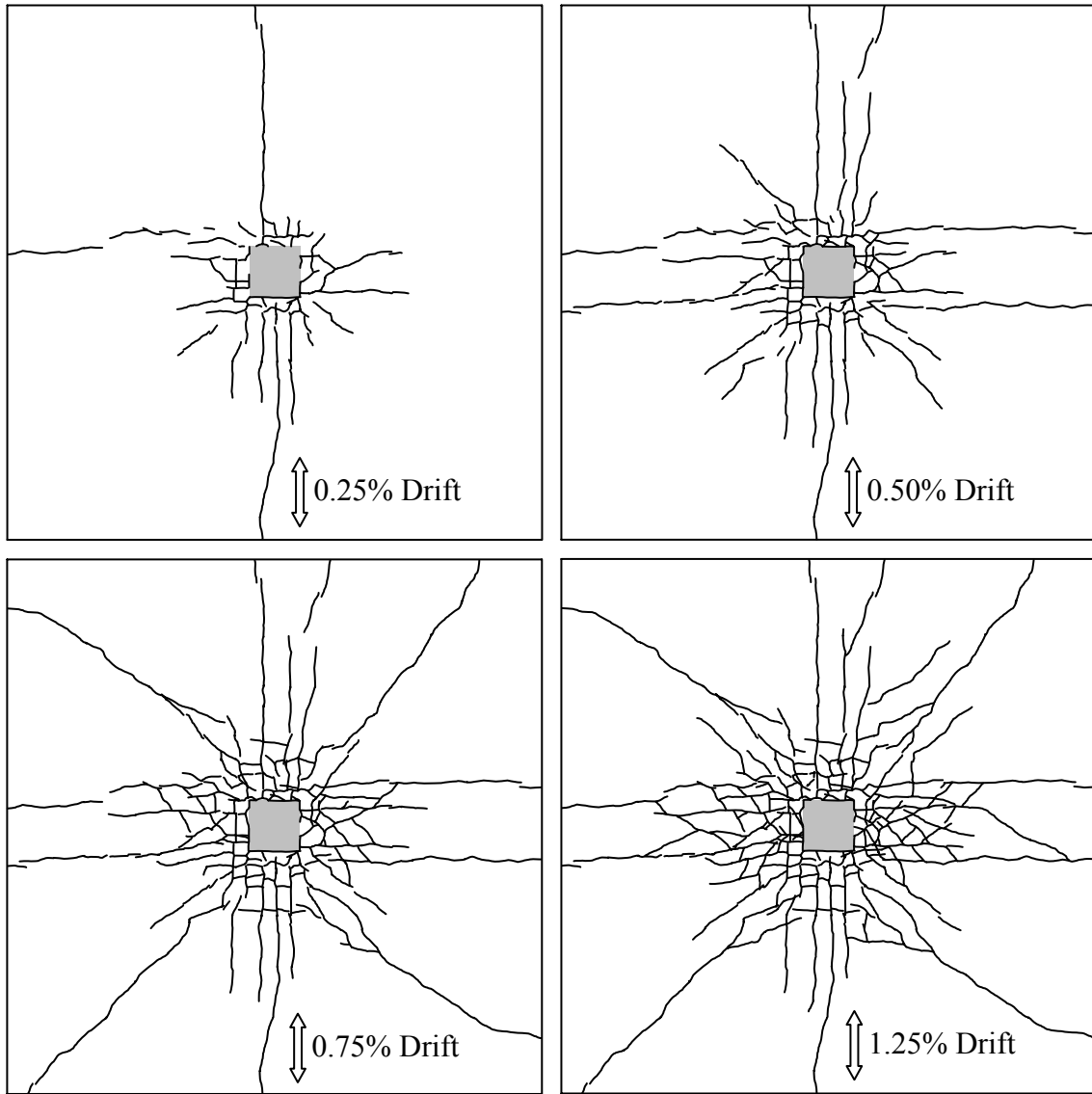


Figure 3.16: Top cracking pattern of Specimen LG1.0.

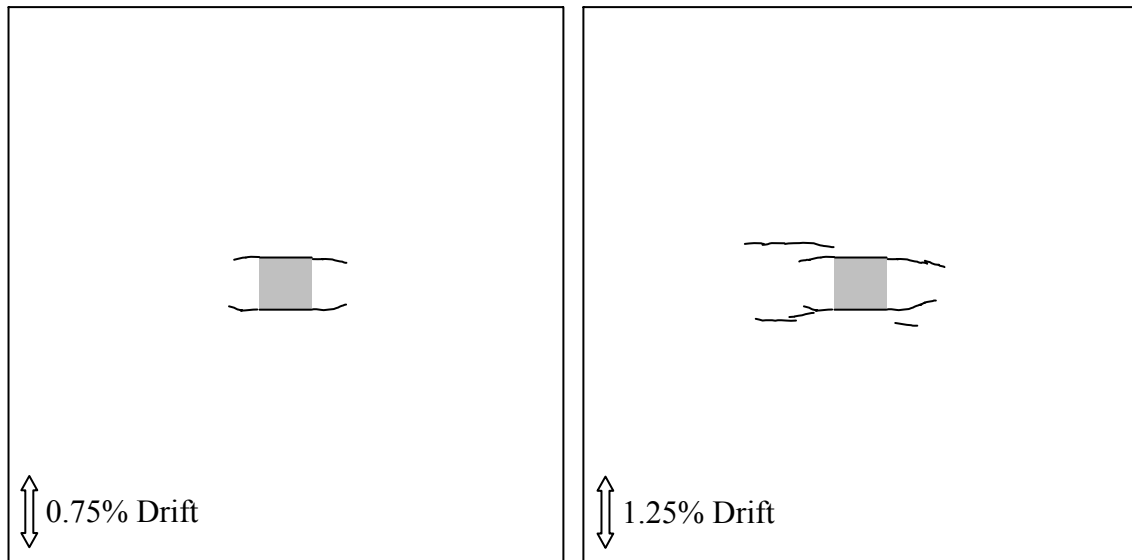


Figure 3.17: Bottom cracking pattern of Specimen LG1.0.

### 3.4.3 Specimen L0.5

Specimen L0.5 developed the same crack pattern as that in Specimen LG0.5 until 1.0% drift (1.25% drift level was not applied to L0.5). The crack distribution on the slab top surface of L0.5 at drift levels of 0.5%, 1.0%, 1.5%, and 2.0% and on the bottom surface at 0.75%, 1.0%, 1.5%, and 2.0% drift is shown in Appendix A

Concrete spalling occurred in Specimen L0.5 at 2.0% drift when the peripheral cracks were widely opened. Concrete delamination was identified from a hollow sound when the spalled concrete surface was tapped with a hammer. The extensive damage around the column at this loading stage, as shown in Figure 3.18, likely indicated the connection failure was imminent.

The connection failure of L0.5 was accompanied by extensive concrete cover spalling as the column was “punched out” and by the slab flexural reinforcement being stripped out (see Figure 3.26) away from the column. The failure pattern of L0.5 is shown in Figures 3.19 and 3.20.

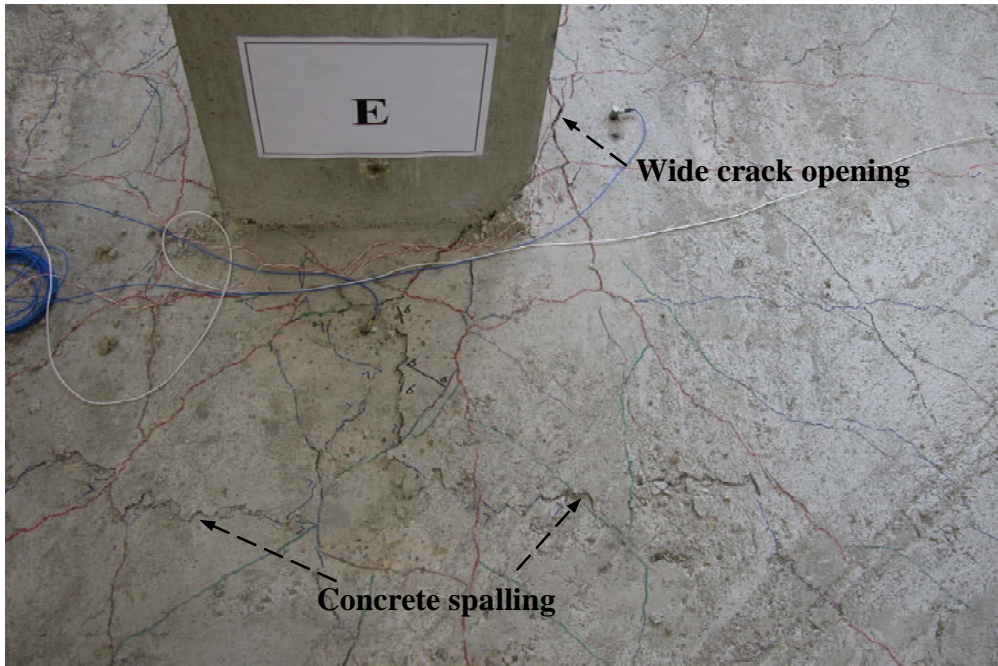


Figure 3.18: Damage around column at 2% lateral drift (Specimen L0.5).



Figure 3.19: Failure pattern of Specimen L0.5.

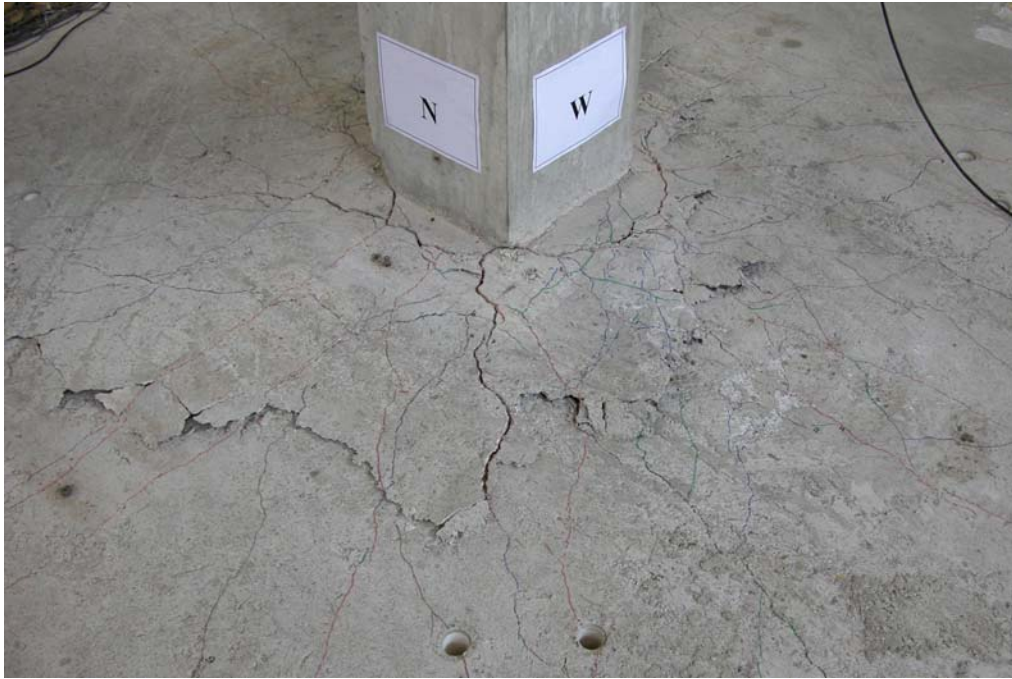


Figure 3.20: Close view of failure pattern of Specimen L0.5.

In all tests, no flexural crack appeared in the columns so that elastic behavior of the column can be assumed throughout the tests.

### **3.5 STEEL STRAIN**

#### **3.5.1 Top Steel Strain of Specimen L0.5**

The tensile strain profile of the top reinforcement (No. 4 bars) at various locations in a quadrant of the slab in Specimen L0.5 is shown in Figures 3.21 and 3.22 to illustrate the spread of slab yielding as lateral deformation was increased. Figure 3.21 shows the steel strains recorded at the peak joint rotation during the first cycle of each lateral drift level. The corresponding gauge locations along a line passing through one column face perpendicular to the loading direction are also shown in Figure 3.21. Figure 3.22 provides the strain values in a similar way except that the strains measured at four locations in a bar parallel to the loading direction are reported.

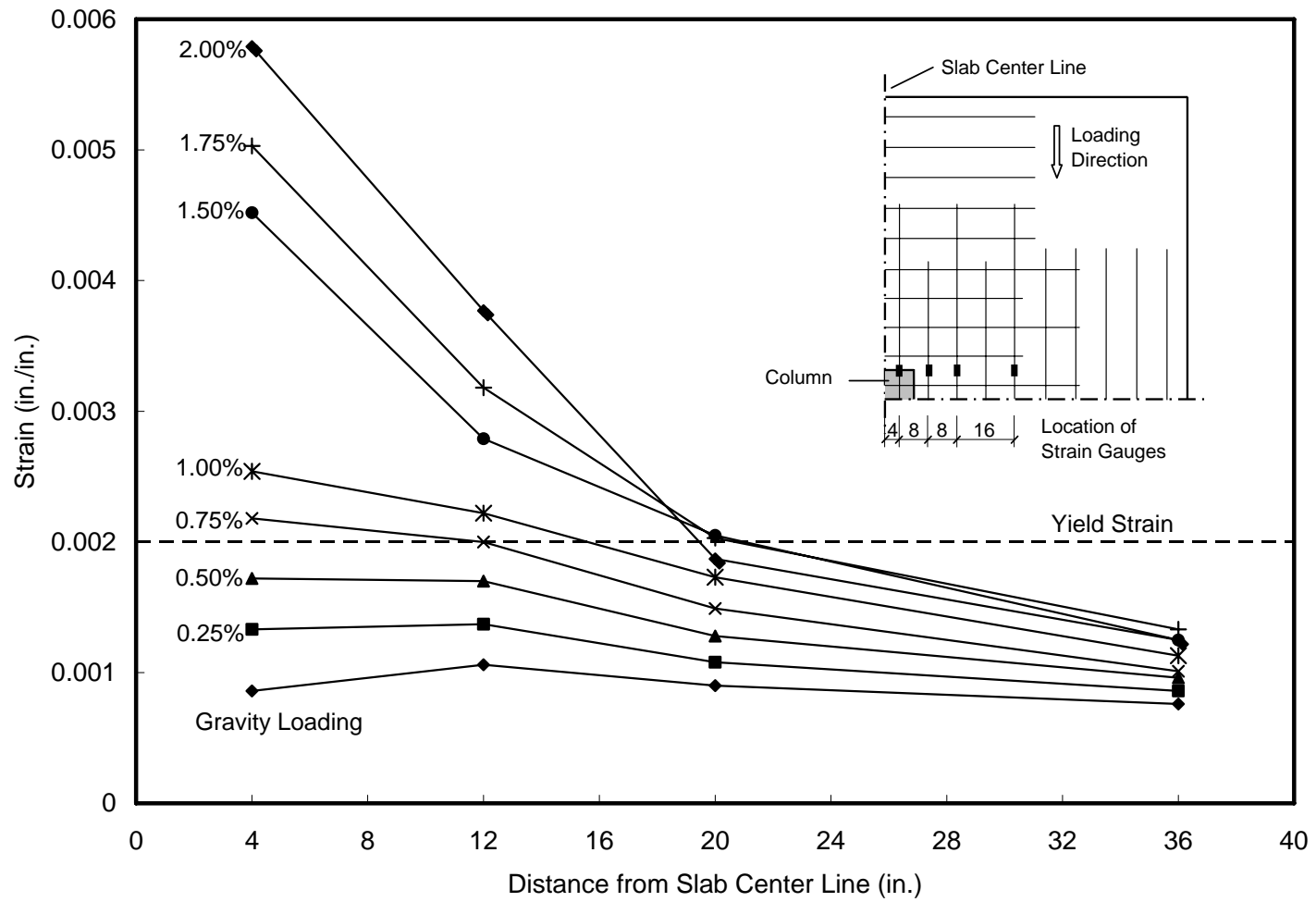


Figure 3.21: Top reinforcement strain of Specimen L0.5 (along transverse direction).

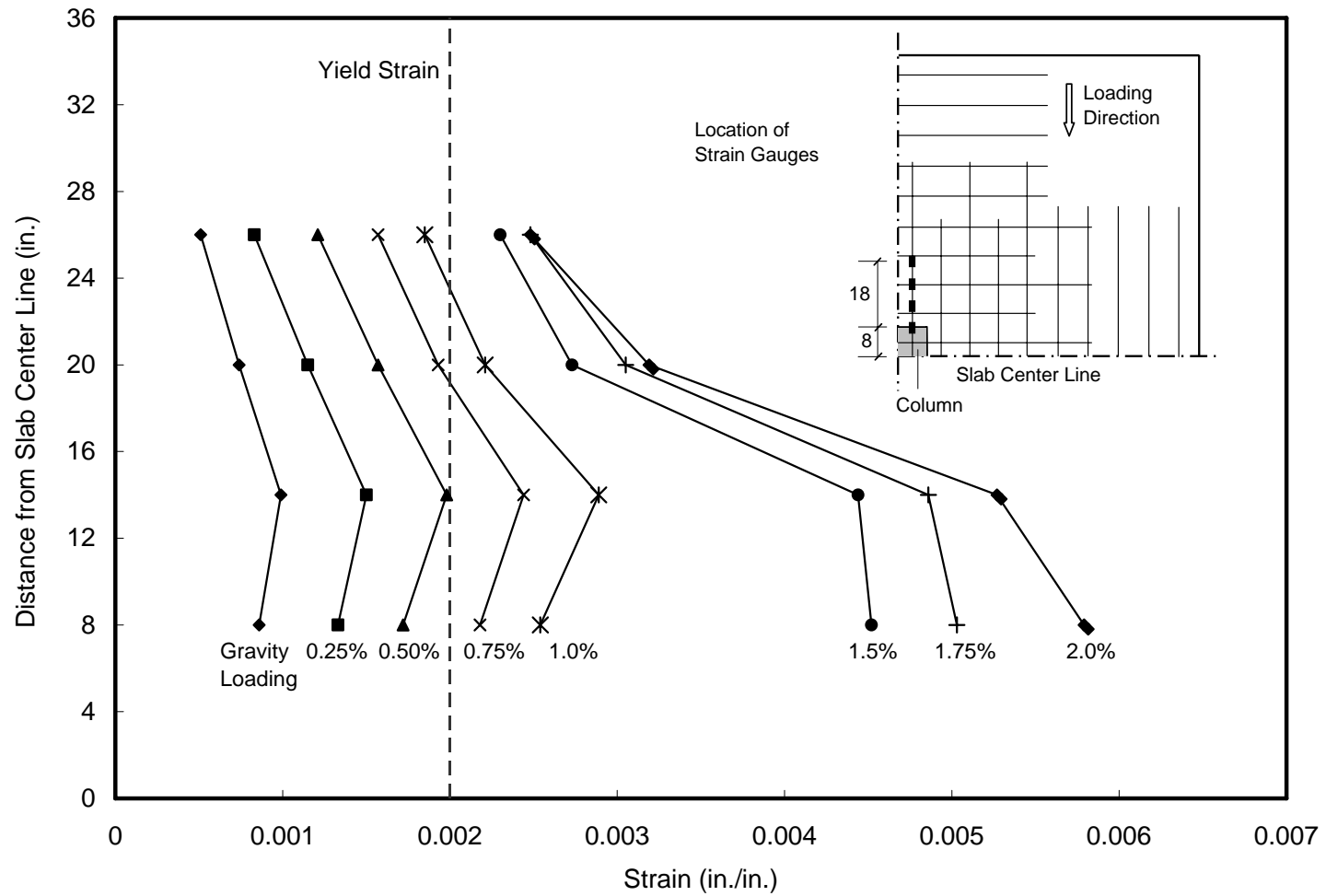


Figure 3.22: Top reinforcement strain of Specimen L0.5 (along longitudinal direction).

It is noted from Figure 2.29 that there was no obvious yielding point for the No. 4 bars used in L0.5. Thus, a yield strain of 0.002 is assumed and shown in Figures 3.21 and 3.22.

The measured maximum tensile strain at various loading stages was always observed at the top bars passing through the column and crossing the peripheral cracks. Under the initially applied gravity load, a strain of nearly half of the yield strain was reached. At 0.50% drift, first yielding occurred around the vicinity of the peripheral cracks at the bending sides and, as the lateral deformation increased, yielding gradually extended outside in both transverse and longitudinal directions. When peak lateral load was reached at 1.5% drift, all bars in a region of 20 inches transversely from the slab center line experienced yielding. Meanwhile, it was observed that the yielding spread 18 inches outside the column face in the lateral loading direction. After the peak load was achieved, large tensile strains were mainly concentrated at the peripheral cracks where the widest crack opening was observed.

### **3.5.2 Top Steel Strain of Specimen LG1.0**

The strain distribution of Specimen LG1.0 at various lateral drift levels is shown in Figures 3.23 and 3.24. As for L0.5, a yield strain of 0.002 was assumed. Some strain gauges experienced damage during lateral loading and, therefore, less information regarding steel strain was provided in LG1.0. First yielding of Specimen LG1.0 occurred at 0.44 % drift, a value slightly less than 0.50% in L0.5. At 1.0% drift, the yielding of LG1.0 extended over the same width as observed in L0.5, whereas yielding was constrained in a more limited region in the longitudinal direction.

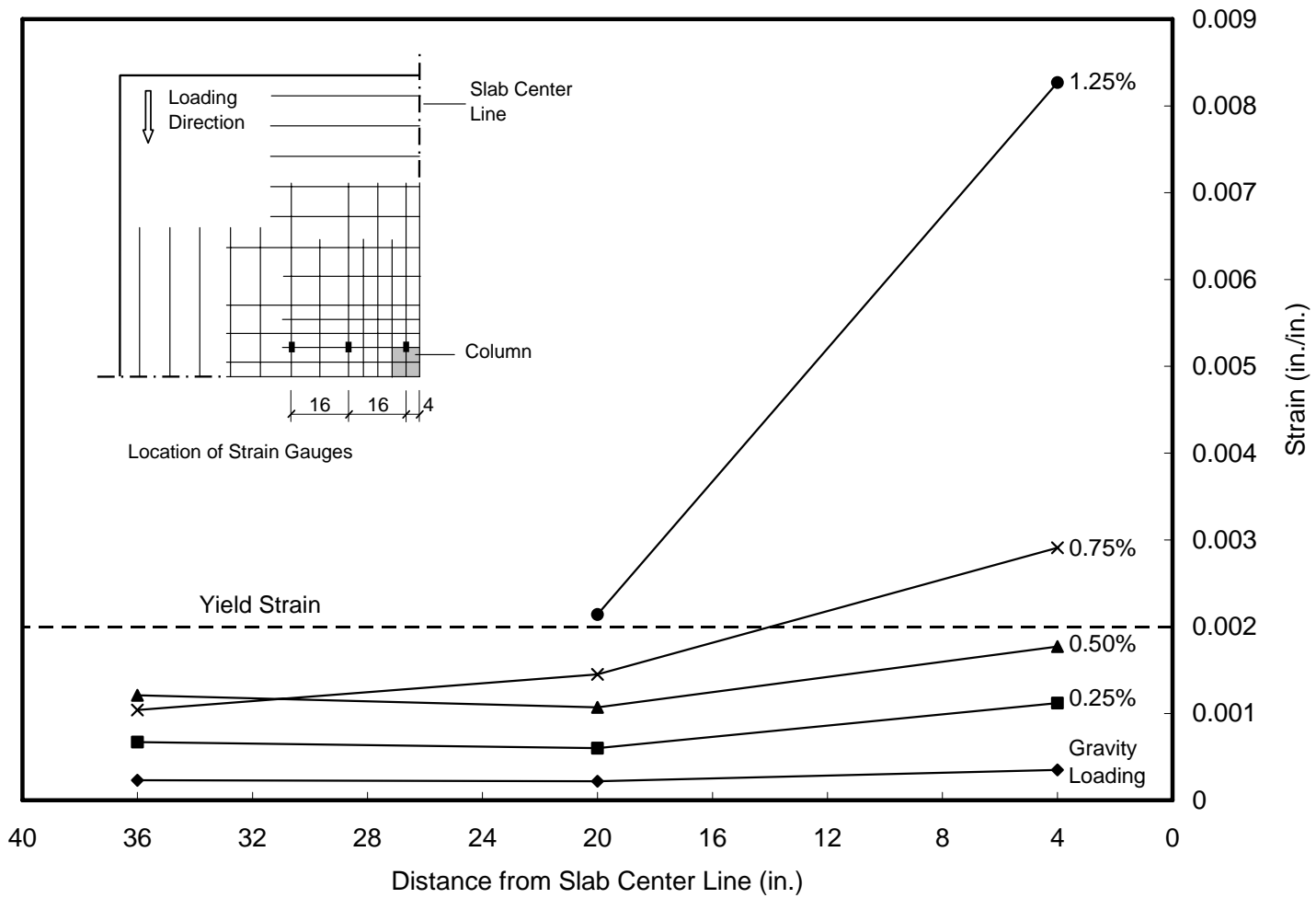


Figure 3.23: Top reinforcement strain of Specimen LG1.0 (along transverse direction).

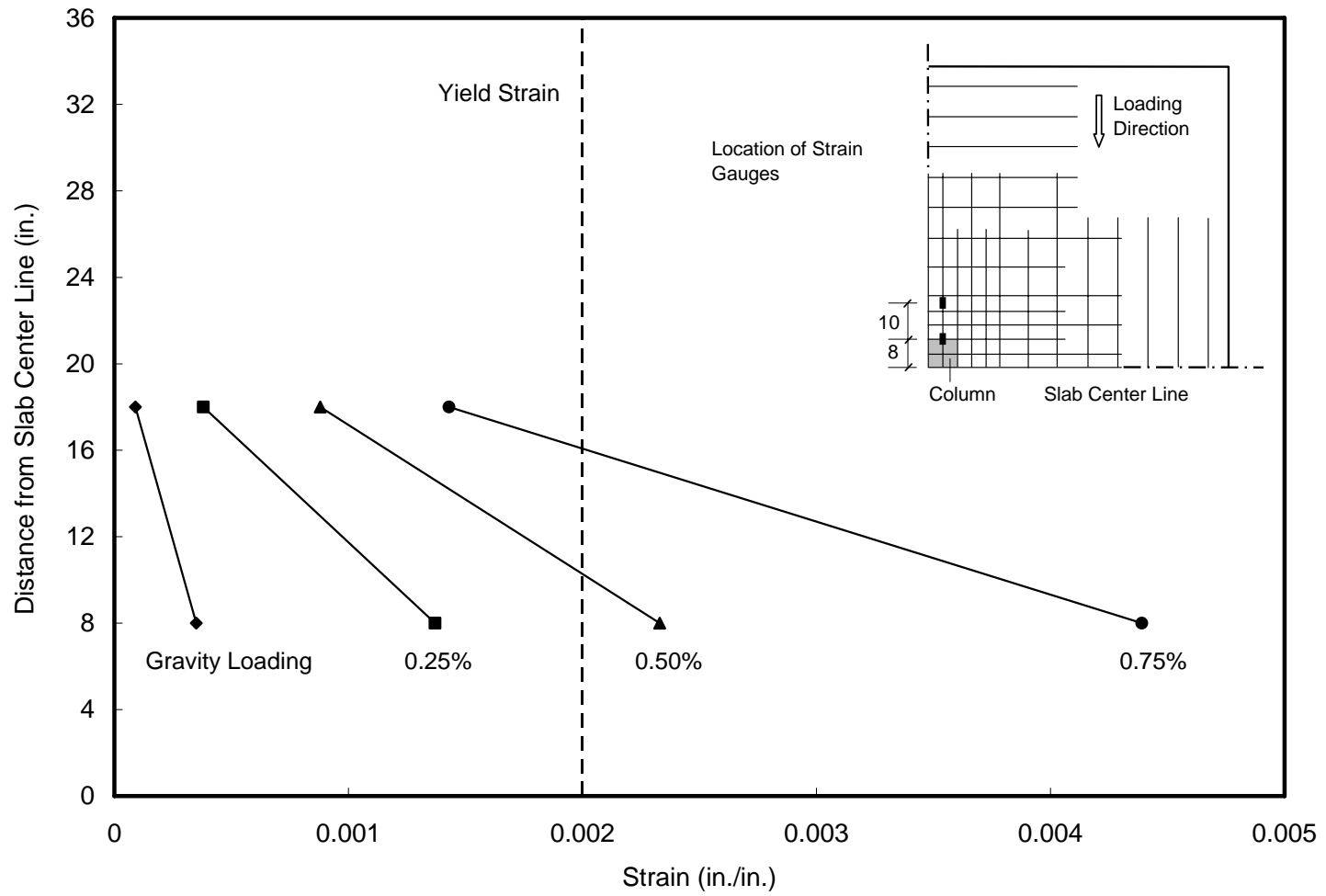


Figure 3.24: Top reinforcement strain of Specimen LG1.0 (along longitudinal direction).

### 3.5.3 Bottom Steel Strain of Specimens L0.5, LG0.5, and LG1.0

Figure 3.25 shows the strain of bottom reinforcement in the lateral loading direction measured at the slab-column intersection. In all tests, the bottom bars were in compression under gravity loading and began developing tensile stress at a drift less than 0.5%. Yielding of bottom reinforcement occurred in Specimen L0.5 at 1.5% drift, coinciding with reaching peak lateral load. When lateral loading was stopped at 1.25% drift, no bottom steel yielding was observed in LG0.5 and LG1.0.

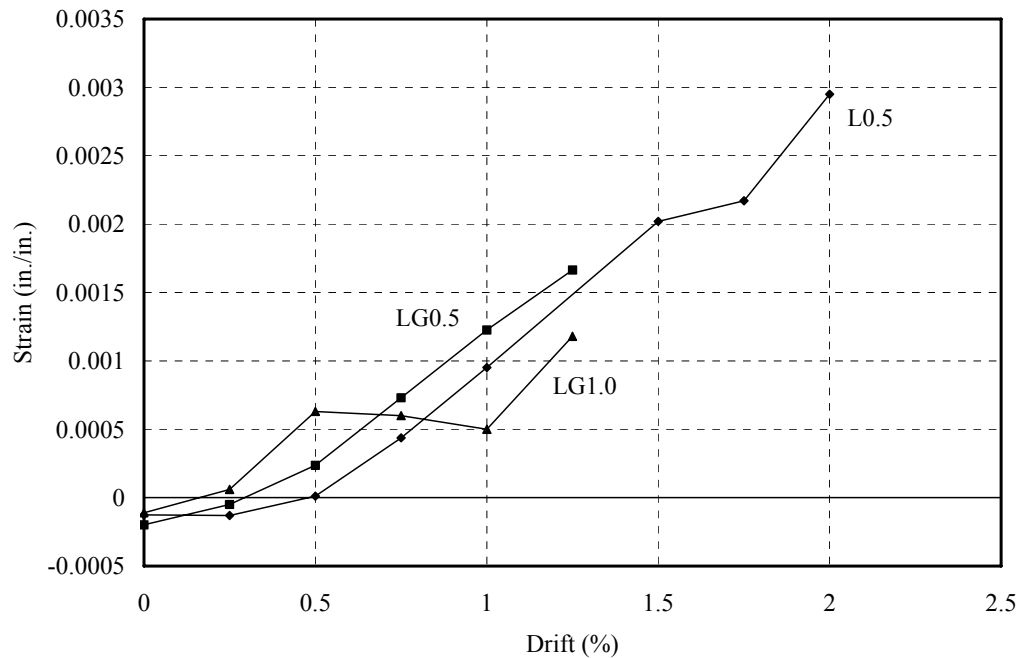


Figure 3.25: Strain of bottom reinforcement for three specimens.

### 3.6 SUMMARY OF TEST RESULTS

The major test results regarding the overall response of L0.5, LG0.5, and LG1.0 subjected to combined lateral and gravity loading are summarized in Table 3.1.

Table 3.1: Experimental Results for Specimens Subjected to Combined Loading

Specimen	Drift at First Yielding (%)	Secant Stiffness (k-in/rad)		Peak Lateral Load		Max. Drift (%)
		at 0.25% Drift	at 1.0% Drift	Lateral Load (kips)	Drift (%)	
L0.5	0.50	1440	940	11.2	1.5	2.0
LG0.5	0.50	1500	890	NA	NA	NA
L1.0	0.44	2520	1290	NA	NA	NA

### 3.7 FAILURE MECHANISM AND DISCUSSION

Figure 3.26 shows the exposed failure surface of Specimen L0.5 after removing the spalled concrete cover over the top bars. It can be seen that, the failure was generated from the peripheral cracks located four inches away from column faces. The failure surface is more evident in Figure 3.27, after the slab was cut away along two vertical planes three inches away from the column faces.

As shown in Figure 3.28, the failure of Specimen L0.5 initiated from one side of the column where the negative bending due to gravity and lateral load was in the same direction. It appeared that when the slab fractured, it triggered the loss of vertical load resistance and thus exhausted the slab local deformation capacity. The fracture immediately extended into the torsional sides of the slab along the peripheral cracks, the weakest link for carrying gravity shear, and resulted in a truncated failure surface shown in Figure 3.27 that enclosed the whole joint area.

The failure was brittle in the sense that the initial fracture led to an immediate connection failure. However, the gravity load must have dominated the propagation of the brittle fracture, since the failure surface was very similar to that of the specimens subjected to gravity load only (discussed in Chapter 4).

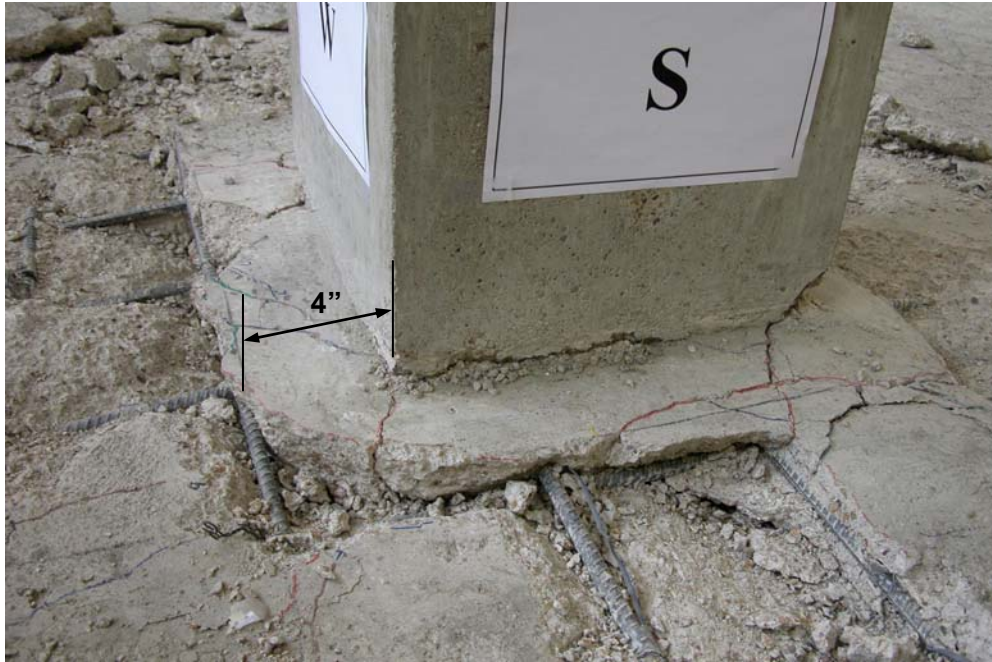


Figure 3.26: Failure surface of Specimen L0.5.

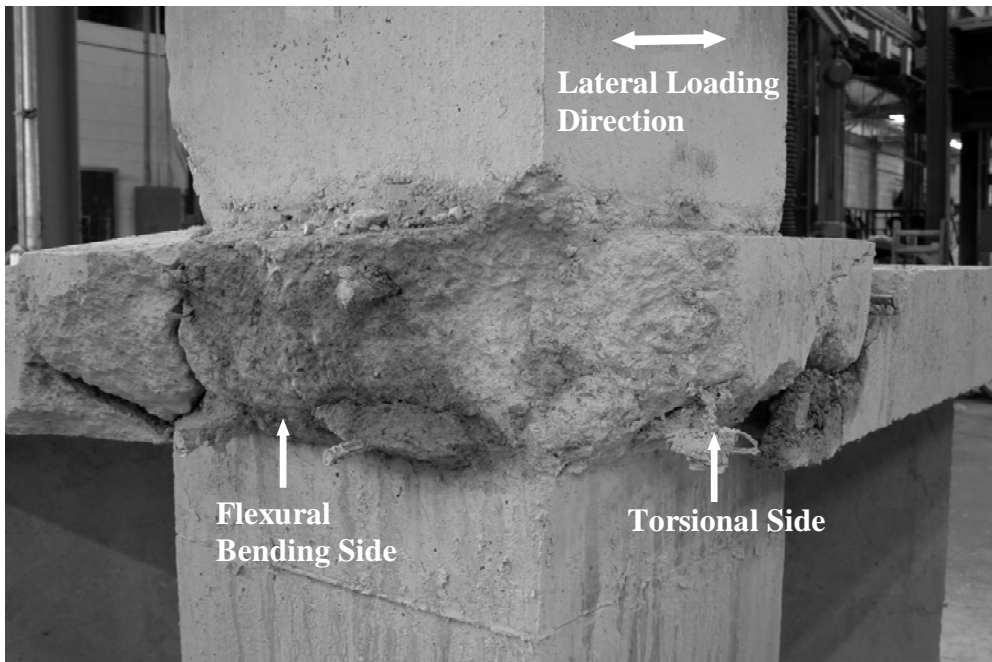


Figure 3.27: Failed joint area of Specimen L0.5.

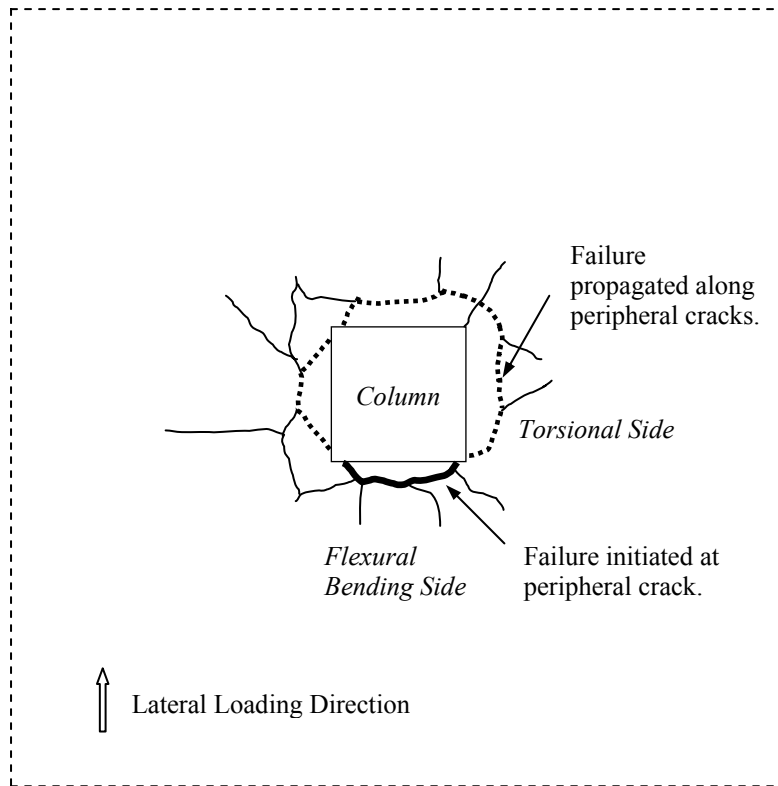


Figure 3.28: Failure initiation and propagation under combined loading.

It is noted that, despite the punching failure mode exhibited in Specimen L0.5, it may not be categorized as a shear failure. The lower failure surface curved down toward the slab-column intersection and indeed presented some characteristics of a shear failure. However, the peripheral cracks that reduced the net area of concrete at the column to carry gravity shear were generated mainly due to slab bending, as indicated by the nearly vertical cracks along most of the slab depth. Moreover, the slab around column had yielded extensively before the occurrence of punching failure. Therefore, a flexure-triggered punching failure would be more appropriate to describe the real failure mechanism of Specimen L0.5.

Figure 3.4 indicates that L0.5 could withstand some additional deformation, though limited, after reaching the peak lateral load. Clearly, the failure of a lightly-reinforced slab-column connection, subjected to a practical level of gravity load (gravity shear ratio  $V_g/V_c = 0.23$  in this study) and lateral displacement reversals, must result from the exhaustion of connection deformation capacity rather than reaching a specific shear stress in the slab around column. The following discussions focus on the factors that affect the connection rotational capacity.

It has been widely accepted that gravity shear level is the determining parameter affecting the connection rotational capacity, as demonstrated by many tests where the deformation capacity was reduced by the increased gravity shear ratio. According to the gravity load level adopted in this study and the comparable test results from literature, it was expected that Specimen L0.5 should be able to endure a lateral drift of at least 3% rather than the recorded 2%. This suggests that other variables may also be influential in the connection deformation capacity.

Table 3.2 provides the measured ultimate drift ratio of four isolated specimens as well as their overall geometries, top reinforcement ratios, gravity load levels, and lateral loading histories.

Table 3.2: Influence of Loading History on Lateral Deformation Capacity

Specimen	Source	Top reinf. ratio (%) (in $c+12d$ )	Slab thick. (in.)	Col. size (in.)	Gravity shear ratio	Total cycles at finishing of 2% drift	Max. drift (%)
SM0.5	Ghali et. al. (1976)	0.50	6	12	0.29	Monotonic loading	6.6
1C	Robertson et. al. (2002)	0.52	4.5	10	0.15	6	3.5
3	Pan and Moehle (1992)	0.61	4.8	10.8	0.22	11	3.2
L0.5	This study	0.50	6	16	0.23	21	2.0

Specimen SM0.5 was tested by Ghali et. al. (1976), 1C by Roberson et. al. (2002), and 3 by Pan and Moehle (1992). These specimens had similar reinforcement ratios and all developed general yielding during the tests. However, because of the different lateral loading histories, significantly different deformation capacities were observed.

Comparison was made first among Specimens SM0.5, 3, and L0.5. The loading history was examined by counting the total number of lateral deformation cycles upon the completion of 2% drift. Such numbers are given in Table 3.2. Despite the much higher gravity shear ratio, Specimen SM0.5, subjected to a monotonic lateral load, exhibited the largest lateral deformation capacity. Nearly identical gravity load levels were applied to Specimens 3 and L0.5. The latter failed at a lower drift ratio, which could be ascribed to the higher number of cycles it had experienced. A similar observation can be made by comparing the test results of Specimens 1C and 3. It is therefore evident that, in addition to gravity load level, the lateral loading history could be another crucial parameter affecting the drift capacity of a slab-column connection.

In fact, after failure the concrete quality at the flexural bending side of Specimen L0.5 (left side shown in Figure 3.27) was found much worse than that at the torsional sides. It was therefore inferred that, the more intensive deformation reversals applied on Specimen L0.5 created more cumulative damage to the slab bending sides, reduced the deformation capacity, and triggered an earlier punching failure.

### **3.8 SUMMARY**

On the basis of test results from this study, the overall behavior of a lightly-reinforced slab-column connection under combined gravity and lateral loading is shown graphically in Figure 3.29 and summarized as follows.

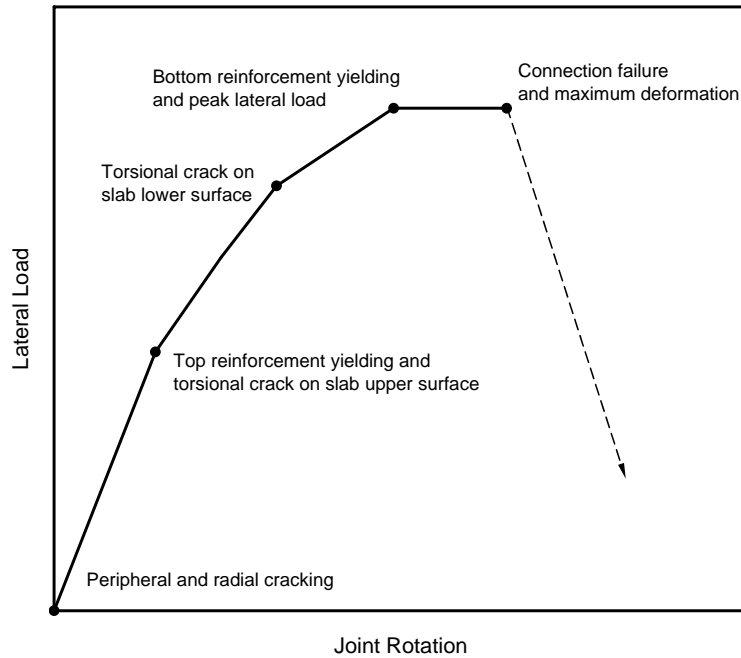


Figure 3.29: Overall behavior of slab-column connections under combined loading.

- (1) Three types of internal forces (flexural moment, shear, and torsional moment) existed around the column to resist the unbalanced moment and gravity shear acting on the connection. As the lateral deformation increased, the connection experienced significant internal force redistribution for both shear and moment.
- (2) The connection was cracked or was approaching cracking under gravity loading. The peripheral cracks around the column outlined the final punching surface.
- (3) Under a small lateral deformation, the top bars yielded first due to negative bending and the yielding was accompanied by significant connection stiffness degradation. This event resulted in lateral force redistribution such that torsion contributed more to the overall resistance and resulted in torsional cracks at the slab top surface.

- (4) As more lateral deformation was imposed on the connection, torsional cracks developed on the slab bottom surface. As a result, the stiffness associated with torsion was reduced and lateral load was further redistributed such that yielding under positive bending was accelerated.
- (5) The maximum lateral load-carrying capacity was reached after positive flexural yielding occurred.
- (6) After peak lateral load was achieved, the additional deformation capacity of a connection was a function of gravity load level and lateral loading history.
- (7) The final failure the connection was manifested by the column being punching out of the slab with a sudden loss of both lateral and gravity load resistance.

## Chapter 4

### Experimental Results of Gravity Load-Carrying Capacity of Slab-Column Connections with and without Earthquake Damage

#### 4.1 GENERAL

Experimental results of four specimens, G0.5, G1.0, LG0.5, and LG1.0, are presented. These specimens were loaded vertically through the column to investigate the punching capacity of interior slab-column connections. Unlike G0.5 and G1.0, LG0.5 and LG1.0 experienced damage under lateral cyclic loading prior to gravity loading to failure. Of particular interest in this part of the study were: (1) behavior and failure mechanism of lightly-reinforced slab-column connections under gravity load only; and (2) effects of previous earthquake damage on the gravity load capacity.

During each test, a monotonic static load was applied upward on the bottom end of the lower column using the test setup shown in Figure 2.23. The loading process for G0.5 and G1.0 was paused briefly three times to mark cracks on the slab top surface. LG0.5 and LG1.0 were continuously loaded to failure because the slabs were cracked extensively during lateral loading.

Behavior of Specimens G0.5 and G1.0 is described first by means of load-deflection relationships, measured strains, crack patterns, and failure mechanisms. The response of Specimens LG0.5 and LG1.0 is reported similarly, however, no strain measurements are reported because after lateral loading reversals, strain readings under gravity load were impossible to evaluate. The weight of column and the weight of the loading system transferred to the column totaled 2.9 kips. To compensate for this effect,

the measured data regarding deflection and load was corrected to reflect true gravity load transferred from the column to the slab and the appropriate deflection.

## 4.2 GRAVITY LOADING RESPONSE OF SPECIMENS G0.5 AND G1.0

### 4.2.1 Load-Deflection Relationship

The load-deflection behavior of Specimens G0.5 and G1.0 is described and compared in Figure 4.1. The abscissa represents the central upward deflection and ordinate represents the gravity load. The loads at slab cracking and first yielding of tensile reinforcement recorded from strain gauges are also shown in this figure. Based on the load-deflection curves and the strains measured in top reinforcement, three loading stages were observed: (1) initial loading to cracking, (2) cracking to first yielding, and (3) first yielding to connection failure.

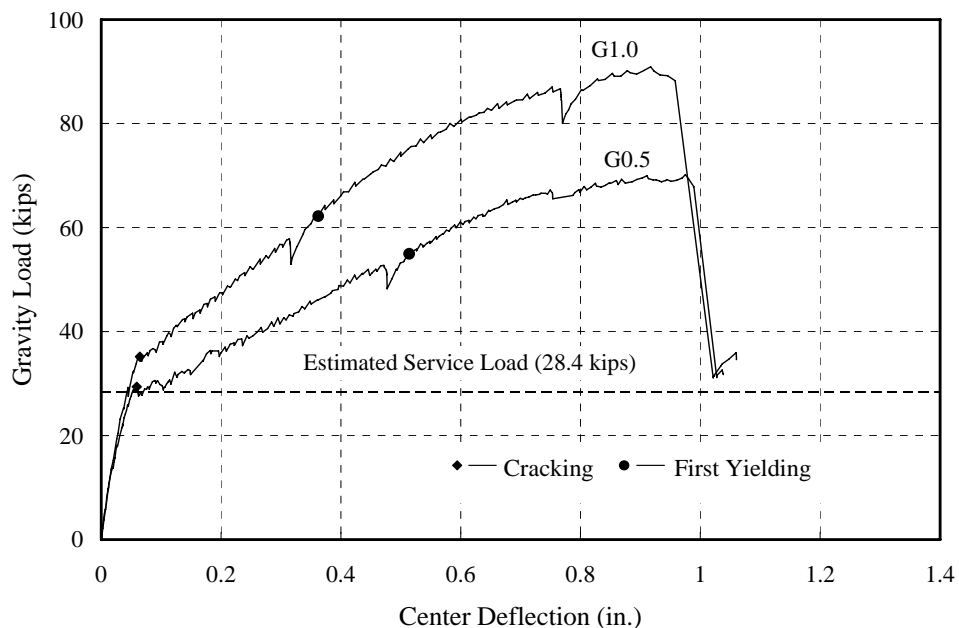


Figure 4.1: Load-deflection curves for Specimens G0.5 and G1.0.

Both specimens exhibited approximately bilinear response between the onset of loading and first yielding. The onset of cracking was not determined by visual inspection, but refers to the load at which there was marked stiffness degradation in the load-deflection curve. As shown in Figure 4.1, the pre-cracking stiffness was largely unaffected by the reinforcement ratio. The cracking load was 28.8 kips for G0.5 and 34.3 kips for G1.0. Furthermore, a flat-plate structure, with the same material and geometric properties as in G0.5, would have a service load of 28.4 kips acting on the connection if a live load of 50 psf and a superimposed dead load of 20 psf are assumed. Thus the test results of G0.5 indicate that the prototype structure should be at the verge of cracking under the assumed service loads.

After slab cracking, the connection stiffness was dependent on the slab top reinforcement ratio at the column. For convenience initial stiffness was defined as the ratio of load to deflection measured at the cracking, while post-cracking stiffness was determined from the increments of load and deflection between cracking and first yielding. It was found that the ratio of initial to post-cracking stiffness is 12% for Specimen G0.5 and 17% for Specimen G1.0. Very few new cracks were observed during the second loading stage, from slab cracking to first yielding, where the load-deflection response was nearly linear. Thus it can be assumed that the increased deformations in this loading stage primarily resulted from crack opening in the vicinity of column.

First yielding occurred at a load of 55.0 kips for Specimen G0.5 and 62.3 kips for Specimen G1.0. After yielding, the connection stiffness gradually degraded due to spread of yielding across the slab and increasing elongation of the reinforcement.

The measured peak load was 70.2 kips for G0.5 and 90.6 kips for G1.0. Clearly, the reinforcement ratio significantly affected the connection strength. As ultimate strength was reached, the load-deflection curves were flat. Punching failure occurred at a

deflection of nearly one inch for both specimens, at which point when the load suddenly dropped to 32 kips.

The punching capacities of both specimens were lower than the nominal two-way shear strength calculated using either ACI 318-05 or CEB-FIP MC90, although the latter provided closer results. The test results as well as the material properties of Specimens G0.5 and G1.0 are summarized in Table 4.1.

Table 4.1: Summary of Test Results of Specimens G0.5 and G1.0

Specimen	G0.5	G1.0
$f_c'$ (psi)	4550	4070
Reinforcement ratio in $c+3h$ (%)	0.5	1.0
$f_y$ (ksi) (yield strength for No.4 bar)	61	61
Cracking load (kips)	28.8	34.3
Initial stiffness (k/in.)	496	545
Load at first yielding (kips)	55.0	62.2
Deflection at first yielding (in.)	0.51	0.36
Post-cracking stiffness (k/in.)	60.6	94.3
Ratio of initial to post-cracking stiffness	0.12	0.17
Peak load (kips)	70.2	90.9
Deflection at failure (in.)	0.99	0.96
Measured strength / calculated strength (ACI 318-05)	0.62	0.85
Measured strength / calculated strength (CEB-FIP MC90)	0.75	0.88

## 4.2.2 Cracking Pattern and Failure

### 4.2.2.1 Specimen G0.5

The cracking pattern and failure of Specimen G0.5 are shown in Figure 4.2. The cracks were marked with red, blue, and green colors when the loading was paused at 27, 67, and 47 kips, respectively. One peripheral crack formed at each side of the column

along a reinforcing bar located 4 in. from the column face. With increasing load, the peripheral cracks extended horizontally outward from the column and curved down to the intersection of column and slab bottom surface to form a classic pyramid-shape punching surface. The maximum width of peripheral cracks on the slab upper surface measured at loads of 29, 52, and 67 kips was 0.005, 0.04, and 0.08 in., respectively.

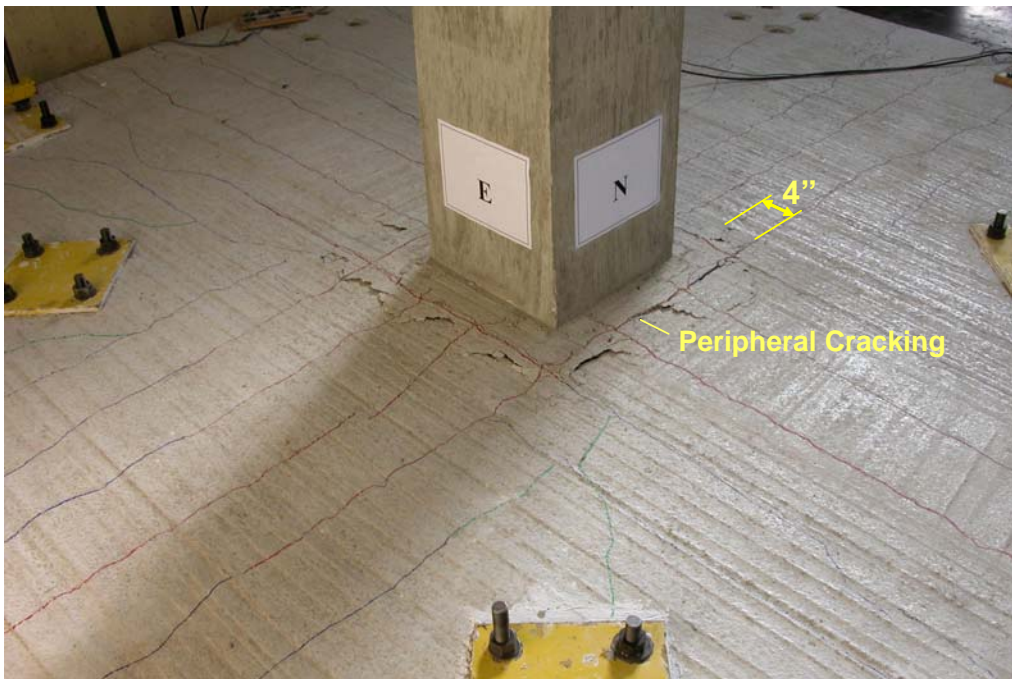


Figure 4.2: Cracking pattern and failure of Specimen G0.5.

Most cracks in the slab upper surface, other than the peripheral cracks, developed along the top reinforcements outside the immediate vicinity of column and were perpendicular to the column face at each side, reflecting the orientation of the slab bending moment vector. No flexural crack was noted in G0.5 at the column face until punching failure occurred. The term inclined crack will be used to identify the peripheral crack.

After failure, Specimen G0.5 was repaired by pouring epoxy into the cracks where the failure surface formed. After retesting the strengthened specimen, the slab was cut along two vertical planes approximately three inches away from the column surface. The cut faces of Specimen G0.5 are shown in Figure 4.3, where the dark curved lines on the slab vertical surface are the epoxy that was poured into the inclined cracks. These lines of epoxy help to delineate the punching failure surface (prior to strengthening) as well as the narrow zone of concrete underneath the inclined crack. Careful inspection indicated that the inclined crack was initially perpendicular to the slab top surface and curved toward the corner between the slab bottom surface and the column face.

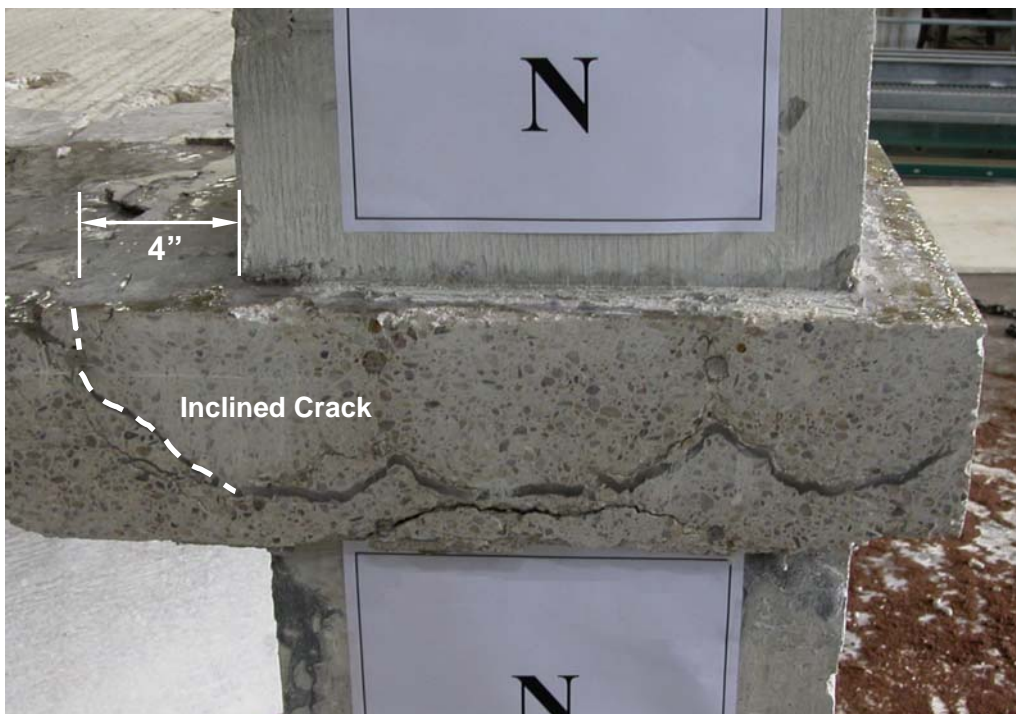


Figure 4.3: Punching surface of Specimen G0.5.

#### ***4.2.2.2 Specimen G1.0***

As shown in Figure 4.4, Specimen G1.0 had a damage pattern similar to that in G0.5 (Cracks were marked with blue color at a load of 57 kips and green color at 87 kips). However, some noticeable differences existed: (1) fewer cracks along the bars were generated on the slab surface; (2) concrete cover spalled over a larger area of the slab at punching failure; (3) the critical cracks that formed the failure surface could not be recognized solely from the slab top surface because the crack widths were similar to adjacent cracks; and (4) the inclined crack, identified from the slab cross sections shown in Figure 4.5, was initiated by a crack 8 inches from the column face, forming a more acute angle relative to the slab plane.

Flexural cracking was observed at the slab-column interface in G1.0 but did not occur simultaneously in all four sides. Some cracks were generated between loads of 27 and 57 kips, whereas others between 57 and 87 kips. These cracks remained narrow and did not significantly change the load-deflection response. It was therefore inferred that such cracks were less important than the inclined cracks.

Yield-line theory has been commonly used to determine the gravity load capacity of slab-column connections that fail in a flexural mode. It is interesting to note that the cracking pattern of G1.0 suggested development of yield lines as shown in Figure 4.6(a). Figure 4.6 (b) shows another mechanism that can be used to analyze the flexural capacity of specimens subjected to gravity loading and simply-supported on four edges with the corners free to lift, as shown in Figure 1.3(a). Nevertheless, the cracking pattern outside the joint region, as shown in Figure 4.4, does not favor the mechanism in Fig 4.6(b).

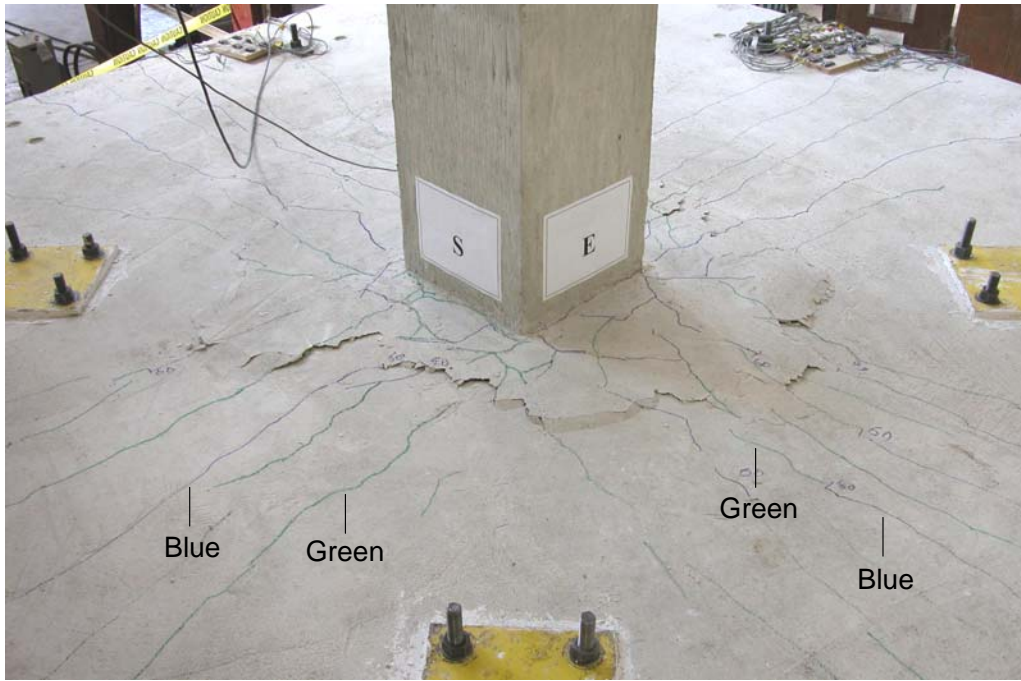


Figure 4.4: Cracking and failure patterns of Specimen G1.0.

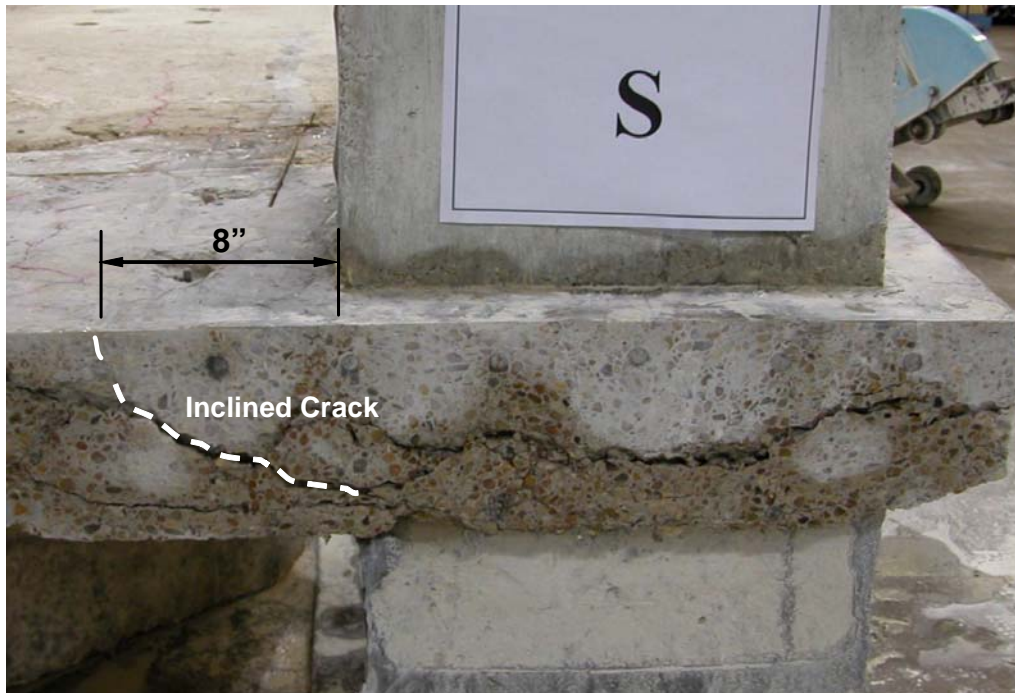


Figure 4.5: Punching surface of Specimen G1.0.

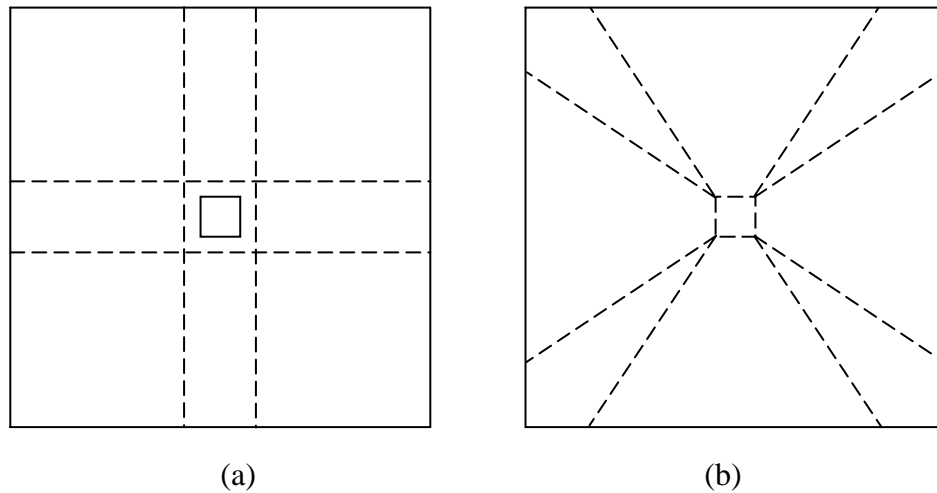


Figure 4.6: Two yield-line mechanisms for isolated slab-column connections.

### 4.2.3 Stain Distribution

#### 4.2.3.1 Steel Strains

The reinforcement strain recorded around the column is presented to facilitate understanding the connection behavior. The strain gauge location and the relationship between strain and the normalized load expressed as the ratio of load,  $V$ , to the ultimate strength,  $V_u$ , are shown in Figure 4.7 for G0.5 and Figure 4.8 for G1.0.

The strains shown in Figures 4.7 and 4.8 were measured in one quadrant of the slab from three gauges on top reinforcement mat (T1, T2, and T3) and one gauge on bottom mat (B1). Gauge T1 was located immediately at the column face. Gauge T2 was spaced 10 in. from T1 in the longitudinal direction and 16 in. from T3 in the transverse direction. In addition, a positive sign is given to tensile strains and negative to compressive strains. It is noted that the measured strains were not symmetrical around the column and the strains presented here provided a qualitative indication of strain distribution and the strain rate as load increased.

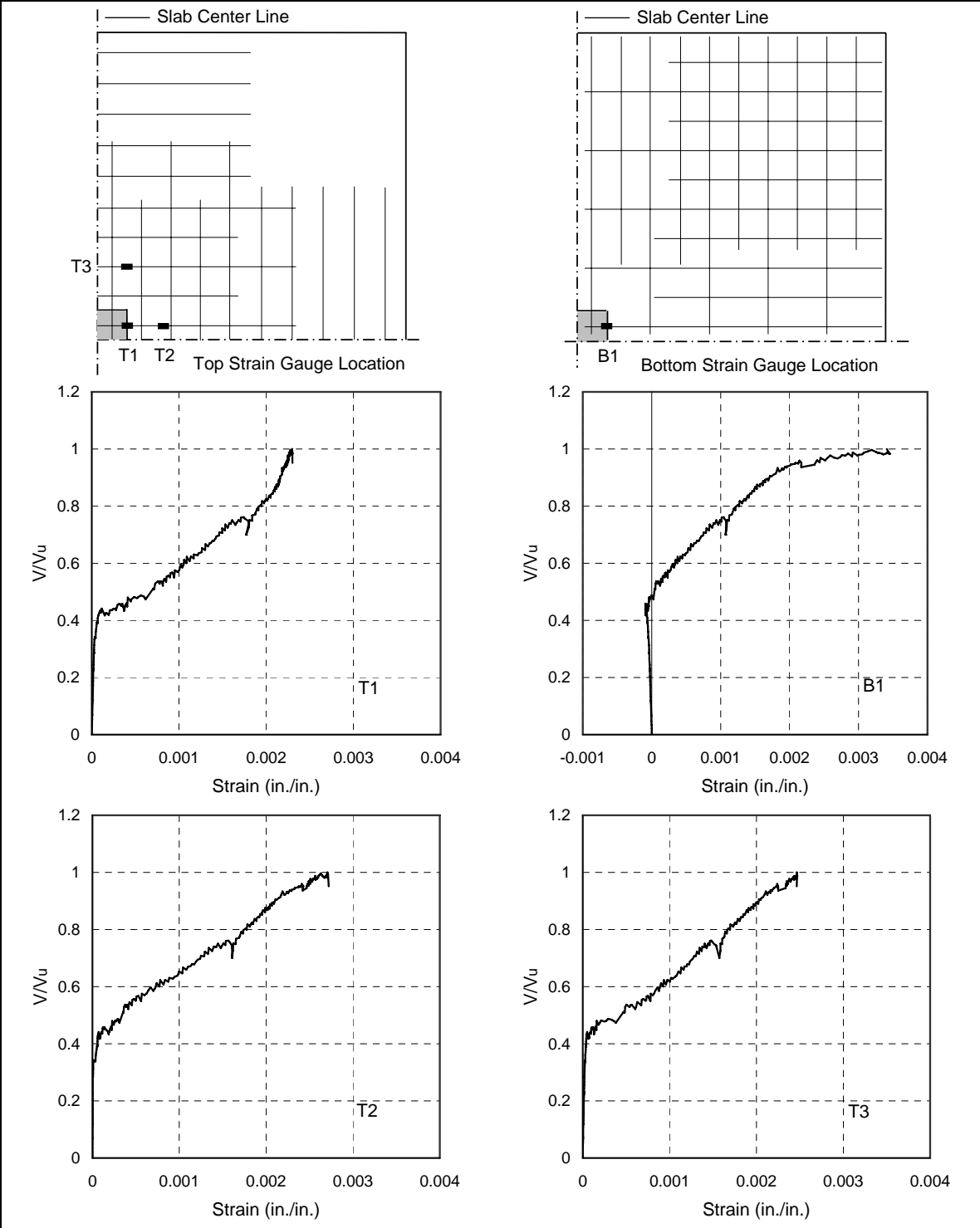


Figure 4.7: Measured steel strains of Specimen G0.5.

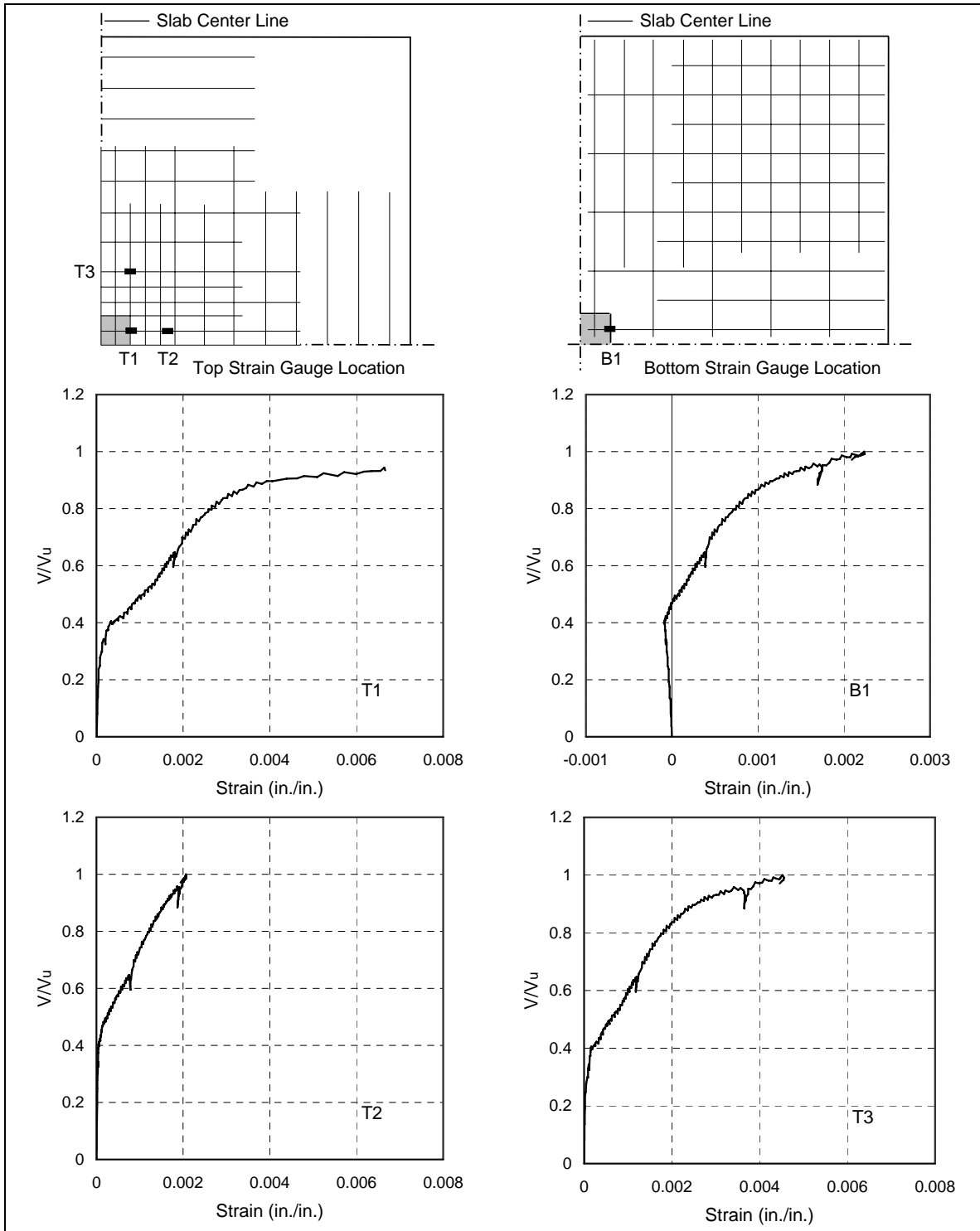


Figure 4.8: Measured steel strains of Specimen G1.0.

The inclined crack in G1.0 was generated between strain gauges T1 and T2 but was closer to T2 (as shown in Figure 4.9). Therefore, it is believed that the strain measurement from T2 better represented the top steel strain at the inclined crack.

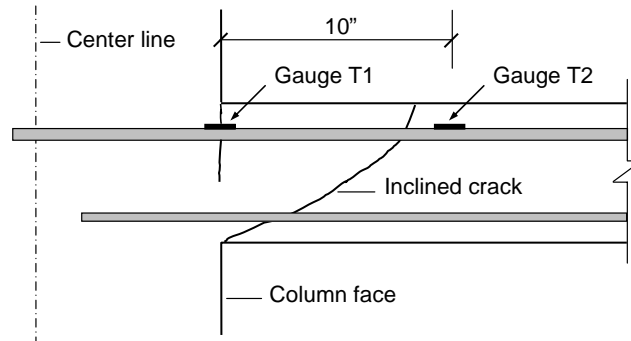


Figure 4.9: Location of strain gauges T1 and T2 in Specimen G1.0.

G0.5 and G1.0 exhibited similar load-strain histories. In the initial loading stage, the measured tensile strains at the vicinity of column were small and, as expected, the bottom bars developed compressive stresses. The appearance of inclined cracks at about  $0.4V_u$  to  $0.45V_u$  significantly changed the strain distribution. First, the gradient of load-strain curves for slab top reinforcement was significantly reduced at all three top gauge locations, indicating that, as the concrete tensile capacity was lost, the top bars were resisting negative bending. Second, at the same load level, the strain measured at T3 was only slightly lower than that at T1, showing that high negative moment had spread outward from the column face. Third, the load-strain curve of the bottom reinforcement at column face (gauge B1) changed from compression to tension at about  $0.5V_u$ .

First yielding occurred around the column at approximately  $0.7V_u$  for Specimen G0.5 and  $0.8V_u$  for G1.0. The loads at yielding were determined based on an assumed yield strain of 0.002 since no yielding plateau existed in the steel stress-strain curves (Figure 2.29, No. 4 bar). First yielding in a slab is generally not as significant as in a

beam where significant stiffness degradation accompanies yielding. In a slab-column connection, there is a transverse redistribution of moment to reinforcement away from the column. As a result, the opening of inclined cracks in these specimens was more gradual.

From the recorded strain at gauge T3 and its location, it was speculated that, when the peak loads were reached, the yielding in the top mat had spread at least 12 in. from the column face in both specimens, indicating yielding over approximately 20% of the column strip. It is noteworthy that, for both G0.5 and G1.0, the tensile strains measured from gauge B1 at peak loads were even larger than the yield strain. The high strain values may result from the localized bending at the “root” of the crack due to the rotation of section, as shown in Figure 4.10. In this case, the area of concrete in compression underneath the inclined crack to resist shear will be small.

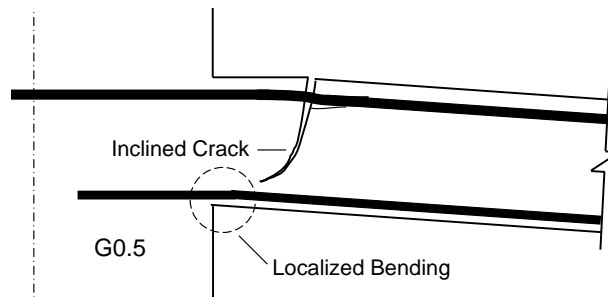


Figure 4.10: Localized bending due to slab rotation (G0.5).

#### 4.2.3.2 Concrete Strains

The measured strength of lightly-reinforced connection G0.5 was not only lower than the strength calculated using ACI 318-05 two-way shear design provisions but also lower than the capacity based on CEB-FIP MC90 in which the effect of reinforcement ratio is taken into account. It was noted that G0.5 had a larger  $c/d$ -ratio than most tests previously reported. However, the effect of this ratio was not considered in either

Equation 1.9 or Equation 1.12. Since the  $c/d$ -ratio may provide an indication of lateral restraint on the slab concrete at the connection, concrete compressive strains were measured on the slab bottom surface. Concrete strain measurements were also needed to verify that concrete underneath the bottom bars at the column was in compression although high values of tensile strain were recorded in the bottom bars at the peak load. Therefore, concrete strain gauges were attached in both tangential and radial directions on the slab bottom surface around all four column sides of Specimen G1.0.

The measured strains at one side of the column and the gauge locations are shown in Figure. 4.11, where WT is the concrete strain gauge mounted in the tangential direction and WR in the radial direction.

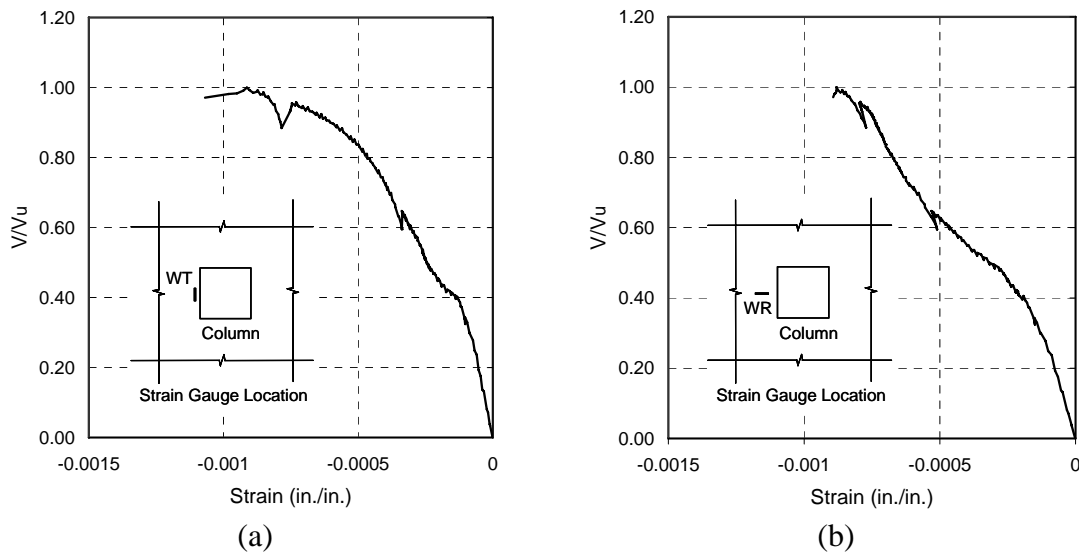


Figure 4.11: Concrete strain of G1.0: (a) tangential strain; and (b) radial strain.

At the ultimate load for G1.0, concrete tangential strain at the slab compressive surface,  $\epsilon_t$ , was about 0.001, as opposed to  $\epsilon_t = 0.0022$  that was recorded in the tests by Osman et al. (2000, specimens NSLW1.0P and NSNW0.5P,  $c/d = 2.17$ ). This indicates that the  $c/d$  ratio may affect the lateral restraint on concrete in compression and thus

affect the connection punching strength. The effect of  $c/d$ -ratio was further examined using more test data and will be discussed in Chapter 5. The largest concrete compressive strain in the radial direction was around 0.001, a value far less than concrete strains associated with crushing or spalling. This is consistent with the observation that concrete crushing was never observed at failure of a slab-column connection.

### 4.3 PUNCHING STRENGTH OF EARTHQUAKE-DAMAGED CONNECTIONS

The gravity load versus slab center deflection response of Specimens LG0.5 and LG1.0 is compared with that of G0.5 and G1.0 in Figures 4.12 and 4.13. Due to the damage induced by lateral loading, the initial stiffness of LG0.5 and LG1.0 was much lower than their undamaged counterparts. The most significant result was that, despite the extensive slab cracking shown in Figures 3.14 and 3.16, the ultimate strength of LG0.5 and LG1.0 was nearly identical to that of G0.5 and G1.0, respectively. In other words, the slab damage due to the previously applied cyclic loading up to 1.25% drift had no detrimental effect on the connection gravity load-carrying capacity.

As shown in Figure 4.12 and 4.13, LG0.5 and LG1.0 exhibited similar load-deflection response as failure was approached. The failure surfaces and damage patterns of these specimens are shown in Figures B.1 through B.4 in Appendix B. The material properties, punching strength, and ultimate deformation of LG0.5 and LG1.0 are summarized in Table 4.2.

Table 4.2: Summary of Test Results of Specimens LG0.5 and LG1.0

Specimen	$f_c'$ (psi)	$f_y^*$ (ksi)	$V_u$ (kips)	Deflection at Failure (in.)
LG0.5	4860	66	72.8	1.07
LG1.0	4000	61	89.9	0.78

\* Measured yield strength for No.4 bars (Stress-strain curve is given in Chapter 2).

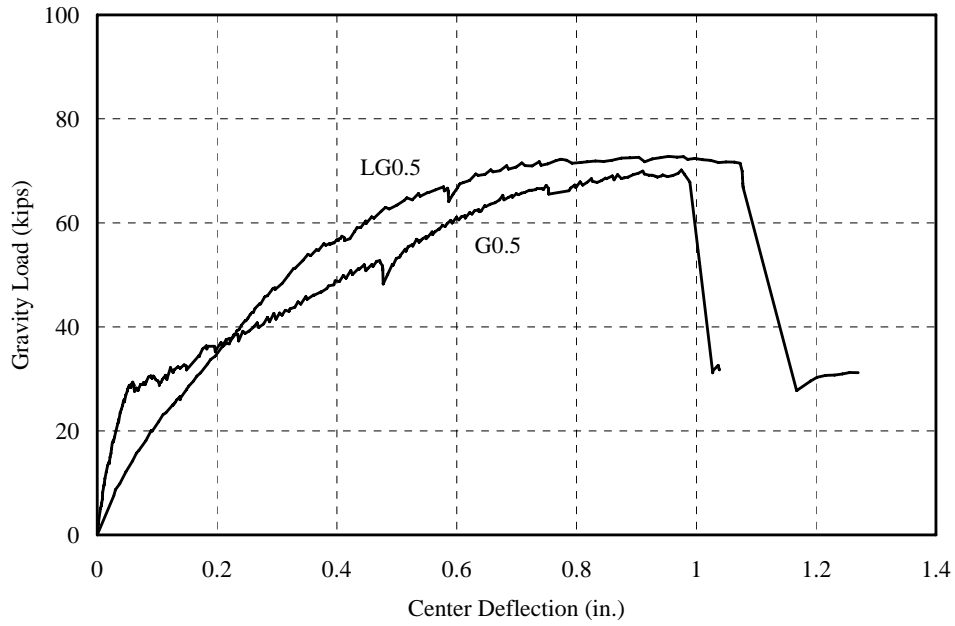


Figure 4.12: Load-deflection curves for Specimens LG0.5 and G0.5.

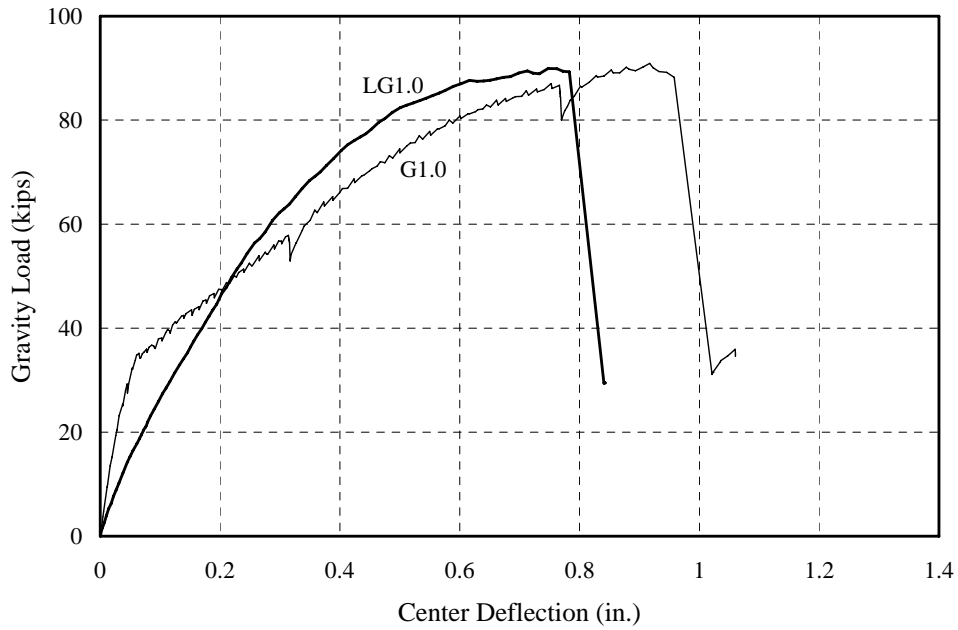


Figure 4.13: Load-deflection curves for Specimens LG1.0 and G1.0.

## 4.4 BEHAVIOR OF LIGHTLY-REINFORCED SLAB-COLUMN CONNECTIONS

### 4.4.1 Summary of Response of Lightly-Reinforced Slab-Column Connections

The behavior of the lightly-reinforced slab-column connections can be summarized as follows: (1) inclined cracks in the slab were generated in the negative bending zone around the column and extended outward from the column and downward through the slab depth; (2) slab top reinforcement crossing the inclined cracks yielded and yielding spread out from the column; (3) once the maximum load was reached failure occurred with limited additional deformation; and (4) the concrete cover over the top bars spalled as punching failure occurred along a surface defined by the inclined cracks.

Since reinforcement is often a crack former, the inclined cracking always occurred above top bars transverse to the direction of bending and their location depended upon the top reinforcement ratio. Figure 4.14 illustrates the configurations of inclined cracks for Specimen G0.5 and G1.0. The inclined cracking led to significant internal force redistribution such that the top bars out of the final failure surface also provided restraint to the opening of inclined cracks and their extension along the slab depth.

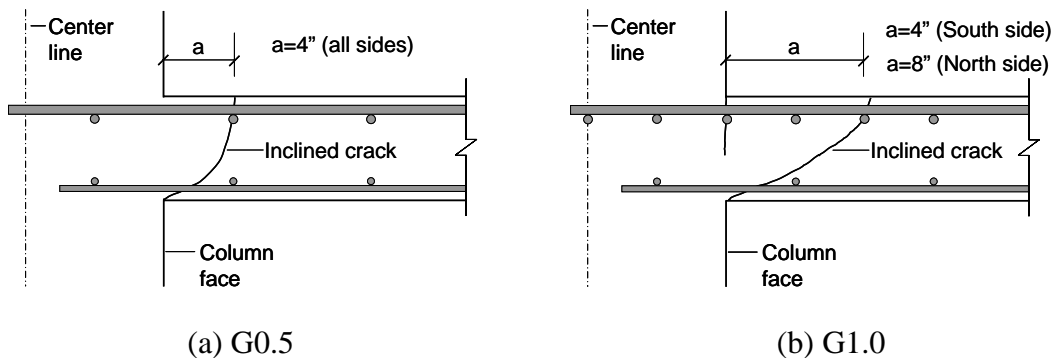


Figure 4.14: Orientation of the inclined cracks.

## 4.4.2 Failure Mechanism of Lightly-Reinforced Slab-Column Connections

### 4.4.2.1 Local Deformation Capacity of the Slab

As indicated by the load-deflection response (Figures 4.12 and 4.13), G0.5, G1.0, LG0.5, and LG1.0 exhibited general yielding prior to punching failure. Therefore, reaching a critical gravity shear at the column was not the reason for failure of these lightly-reinforced slab-column connections. Instead, the connection failure resulted from reaching a critical slab deformation capacity that is associated with the complex state of stress at the inclined cracks.

Comparison of test results of G0.5, LG0.5, and L0.5 provide valuable information regarding connection deformation capacity. The bilinear load-deflection response in G0.5 and the measured steel tensile strains in G0.5 and L0.5 indicate that, in both gravity loading and combined loading, the connection deformation was concentrated at the inclined cracks. Thus, it was assumed that the slab outside the inclined cracks rotated as a rigid body after the inclined cracking.

Figure 4.15 shows schematically the deformation mechanism for specimens under two types of loading after the generation of inclined cracks that occurred at an assumed distance of  $0.5d$  from the column face. In this figure,  $R$  denotes the radius from the column center to the supporting struts,  $\theta$  the slab rotation relative to the slab-column joint defined by the area located within  $c+d$ ,  $\delta$  the increased slab central deflection after inclined cracking occurred,  $\beta$  the joint rotation, and  $\alpha$  the slab rotation caused by  $\delta$ .  $\beta$  can be approximated by the lateral drift if the column is stiff as is the case here. For G0.5 and LG0.5 subjected to gravity load,  $\theta$  is equal to  $\alpha$ . For L0.5 subjected to combined gravity and lateral loading,  $\theta$  is the summation of  $\alpha$  and  $\beta$ .

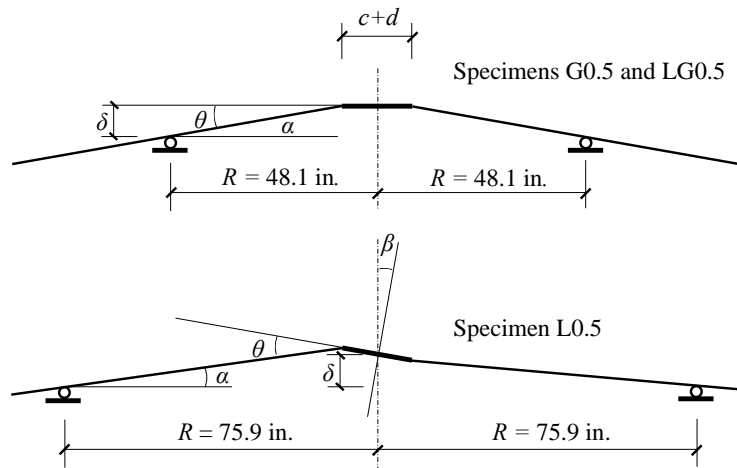


Figure 4.15: Illustration of connection local deformation.

The values of  $\alpha$ ,  $\beta$ , and  $\theta$  (shown in Table 4.3) at the failure of G0.5 and LG0.5 and at the maximum lateral drift of L0.5 were determined from the deflection  $\delta$  measured at the slab center and the lateral displacement measured at the top column. The nearly identical values of  $\theta$  suggest that the exhaustion of local slab deformation capacity at the column led to punching failure. In addition, for connections with a given slab local rotational capacity of  $\theta$ , the slab deformation capacity consumed by increased gravity load would always reduce the reserved capacity for the following lateral loading. Thus, the observation regarding the effect of gravity load on connection lateral drift capacity during a combined loading can be explained.

Table 4.3: Slab Maximum Local Deformation (G0.5, LG0.5, and L0.5)

Specimen	$\delta$ (in.)	$\alpha$ (rad.)	$\beta$ (rad.)	$\theta = \alpha + \beta$ (rad.)
G0.5	0.94	0.025	0	0.025
LG0.5	1.07	0.028	0	0.028
L0.5	0.50	0.008	0.020	0.028

#### 4.4.2.2 Internal Forces at the Inclined Crack

A slab-column connection loaded concentrically always reaches punching failure whether or not its overall behavior is ductile. It follows that the connection deformation capacity must depend on the stress state at punching, the main focus of the following qualitative discussions.

All the actions applied to the cracked surface of a connection immediately prior to the failure must be considered. It was observed that the inclined crack opened widely at the top surface of the slab and tended to be horizontal at its lower end, as shown in Figure 4.3, it was assumed that aggregate inter-lock provided negligible shear resistance. All other internal force resultants acting on one side of the failure surface are shown in Figure 4.16, where  $N_1$  denotes the tensile force in top bars,  $N_2$  the compressive force in bottom bars,  $N_c$  the compressive force in concrete,  $V_{d,1}$  the shear force carried by top bars,  $V_{d,2}$  the shear in bottom bars, and  $V_c$  the shear resistance from concrete in compression.

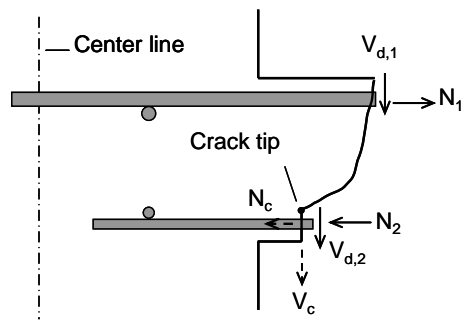


Figure 4.16: Internal forces acting on the slab-column joint.

Based on available test data from the literature, it seems certain that, regardless of the reinforcement ratio, punching failure was preceded by the yielding of top bars crossing the inclined cracks. First yielding did not necessarily lead to an instantaneous connection failure. However, it could be essential for punching failure because yielding

may accelerate the bending moment redistribution that resulted in yielding across a larger portion of the slab and contributed to the final failure, as will be discussed later.

Equilibrium in the horizontal direction provides no insight for determining the connection capacity, because the compressive forces,  $N_2$  and  $N_c$ , do not have to balance the tensile force developed in the top bars. In addition, the plane-strain assumption used to analyze the flexural capacity of a beam or one-way slab does not hold for the inclined cracking of a slab-column connection. Therefore, attention was given to the vertical forces acting on the failure face including  $V_{d,1}$  (the dowel action),  $V_{d,2}$ , and  $V_c$ . It is of particular interest to analyze the distribution of these forces that transfer gravity load from the slab to the column.

#### ***Shear Resisted by Concrete, $V_c$***

As discussed in Section 4.2.3.1, the area of concrete in compression to carry shear in G0.5 and G1.0 was sufficiently small at peak load. In addition, the test results of LG0.5 and LG1.0 provide important information regarding the role of concrete in resisting the shear force. After experiencing a 1.25% lateral drift in combined loading, cracks due to slab positive bending were observed on the slab bottom surface (Figures 3.15 and 3.17) and they connected with the inclined cracks generated from the slab top surface. Hence, concrete at two bending faces of the column was fully cracked before the gravity loading tests were carried out. Considering that the damage caused by lateral deformation reversals did not affect the connection pure gravity load capacity, it was concluded that concrete may not be the major source of shear resistance of a lightly-reinforced slab-column connection.

### ***Shear Resisted by Bottom Reinforcement, $V_{d,2}$***

Existing mechanical models generally ignore  $V_{d,2}$  on the basis of a widely quoted statement “the ultimate shearing capacity is not dependent upon the compressive reinforcement” (Elstner and Hognestad, 1956). However, Elstner and Hognestad classified the failure mode of a connection into flexural and shear failures and the conclusion was derived from the tests of specimens with tensile reinforcement ratios larger than 2% that failed in shear. Thus, the above assertion may not be applicable to a lightly-reinforced slab-column connection. Instead, the bottom bars may carry a significant portion of the gravity load, as shown by comparisons of the following four tests. Two specimens, B-2 and B-4 tested by Elstner and Hognestad (1956), had no compressive reinforcement; two other specimens, Ref-0.35% and Ref-0.5% tested by Ebead and Marzouk (2004), had a compressive mat of slab reinforcement with a 0.35% reinforcement ratio. The test results as well as the geometrical and material properties of these four specimens are summarized in Table 4.4.

Table 4.4: Contribution of Compressive Reinforcement to Punching Strength

Label	Slab-thickness (in.)	$d$ (in.)	$c$ (in.)	$f_c'$ (psi)	$\rho$ (%)	$\rho f_y$ (psi)	Existence of bottom bar	$V_u$ (kips)	$\frac{V_u}{\sqrt{f_c' \rho f_y}}$
Ref-0.35%	5.9	4.5	9.84	4350	0.35	229	Yes	56	56
<b>B-2</b>	6	4.5	10	6900	0.5	233	<b>No</b>	<b>45</b>	<b>35</b>
Ref-0.5%	5.9	4.5	9.84	5080	0.50	326	Yes	74	58
<b>B-4</b>	6	4.5	10	6920	0.5	435	<b>No</b>	<b>75</b>	<b>43</b>

Ref-0.35% and B-2 had nearly identical tensile reinforcement strength as measured by  $\rho f_y$ . The concrete strength of Ref-0.35% was 37% lower than that of B-2, but

the ultimate strength of Ref-0.35% was 24% higher. Even if both steel tensile strength and concrete compressive strength of Ref-0.5% were much less than in B-4, Ref-0.5% achieved a similar punching capacity to that of B-4. To eliminate the effect of material strength on specimen capacity, the test results were evaluated using the ratio of  $V_u$  to  $\sqrt{f_c' \rho f_y}$ . From the so normalized connection strength as shown in the last column of Table 4.4, it can be seen that the presence of compressive reinforcement increased the connection strength by at least 30%, indicating the contribution of bottom bars to the connection punching strength.

#### ***Shear Resisted by Top Reinforcement, $V_{d,1}$***

Shear resistance also comes from the doweling force,  $V_{d,1}$ , for a slab-column connection. Once an inclined crack opens up, a relative displacement in the vertical direction between the two sides of crack takes place, as shown in Figure 4.17. The doweling effect from the top bars produces an out-of-plane uplifting force in concrete at the right side of the inclined crack and tends to split the interface between concrete and reinforcement.

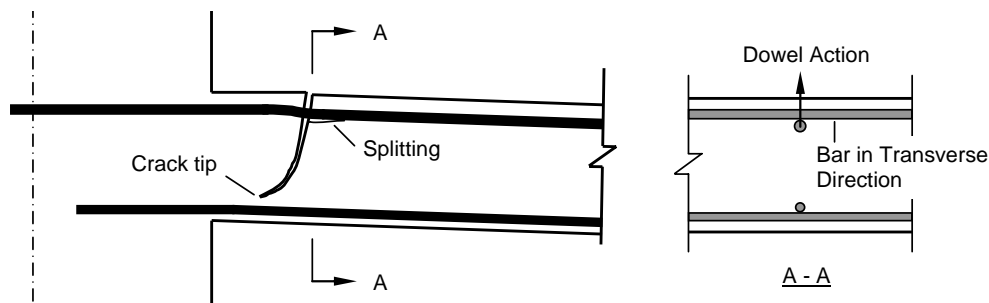


Figure 4.17: Concrete splitting due to dowel action.

The concrete surrounding the top bars resists the up-lifting force and so does the top reinforcement placed transversely on the dowel bars. Dowel action is effective only if

the surrounding concrete and reinforcement in the transverse direction provide enough confinement such that the splitting is restrained. In other words, if splitting does not extend, it may not trigger an instant loss of the doweling effect. It is interesting to note from the measured steel strains that a punching failure occurred in G0.5 and G1.0 soon after the yielding had spread away from the column. It is possible that extensive yielding diminished the constraint from the transverse reinforcement and thus resulted in an unstable propagation of splitting cracks. Once the dowel action disappeared, the inclined cracks immediately propagated down to slab bottom surface without restraint. Hence, unstable concrete splitting could be the reason for punching failure rather than its consequence. This is different from the prevailing assumption that punching failure is caused by the rupture of the reduced concrete compression zone in the slab. The above conclusion could be also applicable to a slab-column connection subjected to combined gravity and lateral loading. In fact, the connection failure of L0.5 occurred soon after horizontal concrete delamination along the top steel mat near the inclined crack was identified. At 2% lateral drift, tapping on the slab surface provided an indication of the extent of the splitting and delamination.

It follows that restraining concrete splitting by increasing the concrete strength or the thickness of concrete cover could enhance the deformation capacity of a lightly-reinforced slab-column connection. This is validated by the following examples. Specimens B-1 and B-2 ( $\rho = 0.5\%$ ) tested by Elstner (1956) were identical except that the concrete compressive strength for B-1 was 2060 psi and that for B-2 was 6900 psi. While B-1 failed at a deflection of 1.1 in., B-2 reached an ultimate deflection of 1.3 in. The two specimens, P11S150 ( $\rho = 0.5\%$ ) and P38S150 tested by Alexander and Simmonds (1992), were different only in the thickness of concrete cover (11 mm for the former and 38 mm for the latter). P11S150 failed in punching at a center deflection of 48 mm,

whereas P38S150 failed at 64 mm. It is noted that the above conclusion could be extended to a slab-column connection subjected to combined gravity and lateral loads, where the deformation capacity is of particular concern.

Based on the discussions presented in this section, a successful mechanical model for the behavior of a slab-column connection should capture the following aspects: (1) effect of tensile reinforcement on the inclined crack location and the connection strength; (2) doweling force,  $V_{d,1}$ , and splitting; (3) shear resistance provided by the bottom reinforcement,  $V_{d,2}$ ; and (4) shear carried by the un-cracked concrete,  $V_c$ .

## Chapter 5

### Shear Strength of Slab-Column Connections under Concentric Gravity Loading

#### 5.1 GENERAL

Experimental research conducted on slab-column connections carrying gravity load only has shown that connection punching capacity is governed by a variety of factors including: (1) concrete strength, (2) flexural reinforcement strength and layout, (3) slab aspect ratio  $c/d$ , (4) size effect, (5) boundary conditions of test specimen, and (6) presence of slab bottom reinforcement. Because of the many variables affecting the connection capacity and the complex distribution of internal forces resisting gravity load, as discussed in Section 4.4.2, it is difficult to establish a mechanical model to describe the connection ultimate strength. Instead, a study using the critical section approach based on available test data was conducted to empirically derive a formula for use in strength evaluation of slab-column connections. Emphasis was given to the first three parameters listed above that affect connection punching strength. The effect of boundary conditions, slab thickness (size effect), and slab bottom reinforcement was not considered in this study due to lack of sufficient test data.

Relevant tests satisfying the following conditions were collected to form the basis of the study: (1) connections constructed with normal-weight concrete and with square columns; (2) slab top tensile reinforcement strength as represented by  $\rho f_y$  less than 1200 psi; (3) no shear reinforcement; and (4) slab thickness at least 3 inch. The collected data for 95 specimens (84 with uniformly distributed slab reinforcement and 11 with banded

bars at the column) reported by several investigators covered a wide range of slab properties. The range of major parameters including concrete strength ( $f_c'$ ), tensile reinforcement index ( $\rho f_y$ ), slab thickness ( $h$ ), and the ratio of column size to slab effective depth ( $c/d$ -ratio) for the specimens without banded bars is shown in Figure 5.1. The details regarding these tests are given in Appendix C.

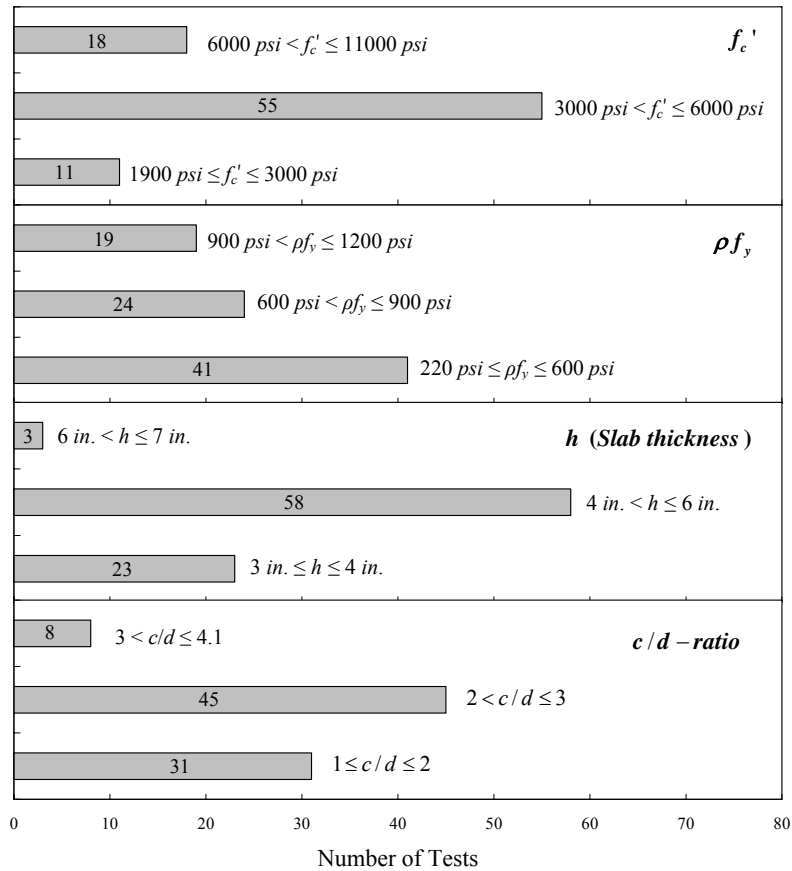


Figure 5.1: Range of parameters in database (84 tests).

## 5.2 USING CODE EQUATIONS TO ESTIMATE CONNECTION SHEAR STRENGTH

According to Equation 1.9, the two-way shear strength of a slab-column connection supported on the square column defined in ACI 318-05 can be expressed as (without using  $\phi$  factor)

$$V_c = 4\sqrt{f_c} 'b_o d \tag{5.1}$$

where  $b_o = 4d(c + d)$ .

As discussed in Section 1.4.1.3, the above equation was developed based on specimens that failed in shear. Thus, Equation 5.1 was not developed for preventing a punching failure that occurs after the flexural capacity of the slab is reached. The equation should not be used to estimate the gravity load-carrying capacity of slab-column connections in which the slab is lightly reinforced and the slab flexural capacity in the vicinity of the column is realized before shear distress is evident. As an illustration, Equation 5.1 was applied to the previously-described 84 specimens with uniformly distributed slab flexural reinforcement. Figure 5.2 shows the measured strength and the strength estimated based on Equation 5.1.

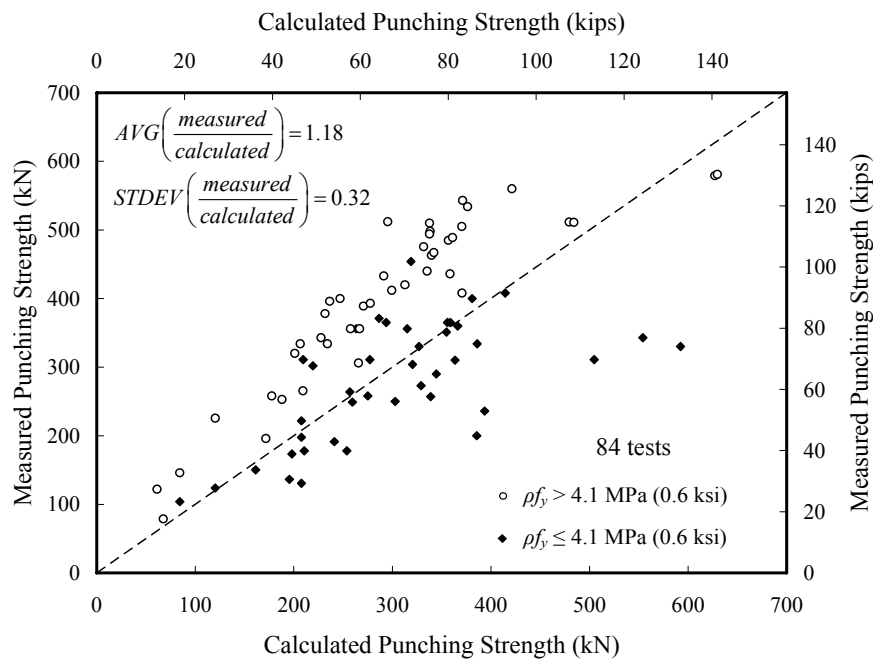


Figure 5.2: Comparison between measured and calculated strength (ACI 318-05).

Figure 5.2 indicates that all specimens, for which Equation 5.1 overestimates the punching capacity, have a low value of tensile reinforcement index,  $\rho f_y$ , equal to or less than 0.6 ksi (for Grade 60 steel,  $\rho \leq 1\%$ ). In addition, Equation 5.1 consistently underestimates the punching capacity of most specimens with  $\rho f_y > 0.6$  ksi (for Grade 60 steel,  $\rho > 1\%$ ).

The two-way shear design equation recommended in CEB-FIP MC90 code (without the partial safety factor) was also applied to specimens shown in Figure 5.2. The comparison between the calculated strength according to Equation 1.12 and the measured strength is shown in Figure 5.3.

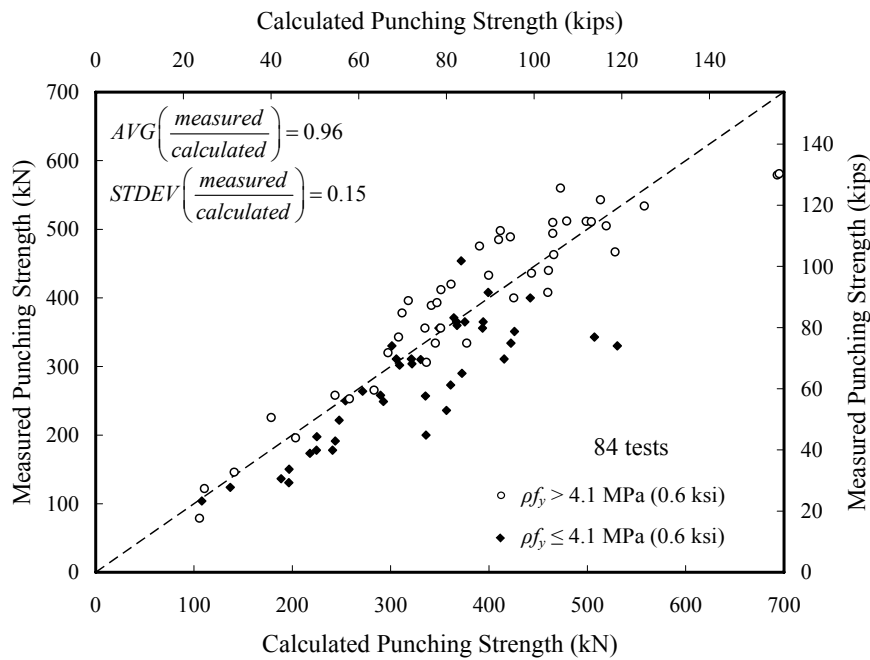


Figure 5.3: Comparison between measured and calculated strength (CEB-FIP MC90).

Figure 5.3 indicates that, Equation 1.12 provides a better estimate of connection punching strength by considering more variables, as shown by the reduced data scatter. However, the CEB equation still overestimates the capacity of most lightly-reinforced

slab-column connections. Table 5.1 gives the average and standard deviation of the ratio of strength calculated based on codes to that measured from tests.

Table 5.1: Average and Standard Deviation of Calculated Connection Strength

Code	Average of $\frac{V_{u,measured}}{V_{u,calculated}}$	Standard Deviation of $\frac{V_{u,measured}}{V_{u,calculated}}$
ACI 318-05	1.18	0.32
CEB-FIP MC90	0.96	0.15

### 5.3 EVALUATION OF PUNCHING STRENGTH BASED ON TEST DATA

The punching strength was assumed in this study to take the following general form

$$V_n = k \cdot (f_{ct})^\alpha \cdot (\rho f_y)^\beta \cdot A_c \cdot y \left( \frac{c}{d} \right) \quad (5.2)$$

where  $f_{ct}$  is concrete tensile strength;  $\rho$  and  $f_y$  are slab tensile reinforcement ratio and yield strength,  $A_c = 4d(c+2s)$  is the area of a critical section located at a distance  $s$  from the column faces (shown in Figure 5.4);  $y$  is a dimensionless function of  $c/d$ -ratio. The parameters,  $k$ ,  $\alpha$ ,  $\beta$ ,  $s$ , and the expression of  $y$  were determined analyses of the data.

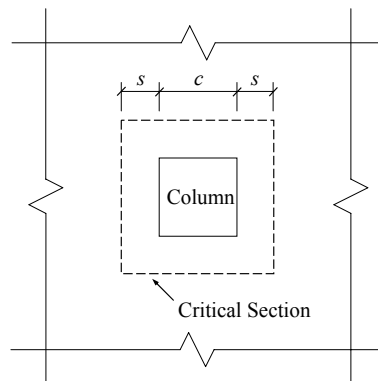


Figure 5.4: Critical section for calculating punching strength.

Assuming  $f_{ct}$  is proportional to  $\sqrt{f_c'}$ , Equation 5.2 is rewritten as

$$V_n = k \cdot (f_c')^{\frac{\alpha}{2}} \cdot (\rho f_y)^\beta \cdot A_c \cdot y \left( \frac{c}{d} \right) \quad (5.3)$$

Test data from specimens with top bars evenly-distributed in two orthogonal directions of the slab were used to generate Equation 5.3. If the concrete strength was reported as cube compressive strength,  $f_{cu}$ , value was transformed to cylinder compressive strength according to

$$f_c' = 0.80 f_{cu} \quad (5.4)$$

### 5.3.1 Effects of Concrete and Flexural Reinforcement

#### 5.3.1.1 Data Analysis Procedures

To examine the effects of a single variable on connection punching capacity while eliminating the influence of others, the following procedures were used:

- (1) An intermediate term  $Y$  was defined as  $Y = (f_c')^{\alpha/2}$  or  $Y = (\rho f_y)^\beta$  when the effects of concrete strength and slab flexural reinforcement were evaluated. The specimens with nearly identical properties (difference limited to 5%), except for the variable contained in the term  $Y$  to be examined, were placed into the same group. For example, when investigating the influence of concrete strength, the specimens with similar values of  $\rho f_y$ , column size, and slab effective depth but with different concrete strength formed a data group. Each group consisted of at least two specimens. Using this approach,  $m$  groups were generated, as indicated in Tables 5.2 and 5.3.
- (2) An initial value was chosen for the parameter ( $\alpha$  or  $\beta$ ) and the ratio of measured strength  $V_{ij}$  to  $Y_{ij}$  was calculated for each specimen. The subscript  $i$  denotes the group ( $i = 1, 2, \dots, m$ ) and  $j$  the specimen in each group ( $j = 1, 2, \dots, n_i$ ). Clearly,

this ratio should be similar for tests in the same group if the initial value of  $\alpha$  or  $\beta$  closely reflects the contribution of the investigated variable (concrete strength or flexural reinforcement). The average ratio for each group, as defined by the following equation, was then calculated.

$$\bar{X}_i = \frac{\sum_{j=1}^{n_i} \frac{V_{ij}}{Y_{ij}}}{n_i} \quad (5.5)$$

- (3) For each specimen, the deviation of the prediction from the average of the corresponding group was defined as

$$e_{ij} = \frac{\left| \frac{V_{ij}}{Y_{ij}} - \bar{X}_i \right|}{\bar{X}_i} \quad (5.6)$$

- (4) The average deviation for all tests used in the analysis was calculated as follows:

$$\bar{e} = \frac{\sum_{i=1}^m \sum_{j=1}^{n_i} e_{ij}}{\sum_{i=1}^m n_i} \quad (5.7)$$

- (5) The average deviation,  $\bar{e}$ , was minimized by adjusting the value of  $\alpha$  or  $\beta$  and repeating steps (2) to (4).

### 5.3.1.2 Analysis Results

Twenty-four specimens placed in 9 groups were used to evaluate the effects of concrete strength on connection punching capacity. In these specimens, concrete strength ranged from 13.7 MPa (1990 psi) to 70.0 MPa (10200 psi) and top reinforcement was distributed evenly in two orthogonal directions in the slab, i.e., no reinforcement concentration existed. The data analysis results for three cases:  $\alpha = 1$ ,  $2/3$ , and  $1/2$  are listed in Table 5.2.  $\alpha = 1$  is consistent with the assumption used for Equation 5.1, that is,

connection two-way shear strength is proportional to  $\sqrt{f_c'}$ .  $\alpha = 2/3$  corresponds to the assumed effect of concrete strength on connection strength in CEB-FIP MC90 code. In Table 5.2, Column (2) gives the numbering of specimens listed in Appendix C and Column (6) provides the measured connection punching strength. It was found that assuming punching strength to be proportional to  $(f_c')^{0.25}$  ( $\alpha = 0.5$ ) resulted in the least average deviation,  $\bar{e}$ . It appeared that both ACI 318-05 and CEB-FIP MC90 codes may have overestimated the effect of concrete strength.

Table 5.2: Effects of Concrete Strength on Connection Punching Strength

(1)	(2)	(3)	(4)	(5)	(6)	(7)	(8)	(9)
Group	No.*	Label	$f_c'$ (MPa)	$\rho f_y$ (MPa)	$V_u$ (kN)	$e$ ( $\alpha = 1$ )	$e$ ( $\alpha = 2/3$ )	$e$ ( $\alpha = 1/2$ )
1	1	A-2a	13.7	7.93	334	0.021	0.063	0.104
	2	A-2b	19.5	7.93	400	0.023	0.004	0.018
	3	A-2c	37.5	7.93	467	0.138	0.064	0.026
	4	A-7b	27.9	7.93	512	0.094	0.131	0.149
2	5	NS1	42.0	7.22	320	0.071	0.029	0.009
	6	HS3	69.0	7.22	356	0.071	0.029	0.009
3	7	SR2-C1-F0	16.9	6.31	146	0.040	0.099	0.128
	8	SR2-C2-F0	34.4	6.31	226	0.040	0.099	0.128
4	11	NS2	30.0	4.63	396	0.106	0.036	0.000
	15	HS6	70.0	4.63	489	0.106	0.036	0.000
5	16	N.H.Z.S.1.0	32.2	4.60	476	0.114	0.067	0.042
	37	N.N.Z.S.1.0	37.2	4.60	485	0.056	0.036	0.025
	41	H.H.Z.S.1.0	67.2	4.60	512	0.171	0.102	0.067
6	42	A-1a	14.1	3.82	302	0.130	0.040	0.003
	44	A-1b	25.2	3.82	365	0.020	0.035	0.041
	62	A-1c	29.0	3.82	356	0.072	0.037	0.020
	63	A-1d	36.8	3.82	351	0.188	0.123	0.089
	65	A-1e	20.3	3.82	356	0.110	0.085	0.072
7	66	SR1-C1-F0	16.9	2.84	104	0.090	0.031	0.001
	67	SR1-C2-F0	34.4	2.84	124	0.090	0.031	0.001
8	81	9	26.9	2.50	408	0.001	0.021	0.032
	82	9a	21.0	2.50	360	0.001	0.021	0.032
9	83	B-1	14.2	1.62	178	0.239	0.142	0.093
	84	B-2	47.6	1.61	200	0.239	0.142	0.093
						$\bar{e} = 0.093$	$\bar{e} = 0.066$	$\bar{e} = \mathbf{0.048}$

\* References are provided in Appendix C.

Table 5.3: Effects of Slab Tensile Reinforcement on Connection Punching Strength

(1)	(2)	(3)	(4)	(5)	(6)	(7)	(8)	(9)
Group	No.*	Label	$\rho f_y$ (MPa)	$f_c'$ (MPa)	$V_u$ (kN)	$e$ ( $\beta = 0$ )	$e$ ( $\beta = 1/3$ )	$e$ ( $\beta = 1/2$ )
1	6	A-2a	7.93	13.7	334	0.231	0.019	0.138
	1	A-1a	3.82	14.1	302	0.113	0.132	0.123
	15	B-1	1.62	14.2	178	0.344	0.112	0.016
2	81	SR1-C1-F0	2.84	16.9	104	0.169	0.037	0.029
	83	SR2-C1-F0	6.31	16.9	146	0.169	0.037	0.029
3	7	A-2b	7.93	19.5	400	0.058	0.063	0.124
	5	A-1e	3.82	20.3	356	0.058	0.063	0.124
4	23	S5-60	4.23	22.2	343	0.049	0.017	0.001
	27	S5-70	5.11	23.0	378	0.049	0.017	0.001
5	24	S1-70	5.11	24.5	393	0.044	0.022	0.055
	2	A-1b	3.82	25.2	365	0.030	0.001	0.016
	28	H-1	3.77	26.1	371	0.014	0.021	0.039
6	9	A-4	3.82	26.1	400	0.258	0.120	0.049
	14	A-13	1.62	26.2	236	0.258	0.120	0.049
7	11	A-7b	7.93	27.9	512	0.374	0.101	0.031
	3	A-1c	3.82	29.0	356	0.045	0.023	0.030
	78	Ref-0.35%	1.58	30.0	250	0.329	0.078	0.061
8	82	SR1-C2-F0	2.84	34.4	124	0.292	0.166	0.101
	84	SR2-C2-F0	6.31	34.4	226	0.292	0.166	0.101
9	57	FS-1	2.56	35.4	174	0.119	0.052	0.018
	60	FS-19	1.70	34.5	137	0.119	0.052	0.018
10	80	Ref-1.0%	4.35	36.0	420	0.053	0.047	0.097
	8	A-2c	7.93	37.5	467	0.053	0.047	0.097
11	77	SR-1	3.74	36.8	365	0.034	0.048	0.058
	4	A-1d	3.82	36.8	351	0.071	0.091	0.103
	63	N.N.Z.S.1.0	4.60	37.2	485	0.283	0.180	0.129
	70	NSNW0.5P	2.25	37.8	310	0.179	0.041	0.033
12	33	S-1	2.57	38.9	198	0.078	0.081	0.079
	34	S-7	3.43	38.9	222	0.209	0.101	0.047
	35	S-19	1.71	38.9	131	0.287	0.182	0.126
13	16	B-2	1.61	47.6	200	0.251	0.151	0.100
	17	B-4	3.00	47.7	334	0.251	0.151	0.100
14	38	HS1	2.41	67.0	178	0.318	0.156	0.069
	41	HS3	7.22	69.0	356	0.364	0.170	0.075
	39	HS2	4.13	70.0	249	0.046	0.014	0.006
15	45	HS8	5.44	69.0	436	0.049	0.068	0.081
	43	HS5	3.14	68.0	365	0.203	0.062	0.013
	44	HS6	4.63	70.0	489	0.067	0.104	0.118
	46	HS9	7.89	74.0	543	0.185	0.026	0.050
						$\bar{e} =$ 0.164	$\bar{e} =$ 0.081	$\bar{e} =$ <b>0.065</b>

\* References are provided in Appendix C.

Thirty-nine tests without banded reinforcement at the column were placed in 15 groups to investigate the effects of slab tensile reinforcement on connection strength. The values of  $\rho f_y$  for these specimens range from 1.58 MPa (230 psi) to 7.93 MPa (1150 psi). The analytical results are presented in Table 5.3. It was found that a value of  $\beta = 0.5$  best described the effects of slab flexural reinforcement. The significant contribution of slab flexural reinforcement is not surprising since tests indicated that:

- Response of lightly-reinforced slab-column connections is dominated by flexure.
- Flexural reinforcement restrains the propagation of inclined cracking that takes place when loads as low as fifty percent of the ultimate load are reached.
- As flexural strength increases, concrete strain tangential to the column face at the compressive surface of slab also increases (Marzouk and Hussein, 1991). The resulting restraint from the surrounding slab enhances the effect of tri-axial state of stress for concrete in the connection region.
- Once an inclined crack develops, tensile longitudinal reinforcement provides a doweling force at the crack and may provide a significant fraction of the punching strength. Even though the doweling effect is difficult to formulate at the current stage of knowledge, it may provide as much as 30 percent of the punching strength (Kinnunen and Nylander, 1960).

### **5.3.2 Critical Section Location**

The procedures described previously were similarly applied to 10 groups of test data (49 specimens, shown in Table 5.4) to determine an appropriate critical section location defined by the value of  $s$  in Figure 5.4. In each group, the specimens had nearly identical values of effective depth  $d$  and  $c/d$ -ratio.

Table 5.4: Data Grouping for Determination of Critical Section

Group	1	2	3	4	5	6	7	8	9	10
Specimen *					23				1-5	
	66	9	47	72	27	81-84	42-46	62-65	15-19	33-35
	67	14	48	73	32			70	24	37-41
									28	57
									78	60
								79		

\* Numbering and details of the specimens are shown in Appendix C.

The conclusions drawn previously regarding the contribution of concrete strength and flexural strength ( $\alpha = \beta = 0.5$ ) were incorporated and the following ratio for varying values of  $s$  ( $s = 0, 0.5d, d, 1.5d, 2.0d$ ) was calculated for each specimen:

$$Y = \frac{V_u}{(f_c')^{\frac{1}{4}} (\rho f_y)^{\frac{1}{2}} A_c} = \frac{V_u}{(f_c')^{\frac{1}{4}} (\rho f_y)^{\frac{1}{2}} [4d(c+2s)]} \quad (5.8)$$

The results of  $\bar{e}$  with respect to different values of  $s$  are shown in Table 5.5. It appears that the strength prediction is insensitive to the location of assumed critical section. As demonstrated from the tests, the location of the failure surface under gravity loading varied from case to case. For example, the inclined crack was initiated at top surface of slab around 4 in. ( $0.8d$ ) away from the column face for Specimen G0.5 and 8 in. ( $1.6d$ ) for Specimen G1.0. For convenience,  $s = 0.5d$  was adopted in this study because this value has been used to define the critical section in the ACI code since the 1960's.

Table 5.5: Determination of Critical Section Location

$s$	0	$0.5d$	$d$	$1.5d$	$2.0d$
$\bar{e}$	0.075	0.075	0.075	0.074	0.075

### 5.3.3 Effects of $c/d$ -Ratio

Review of the data indicted a pronounced tendency toward decreased connection strength with increased  $c/d$ -ratio. To illustrate this situation, the following ratio as a function of  $c/d$ -ratio was evaluated for specimens with a slab thickness about 150 mm (6 in.) and the results are plotted in Figure 5.5.

$$Y = \frac{V_u}{(f_c')^{\frac{1}{4}}(\rho f_y)^{\frac{1}{2}}[4d(c+d)]} \quad (5.9)$$

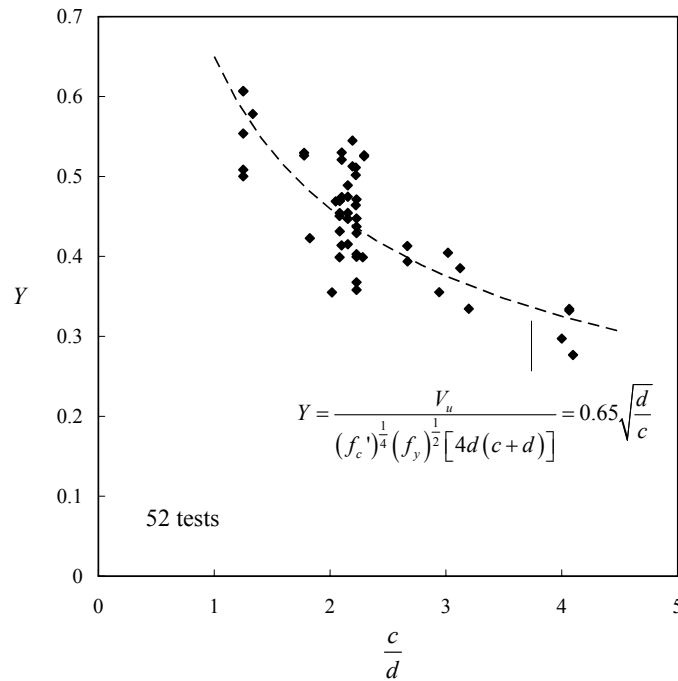


Figure 5.5: Effect of  $c/d$ -ratio on connection strength (52 tests).

The  $c/d$ -ratio is likely related to the lateral restraint imposed on concrete at the base of the inclined crack. The concrete is under a tri-axial state of stress. Considering that, as the  $c/d$ -ratio increases, the shear strength should not reduce to zero and based on a regression analysis (as shown in Figure 5.5), the effect of  $c/d$ -ratio on connection strength can be expressed by taking function  $y$  in Equation 5.3 as

$$y\left(\frac{c}{d}\right) = \sqrt{\frac{d}{c}} \quad (5.10)$$

### 5.3.4 Formulation of Connection Punching Strength

Based on data analyses described above, the punching strength of a slab-column connection was determined as:

$$V_n = 0.65\xi A_c \left(\rho f_y \sqrt{f_c'}\right)^{\frac{1}{2}} \quad (\text{in SI units}) \quad (5.11)$$

$$V_n = 2.3\xi A_c \left(\rho f_y \sqrt{f_c'}\right)^{\frac{1}{2}} \quad (\text{in US customary units}) \quad (5.11a)$$

where  $A_c$  is area of the critical section;

$$A_c = 4d(c+d) \quad (5.12)$$

$\xi$  represents the effect of  $c/d$ -ratio;

$$\xi = \sqrt{\frac{d}{c}} \quad (5.13)$$

Comparison of punching capacity calculated using Equations 5.11 and 5.11a with the measured strength (for the same database used in Figures 5.2 and 5.3) is shown in Figure 5.6. Calculated values are closer to measured values and the standard deviation of the ratio of measured to calculated strength that indicates data scatter is significantly reduced from 0.32 (Figure 5.2) to 0.13.

It is noted that Equations 5.11 and 5.11a were developed from isolated slab-column connections, except for the test by Gardner and Shao (1996). The isolated connection tests usually did not simulate the slab continuity existing in a typical flat-plate structure. It has been long argued that the punching resistance in an actual structure, due to the in-plane restraints, should be higher than that derived from the single connection tests. In addition, tests by Alexander and Simmonds (1992) have demonstrated that the

rotational restraint applied at specimen boundaries can increase the connection punching strength by at least 10 percent.

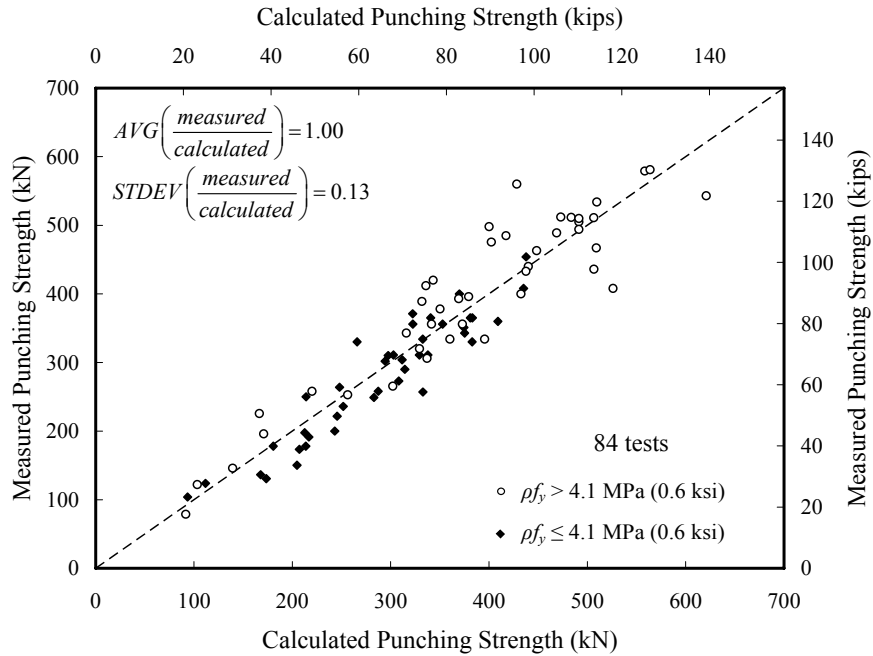


Figure 5.6: Comparison of measured strength and calculated strength based on the proposed formulation (Equations 5.11 and 5.11a).

A reduction factor of 0.83 was applied to the right-hand-side of Equations 5.11 and 5.11a to derive a characteristic strength. Using this reduction factor, 95% of the test results exceed the nominal strength. The resulting characteristic punching strength of a slab-column connection is given as

$$V_n = 0.54\xi A_c \left( \rho f_y \sqrt{f_c'} \right)^{\frac{1}{2}} \quad (\text{in SI units}) \quad (5.14)$$

$$V_n = 1.9\xi A_c \left( \rho f_y \sqrt{f_c'} \right)^{\frac{1}{2}} \quad (\text{in US customary units}) \quad (5.14a)$$

The characteristic strength calculated based on Equations 5.14 and 5.14a for the same 84 specimens used previously is shown in Figure 5.7.

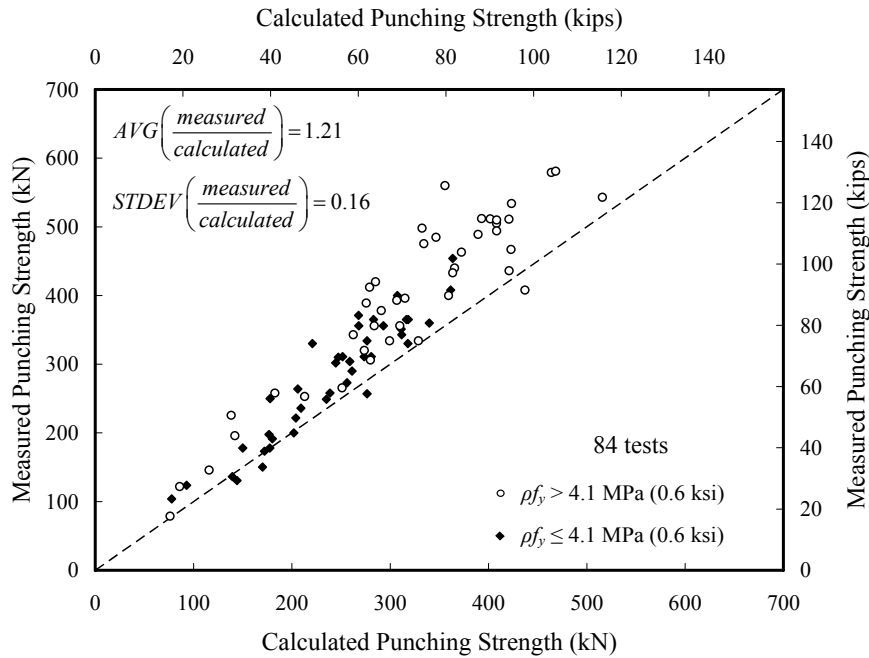


Figure 5.7: Comparison of measured strength and calculated strength based on the proposed formulation (Equations 5.14 and 5.14a).

### 5.3.5 Reinforcement Concentration

Equations 5.11 and 5.11a were established from tests with uniformly spaced reinforcement. Banded flexural reinforcement at the column is often used for two reasons: (1) to increase slab stiffness, and (2) to allow the connection to carry unbalanced moments imposed by lateral deformation as well as by gravity loads. Therefore, the area where banded reinforcement is effective for punching strength, i.e., the area where the reinforcement ratio  $\rho$  is evaluated, must be defined. For this purpose, the strength of 11 specimens with concentrated flexural reinforcement was evaluated according to Equation 5.11 or 5.11a using reinforcement ratios defined over various slab widths centered on the column. As shown in Table 5.6, the reinforcement ratio defined in a width  $c+12d$  provided the best estimate of the test results. For convenience of practical application, the

top reinforcement ratio  $\rho$  in Equations 5.11, 5.11a, 5.14, and 5.14a can be approximately evaluated over the column strip of the slab.

Table 5.6: Effective Area of Banded Reinforcement

No.	Specimen	$V_{u,measured} / V_{u,calculated}$			
		$c+6d$	$c+8d$	$c+10d$	$c+12d$
12	A-9	0.83	0.87	0.90	0.92
13	A-10	0.84	0.88	0.92	0.94
20	S2-60	1.00	1.02	1.03	1.04
21	S3-60	0.93	0.98	1.02	1.05
22	S4-60	0.78	0.84	0.89	0.93
25	S3-70	0.86	0.90	0.93	0.96
26	S4-70	0.72	0.78	0.82	0.86
55	P19S75	0.74	0.77	0.78	0.80
56	P19S50	0.80	0.84	0.88	0.90
69	NB	0.84	0.90	0.94	0.98
87	G1.0	0.91	0.94	0.98	1.00
Average		0.84	0.88	0.92	<b>0.95</b>

### 5.3.6 Use of Proposed Equation for Connection Shear Strength

Equations 5.11 and 5.11a were developed based on test data of interior slab-column connections supported on square columns and subjected to concentric gravity loads. The proposed equations formed the basis of maximum shear that can be developed at slab-column connections under lateral loading, as will be discussed in Section 6.2.2.2.

## Chapter 6

### **A Model for Behavior of Interior Slab-Column Connections Transferring Gravity Shear and Unbalanced Moment**

#### **6.1 GENERAL**

Reinforced concrete flat-plate systems have been widely used for residential or office buildings in seismic regions. When used in combination with perimeter moment frames or shear walls, the slab-column connections are generally designed to carry only gravity load. As a result, top tensile reinforcement ratios of slab within the column strip typically range from 0.5% to 1.5% in slab-column connections.

Performance-based seismic design and evaluation criteria have been adopted in FEMA 356. In addition to collapse prevention under a severe earthquake, it is required that a structure, in general, behave elastically during frequently occurring earthquakes and that damage be limited during moderate earthquakes. Due to the multilevel criteria and the significant cost involved in seismic upgrading, the inherent strength and stiffness contributed by existing slab-column frames should be considered in seismic evaluations and retrofit designs. Dovich and Wight (2005) conducted a case study on a four story flat-plate structure containing perimeter moment-resisting frames and nine interior slab-column connections in each floor. Based on their inelastic analysis using an equivalent beam width model, the slab-column frames contributed more than 30% of the overall lateral stiffness and strength.

If the first vibration mode dominates the response of a flat-plate structure under lateral loading, one approach for carrying out performance-based evaluations requires a

static nonlinear analysis, also known as push-over analysis. For such analyses, the definition of nonlinearity of slab-column framing including strength as well as stiffness is of particular concern.

Equivalent beam width method and beam analogy are two approaches for evaluating connection lateral strength. The beam analogy concept is more attractive since it describes all actions including shear, flexure, and torsion acting on the critical section of a connection. Despite the complexity in applying this approach to the design of slab-column frames, it is suitable for structural evaluation when geometry and material properties of a connection are given.

The objective of this chapter is to establish an analytical model for lightly-reinforced interior slab-column connections for use in pushover analyses. The lateral strength of connections supported on square columns was first evaluated using ACI code design equations. Then, based on a beam analogy concept, an algorithm was developed for evaluating connection lateral strength and a simple 2D frame model that describes the overall nonlinear behavior of interior slab-column connections was proposed. The stiffness parameters of all frame components were determined from three cyclic loading tests conducted as part of this study. The suggested model was assessed by comparing the calculated and measured response of five tests reported in the literature.

## **6.2 CONNECTION STRENGTH**

### **6.2.1 ACI Building Code Procedures**

For slab-column connections with square columns carrying both gravity shear,  $V_g$ , and unbalanced moment,  $M_u$ , the design approach recommended in ACI 318-05 is shown in Figure 6.1. It is assumed that a portion ( $\gamma_v = 40\%$ ) of  $M_u$  is transferred by eccentric

shear stress, while the remaining portion ( $\gamma_f = 60\%$ ) of  $M_u$  is resisted by flexure provided by the reinforcement situated within a width  $c+3h$  at the column.

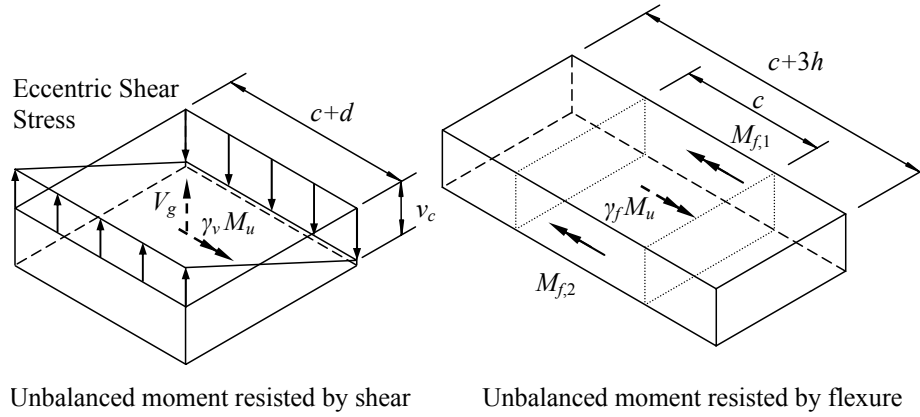


Figure 6.1: ACI 318-05 design approach for connections transferring unbalanced moment and gravity shear.

Following the above assumptions, the unbalanced moment at shear failure,  $M_{u,v}$ , and at flexural failure,  $M_{u,f}$ , can be determined from Equations 6.1 and 6.3, respectively. The minimum of  $M_{u,v}$  and  $M_{u,f}$  provides an estimation of the connection lateral resistance,  $M_{ACI}$ , as well as the corresponding failure mode.

$$M_{u,v} = \frac{2(V_c - V_g)J_c}{\gamma_v(c+d)A_c} = \frac{5(V_c - V_g)}{(c+d)A_c} \quad (6.1)$$

where

$$J_c = \frac{2}{3}d(c+d)^3 + \frac{1}{6}(c+d)d^3 \quad (6.2)$$

$$M_{u,f} = \frac{M_{f,1} + M_{f,2}}{\gamma_f} = \frac{M_{f,1} + M_{f,2}}{0.6} \quad (6.3)$$

Equations 6.1 and 6.3 were applied to 35 tests reported earlier in the literature and in this study. These tests were conducted on isolated or continuous specimens with square

columns to investigate the connection behavior under simulated seismic lateral loads. Tests simulating the effects of pattern gravity loads were not included. The specimen geometry, top reinforcement ratio evaluated over a width of  $c+12d$  at the column, and the gravity shear ratio,  $V_g/V_c$ , reflecting the gravity load level are given in Table 6.1. Specimens 1, 2, 12, 13, 15, 16, and 17 were tested under monotonic lateral loading and all other specimens were subjected to cyclic loads. It was assumed that the loading scheme, monotonic or cyclic lateral loading, had negligible effect on connection overall strength.

The calculated strength,  $M_{ACI}$ , the measured unbalanced moment,  $M_{test}$ , and expected failure mode are presented in Table 6.2. “S” and “F” are given in Column (9) to designate the shear failure and flexural failure. The measured unbalanced moment carrying capacity was determined from the measured peak lateral loads. The slab flexural capacity in a slab width  $c+3h$  for positive bending,  $M_{f,1}$ , and for negative bending,  $M_{f,2}$ , was calculated using Equations 6.4 and 6.5.

$$M_{f,1} = A_{s,1}f_{y,1}d_1 \frac{(c+3h)}{s_1} \left( 1 - 0.59 \frac{A_{s,1}f_{y,1}}{s_1 d_1 f_c'} \right) \quad (6.4)$$

$$M_{f,2} = A_{s,2}f_{y,2}d_2 \frac{(c+3h)}{s_2} \left( 1 - 0.59 \frac{A_{s,2}f_{y,2}}{s_2 d_2 f_c'} \right) \quad (6.5)$$

where  $A_{s,1}$ ,  $f_{y,1}$ ,  $d_1$ , and  $s_1$  denote the bar area, yield strength, effective depth, and average spacing of top reinforcement placed in the lateral loading direction within a width  $c+3h$  centered on the column, respectively.  $f_{y,2}$ ,  $d_2$ , and  $s_2$  have the similar meaning as those in Equation 6.4, but for the bottom reinforcement.

For connections without continuous bottom reinforcement through the column,  $f_{y,2}$  may not be developed. In this case,  $M_{f,2}$  is limited to the flexural cracking moment evaluated in  $c+3h$ .

Table 6.1: Properties of Specimens Subjected to Combined Loading

No.	Source	Label	Column size, $c$ (in)	Slab thickness, $h$ (in)	$V_g/V_c$	Reinforcement ratio (%)	
						Top	Bottom
1	Hanson and Hanson (1968)	A1*	6	3	0	1.63	1.63
2		A2*	6	3	0	1.63	1.63
3	Hawkins et al. (1974)	S1	12	6	0.34	1.29	0.56
4		S2	12	6	0.45	0.9	0.47
5		S3	12	6	0.43	0.57	0.46
6		S4	12	6	0.41	1.29	0.56
7	Kano and Yoshizaki (1975)	H5	7.9	3.9	0	0.7	0.70
8		H6	7.9	3.9	0	1.12	1.12
9		H9	7.9	3.9	0.31	0.7	0.70
10		H10	7.9	3.9	0.32	1.12	1.12
11		H11	7.9	3.9	0.64	1.12	1.12
12	Islam and Park (1976)	1*	9	3.5	0.20	1.14	0.57
13		2*	9	3.5	0.15	1.14	0.57
14		3C	9	3.5	0.20	1.14	0.57
15	Ghali et al. (1976)	SM0.5*	12	6	0.29	0.50	0.17
16		SM1.0*	12	6	0.31	1.00	0.33
17		SM1.5*	12	6	0.28	1.50	0.50
18	Morrison et al. (1983)	S1	12	3	0	0.69	0.69
19		S2	12	3	0	1.03	1.03
20		S3	12	3	0	1.38	1.38
21		S4	12	3	0.08	1.03	1.03
22		S5	12	3	0.16	1.03	1.03
23	Pan and Moehle (1992)	1	10.8	4.8	0.35	0.61	0.24
24		3	10.8	4.8	0.18	0.61	0.24
25	Robertson and Durrani (1992)	A	10	4.5	0.18	0.52	0.40
26		B	10	4.5	0.37	0.52	0.40
27		C	10	4.5	0.51	0.52	0.40
28	Wey and Durrani (1992)	SC0	10	4.5	0.26	0.52	0.40
29	Durrani, Du, and Luo (1995)	DNY_1	10	4.5	0.27	0.62	0.09
30		DNY_2	10	4.5	0.40	0.62	0.09
31		DNY_3	10	4.5	0.24	0.62	0.17
32		DNY_4	10	4.5	0.29	0.62	0.09
33	Roberson et al. (2002)	1C	10	4.5	0.16	0.52	0.40
34	Stark and Bayrak (2005)	C02	12	4.5	0.40	1.03	0.51
35	Current study	L0.5	16	6	0.23	0.50	0.28

\* Monotonic lateral loading.

Table 6.2: Unbalanced Moment and Failure Mode Based on ACI 318-05 Procedures

(1)	(2)	(3)	(4)	(5)	(6)	(7)	(8)	(9)
	Source	Label	$M_{u,f}$ (k-in)	$M_{u,v}$ (k-in)	$M_{ACI}$ (k-in)	$M_{test}$ (k-in)	$\frac{M_{ACI}}{M_{test}}$	Expected Failure Mode
1	Hanson and Hanson (1968)	A1	212	138	138	198	0.70	S
2		A2	218	140	140	215	0.65	S
3	Hawkins et al. (1974)	S1	1545	779	779	1280	0.61	S
4		S2	1143	561	561	778	0.72	S
5		S3	677	581	581	475	1.22	S
6		S4	1532	667	667	1110	0.60	S
7	Kano and Yoshizaki (1975)	H5	351	299	299	376	0.80	S
8		H6	579	299	299	470	0.64	S
9		H9	334	204	204	287	0.71	S
10		H10	450	199	199	313	0.64	S
11		H11	450	106	106	219	0.48	S
12	Islam and Park (1976)	1	217	249	217	270	0.80	F
13		2	229	288	229	334	0.69	F
14		3C	195	264	195	317	0.61	F
15	Ghali et al. (1976)	SM0.5	549	1017	549	888	0.62	F
16		SM1.0	1055	949	949	1128	0.84	S
17		SM1.5	1632	1079	1079	1176	0.92	S
18	Morrison et al. (1983)	S1	130	537	130	310	0.42	F
19		S2	194	470	194	345	0.56	F
20		S3	257	462	257	372	0.69	F
21		S4	187	433	187	319	0.59	F
22		S5	198	395	198	336	0.59	F
23	Pan and Moehle (1992)	1	508	559	508	566	0.90	F
24		3	506	677	506	866	0.58	F
25	Robertson and Durrani (1992)	A	472	510	472	586	0.81	F
26		B	491	381	381	366	1.04	S
27		C	492	305	305	240	1.27	S
28	Wey and Durrani (1992)	SC0	600	513	513	546	0.94	S
29	Durrani, Du, and Luo (1995)	DNY_1	310	476	310	418	0.74	F
30		DNY_2	296	337	296	296	1.00	F
31		DNY_3	294	415	294	428	0.69	F
32		DNY_4	282	344	282	390	0.72	F
33	Roberson et al. (2002)	1C	481	544	481	453	1.06	F
34	Stark et al. (2005)	C02	681	389	389	393	0.99	S
39	Current study	L0.5	696	1400	696	1137	0.61	F

The ratios of  $M_{ACI}$  to  $M_{test}$  given in Column (8) of Table 6.2 indicate that the strength of a slab-column connection may be significantly underestimated if lateral load is applied to the connection. The underestimation for specimens that failed in flexure likely resulted from the low value of  $\gamma_v = 0.4$  assumed in the code approach. Such conservativeness may not always be beneficial since it may require an unnecessary amount of flexural reinforcement to be placed in the  $c+3h$  region at the column, resulting in not only construction congestion but also a reduction of connection deformation capacity. The latter effect has already been demonstrated in the tests conducted by Ghali et al. (1976), as discussed in Chapter 1. However, simply increasing the value of  $\gamma_v$  (decreasing  $\gamma_f$ ) or increasing the width over which  $M_{u,sf}$  is evaluated will not reduce the data scatter reflected by the ratios of  $M_{ACI}/M_{test}$  in Table 6.2 that range from 0.42 to 1.06 for the specimens that failed in flexure.

For connections that fail in shear, the assumption that shear stress varies linearly on the critical sections parallel to the lateral loading direction may lead to very conservative unbalanced moment transfer capacity. It is believed that such an assumption underestimates the torsional resistance and, therefore, the lateral strength of a connection.

### **6.2.2 Beam Analogy Approach**

Tests indicated that slab inelastic flexural deformation was not concentrated at the slab-column interface but at the inclined cracks where the punching failure under lateral deformation was triggered. In addition, a critical section located  $0.5d$  away from the column faces has been suggested for Equations 5.11 and 5.11a to determine connection punching strength under gravity load. Thus, for convenience, the beam analogy procedures described in this study were based on the above-mentioned critical section location for both flexure and shear. Figure 6.2 shows the internal forces acting on the

critical section that must balance the external moment,  $M_u$ , and the gravity shear transferred from slab to column,  $V_g$ . Among the four critical section faces, two are referred to as bending faces: the front and back faces with respect to the lateral loading direction. The other two faces are termed as side faces.

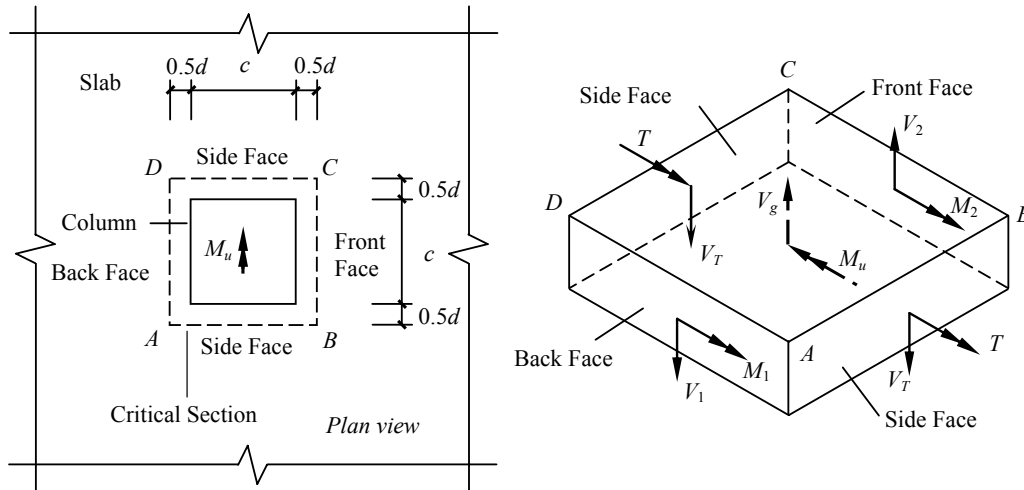


Figure 6.2: Internal forces acting on the critical sections.

The vector notation for the internal forces is given as follows:  $M_1$  and  $V_1$  are flexural moment and shear at the back face subjected to negative bending (top steel in tension);  $M_2$  and  $V_2$  are flexural moment and shear at the front face under positive bending;  $T$  and  $V_T$  are torsion and shear at the side faces. The above actions must satisfy the following equilibrium equations.

$$M_u = M_1 + M_2 + 2T + M_{v,1} + M_{v,2} \quad (6.6)$$

$$V_g = V_1 - V_2 + 2V_T \quad (6.7)$$

where  $M_{v,1}$  and  $M_{v,2}$  represent lateral resistance from shear at the back and front faces of the critical sections and are computed respect to the joint centroid.

$$M_{v,1} = V_1 \frac{c+d}{2} \quad (6.8)$$

$$M_{v,2} = V_2 \frac{c+d}{2} \quad (6.9)$$

Since slab-column connections are statically indeterminate and internal forces at the critical section, especially shear and torsion, can not be measured in a test, a series of assumptions must be made for modeling the connection lateral strength. The formulations for various actions and the associated assumptions are presented in the following sections.

### **6.2.2.1 Unbalanced Moment Resisted by Flexure at Bending Faces**

The top reinforcement likely yields early during the lateral loading at the back face of the critical section where both lateral and gravity loads introduce negative bending. It was assumed that, for a typical slab-column connection, the flexural strength for negative bending at this face, as defined by Equation 6.10, can always be fully developed.

$$M_{n,1} = A_{s,1} f_{y,1} d_1 \frac{(c+d)}{s_1} \left( 1 - 0.59 \frac{A_{s,1} f_{y,1}}{s_1 d_1 f_c'} \right) \quad (6.10)$$

where  $A_{s,1}$ ,  $f_{y,1}$ ,  $d_1$ , and  $s_1$  denote the bar area, yield strength, effective depth, and average spacing of top reinforcement placed in the lateral loading direction within a width  $c+d$  centered on the column, respectively.

If the gravity load level and top reinforcement ratio are such that the connection exhibits general yielding prior to punching failure, then the bottom bars passing through the front face of the critical section may develop yielding. The flexural capacity for positive bending is defined as

$$M_{n,2} = A_{s,2} f_{y,2} d_2 \frac{(c+d)}{s_2} \left( 1 - 0.59 \frac{A_{s,2} f_{y,2}}{s_2 d_2 f_c'} \right) \quad (6.11)$$

where  $f_{y,2}$ ,  $d_2$ , and  $s_2$  have the similar meaning as those in Equation 6.10, but for the bottom reinforcement.

For connections without continuous bottom reinforcement through the column,  $M_{n,2}$  was limited to the flexural cracking moment evaluated in a width  $c+d$  at the column. In addition, neither strain hardening nor shear-flexure interaction was considered.

### 6.2.2.2 Unbalanced Moment Resisted by Shear at Bending Faces

It was assumed that  $V_{n,1}$  and  $V_{n,2}$ , the maximum shear values for  $V_1$  and  $V_2$  that can be developed at the front and back faces of the critical section are limited to

$$V_{n,1} = \frac{1}{4} V_n^{[1]} \quad (6.12)$$

$$V_{n,2} = \frac{1}{4} V_n^{[2]} \quad (6.13)$$

In the above equations,  $V_n^{[1]}$  is the punching capacity of a connection subjected only to gravity load and can be determined from Equation 5.11 or 5.11a.  $V_n^{[2]}$ , however, is the punching capacity if a load acts in the opposite direction on the slab and causes tension in the slab bottom surface at the column. The variables in Equation 5.11 or 5.11a should be associated with the bottom reinforcement properties to calculate  $V_n^{[2]}$ .

$$V_n = 0.65 \xi A_c \left( \rho f_y \sqrt{f_c'} \right)^2 \quad (\text{in SI units}) \quad (5.11)$$

$$V_n = 2.3 \xi A_c \left( \rho f_y \sqrt{f_c'} \right)^2 \quad (\text{in US customary units}) \quad (5.11a)$$

The connection rotational resistance from shear  $V_{n,1}$  and  $V_{n,2}$  is calculated as a moment about the critical section centroid as

$$M_{vn,1} = V_{n,1} \left( \frac{c+d}{2} \right) \quad (6.14)$$

$$M_{vn,2} = V_{n,2} \left( \frac{c+d}{2} \right) \quad (6.15)$$

### **6.2.2.3 Unbalanced Moment Resisted by Torsion at Side Faces**

It was assumed that, at the side faces, the existence of shear always reduces the torsional capacity. The interaction between shear and torsion was assumed to take the form of

$$f \left( \frac{V_T}{V_{n,1}}, \frac{T_n}{T_0} \right) = 0 \quad (6.16)$$

where  $f$  is a function to be determined,  $T_n$  and  $T_0$  are the torsional strength with and without the presence of  $V_T$ .

The pure torsional capacity  $T_0$  was investigated first according to available test data, and then an interaction relationship between shear and torsion was developed.

#### **Pure Torsional Strength, $T_0$**

Using the test setup shown in Figure 6.3, Kanoh and Yoshizaki (1979) conducted a series of tests to determine  $T_0$  for slab-column connections without transferring gravity shear. In the tests, the slab was connected to one face of the column and pin-supported at two slab edges. Torsion was induced by applying a monotonic lateral load on the column. Although the physical conditions for torsion of a typical slab-column connection could not be fully duplicated, such a test scheme provided an approach for investigating pure torsional resistance. It was observed that  $T_0$  and the column rotation at which general yielding occurred were largely unaffected by the reinforcement ratio and slab width. In

addition, the column ultimate rotation was as high as 0.02 to 0.04 radians, indicating a relatively ductile failure mode.

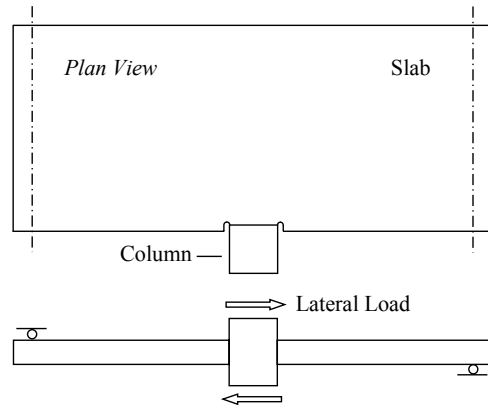


Figure 6.3: Test scheme for determining  $T_0$  (Kano and Yoshizaki, 1979).

$T_0$  can also be implicitly estimated using tests of slab-column connections transferring only unbalanced moment. Such tests have been carried out by Kano and Yoshizaki (1975) and Morrison et al. (1983) using a test setup shown in Figure 6.4(a) and (b), respectively. The tests, different from those illustrated in Figure 6.3, were conducted on conventional isolated connections with continuous slab surrounding the column. In addition, a cyclic lateral load was applied to simulate the seismic effects.

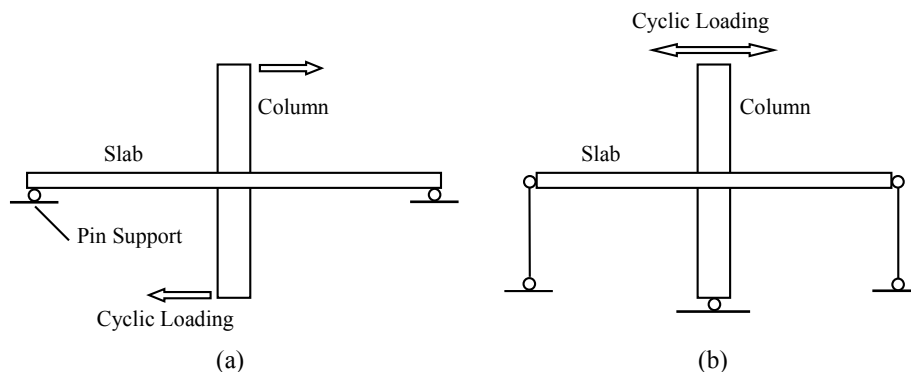


Figure 6.4: Test setups for lateral loading without applying gravity load.

Since no gravity load was applied and general yielding was observed in the tests, it can be assumed that all internal actions at the critical section developed and maintained their full capacity. Thus,  $T_0$  can be determined from equilibrium as

$$T_0 = 0.5 \left[ M_u - M_{n,1} - M_{n,2} - (V_{n,1} + V_{n,2}) \frac{c+d}{2} \right] \quad (6.17)$$

Properties of the above-mentioned tests and the values of  $T_0$  determined from tests for specimens shown in Figure 6.3 and  $T_0$  calculated from Equation 6.17 for specimens shown in Figure 6.4 are given in Table 6.3.

Table 6.3: Properties of Specimens for Determining  $T_0$

(1)	(2)	(3)	(4)	(5)	(6)	(7)	(8)	(9)	(10)
Source	Label	$c$ (in.)	$h$ (in.)	$d$ (in.)	$f_c'$ (psi)	$\rho$ (%)	$f_y$ (ksi)	$T_0$ (k-in)	$\frac{v_r}{\sqrt{f_c'}}$
Kano and Yoshizaki (1979)	T2*	7.87	3.94	3.15	3730	0.97	54.7	67.4	17.4
	T3*	7.87	3.94	3.15	3730	1.93	54.7	89.6	23.1
	T4*	7.87	3.94	3.15	3730	0.55	54.7	67.8	17.5
Kano and Yoshizaki (1975)	H5	7.87	3.94	3.15	3310	0.97	52.3	83.5	25.8
	H6	7.87	3.94	3.15	3310	1.93	52.3	86.5	23.8
Morrison et al. (1983)	S1	12	3	2.38	6641	0.65	46.8	66.7	24.4
	S2	12	3	2.38	5090	0.98	47.9	64.6	27.2
	S3	12	3	2.38	4916	1.31	48.6	63.8	25.5

\* Using test scheme shown in Figure 6.3.

Comparing the values in Columns (7) and (9) of Table 6.3 for each series of tests does not reveal a clear trend regarding the effect of slab flexural reinforcement on connection torsional resistance. For lack of sufficient test data to quantify the influence of reinforcement and for the sake of simplicity,  $T_0$  was defined as a function of critical section geometry and concrete strength. It was assumed that, at  $T_0$ , the concrete within a width  $c+d$  and between the centroids of top and bottom reinforcement layers at the side faces of the critical section, as shown in Figure 6.5, can develop full plasticity.

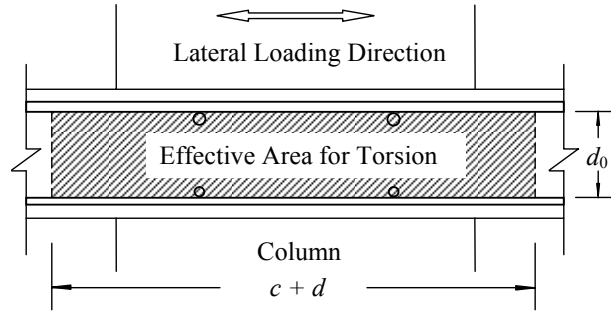


Figure 6.5: Effective area of calculating torsional capacity  $T_0$ .

The torsional capacity of a solid rectangular cross section at full plasticity can be expressed as

$$T = \alpha_p x^2 y \tau_p \quad (6.18)$$

where  $\tau_p$  is the plastic shearing stress,  $x$  is the shorter dimension of the section,  $y$  is the longer dimension, and  $\alpha_p$  is a parameter dependent of the ratio of  $y/x$ .

Taking the above form, the plastic torsional capacity at the one side face of the critical section of a slab-column connection was defined as

$$T_0 = v_T (c + d) d_0^2 \quad (6.19)$$

where  $v_T$  is the nominal torsional shear stress that was assumed to be proportional to  $\sqrt{f_c'}$  and  $d_0$  is the distance between the center of top and bottom reinforcement layers, as shown in Figure 6.5.

Column (10) in Table 6.3 provides the ratio of  $v_T$  to  $\sqrt{f_c'}$  for each test. Based on the results for Specimens H5, H6, S1, S2, and S3 with a continuous slab at the column,  $v_T$  was defined as  $v_T = 25\sqrt{f_c'}$  (psi) or  $v_T = 2.1\sqrt{f_c'}$  (MPa) and  $T_0$  was determined as

$$T_0 = 2.1\sqrt{f_c'}(c + d)d_0^2 \quad (\text{in SI units}) \quad (6.20)$$

$$T_0 = 25\sqrt{f_c'}(c + d)d_0^2 \quad (\text{in US customary units}) \quad (6.21)$$

It is noted that the strength value of  $v_T$  used here is about six times larger than the shear stress at cracking for a beam (with a section of  $c+d$  by  $d$ ) subjected to pure torsion. The significantly enhanced strength can be attributed partly to the presence of slab flexural reinforcement and partly to the restraint due to slab continuity.

### ***Interaction between $T_n$ and $V_T$***

Table 6.2 indicates that, except for Specimen 16, the specimens that satisfied the following conditions achieved general yielding prior to the connection failure: (1) top reinforcement ratio in  $c+12d$  region was less than 1.5%; and (2) gravity shear ratio,  $V_g/V_c$ , was no larger than 0.40, where  $V_c$  is the code-defined two-way shear strength of a connection. It was therefore assumed that the full capacities of  $M_1$ ,  $M_2$ ,  $V_1$ , and  $V_2$  were developed in these specimens at the maximum unbalanced moment. Such specimens (28 tests) are listed in Table 6.4 and were used to formulate an appropriate shear-torsion interaction equation because shear  $V_T$  and torsion  $T_n$  can be determined from equilibrium using Equations 6.6 through 6.9.

Various interaction relationships having the form of Equation 6.16 were examined. It was found that the linear function as expressed in Equation 6.22 resulted in reasonable agreement between the calculated connection lateral resistance,  $M_u$ , and the measured,  $M_{test}$ . The ratios of  $M_u/M_{test}$  are given in Column (9) of Table 6.4.

$$\frac{T_n}{T_0} + \frac{V_T}{V_{n,1}} = 1 \quad (6.22)$$

Based on Equations 6.7 and 6.22, the torsional strength,  $T_n$ , in the presence of gravity shear,  $V_g$ , for a slab-column connection was determined as

$$T_n = \left( 1 - \frac{V_g - V_{n,1} + V_{n,2}}{2V_{n,1}} \right) T_0 \quad (6.23)$$

Table 6.4: Calculated Connection Strength Based on Suggested Beam Analogy

(1)	(2)	(3)	(4)	(5)	(6)	(7)	(8)	(9)
	Source	Label	$M_1+M_2$ (k-in)	$M_{v,1}+M_{v,2}$ (k-in)	$2T$ (k-in)	$M_u$ (k-in)	$M_{test}$ (k-in)	$\frac{M_u}{M_{test}}$
3	Hawkins et al. (1974)	S1	393	353	381	1127	1280	0.88
6		S4	391	347	303	1041	1110	0.94
7	Kanoh and Yoshizaki (1975)	H5	107	81	177	364	376	0.97
8		H6	194	102	177	473	470	1.01
9		H9	102	78	53	232	287	0.81
10		H10	143	88	94	325	313	1.04
12	Islam and Park (1976)	1	78	79	100	258	270	0.95
13		2	83	84	124	292	334	0.87
14		3C	70	76	103	249	317	0.79
15	Ghali et al. (1976)	SM0.5	187	269	484	939	888	1.06
16		SM1.0*	359	371	649	1379	1128	1.22
18	Morrison et al. (1983)	S1	53	81	180	315	310	1.02
19		S2	80	94	158	332	345	0.96
20		S3	105	109	155	370	372	0.99
21		S4	77	93	122	291	319	0.91
22		S5	81	96	83	260	336	0.77
23	Pan and Moehle (1992)	1	197	176	212	585	566	1.03
24		3	197	173	408	778	866	0.90
25	Robertson and Durrani (1992)	A	211	139	206	556	586	0.95
26		B*	219	140	59	418	366	1.14
28	Wey and Durrani (1992)	SC0	207	151	162	520	546	0.95
29	Durrani, Du, and Luo (1995)	DNY_1	118	99	219	436	418	1.04
30		DNY_2	112	92	107	311	428	1.05
31		DNY_3	112	101	202	414	390	0.97
32		DNY_4	107	85	181	373	586	0.96
33	Roberson et al. (2002)	1C	155	130	219	504	453	1.11
34	Stark and Barak (2005)	C02	168	160	65	392	393	1.00
35	Current study	L0.5	273	351	548	1173	1135	1.03

\* No general yielding existed.

Columns (4), (5), and (6) of Table 6.4 provide the calculated connection lateral resistance from flexure, shear, and torsion, respectively. According to these data, the fraction of the unbalanced moment resisted by flexure ranges from 17% to 52%, by shear

from 22% to 41%, and by torsion from 14% to 57%. Clearly, each action of flexural, shear, and torsion may contribute a significant portion of the total resistance.

The moment transfer capacity estimated using the suggested approach and ACI procedures for the specimens listed in Table 6.4 are compared in Figure 6.6 with the measured connection strength. The ratios of calculated to measured strength and the relatively low standard deviation of the ratio of  $M_u/M_{test}$  provide an indication that flexural, shear, and torsional strengths were defined appropriately.

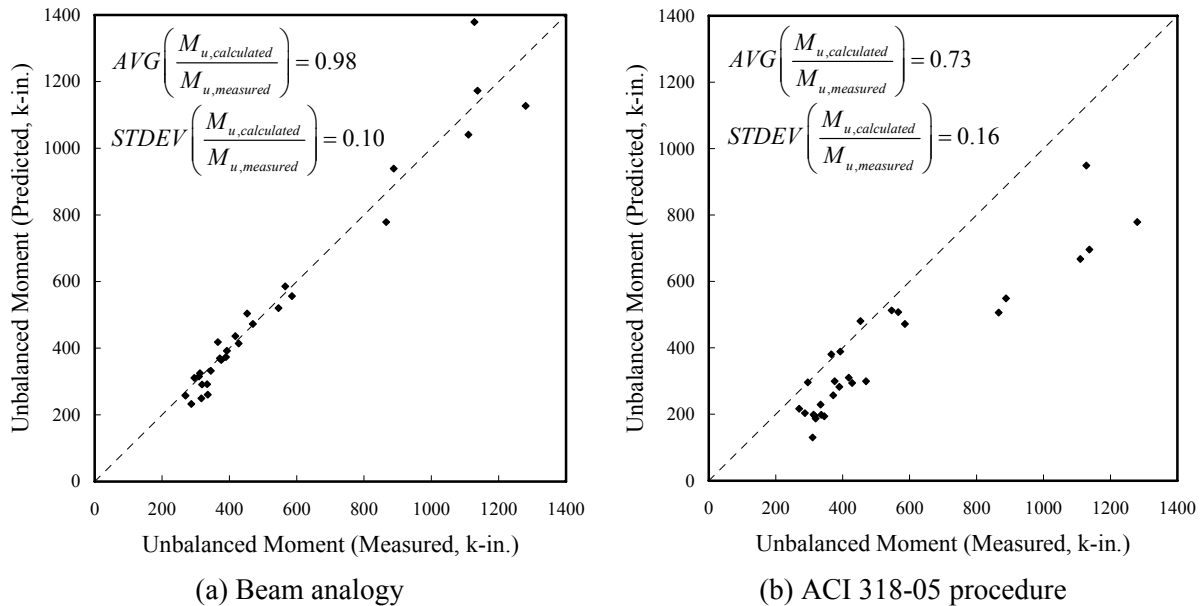


Figure 6.6: Comparison of calculated strength using beam analogy and ACI approach for 28 specimens ( $\rho < 1.5\%$ ,  $V_g/V_c \leq 0.40$ ).

It should be noted that the suggested approach need not be limited to connections with low reinforcement ratios and low gravity load levels. The exclusion of slab-column connections with larger reinforcement ratios or higher gravity shear ratios from the test database simply means that, for such connections, moment as well as shear at the front face and torsion at the back faces of the critical section may not be able to develop their

full capacity prior to the connection failure. In such situation, the values of these actions can not be determined from the test data and consequently the  $T-V$  interaction can not be developed based on those tests. In fact, slab-column connections with  $\rho \geq 1.5\%$  or  $P_g/P_0 > 0.40$  are atypical of flat-plate structures.

### **6.3 ANALYSIS OF SLAB-COLUMN FRAMES**

#### **6.3.1 General Model**

An equivalent 2D frame approach was investigated to reduce the computational cost and complexity associated with 3D analysis of flat-plate structures. The continuous structure is first discretized into several subassemblies by cutting it along the slab center lines parallel to the lateral loading direction. The substructures should satisfy lateral deformation compatibility and each is modeled as an equivalent beam-column frame to resist a portion of the lateral load. It is expected that the nonlinearity of such a frame under monotonic lateral loading in a pushover analysis can simulate the strength and stiffness degradation of a three-dimensionally continuous slab-column system subjected to cyclic lateral loading. Only interior slab-column connections were considered in this study.

Figure 6.7 shows a segmental flat-plate substructure bounded by two slab center lines along the lateral loading direction and containing two interior connections. The substructure can be subdivided into two regions: (1) joints enclosed by the critical sections (dotted lines around the columns) and assumed to be rigid; and (2) the remaining part of slab.

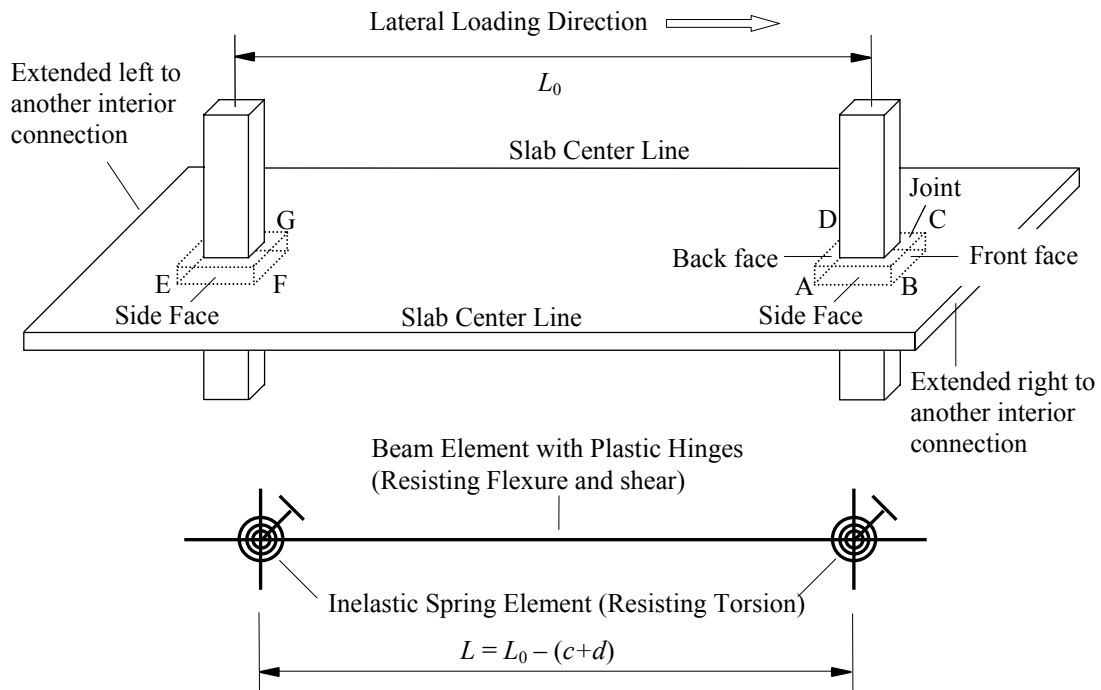


Figure 6.7: 2D model of interior slab-column connections.

To utilize the connection strength models described in Section 6.2.2, a prismatic beam element with a width of  $c+d$ , the width of the critical section, and a depth of  $h$  was used in the model to connect two adjacent slab-column joints in the lateral loading direction. As shown in Figure 6.8, the beam element contains two conventional components, an elastic beam and zero-length plastic moment hinges. The plastic hinges are located at the front and back faces of the critical section and are used to represent flexural nonlinearity. It was observed from tests of Specimens L0.5, LG0.5, and LG1.0 that connection deformation resulted mainly from inelastic deformation localized at inclined cracks near the column. Therefore, all plastic deformations were assumed to be concentrated at the zero-length plastic hinges. The plastic hinge is initially rigid and rotates only after a moment threshold is reached. The beam segment between hinges was assumed elastic and its stiffness characteristics were associated with slab bending. The

resistance from torsion was modeled by a nonlinear spring element resisting rotational deformation.

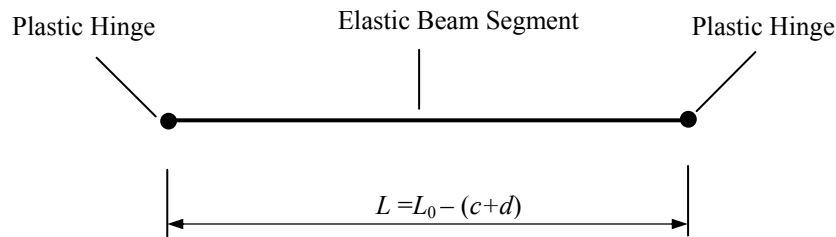
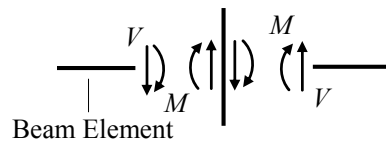
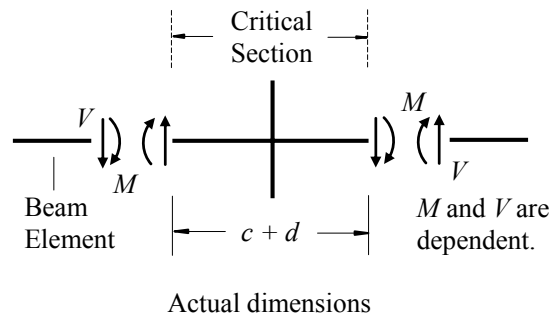


Figure 6.8: Beam element with plastic hinges.

The notation and sign convention for flexure, shear, and torsion acting on the critical section of the right-side interior connection shown in Figure 6.7 are consistent with those shown in Figure 6.2. As discussed in Chapter 3, from initial gravity loading to connection failure, the specimens experienced significant internal force redistribution. The model, based on a beam analogy approach, was established to capture both strength and stiffness characteristics associated with those actions.

When using a 2D frame analogy, shear force at the beam ends depends on moments acting on the beam element. However, such constraint can not reflect the real state of stress of a 3D slab-column connection since the equilibrium-restrained shear could significantly deviate from actual shear ( $V_1$  and  $V_2$ ) at the critical section. For this reason,  $V_1$  and  $V_2$  and their contribution to lateral resistance,  $M_{v,1}$  and  $M_{v,2}$ , were modeled separately. Meanwhile, the resistance from equilibrium-restrained shear must be eliminated. This was achieved by modeling the joint region as a point and defining the length of beam element as  $L = L_0 - (c + d)$ , where  $L_0$  is the column center-to-center distance in the lateral loading direction. In this way, as shown in Figure 6.9, equilibrium-

restrained shear results in no lateral resistance due to the zero dimension of the critical section.



With zero-length rigid end zone (Model):  
 $V$  does not contribute to lateral resistance.

Figure 6.9: Modeling of joint region (eliminating effects of equilibrium-restrained shear).

Two types of connection deformation were considered: connection rotation,  $\gamma$ , representative of connection global deformation and plastic hinge rotation,  $\theta$ , the localized deformation at the critical section. The physical representation of  $\gamma$  and  $\theta$  are illustrated in Figure 6.10, where the straight line  $S_1OS_2$  is tangential to the deformed column axis at joint O, line  $P_1OP_2$  is perpendicular to  $S_1OS_2$ ,  $ON_1$  and  $ON_2$  are tangential to the deformed equivalent beam at O.  $\gamma$  can be determined from story lateral drift and column flexural deformation and can be approximated as the inter-story drift if the column deformation is negligible. No attempt was made in this study to investigate the connection ultimate rotational capacity,  $\gamma_u$ .

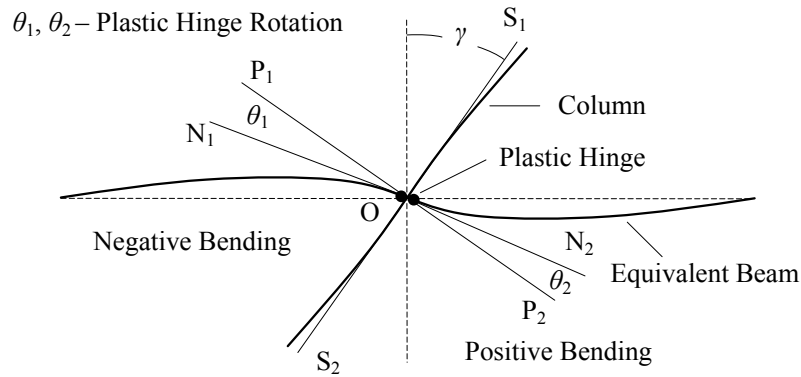


Figure 6.10: Joint rotation and plastic hinge rotation.

### 6.3.2 Model for Beam Element

#### 6.3.2.1 Moment Provided by Flexure, $M_1$ and $M_2$

An elastic-perfectly plastic moment-rotation relationship shown in Figure 6.11 was assumed for plastic hinge at the back face of the critical section, where the moment and shear due to lateral load are added to the moment and shear induced by gravity load,  $M_{g,1}$  and  $V_{g,1}$ . The plastic hinge rotates when the flexural capacity for negative bending,  $M_{n,1}$ , is reached at a joint rotation of  $\gamma_{y,1}$ .

At the plastic hinge at the front face of the critical section, gravity load results in moment and shear  $M_{g,2}$  and  $V_{g,2}$ . According to the sign convention prescribed in Figure 6.2,  $M_{g,1} = -M_{g,2}$  and  $V_{g,1} = -V_{g,2}$ .  $M_{g,1}$ ,  $M_{g,2}$ ,  $V_{g,1}$ , and  $V_{g,2}$  can be estimated based on available formulations (Timoshenko and Woinowsky-Krieger, 1959) or elastic finite element analyses. The monotonic lateral load subsequently applied may overcome the initial negative bending at this hinge and develop positive bending (bottom reinforcement in tension). The joint rotation when the flexural capacity of the plastic hinge under positive bending,  $M_{n,2}$ , is reached is denoted as  $\gamma_{y,2}$ . Compared with monotonic lateral loading, cyclic loading generally leads to more slab stiffness degradation and, therefore,

the yielding of bottom reinforcement should occur later. As shown in Figure 6.11, if an elastic-perfectly plastic model is used for this hinge in the pushover analysis, premature positive yielding would occur at a joint rotation  $\gamma_p$  instead of the expected  $\gamma_{y,2}$ . Hence, an intermediate point C that defined the elastic limit was used and a tri-linear relationship between positive bending moment and joint rotation was adopted. Immediately after the moment  $M_C$  is reached, the plastic hinge under positive bending becomes less stiff and, once  $M_{n,2}$  is achieved at joint rotation  $\gamma_{y,2}$ , the hinge is fully plastic. The definitions of  $M_{n,1}$  and  $M_{n,2}$  have been given in Equations 6.10 and 6.11.

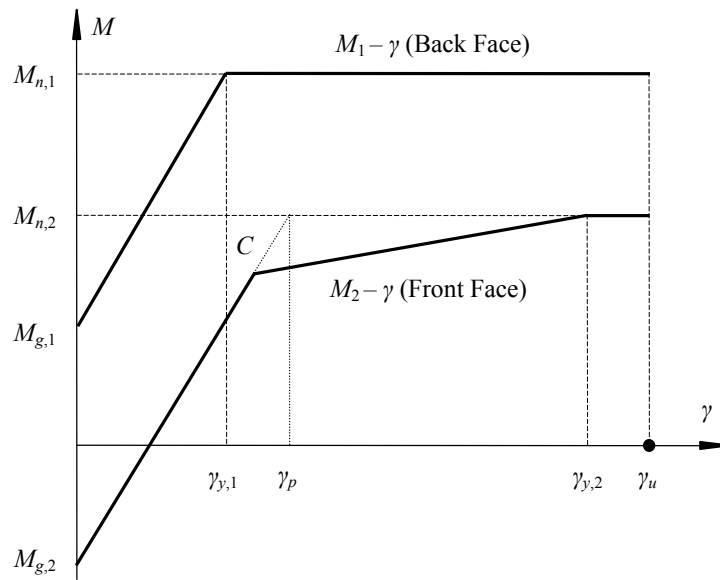


Figure 6.11: Inelastic models for unbalanced moment resisted by flexure.

### 6.3.2.2 Moment Provided by Shear, $M_{v,1}$ and $M_{v,2}$

The moment produced by gravity shear is calculated as

$$M_{vg,1} = 0.5(c + d)V_{g,1} \quad (6.24)$$

$$M_{vg,2} = 0.5(c + d)V_{g,2} \quad (6.25)$$

Tests indicated that a lightly-reinforced slab-column connection fails in punching after exhibiting general yielding. This implies that, after a certain amount of connection deformation, shear at the bending face of the critical section can be held approximately constant while the connection rotational deformation keeps increasing until punching is initiated at the back face of the critical section. Therefore, a nonlinear relationship was used to model shear,  $V_2$  and  $V_1$ , and the corresponding lateral resistance,  $M_{v,1}$  and  $M_{v,2}$ . Since shear force at a critical section face can not be measured from tests, it was assumed for simplicity that the flexural capacity and the maximum shear are reached simultaneously at a plastic hinge. A bilinear relationship shown in Figure 6.12 was assumed between  $M_{v,1}$  and  $M_{v,2}$  and joint rotation  $\gamma$ .  $M_{vn,1}$  and  $M_{vn,2}$ , the maximum values for  $M_{v,1}$  and  $M_{v,2}$ , were defined by Equations 6.14 and 6.15.

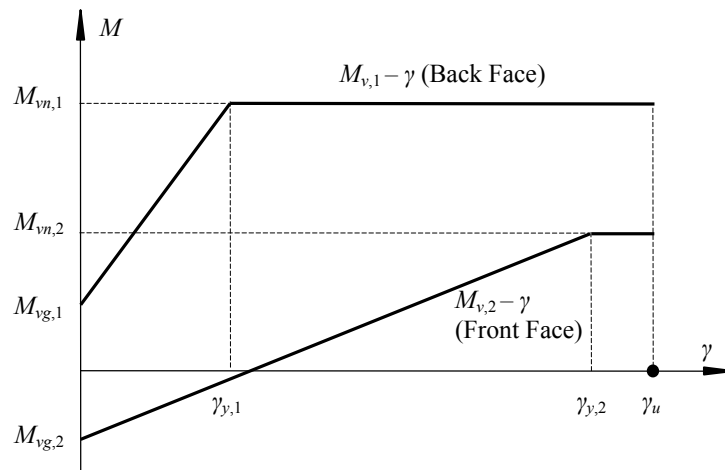


Figure 6.12: Inelastic models for unbalanced moment resisted by shear.

### 6.3.2.3 Combined Resistance from Flexure and Shear

The unbalanced moment resisted by flexural and shear at a plastic hinge can be combined to simplify the analytical model. The combined actions are defined in the following equations and illustrated in Figure 6.13.

$$M_1^* = M_1 + M_{v,1} \quad (6.26)$$

$$M_2^* = M_2 + M_{v,2} \quad (6.27)$$

$$M_{n,1}^* = M_{n,1} + M_{vn,1} \quad (6.28)$$

$$M_{n,2}^* = M_{n,2} + M_{vn,2} \quad (6.29)$$

$$M_{g,1}^* = M_{g,1} + M_{vg,1} \quad (6.30)$$

$$M_{g,2}^* = M_{g,2} + M_{vg,2} \quad (6.31)$$

where  $M_i^*$ ,  $M_{n,i}^*$ , and  $M_{g,i}^*$  ( $i = 1, 2$ ) are referred to as the equivalent moment, equivalent ultimate flexural strength, and equivalent moment induced by gravity load.

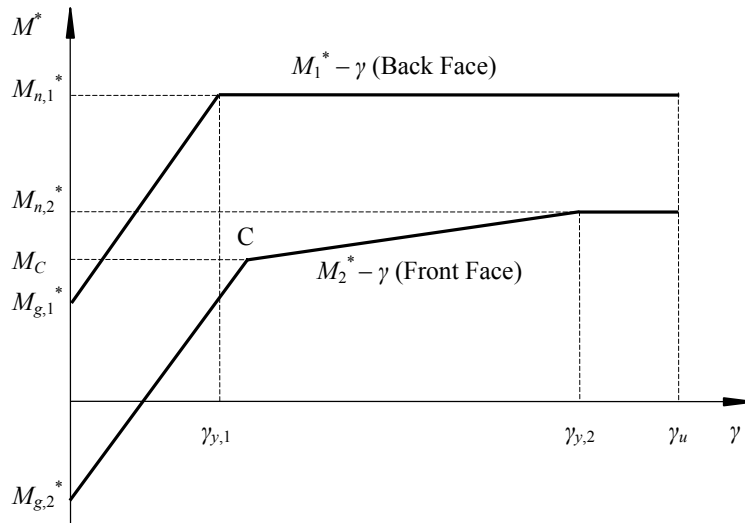


Figure 6.13: Inelastic models for combined lateral resistance from flexure and shear.

Connection lateral stiffness decreases with increased gravity load applied on the slab. Thus, the choice of the intermediate point C in the tri-linear model for positive bending should reflect this trend so that slab softening starts earlier when higher gravity load exists. The  $V_g/V_c$ -ratio has been commonly used as an index of gravity load level.

However, the ratio of  $M_{g,1}$  to  $M_{n,1}$  was considered in this study to define  $M_C$  since it is slab bending that causes slab flexural cracking and reduces the slab stiffness.  $M_C$  is defined herein as

$$M_C = \left( 1 - \frac{M_{g,1}}{M_{n,1}} \right) M_{n,2}^* \quad (6.32)$$

The plastic hinge property is generally specified as a moment-plastic hinge rotation relationship in a nonlinear frame analysis. The relation between the equivalent moment and plastic hinge rotation,  $M^* - \theta$ , for positive and negative bending is illustrated in Figure 6.14. The expressions of  $M_{n,1}^*$ ,  $M_{n,2}^*$ , and  $M_C$  have been given previously, whereas the rotational stiffness,  $K$ , of the plastic hinge under positive bending was calibrated from test data, as discussed in Section 6.3.5.

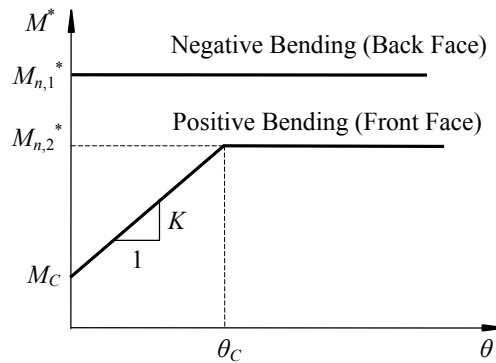


Figure 6.14: Modeling of plastic hinge properties.

For the elastic beam between two plastic hinges,  $I_0$  expressed in Equation 6.33 can not be directly used to define the moment of inertia, because the slab stiffness characteristics and the resistance provided by shear must be considered. An equivalent moment of inertia, denoted as  $I^*$ , was calibrated using test data, as discussed later in Section 6.3.5.

$$I_0 = \frac{1}{12}(c + d)h^3 \quad (6.33)$$

### 6.3.3 Model for Torsion

As shown in Figure 6.15, the nonlinearity of torsion was modeled by a bilinear relationship between total torsional resistance from two side faces of the critical section,  $2T$ , and joint rotation,  $\gamma$ .

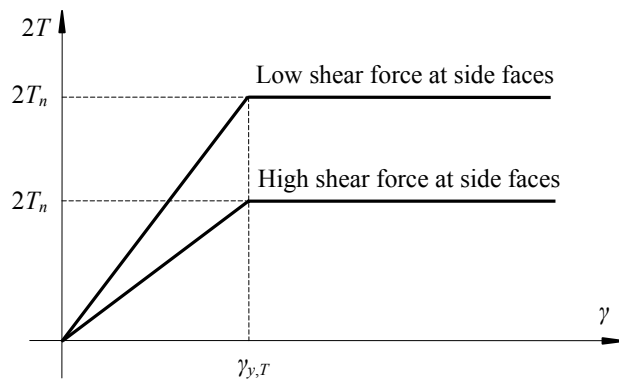


Figure 6.15: Inelastic modeling for torsion.

Based on monotonic loading tests carried out by Kanoh and Yoshizaki (1979),  $\gamma_{y,T}$ , the joint rotation at which idealized torsional yielding occurs, could be defined approximately at 0.01 radian and this value was largely independent of the reinforcement ratio. It can be expected however that stiffness degradation due to cyclic loading may postpone torsional yielding. In addition,  $\gamma_{y,T}$  could be a function of other variables such as gravity load level and test boundary conditions. Since such test data are not available, a constant value of  $\gamma_{y,T}$  was assumed and determined from tests to reflect the torsional stiffness.

### 6.3.4 Summary of Nonlinear Modeling

The effects of gravity load on connection behavior are reflected by the proposed nonlinear models and illustrated in Figure 6.16.

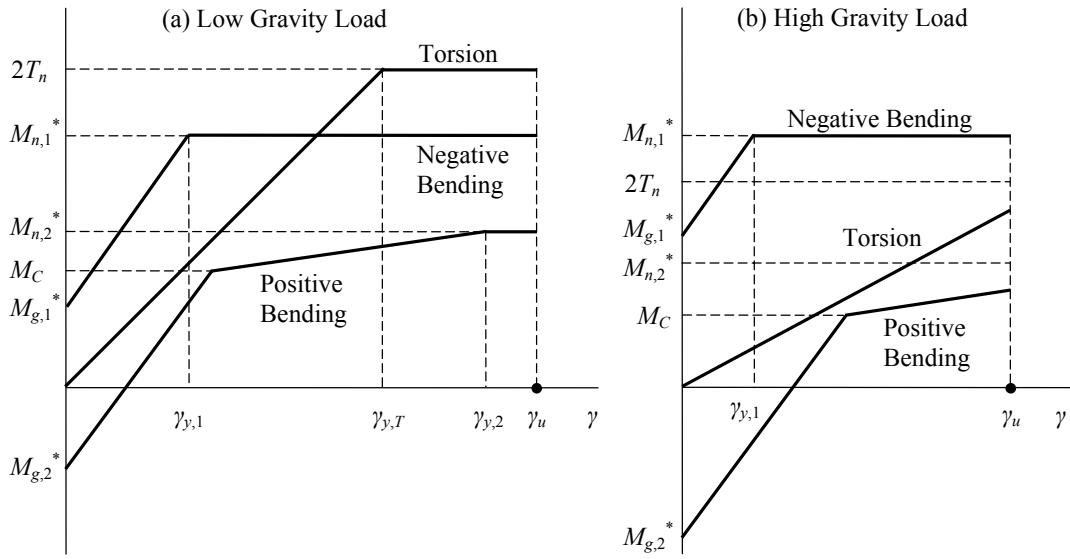


Figure 6.16: Gravity load effect on connection inelastic behavior.

First, based on Equation 6.23, higher gravity load reduces the torsional capacity and thus, as shown in Figure 6.15, reduces the torsional stiffness because yielding was assumed to occur at a constant joint rotation. Second, under lower gravity load,  $M_{n,1}^*$ ,  $M_{n,2}^*$ , and the torsional capacity,  $2T_n$ , can be achieved before connection fails in punching. In contrast, higher gravity load introduces higher  $M_g^*$ , which requires less unbalanced moment to develop  $M_{n,1}^*$  at the back face but larger unbalanced moment to reach  $M_{n,2}^*$  at the front face. Since the connection rotational capacity,  $\gamma_u$ , is reduced by increased gravity load, it is likely that only  $M_{n,1}^*$  representing the resistance from flexure and shear at the back face of the critical section can be developed. Accordingly,

the connection fails in a non-ductile manner without exhibiting general yielding in a load-drift response envelope.

### **6.3.5 Calibration of Stiffness Parameters, $I^*$ , $\gamma_{y,T}$ , and $K$**

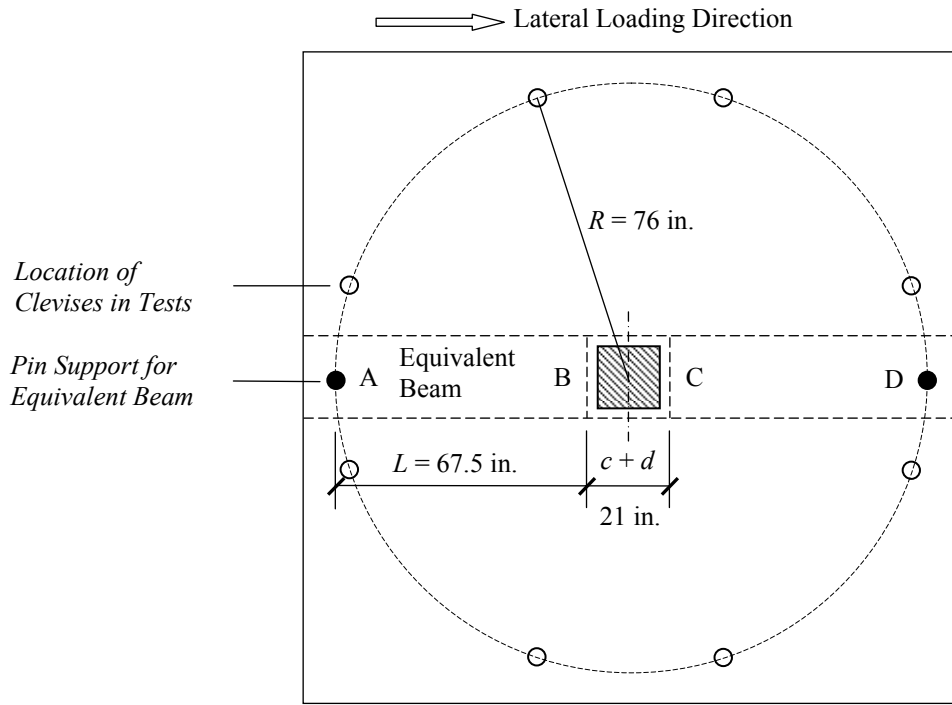
#### ***6.3.5.1 Equivalent Frame Models of Specimens***

The stiffness parameters,  $I^*$ ,  $\gamma_{y,T}$ , and  $K$  were calibrated from the test results of Specimens L0.5, LG0.5, and LG1.0. From the test scheme shown in Figure 2.20 for combined gravity and lateral loading, an equivalent frame model was established, as illustrated in Figure 6.17.

The model contains three components: (1) two equivalent beams AB and CD, (2) a spring element restraining joint rotation, and (3) a column. The equivalent beams are pin-supported at one end (points A and D) and connected to the column by the plastic hinges. Pins were assumed to be located on a circle with a radius of 76 in. measured from the column center to the slab supports where the vertical struts functioning as rollers were located. Based on the slab and column geometry, the length of each equivalent beam,  $L$ , was determined to be 67.5 in.

Joint rotation,  $\gamma$ , was determined from the measured lateral drift and calculated column lateral deflection. Due to the size and the high flexural reinforcement ratio in the column, column deformation of all specimens can be considered to be negligible. The flexural and shear capacities,  $M_{n,1}$ ,  $M_{n,2}$ ,  $V_{n,1}$ , and  $V_{n,2}$ , of L0.5, LG0.5, and L1.0 were calculated from the specimen properties using the formulations given previously. Then  $M_{n,1}^*$ ,  $M_{n,2}^*$ , and  $M_C$  for the plastic hinges of the equivalent beams and torsional strength,  $2T_n$ , for the spring element were determined. The above strength parameters, measured connection rotation at two characteristic loading stages,  $\gamma_{y,1}$  and  $\gamma_{y,2}$ , and other parameters

needed for calibrating stiffness parameters through nonlinear analyses are summarized in Table 6.5.



Plan View of Specimens L0.5, LG0.5, and LG1.0 (Lateral Loading)

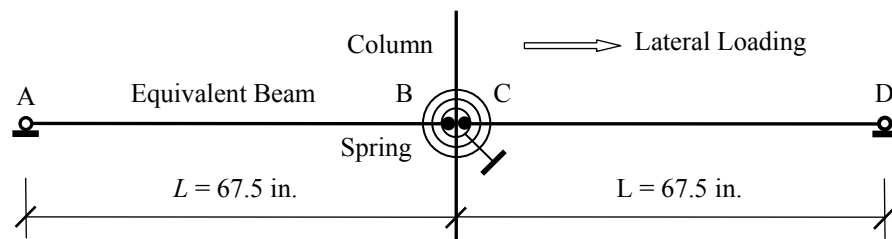


Figure 6.17: Equivalent beam model for test specimens (lateral loading).

Table 6.5: Data for Calibrating Stiffness Parameters

Parameters Needed for Analysis		L0.5	LG0.5	L1.0
Calculated Values	$I_0$ (in <sup>4</sup> )	378	378	378
	$V_{n,1}$ (kip)	19.4	20.4	23.2
	$V_{n,2}$ (kip)	14.0	15.3	13.7
	$M_{n,1}$ (k-in)	178	175	308
	$M_{n,2}$ (k-in)	96	101	89
	$2T_n$ (k-in)	548	549	727
	$M_{n,1}^*$ (k-in)	382	390	551
	$M_{n,2}^*$ (k-in)	242	261	232
	$M_C$ (k-in)	99	75	147
	$M_{g,1} = -M_{g,2}$ (k-in)	105	125	113
	$V_{g,1} = -V_{g,2}$ (kip)	5.88	6.70	6.03
	$M_{g,1}^* = -M_{g,2}^*$ (k-in)	167	195	176
	Measured Values	$V_g$ (kip)	23.5	26.8
$\gamma_{y,1}$ (rad.)		0.0049	0.0048	0.0048
$\gamma_{y,2}$ (rad.)		0.015	0.015	0.015
$\gamma_u$ (rad.)		-	-	0.02

### 6.3.5.2 Joint Rotation at Torsional Yielding, $\gamma_{y,T}$

The measured steel strains indicated that top flexural reinforcement of L0.5, LG0.5, and LG1.0 reached yielding under negative bending at 0.5% lateral drift. As shown in Figure 3.7, the response envelopes for these specimens after 0.5% drift are almost parallel to each other. Given that torsion contributed a significant portion (47%) of the lateral load resistance and the layout of bottom reinforcement carrying positive bending was identical for these specimens, torsional yielding in the model should not occur before 1.25% drift, at which point combined loading for Specimens LG0.5 and LG1.0 was stopped. Moreover, the peak lateral load was achieved in L0.5 at 1.5% drift, indicating that torsional yielding should occur no later than 1.5% drift in the pushover analysis. Thus, the joint rotation at torsional yielding,  $\gamma_{y,T}$  was assumed as

$$\gamma_{y,T} = 0.015 \quad (6.34)$$

The above value is coincidentally equal to the joint rotation at which bottom reinforcement yielded and the peak lateral load was reached in Specimen L0.5.

### 6.3.5.3 Equivalent Moment of Inertia, $I^*$ , and Positive Bending Stiffness Parameter, $K$

Step-by-step nonlinear analyses were carried out for Specimens L0.5, LG0.5, and LG1.0. Experimental results from these tests were processed to calibrate the stiffness parameters,  $I^*$  and  $K$ , based on the criterion that the response of an equivalent frame under monotonic loading can mimic the response envelope of specimens at two characteristic points shown in Figure 6.18: (1) Point A, yielding under negative bending that occurred at joint rotation  $\gamma_{y,1}$  and (2) Point B, maximum unbalanced moment that occurred when the flexural capacity for positive bending was reached at  $\gamma_{y,2}$ . Joint rotation is defined in Figure 6.10. The values of  $I^*$  and  $K$  of three specimens were calculated at these two loading stages and then the formulations for  $I^*$  and  $K$  were generalized for connections with different properties.

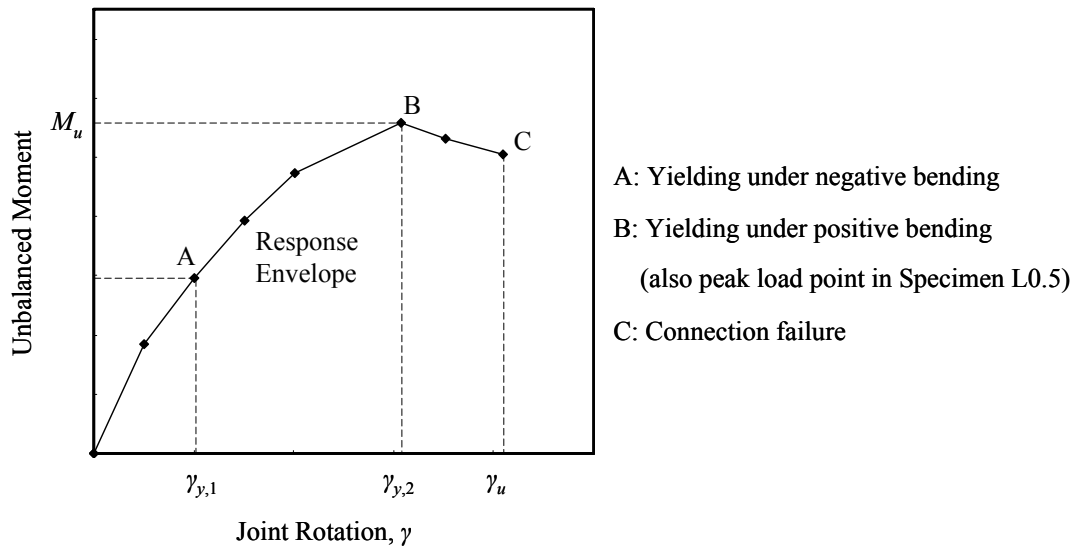


Figure 6.18: Characteristic points used to calibrate stiffness parameters.

### **Gravity Loading**

Due to symmetry, the initially applied gravity load results in no joint rotation, i.e.,  $\gamma = 0$ . The moment and shear induced by gravity load at the critical section,  $M_{g,1}$ ,  $M_{g,2}$ ,  $V_{g,1}$ , and  $V_{g,2}$ , were determined from inelastic finite element analyses using 8-node shell elements with reduced integration for the slab and smeared concrete cracking for concrete. The analysis results are presented in Table 6.5.

### **Lateral Loading until Yielding Due to Negative Bending at Plastic Hinge B**

After applying lateral load, the increase of negative moment at hinge point B between the two loading stages, gravity loading and negative yielding, is expressed as

$$\Delta M_{BA} = M_{n,1}^* - M_{g,1}^* = \frac{3EI^* \Delta\gamma}{L} = \frac{3EI^* \gamma_{y,1}}{L} \quad (6.35)$$

Thus, the equivalent moment of inertia is determined as

$$I^* = \frac{(M_{n,1}^* - M_{g,1}^*)L}{3E\gamma_{y,1}} \quad (6.36)$$

The results of  $I^*$  for three specimens based on the above equation are given in Table 6.6.

Table 6.6: Calibration of Equivalent Moment of Inertia

Specimen	$\gamma_{y,1}$	$I^*$ (in <sup>4</sup> )	$\rho_1$ in $c+12d$ (%)	$M_{g,1} / M_{n,1}$	$I^* / I_0$
L0.5	0.0049	276	0.50	0.59	0.73
LG0.5	0.0048	224	0.50	0.71	0.59
LG1.0	0.0048	469	0.76	0.37	1.24

To establish a generalized expression of  $I^*$  for the equivalent beam, the slab tensile reinforcement ratio and gravity load level are considered since tests have indicated

the effects of these two factors on the connection lateral stiffness. The reinforcement ratio denoted as  $\rho_1$  is evaluated in a width  $c+12d$  at the column. Gravity load level is represented by  $M_{g,1}/M_{n,1}$  for the same reason as for formulating  $M_C$ .  $I^*$  was assumed to be a linear function of these variables as expressed by

$$I^* = \left( a + b\rho + c \frac{M_{g,1}}{M_{n,1}} \right) I_0 \quad (6.37)$$

where  $a$ ,  $b$ , and  $c$  are three constants.

From the values of  $I^*$ ,  $M_{g,1}/M_{n,1}$ , and  $\rho_1$  given in Table 6.6,  $a$ ,  $b$ , and  $c$  were uniquely determined and the  $I^*$  was suggested as

$$I^* = \left( 0.9 + 100\rho_1 - 1.2 \frac{M_{g,1}}{M_{n,1}} \right) I_0 \quad (6.38)$$

#### ***Lateral Loading until Yielding Due to Positive Bending at Plastic Hinge C***

$\Delta\gamma^{(1)}$ , the joint rotation between starting lateral loading and reaching positive bending moment  $M_C$  at plastic hinge C (front face of the critical section), can be expressed as

$$\Delta\gamma^{(1)} = \frac{(M_C - M_{g,2}^*)L}{3EI^*} \quad (6.39)$$

Once  $M_C$  is reached, according to the model presented in Figure 6.14, the plastic hinge rotates with a rotational stiffness of  $K$ . As the positive bending moment at hinge C increases from  $M_C$  to  $M_{n,2}^*$ , the corresponding increment of joint rotation is

$$\Delta\gamma^{(2)} = (M_{n,2}^* - M_C) \left( \frac{L}{3EI^*} + \frac{1}{K} \right) \quad (6.40)$$

From Equations 6.39 and 6.40, the joint rotation at yielding of plastic hinge under positive bending is determined as

$$\gamma_{y,2} = \Delta\gamma^{(1)} + \Delta\gamma^{(2)} = \frac{(M_{n,2}^* - M_{g,2}^*)L}{3EI^*} + \frac{M_{n,2}^* - M_C}{K} \quad (6.41)$$

Thus, the rotational stiffness  $K$  can be derived as

$$K = \frac{M_{n,2}^* - M_C}{\gamma_{y,2} - \frac{(M_{n,2}^* - M_{g,2}^*)L}{3EI^*}} \quad (6.42)$$

Introducing a parameter,  $k$ , to reflect the gravity load effect, it was assumed that  $K$  can be generalized as

$$K = k \left( \frac{EI_0}{d} \right) \quad (6.43)$$

As the gravity load applied on the connection reduces to zero,  $M_{g,1}$  vanishes. Consequently, according to Equation 6.32,  $M_C$  should inversely increase to  $M_{n,2}^*$  and an elastic-perfectly plastic behavior of plastic hinge would result. It is noted that, as the gravity load decreases to zero, so should  $K$ . The gravity load effect was taken into account by expressing  $k$  in Equation 6.43 as a function of the  $M_{g,1}/M_{n,1}$  ratio.

Linear interpolation of the measured steel strains in LG0.5 and LG1.0 at 0.75% and 1.25% drift indicates that the bottom reinforcement would likely yield at a joint rotation of  $\gamma_{y,2} = 0.015$ . The values of  $k$  were determined from Equations 6.42 and 6.43 as 0.10 for L0.5, 0.16 for LG0.5, and 0.032 for LG1.0. Based on the above data and the corresponding values of  $M_{g,1}/M_{n,1}$ , an expression of  $k$  shown in Equation 6.44 was determined from data fitting. The resulting expression of  $K$  is given in Equation 6.45.

$$k = 0.5 \left( \frac{M_{g,1}}{M_{n,1}} \right)^3 \quad (6.44)$$

$$K = 0.5 \left( \frac{M_{g,1}}{M_{n,1}} \right)^3 \left( \frac{EI_0}{d} \right) \quad (6.45)$$

### Connection Failure

Since yielding due to negative bending occurred at  $\gamma_{y,1} = 0.005$  in L0.5 and the maximum joint rotation was achieved at  $\gamma_u = 0.02$ , the plastic hinge rotation under negative bending was determined as  $\theta_{u,1} = 0.015$ . This deformation capacity is close to the maximum allowable plastic hinge rotation specified in FEMA 356 for a slab-column frame that has continuous bottom reinforcement at the columns and functions as a primary structural component for Collapse Prevention performance level.

#### 6.3.5.4 Response of Specimens L0.5 and LG 1.0 Based on Proposed Model

The unbalanced moment versus joint rotation response based on the described model is plotted against the response envelope curve for Specimens L0.5 and LG1.0 in Figure 6.19.

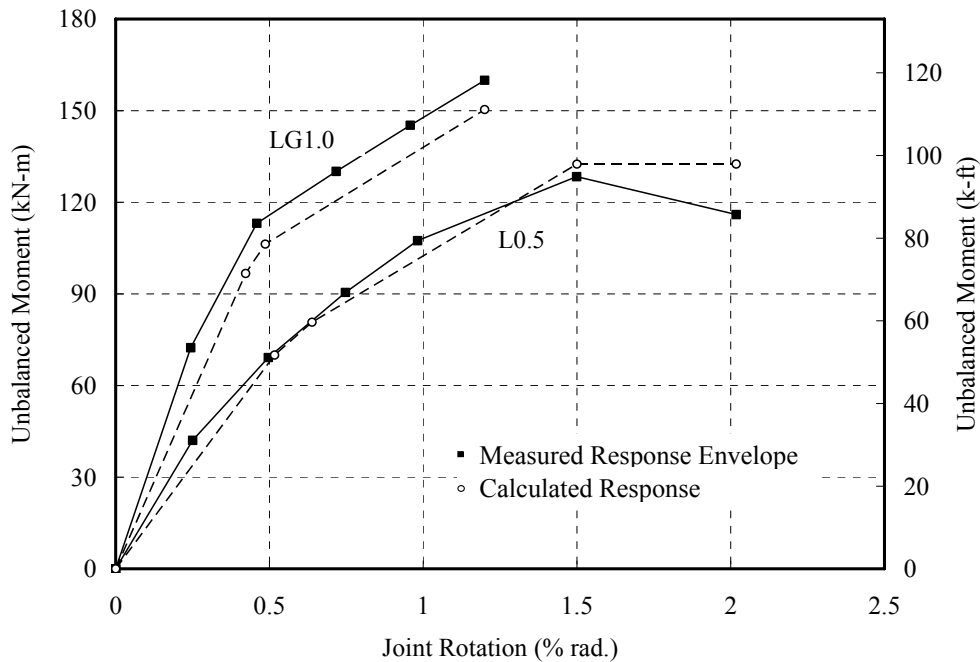


Figure 6.19: Comparison of analytical and experimental results (L0.5 and LG1.0).

Note that the stiffness parameter  $\gamma_{y,T}$  was determined for torsion solely based on the test data of Specimens L0.5. In addition,  $I^*$  and  $K$  were determined from tests of L0.5, LG0.5, and LG1.0 at different loading stages for negative bending and positive bending, respectively. Even though the stiffness parameters were calibrated from these tests, the comparison between the calculated and measured response still can be used to assess the suggested model because the unbalanced moment is resisted by the resultant action of torsion, negative bending, and positive bending moment at a connection. As shown in Figure 6.19, reasonable agreement between the calculated and measured response was achieved. Further validation of the proposed model is presented in Section 6.3.7.

### 6.3.6 Summary of Analysis Procedures

The proposed inelastic model for interior slab-column connections is illustrated by an equivalent planar frame in Figure 6.20, where the necessary strength and stiffness parameters for the beam and spring elements are summarized.

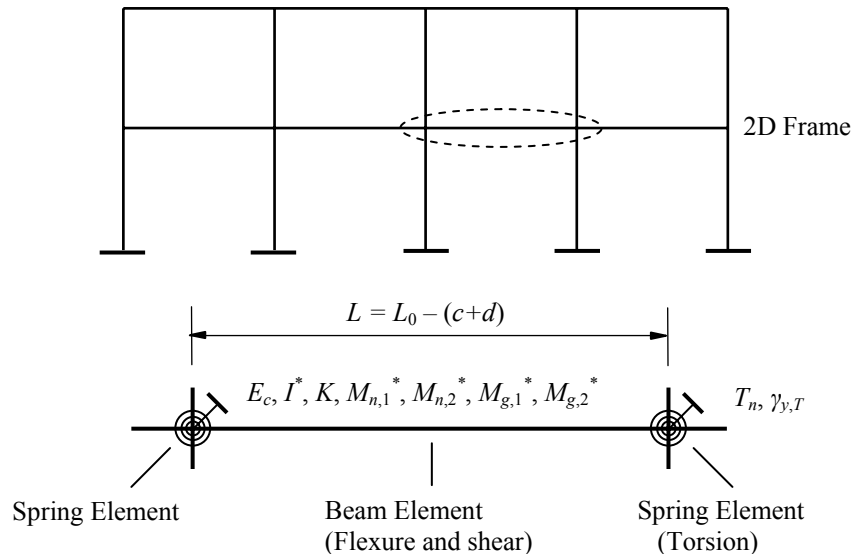


Figure 6.20: 2D frame model and input data for strength and stiffness parameters.

The suggested analytical procedures for interior slab-column connections in a pushover analysis are summarized as follows:

- (1) Determine the length  $L$  and  $I_0$  for the equivalent beam element from slab-column connection geometry.
- (2) From analysis, determine the moment and shear due to gravity load,  $M_{g,1} = -M_{g,2}$  and  $V_{g,1} = -V_{g,2}$ . Calculate  $M_{vg,1}$  and  $M_{vg,2}$  according to Equations 6.24 and 6.25.

$$M_{vg,1} = 0.5(c + d)V_{g,1} \quad (6.24)$$

$$M_{vg,2} = 0.5(c + d)V_{g,2} \quad (6.25)$$

- (3) From Equations 6.10, 6.11, 6.14, and 6.15 calculate the maximum lateral resistance from flexure and shear at the bending faces of the critical section including  $M_{n,1}$ ,  $M_{n,2}$ ,  $M_{vn,1}$ , and  $M_{vn,2}$ .

$$M_{n,1} = A_{s,1}f_{y,1}d_1 \frac{(c + d)}{s_1} \left( 1 - 0.59 \frac{A_{s,1}f_{y,1}}{s_1 d_1 f_c'} \right) \quad (6.10)$$

$$M_{n,2} = A_{s,2}f_{y,2}d_2 \frac{(c + d)}{s_2} \left( 1 - 0.59 \frac{A_{s,2}f_{y,2}}{s_2 d_2 f_c'} \right) \quad (6.11)$$

$$M_{vn,1} = V_{n,1} \left( \frac{c + d}{2} \right) \quad (6.14)$$

$$M_{vn,2} = V_{n,2} \left( \frac{c + d}{2} \right) \quad (6.15)$$

- (4) Calculate strength parameters for the plastic hinge of the equivalent beam element including  $M_{n,1}^*$ ,  $M_{n,2}^*$ , (Equations 6.28 and 6.29), and  $M_C$  (Equation 6.32).

$$M_{n,1}^* = M_{n,1} + M_{vn,1} \quad (6.28)$$

$$M_{n,2}^* = M_{n,2} + M_{vn,2} \quad (6.29)$$

$$M_C = \left(1 - \frac{M_{g,1}}{M_{n,1}}\right) M_{n,2}^* \quad (6.32)$$

- (5) Calculate the equivalent moment due to gravity load at plastic hinge,  $M_{g,1}^*$  and  $M_{g,2}^*$  (Equations 6.30 and 6.31).

$$M_{g,1}^* = M_{g,1} + M_{vg,1} \quad (6.30)$$

$$M_{g,2}^* = M_{g,2} + M_{vg,2} \quad (6.31)$$

- (6) Calculate the total torsional capacity at the two side faces of critical section,  $2T_n$ , based on Equation 6.23.

$$T_n = \left(1 - \frac{V_g - V_{n,1} + V_{n,2}}{2V_{n,1}}\right) T_0 \quad (6.23)$$

- (7) Define  $\gamma_{y,T} = 0.015$  and calculate the equivalent moment of inertia,  $I^*$  (Equation 6.38), and rotational stiffness of plastic hinge under positive bending,  $K$  (Equation 6.45).

$$I^* = \left(0.9 + 100\rho_1 - 1.2 \frac{M_{g,1}}{M_{n,1}}\right) I_0 \quad (6.38)$$

$$K = 0.5 \left(\frac{M_{g,1}}{M_{n,1}}\right)^3 \left(\frac{EI_0}{d}\right) \quad (6.45)$$

- (8) According to the stiffness and strength parameters determined in the previous steps, construct the nonlinear constitutive relation (backbone curve) for flexure and torsion, as shown in Figures 6.14 and 6.15.

- (9) Conduct pushover analysis.

### **6.3.7 Verification for the Suggested Analytical Model**

#### ***6.3.7.1 Description of Tests for Verification***

Using the proposed model, gravity loads may significantly affect (1) torsional strength and stiffness, (2) equivalent moment of inertia for beam element,  $I^*$ , and (3) rotational stiffness of plastic hinge under positive bending,  $K$ . Thus, to evaluate the suggested model, it is essential that the gravity shear was maintained in the tests used for verification.

In some isolated slab-column connection tests, gravity load was simulated solely by placing additional weights to the slab using a test setup B shown in Figure 1.9. After applying lateral load, slab cracking and softening led to redistribution of the vertical load. As a result, the gravity load transferred from slab to column decreased significantly. In the early slab-column connection tests, cyclic load using a load-control mode was applied at the slab edges while the column was hold in position (scheme A in Figure 1.9). The hysteretic behavior of such specimens, especially the stiffness characteristics could be different from those of a cyclic test controlled by displacement. In addition, since the behavior of exterior slab-column connections was not addressed in this study, the multi-span slab-column specimens, such as those tested by Durrani et al. (1995), could not be used to examine the proposed model. Thus, although 28 specimens subjected to cyclic lateral loads are shown in Table 6.1, only 16 tests provided complete data and were suitable for examining the proposed nonlinear equivalent frame model.

Five tests conducted on isolated interior slab-column connections, as shown in Figure 6.21 were used to assess the appropriateness of the proposed model: Specimens H-5 and H-10 tested by Kanoh and Yoshizaki (1975); 1 and 3 by Pan and Moehle (1992); and C-02 by Stark, Binici, and Bayrak (2005). These specimens were tested using

different boundary conditions and covered a wide range of slab and column geometry, material strength, reinforcement ratio, and gravity load level, as shown in Table 6.7.

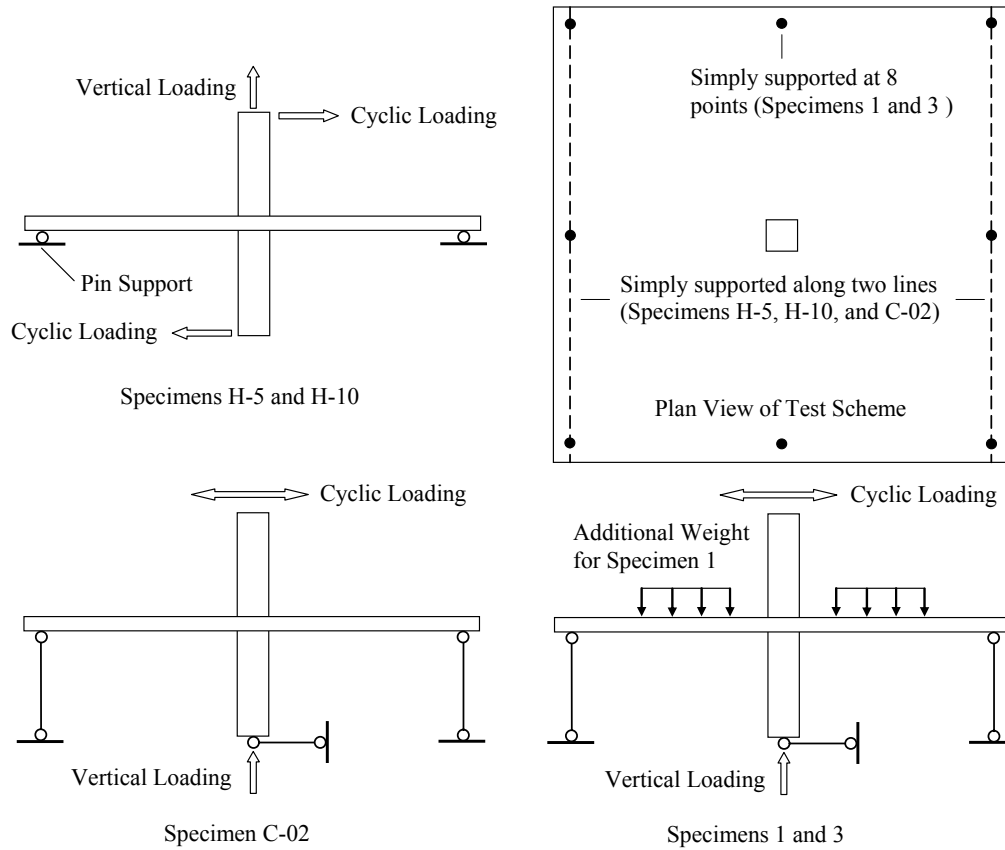


Figure 6.21: Test setups of the Specimens used for verifying the proposed model.

Table 6.7: Properties of Specimens for Examining Suggested Model

Specimen	Slab size (in.)	Slab thickness, $h$ (in.)	Column size, $c$ (in.)	$d$ (in.)	$f'_c$ (psi)	$f_y$ (ksi)	$V_g$ (kips)	$\rho$ in $c+d^*$ (%)	$\rho$ in $c+12d^\dagger$ (%)	$V_g/V_c$
H-5	94.5	3.94	7.87	3.15	3310	52.3	0	0.92 (0.92)	0.70 (0.70)	0
S2	72	3	12	2.38	5090	47.9	0	0.98 (0.98)	1.03 (1.03)	0
3	144	4.8	10.8	4.07	4550	68.4	12	0.86 (0.29)	0.61 (0.24)	0.18
H-10	94.5	3.94	7.87	3.15	3140	49.5	9.88	1.85 (0.98)	1.12 (0.56)	0.32
1	144	4.8	10.8	4.07	4825	68.4	23.3	0.86 (0.29)	0.61 (0.24)	0.35

\* Based on the effective depth for bars along lateral loading direction. Numbers in parentheses are for bottom bars.

† Based on the average effective depth. Numbers in parentheses are for bottom bars.

The slabs of Specimens 1 and 3 were supported on eight struts, which ensured a symmetrical distribution of shear and bending moment at the column under the initially applied gravity load. In the tests for H-5, H-10, and C-02, slabs were simply supported on two slab edges representing the contraflexural lines for the prototype structure under lateral loading while the other edges parallel to the lateral loading direction were unrestrained.

### ***6.3.7.2 Nonlinear Analyses and Results***

The proposed analytical model was applied to the five specimens. Comparison, as shown in Figures 6.22 through 6.24, was made between the calculated connection behavior and response envelopes derived from the test data. Since connection lateral deformation capacity was not investigated in this study, analyses were terminated when joint rotations at which the connections failed in the tests were reached.

Reasonable agreement was achieved between the calculated and measured response. The good correlation can be attributed to: (1) relatively accurate prediction of the strength of connections and (2) appropriate definition of the stiffness parameters that took into account the effects of slab flexural reinforcement ratio and gravity load level.

It should be pointed out that the flexural yielding under negative bending and the reaching of  $M_C$  (the elastic limit) under positive bending usually occur early under lateral loading. Thus, the profile of load-deformation response based on the proposed model may be governed by the torsional stiffness. Because of the limited information, it was assumed that torsion reaches its capacity at a constant joint rotation of  $\gamma_{y,T} = 0.015$ . It appears from Figure 6.22 that, if a  $\gamma_{y,T} = 0.02$  radian was used, the prediction could be improved for Specimens H-5 and H-10 that had thinner slabs compared with other specimens. Hsu (1968) conducted a series of tests on pure torsional capacity of reinforced

concrete rectangular members. The average twisting angle at the peak torques was around 0.08 deg./in. for B series (cross section 15 in. by 10 in., length 122 in.) and 0.13 deg./in. for N series (cross section 12 in. by 6 in., length 86 in.). These results suggest that  $\gamma_{y,T}$  could be a function of the slab thickness.

In addition, the analyses based on the suggested model underestimated the connection stiffness in the initial lateral loading stage. This is expected because the connection behavior was simulated in the model after flexural yielding due to negative bending.

The proposed model provides a means for including slab-column connection response in a general pushover analysis of a structure. As more test data become available, the model can be improved.

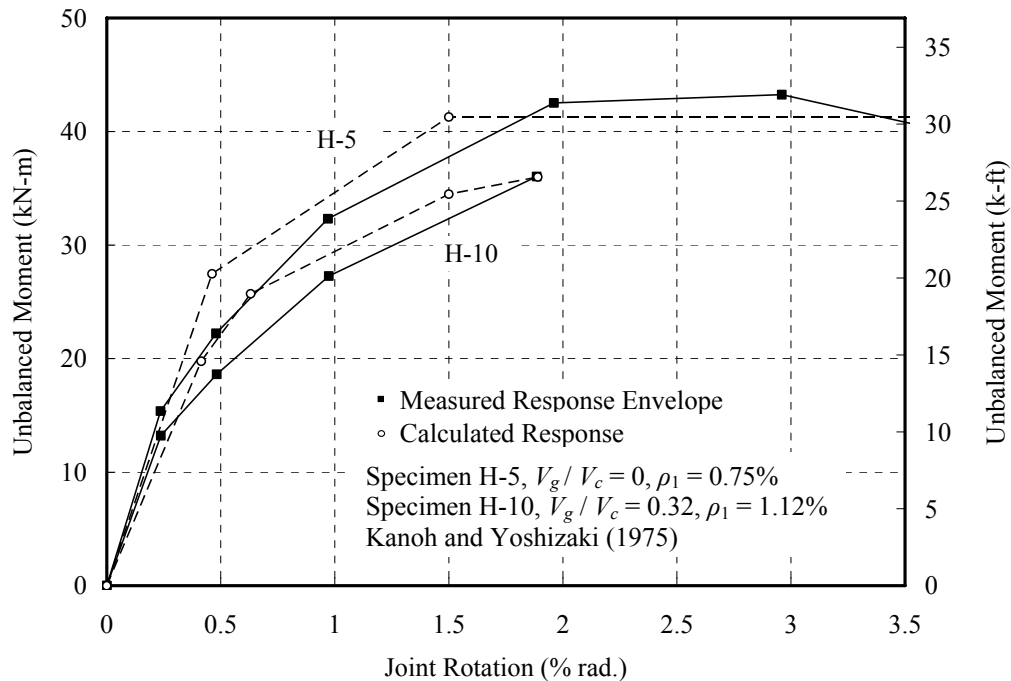


Figure 6.22: Comparison of analytical and experimental results (Specimens H-5 and H-10).

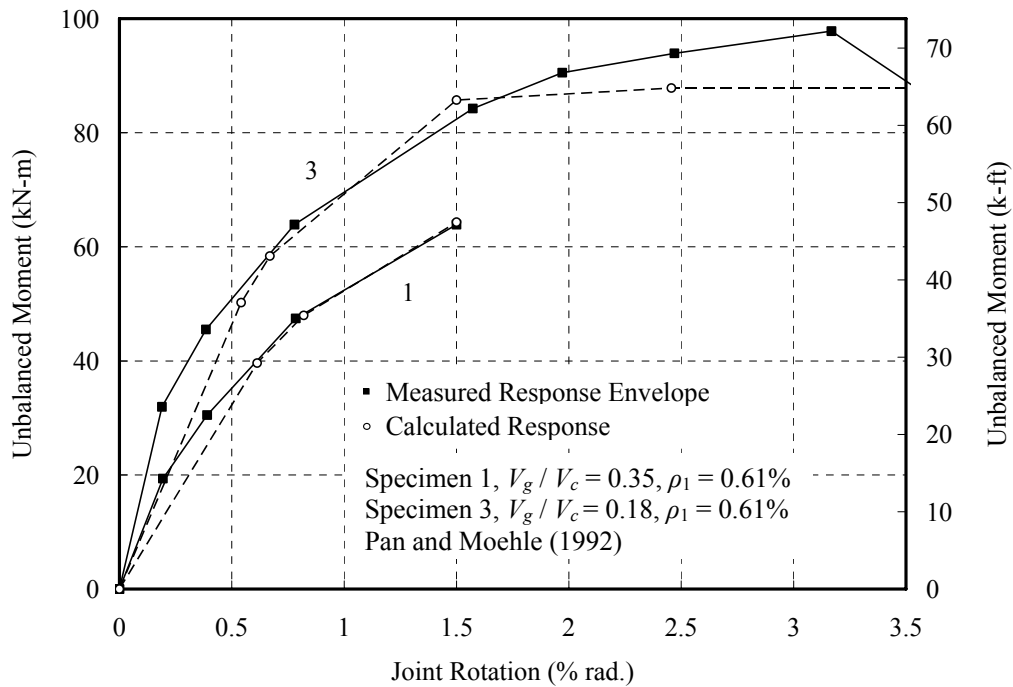


Figure 6.23: Comparison of analytical and experimental results (Specimens 1 and 3).

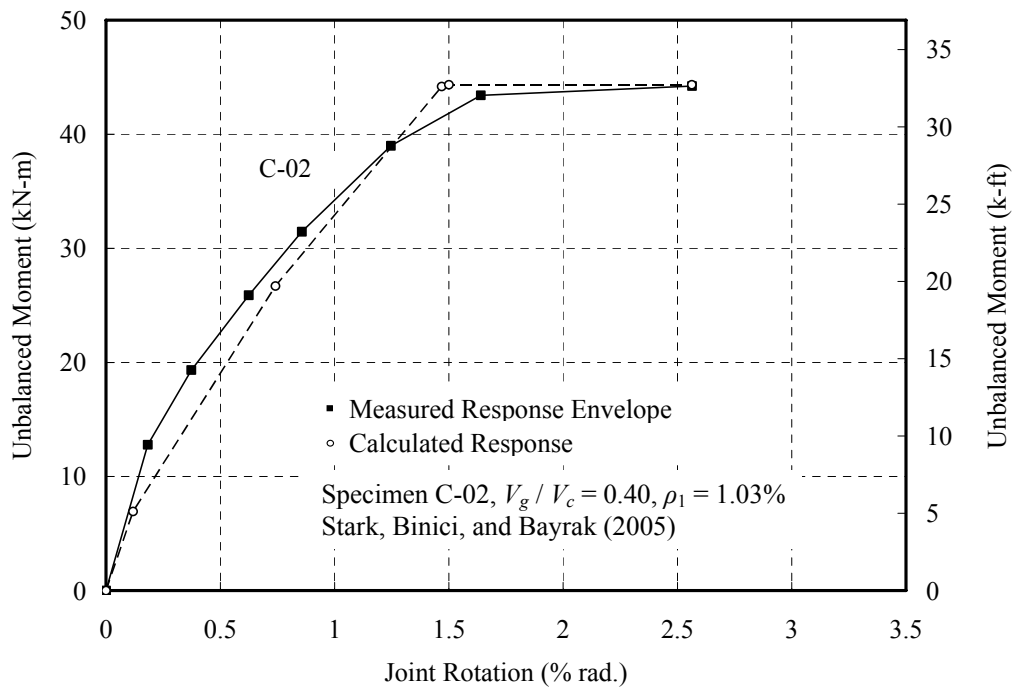


Figure 6.24: Comparison of analytical and experimental results (Specimen C-02).

## Chapter 7

### Summary and Conclusions

#### 7.1 SUMMARY

The investigation presented in this study contained three phases. First, laboratory tests were conducted on five large-scale isolated slab-column connections typical of existing flat-plates. The load histories applied included (1) gravity loading to failure for connections without damage, (2) combined constant gravity loading and cyclic lateral loading to failure, and (3) combined loading to produce damage in the slab (but without failure) followed by vertical loading to failure to investigate the gravity load capacity of earthquake-damaged slab-column connections.

Second, ACI and CEB code equations for connection two-way shear strength were examined using available test data. Effects of slab flexural reinforcement, concrete strength, critical section location, slab aspect ratio ( $c/d$ -ratio), and slab reinforcement concentration at the column on punching strength of a connection subjected to gravity loading were investigated. An equation that included above parameters was developed for the shear capacity of interior slab-column connections.

Third, an algorithm for estimating lateral strength of lightly-reinforced interior slab-connections that considered the resistance from flexure, shear, and torsion at the critical section was proposed. Using a beam analogy approach, an inelastic behavioral model simulating the response envelopes of slab-column connections subjected to cyclic lateral loading was developed for use in pushover analyses of flat-plates. Test results independent of this study were used to verify the proposed analytical model.

## 7.2 CONCLUSIONS

### 7.2.1 Experimental Results

Based on the observation from tests conducted in this study, the following conclusions for lightly-reinforced slab-column connections were reached:

- (1) The connections failed in punching after extensive flexural yielding under the three types of loading conditions adopted in this study.
- (2) The connection shear capacity and lateral stiffness were significantly higher in specimens with a higher reinforcement ratio.
- (3) The damage to slab concrete near the column under cyclic load up to 1.25% drift did not reduce the connection gravity load-carrying capacity. However, seismic damage significantly reduced the connection stiffness.
- (4) Concrete splitting along the top reinforcement led to connection punching failure and thus the exhaustion of slab deformation capacity.
- (5) Connections subjected to gravity loads and combined gravity and lateral loading experienced the same local slab rotational deformation at punching failure.

### 7.2.2 Shear Strength of Slab-Column Connections

Analyses of available test data of interior slab-column connections subjected to concentric gravity loading indicated that:

- (1) The capacity of slab-column connections estimated using ACI 318-05 two-way shear design equations varied remarkably from the test results. ACI code provisions for two-way shear strength do not appear to be appropriate for evaluating the gravity load capacity of lightly-reinforced connections.
- (2) Contribution of concrete strength was best described by assuming connection punching capacity to be proportional to  $(f_c')^{0.25}$  instead of  $\sqrt{f_c'}$ .

- (3) Amount and strength of slab tensile reinforcement and  $c/d$ -ratio significantly affected the connection strength.

Based on regression analyses, an equation was developed to estimate gravity load capacity of interior slab-column connections and was used to estimate the maximum shear that can be developed for a connection subjected to lateral loading.

### **7.2.3 Modeling of Behavior of Slab-Column Connections Subjected to Lateral Loads**

Applying ACI 318-05 design equations to specimens transferring both gravity shear and unbalanced moment indicated that lateral strength of most connections tested was greater than estimated using code procedures. The equations are conservative for design but may be too conservative for use in evaluation of existing flat-plate structures thereby making structural retrofit more costly and less feasible.

This study provided an alternate approach for evaluating lateral strength of lightly-reinforced interior slab-column connections. In the proposed strength model, (1) the unbalanced moment resisted by shear at the critical sections was related to the punching capacity defined earlier in this study, and (2) lateral resistance from torsion with and without the presence of gravity load was defined based on the test data.

A 2D nonlinear frame model for interior slab-column connections for use in pushover analyses was studied with the objective that the response under monotonic loading can be used to simulate and bound the connection behavior under cyclic loads. The lateral resistance from flexure and shear was modeled by an equivalent beam and the resistance from torsion by a spring element. The effects of gravity load and slab flexural reinforcement ratio on connection stiffness degradation were considered and the associated parameters were calibrated from three tests. The effectiveness of the suggested analytical model was validated using test results independent of those used to calibrate the model developed in this study.

### 7.3 SUGGESTIONS FOR FUTURE RESEARCH

The following is recommended for future research:

- (1) Further experimental studies on slab-column connections subjected to lateral loads. Since connection punching failure could be associated with concrete splitting, the connection rotational capacity as a function of the thickness of clear concrete cover and reinforcement ratio and spacing at the vicinity of the column should be investigated. In addition, effects of other variables including column geometry and lateral loading history on connection deformation capacity should also be studied. More instrumentation is suggested to measure the slab rotational deformation at the inclined cracks and to identify the concrete splitting due to the doweling effects of the top reinforcement.
- (2) Extension of the proposed beam model to exterior slab-column connections for use in pushover analyses of flat-plate structures.
- (3) Experimental research on slab-column connections supported on columns with various shapes and subjected to cyclic lateral loads. There are little test data on such cases but they are often used in slab systems.
- (4) Development of a better model for strength of slab-column connections subjected to gravity load. The model should describe the doweling effect provided by the slab tensile reinforcement, shear resisted by bottom reinforcement, and the effect of concrete splitting along top bars.
- (5) Two-way shear strength of connections exposed to fire. The connection fire resistance as a function of slab flexural reinforcement, thickness of concrete cover, and fire temperature and duration can be investigated.

## Appendix A

### Crack Pattern of Specimen L0.5

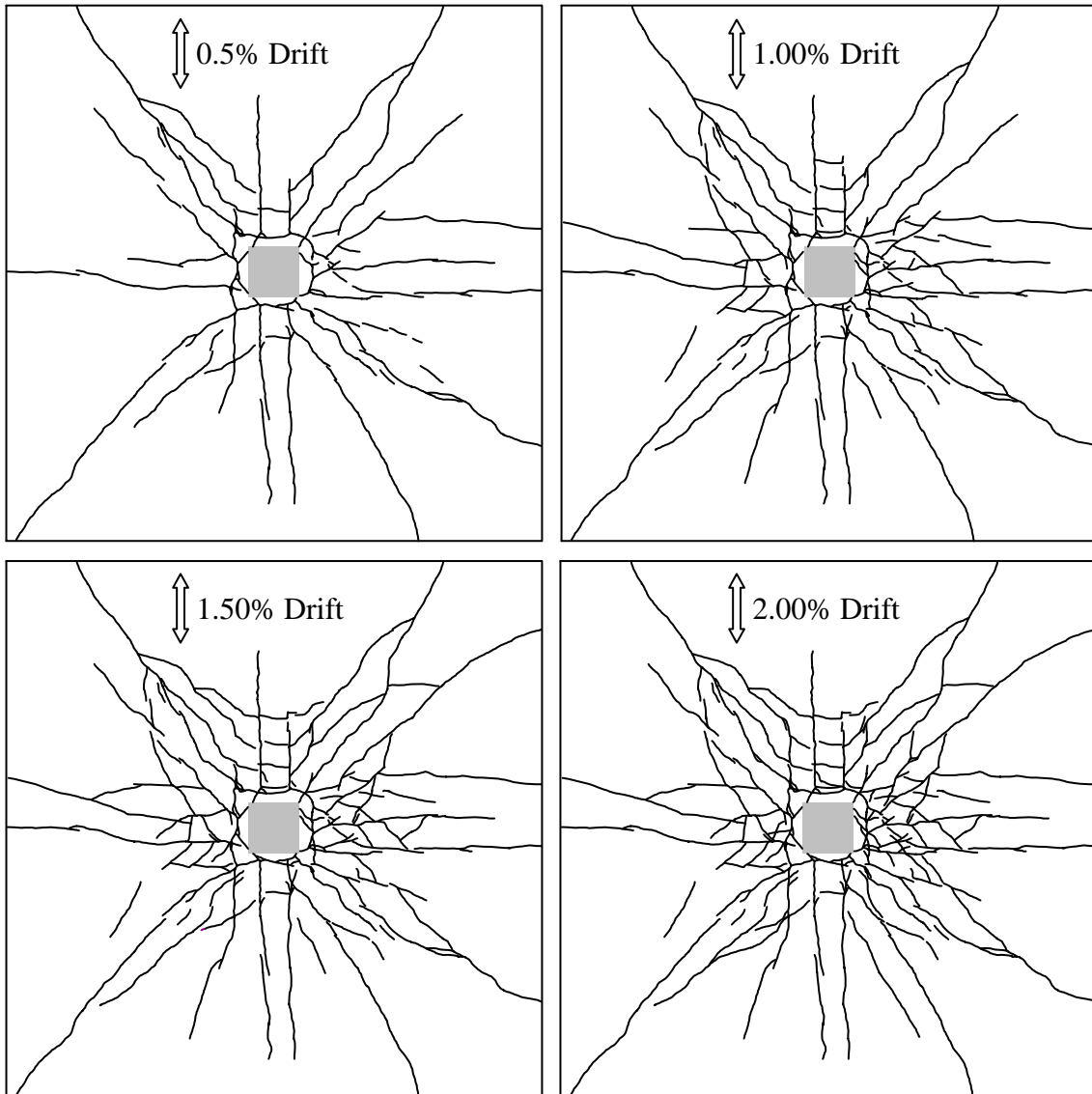


Figure A.1: Top cracking pattern of Specimen L0.5.

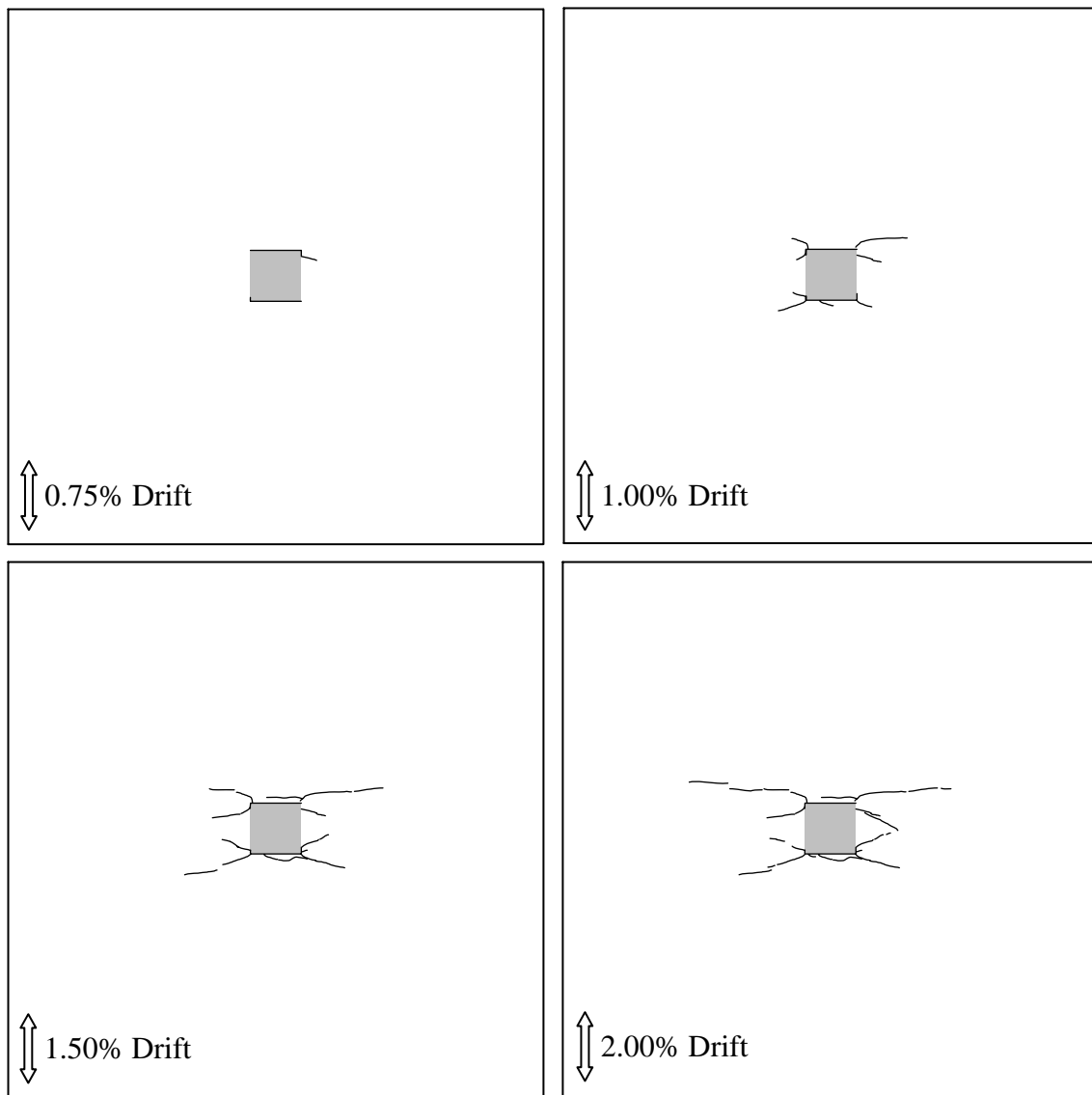


Figure A.2: Bottom cracking pattern of Specimen L0.5.

## Appendix B

### Failure Pattern of Specimens LG0.5 and LG1.0

The Failure patterns and the exposed failure surfaces of Specimen LG0.5 and LG1.0 are presented in Figures B.1 through B.4. These specimens had experienced a lateral drift level of 1.25% before the residual pinching capacity was tested. During the combined gravity and lateral loading, the lateral deformation reversals were applied in the North-South direction. In the following figures, the south side of column was labeled by “S” and the east side of column by “E”.



Figure B.1: Failure pattern of Specimen LG0.5.



Figure B.2: Failure surface of Specimen LG0.5.



Figure B.3: Failure pattern of Specimen LG1.0.



Figure B.4: Failure surface of Specimen LG1.0.

## Appendix C

### Database for Evaluating Punching Strength of Interior Slab-Column Connections

No.	Source	Specimen	$h$ (mm)	$c$ (mm)	$d$ (mm)	$\rho$ (%)	$f_y$ (MPa)	$f_c'$ (MPa)	$V_u$ (KN)
1	Elstner and Hognestad (1956)	A-1a	152	254	118	1.15	332	14.1	302
2		A-1b	152	254	118	1.15	332	25.2	365
3		A-1c	152	254	118	1.15	332	29.0	356
4		A-1d	152	254	118	1.15	332	36.8	351
5		A-1e	152	254	118	1.15	332	20.3	356
6		A-2a	152	254	114	2.47	321	13.7	334
7		A-2b	152	254	114	2.47	321	19.5	400
8		A-2c	152	254	114	2.47	321	37.5	467
9		A-4	152	356	118	1.15	332	26.1	400
10		A-5	152	356	114	2.47	321	27.8	534
11		A-7b	152	254	114	2.47	321	27.9	512
12		A-9*	152	254	114	2.48	321	29.9	445
13		A-10*	152	356	114	2.47	321	29.7	489
14		A-13	152	356	121	0.55	294	26.2	236
15		B-1	152	254	114	0.50	324	14.2	178
16		B-2	152	254	114	0.50	321	47.6	200
17		B-4	152	254	114	0.99	303	47.7	334
18		B-9	152	254	114	2.00	341	43.9	505
19	Moe (1961)	S1-60	152	254	114	1.06	399	23.3	389
20		S2-60*	152	254	114	1.15	399	22.1	356
21		S3-60*	152	254	114	1.18	399	22.6	364
22		S4-60*	152	254	114	1.22	399	23.8	334
23		S5-60	152	203	114	1.06	399	22.2	343
24		S1-70	152	254	114	1.06	482	24.5	393
25		S3-70*	152	254	114	1.18	482	25.4	378
26		S4-70*	152	254	114	1.22	482	35.2	374
27		S5-70	152	203	114	1.06	482	23.0	378
28		H-1	152	254	114	1.15	328	26.1	371
29		R-2	152	152	114	1.15	328	26.6	311
30	M1A	152	305	114	1.50	481	20.8	433	
31	Corley and Hawkins (1968)	AN-1	146	254	111	1.52	403	18.7	334
32		BN-1	146	203	111	1.01	444	20.1	266
33	Swamy and Ali (1982)	S-1	125	150	100	0.56	462	38.9	198
34		S-7	125	150	100	0.74	462	38.9	222
35		S-19	125	150	100	0.37	462	38.9	131
36	Mokhtar et al. (1984)	AB1	150	250	124	1.24	516	36.0	408

Database for Evaluating Punching Strength of Interior Slab-Column Connections  
(Continued)

No.	Source	Specimen	$h$ (mm)	$c$ (mm)	$d$ (mm)	$\rho$ (%)	$f_y$ (MPa)	$f_c'$ (MPa)	$V_u$ (KN)
37	Marzouk and Hussein (1991)	NS1	120	150	95	1.47	490	42.0	320
38		HS1	120	150	95	0.49	490	67.0	178
39		HS2	120	150	95	0.84	490	70.0	249
40		HS7	120	150	95	1.19	490	74.0	356
41		HS3	120	150	95	1.47	490	69.0	356
42		NS2	150	150	120	0.94	490	30.0	396
43		HS5	150	150	120	0.64	490	68.0	365
44		HS6	150	150	120	0.94	490	70.0	489
45		HS8	150	150	120	1.11	490	69.0	436
46		HS9	150	150	120	1.61	490	74.0	543
47		HS11	90	150	70	0.95	490	70.0	196
48		HS12	90	150	70	1.52	490	75.0	258
49		HS14	120	220	95	1.47	490	72.0	498
50		HS15	120	300	95	1.47	490	71.0	560
51		Alexander and Simmonds (1992)	P11S150	155	200	133	0.50	438	33.2
52	P38S150		155	200	106	0.63	438	35.6	264
53	P19S150		155	200	125	0.54	438	26.0	258
54	P19RE		155	200	125	0.54	438	35.3	304
55	P19S75*		155	200	125	0.67	438	26.0	258
56	P19S50*		155	200	125	0.82	438	26.0	319
57	Theodorakopoulos and Swamy (1993)	FS-1	125	150	100	0.56	460	35.4	174
58		FS-8	125	100	100	0.56	460	36.6	150
59		FS-10	125	200	100	0.56	460	36.4	191
60		FS-19	125	150	100	0.37	460	34.5	137
61	Gardner and Shao (1996)	1	140	254	120	0.79	460	21.5	311
62	Marzouk et al. (1996)	N.H.Z.S.1.0	150	250	119	1.00	460	32.2	476
63		N.N.Z.S.1.0	150	250	119	1.00	460	37.2	485
64	Marzouk, and Jiang (1997)	HS17	150	250	120	1.00	490	67.0	511
65	Marzouk et al (1998)	H.H.Z.S.1.0	150	250	119	1.00	460	67.2	512
66	Broms (2000)	9	180	250	150	0.50	500	26.9	408
67		9a	180	250	150	0.50	500	21.0	360
68	McHarg et al. (2000)	NU	150	225	109	1.10	434	30.0	306
69		NB*	150	225	109	1.23	434	30.0	349
70	Osman et al. (2000)	NSNW0.5P	150	250	120	0.50	450	37.8	310
71	Ebead and Marzouk (2002)	C	150	250	109	1.00	435	33.0	412
72	Harajli and Soudki (2003)	SB1	75	100	55	1.07	488	35.5	79
73		SB2	75	100	55	1.50	488	29.1	122
74	Pilakoutas, and Li (2003)	PSS-A	175	200	139	0.72	500	25.8	454
75	Binici and Bayrak (2003)	Control1	152	304	114	1.76	448	28.3	494
76		Control2	152	304	114	1.76	448	28.3	510
77	Ospina et al. (2003)	SR-1	155	250	120	0.87	430	36.8	365

Database for Evaluating Punching Strength of Interior Slab-Column Connections  
(Continued)

No.	Source	Specimen	$h$ (mm)	$c$ (mm)	$d$ (mm)	$\rho$ (%)	$f_y$ (MPa)	$f_c'$ (MPa)	$V_u$ (KN)
78	Ebead and Marzouk (2004)	Ref-0.35%	150	250	114	0.35	450	30.0	250
79		Ref-0.5%	150	250	114	0.50	450	35.0	330
80		Ref-1.0%	150	250	109	1.00	435	36.0	420
81	Li and Chen (2005)	SR1-C1-F0	100	150	70	0.59	482	16.9	104
82		SR1-C2-F0	100	150	70	0.59	482	34.4	124
83		SR2-C1-F0	100	150	70	1.31	482	16.9	146
84		SR2-C2-F0	100	150	70	1.31	482	34.4	226
85	Adetifa and Polak (2005)	SB1	120	150	89	1.20	455	44.0	253
86	This Study	G0.5	152	406	127	0.50	421	31.3	311
87		G1.0*	152	406	127	0.76	421	28.0	407
88	Criswell (1974)	S2075-1	152	254	121	0.79	331	32.5	290
89		S2075-2	152	254	122	0.78	331	29.0	273
90		S2150-1	152	254	124	1.54	331	29.6	463
91		S2150-2	152	254	122	1.56	331	30.1	440
92		S4075-1	152	508	127	0.75	331	26.6	343
93		S4075-2	152	508	124	0.77	331	32.2	330
94		S4150-1	152	508	125	1.52	331	35.4	579
95		S4150-2	152	508	125	1.52	336	35.7	581

**Note:**

- (1) \* denote the specimens with concentrated tensile reinforcement at the column. For these specimens, tensile reinforcement ratio,  $\rho$ , was evaluated in  $c+12d$  centered on the column.
- (2)  $h$  is the slab thickness;  $c$  the column size;  $d$  the average slab effective depth for tensile reinforcement;  $f_y$  is the yield strength of tensile reinforcement;  $f_c'$  concrete compressive strength; and  $V_u$  the measured connection punching strength.

## Appendix D

### Notation

- $A_{s,1}$  = area of top reinforcement
- $A_{s,2}$  = area of bottom reinforcement
- $c$  = size of square column
- $d$  = slab average effective depth
- $d_0$  = distance between the center of top and bottom rebar layers
- $d_1$  = effective depth for top reinforcement under bending
- $d_2$  = effective depth for bottom reinforcement under bending
- $f_c'$  = concrete cylinder compressive strength
- $f_y, f_{y,1}$  = yield strength of slab top reinforcement
- $f_{y,2}$  = yield strength of slab bottom reinforcement
- $h$  = slab thickness
- $I^*$  = equivalent moment of inertia for beam element
- $M_1$  = unbalanced moment resisted by flexure at the back face
- $M_1^*$  = equivalent negative moment for beam element
- $M_2$  = unbalanced moment resisted by flexure at the front face
- $M_2^*$  = equivalent positive moment for beam element
- $M_C$  = moment at an intermediate point  $C$  (elastic limit) for positive bending
- $M_{f,1}$  = flexural capacity for negative bending evaluated in  $c+3h$
- $M_{f,2}$  = flexural capacity for positive bending evaluated in  $c+3h$
- $M_{g,1}$  = bending moment due to gravity load at the back face
- $M_{g,2}$  = bending moment due to gravity load at the front face

- $M_{g,1}^*$  = equivalent moment due to gravity load at the back face  
 $M_{g,2}^*$  = equivalent moment due to gravity load at the front face  
 $M_u$  = unbalanced moment transferred from column to slab  
 $M_{n,1}$  = ultimate strength for  $M_1$   
 $M_{n,1}^*$  = equivalent flexural strength for negative bending  
 $M_{n,2}$  = ultimate strength for  $M_2$   
 $M_{n,2}^*$  = equivalent ultimate flexural strength for positive bending  
 $M_{u,v}$  = unbalanced moment at shear failure (ACI 318-05)  
 $M_{u,f}$  = unbalanced moment at flexural failure (ACI 318-05)  
 $M_{v,1}$  = unbalanced moment resisted by  $V_1$   
 $M_{v,2}$  = unbalanced moment resisted by  $V_2$   
 $M_{vn,1}$  = unbalanced moment resisted by  $V_{n,1}$   
 $M_{vn,2}$  = unbalanced moment resisted by  $V_{n,2}$   
 $s_1$  = average spacing of slab top reinforcement placed in  $c+d$   
 $s_2$  = average spacing of slab bottom reinforcement placed in  $c+d$   
 $T$  = torsion acting on the critical section side faces.  
 $T_0$  = torsional capacity without interaction with shear  
 $T_n$  = torsional capacity with interaction with shear  
 $V_1$  = shear acting on the critical section back face  
 $V_2$  = shear acting on the critical section front face  
 $V_c$  = nominal two-way shear strength (ACI 318-05)  
 $V_{flex}$  = gravity shear at the formation of yield-line mechanism  
 $V_g$  = gravity shear transferred from slab to column  
 $V_{g,1}$  = shear at the critical section back face due to gravity load

- $V_{g,2}$  = shear at the critical section front face due to gravity load  
 $V_n$  = connection nominal punching strength  
 $V_n^{[1]}$  = connection nominal punching strength (when top steel in tension)  
 $V_n^{[2]}$  = connection nominal punching strength (when bottom steel in tension)  
 $V_{n,1}$  = maximum shear at the critical section back face  
 $V_{n,2}$  = maximum shear at the critical section front face  
 $\rho, \rho_1$  = top reinforcement ratio evaluated in  $c+12d$  at the column  
 $\gamma$  = joint rotation  
 $\gamma_f$  = fraction of unbalanced moment transferred by flexure  
 $\gamma_v$  = fraction of unbalanced moment transferred by shear  
 $\gamma_{y,1}$  = joint rotation when  $M_{n,1}$  and  $M_{n,1}^*$  are reached  
 $\gamma_{y,2}$  = joint rotation when  $M_{n,2}$  and  $M_{n,2}^*$  are reached  
 $\gamma_{y,T}$  = joint rotation at torsional yielding  
 $\theta$  = plastic hinge rotation  
 $\theta_C$  = plastic hinge rotation when  $M_C$  is reached  
 $\xi$  = parameter reflecting effect of  $c/d$ -ratio on punching strength

## References

- ABAQUS User's Manual, 2006, ABAQUS Inc.
- Abrams D. 1996. "Effects of Scale and Loading Rate with Tests of Concrete and Masonry Structures," *Earthquake Spectra*, EERI, v.12, No. 1, pp. 13-28.
- ACI Committee 318. 1951. "Building Code Requirements for Reinforced Concrete (ACI 318-51)," American Concrete Institute, Detroit.
- ACI Committee 318. 1956. "Building Code Requirements for Reinforced Concrete (ACI 318-56)," American Concrete Institute, Detroit.
- ACI Committee 318. 1963. "Building Code Requirements for Reinforced Concrete (ACI 318-63)," American Concrete Institute, Detroit.
- ACI Committee 318. 1971. "Building Code Requirements for Reinforced Concrete (ACI 318-71)," American Concrete Institute, Detroit.
- ACI Committee 318. 1989. "Building Code Requirements for Structural Concrete (ACI 318-89)," American Concrete Institute, Farmington Hills, Michigan.
- ACI Committee 318. 2005. "Building Code Requirements for Structural Concrete (ACI 318-05) and Commentary (318R-05)," American Concrete Institute, Farmington Hills, Michigan.
- ACI-ASCE Committee 326 (now 426). 1962. "Shear and Diagonal Tension," *ACI JOURNAL*, Proceedings v. 59, No. 3, pp. 353-396.
- Adetifa, B., and Polak, M. A. 2005. "Retrofit of Slab Column Interior Connections Using Shear Bolts," *ACI Structural Journal*, v.102, No. 2, pp. 268-274.
- Akiyama, H., and Hawkins, N. M. 1984. "Response of Flat Plate Concrete Structures to Seismic and Wind Forces," *Structures and Mechanics Report SM84-1*, Department of Civil Engineering, University of Washington, Seattle, 320 pp.
- Alexander S. D. B., and Simmonds, S. H. 1986. "Shear-Moment Transfer in Column-Slab Connections," *Structural Engineering Report*, No. 141, Department of Civil Engineering, University of Alberta, 95 pp.
- Alexander, S. D. B., and Simmonds, S. H. 1987. "Ultimate Strength of Slab-Column Connections," *ACI Structural Journal*, v.84, No. 3, pp. 225-261.

- Alexander S. D. B., and Simmonds, S. H. 1992. "Punching Shear Tests of Concrete Slab-Column Joints Containing Fiber Reinforcement," *ACI Structural Journal*, v.89, No. 4, pp. 425-432.
- Alexander S. D. B., and Simmonds, S. H. 1992. "Tests of Column-Flat Plate Connections," *ACI Structural Journal*, v. 89, No. 5, pp. 495-502.
- Al-Haddad, M. S., and Wight, J. K. 1986. "Feasibility and Consequences of Moving Beam Plastic Hinging Zones for Earthquake Resistant Design of R/C Buildings," Rep. UMCE 86-1, Department of Civil Engineering, University of Michigan, Ann Arbor.
- American Society of Civil Engineers (ASCE). 2000. "Prestandard and Commentary for the Seismic Rehabilitation of Buildings," FEMA 356, Federal Emergency Management Agency, Washington DC.
- Argudo, J., "Non-Destructive Evaluation of Gravity Load Carrying Capacity and Lateral Load Damage of Reinforced Concrete Slab-Column Connections," PhD dissertation, The University of Texas at Austin, Austin, 2006.
- Bazant, Z. P., and Cao, Z. 1987. "Size Effect in Punching Shear Failure of Slabs," *ACI Structural Journal*, v.84, No. 1, pp. 44-53.
- Binici, B., and Bayrak, O. 2003. "Punching Shear Strengthening of Reinforced Concrete Flat Plates Using Carbon Fiber Reinforced Polymers," *Journal of Structural Engineering*, ASCE, pp. 1173-1182.
- Broms, C. E. 2000. "Elimination of Flat Plate Punching Failure Mode," *ACI Structural Journal*, v. 97, No. 1, pp. 94-101.
- Chen, C., and Li, C. 2005. "Punching Shear Strength of Reinforced Concrete Slabs Strengthened with Glass Fiber-Reinforced Polymer Laminates," *ACI Structural Journal*, v. 102, No. 4, pp. 535-542.
- Comite Euro-International du Beton – Federation International de la Precontrainte (CEB-FIP). 1990. "Model Code 1990," Lausanne, Switzerland, 1990.
- Corley, W. G., and Hawkins, N. M. 1968. "Shearhead Reinforcement for Slabs," *ACI JOURNAL*, Proceedings, v. 65, No. 10, pp. 811-824.
- Criswell, M. E. 1974. "Static and Dynamic Response of Reinforced Concrete Slab-column Connections," *ACI SP-42*, v. 2, pp 721-746.
- Dovich L. M., and Wight J. K. 2005. "Effective Slab Width Model for Seismic Analysis of Flat Slab Frames," *ACI Structural Journal*, v. 102, No. 6, pp. 868-875.

- Durrani, A. J., Du, Y., and Luo, Y. H. 1995. "Seismic Resistance of Nonductile Slab-Column Connections in Existing Flat-Slab Buildings," *ACI Structural Journal*, v. 92, No.4, pp. 479-487.
- Ebead, U., and Marzouk, H. 2002. "Strengthening of Two-way Slabs Using Steel Plates," *ACI Structural Journal*, v. 99, No. 1, pp. 23-31.
- Ebead, U., and Marzouk, H. 2004. "Fiber-Reinforced Polymer Strengthening of Two-way Slabs," *ACI Structural Journal*, v. 101, No. 5, pp. 650-659.
- Elstner, R. C., and Hognestad, E. 1956. "Shearing Strength of Reinforced Concrete Slabs," *ACI JOURNAL*, Proceedings, v. 53, No. 1, pp. 29-58.
- Gardner, N. J., and Shao, X. 1996. "Punching Shear of Continuous Flat Reinforced Concrete Slabs," *ACI Structural Journal*, v. 93, No. 2, pp. 218-228.
- Ghali, A., Elmasri, M. Z., and Dilger, W. 1976. "Punching of Flat Plates under Static and Dynamic Forces," *ACI JOURNAL*, Proceedings v. 73, No. 10, pp. 566-572.
- Ghali, A., and Megally, S., "Stud Shear Reinforcement for Punching: North America and European Practices," Proceedings of the International Workshop on Punching Shear Capacity of RC Slabs, Kungl Tekniska Hogskolan Institute for Bygghonstruktion, Stockholm, Sweden, 2000, pp. 201-209.
- Hanson, N. W., and Hanson, J. M. 1968. "Shear and Moment Transfer between Concrete Slabs and Columns," *Journal of PCA Research and Development Laboratory*, v. 10, No. 1, 16 pp.
- Harajli, M. H., and Soudki, K. A. 2003. "Shear Strengthening of Interior Slab-Column Connections Using Carbon Fiber-Reinforced Polymer Sheets," *Journal of Composites for Construction*, ASCE, v. 7, No. 2, pp. 145-153.
- Hawkins, N. M., Mitchell, D., and Sheu, M. S. 1974. "Cyclic Behavior of Six Reinforced Concrete Slab-Column Specimens Transferring Moment and Shear," Progressive Report 1973-1974, NSF Project GI-38717, Section II, Department of Civil Engineering, University of Washington, Seattle, 50 pp.
- Hsu, T. T. C. 1968. "Torsion of Structural Concrete - Behavior of Reinforced Concrete Rectangular Members," *Torsion of Structural Concrete*, SP-18, American Concrete Institute, Farmington Hills, Michigan, pp. 261-306.
- Hueste, M. B., and Wight J. K. 1999. "Nonlinear Punching Shear Failure Model for Interior Slab-Column Connections," *Journal of Structural Engineering*, ASCE, v. 125, No.9, pp.997-1008.

- Islam, S., and Park, R. 1976. "Tests on Slab-Column Connections with Shear and Unbalanced Flexure," Proceedings, ASCE, v. 102, No. ST3, pp. 549-568.
- Kanoh Y., and Yoshizaki S. 1975. "Experiments on Slab-Column and Slab-Wall Connections of Flat Plate Structures," Concrete Journal, Japan Concrete Institute, v. 13, pp. 7-19, (in Japanese).
- Kanoh Y., and Yoshizaki S. 1979. "Strength of Slab-Column Connections Transferring Shear and Moment," ACI JOURNAL, Proceedings, v. 76, No. 3, pp. 461-478.
- King, S. and Delatte, N. J. 2004. "Collapse of 2000 Commonwealth Avenue: Punching Shear Case Study," Journal of Structural Engineering, ASCE, v. 18, No. 1, pp. 54-61.
- Kinnunen, S., and Nylander, H. 1960. "Punching of Concrete Slabs without Shear Reinforcement," Meddelande Nr 38, Institute for Byggnadsstatik, Kungliga Tekniska Hogskolan, Stockholm.
- Lovrovich, J. S., and McLean, D. I. 1990. "Punching Shear Behavior of Slabs with Varying Span-Depth Ratios," ACI Structural Journal, v.87, No. 5, pp. 507-511.
- Marzouk, H., Emam, M., and Hilal, M. S. 1996. "Effect of High-Strength Concrete Columns on the Behavior of Slab-Column Connections," ACI Structural Journal, v. 93, No. 5, pp. 545-554.
- Marzouk, H., Emam, M., and Hilal, M. S. 1998. "Effect of High-Strength Concrete Slab on the Behavior of Slab-Column Connections," ACI Structural Journal, v. 95, No. 3, pp. 227-237.
- Marzouk H., and Hussein A. 1991 "Experimental Investigation on the Behavior of High-Strength Concrete Slabs," ACI Structural Journal, v. 88, No. 6, pp. 701-713.
- Marzouk, H., and Jiang, D. 1997. "Experimental Investigation on Shear Enhancement Types for High-Strength Concrete Plates," ACI Structural Journal, v. 94, No. 1, 49-58.
- McHarg, P. J., Cook, W. D., Mitchell, D., and Yoon, Y. 2000. "Benefits of Concentrated Slab Reinforcement and Steel Fibers on Performance of Slab-Column Connections," ACI Structural Journal, v. 97, No. 2, pp. 225-234.
- Megally, S., and Ghali, A. 2000. "Punching Shear Design of Earthquake-Resistant Slab-Column Connections," ACI Structural Journal, v. 97, No.5, pp. 720- 730.
- Megally, S., and Ghali, A. 2000. "Punching of Concrete Slabs due to Column Moment Transfer," Journal of Structural Engineering, ASCE, v. 126, No.2, pp. 180-189.

- Moe, J. 1961. "Shearing Strength of Reinforced Concrete Slabs and Footings under Concentrated Loads," Development Department Bulletin No. D47, Portland Cement Association, Skokie, 130pp.
- Mokhtar, A., Ghali, A., and Dilger, W. 1985. "Stud Shear Reinforcement for Flat Concrete Plates," ACI JOURNAL, Proceedings, v. 82, No. 5, pp. 676-683.
- Morrison, D. G., Hirasawa, A. M., and Sozen, M. A. 1983. "Lateral-Load Tests of R/C Slab-Column Connections," Journal Structural Engineering, ASCE, v. 109, No. 11, pp. 2698-2714.
- Osman, M., Marzouk, H., and Helmy, S. 2000. "Behavior of High-Strength Lightweight Concrete Slabs under Punching Loads," ACI Structural Journal, v. 97, No. 3, pp. 492-498.
- Ospina, C. E., Alexander, S. D. B., and Cheng, J. J. R. 2003. "Punching of Two-Way Concrete Slabs with Fiber-Reinforced Polymer Reinforcing Bars and Grids," ACI Structural Journal, v. 100, No. 5, pp. 589-598.
- Pan, A., and Moehle, J. P. 1989. "Lateral Displacement Ductility of Reinforced Concrete Flat Plates," ACI Structural Journal, v. 86, No.3, pp. 250-258.
- Pan, A., and Moehle, J. P. 1992. "An Experimental Study of Slab-Column Connections," ACI Structural Journal, v. 89, No.6, pp. 626-638.
- Park, P. and Gamble, W. L. 2000. "Reinforced Concrete Slabs, 2nd ed.," John Wiley & Sons.
- Pilakoutas, K., and Li, X. 2003. "Alternative Shear Reinforcement for Reinforced Concrete Flat Slabs," Journal of Structural Engineering, ASCE, v. 129, No. 9, pp. 1164-1172.
- Raffaella, G. S., and Wight, J. K.1992. "R/C Eccentric Beam-Column Connections Subjected to Earthquake-Type Loading," Rep. UMCEE 92-18, Department of Civil and Environmental Engineering, University of Michigan, Ann Arbor.
- Regan, P. E., and Braestrup, M. W. 1985. "Punching Shear in Reinforced Concrete," Bulletin D'Information No. 168, Comité Euro-International du Béton, 1985.
- Robertson, I. N. and Durrani A. J. 1992. "Gravity Load Effect on Seismic Behavior of Interior Slab-Column Connections," ACI Structural Journal, v. 89, No.1, pp. 37-45.
- Robertson, I. and Johnson, G. 2006. "Cyclic Lateral Loading of Nonductile Slab-Column Connections," ACI Structural Journal, v. 103, No. 3, pp. 356-364.

- Robertson, I. N., Kawai, T., Lee, J., and Enomoto, B. 2002. "Cyclic Testing of Slab-Column Connections with Shear Reinforcement," *ACI Structural Journal*, v. 99, No. 5, pp. 605-613.
- Stark, A., Binici, B., and Bayrak, O. 2005. "Seismic Upgrade of Reinforced Concrete Slab-Column Connections Using Carbon Fiber-Reinforced Polymers," *ACI Structural Journal*, v. 102, No. 2, pp. 324-333.
- Swamy, R. N., and Ali, S. A. R. 1982. "Punching Shear Behavior of Reinforced Slab-Column Connections Made with Steel Fiber Concrete," *ACI JOURNAL, Proceedings*, v. 79, No. 5, pp. 392-406.
- Talbot, A. N. 1913. "Reinforced Concrete Wall Footings and Column Footings," *Bulletin No. 67, University of Illinois Engineering Experimental Station*, 114 pp.
- Theodorakopoulos, D. D., and Swamy, N. 1993. "Contribution of Steel Fibers to the Strength Characteristics of Lightweight Concrete Slab-Column Connections Failing in Punching Shear," *ACI Structural Journal*, v. 90, No. 4, pp. 342-355.
- Timoshenko, S., and Woinowsky-Krieger, S. 1959. "Theory of Plates and Shells, 2nd ed.," McGraw-Hill, New York, 1959, 580 pp.
- Wey, E. H., and Durrani A. J. 1992. "Seismic Response of Interior Slab-Column Connections with Shear Capitals," *ACI Structural Journal*, v. 89, No. 6, pp. 682-691.
- Widianto, "Rehabilitation of Reinforced-Concrete Slab-Column Connections for Two-way Shear," PhD dissertation, The University of Texas at Austin, Austin, 2006.

## Vita

Ying Tian was born in Tangshan, China on March 20, 1971, the son of Weihua Tian and Aiyun Yao. He received the degree of Bachelor of Science in Civil Engineering at Hebei Polytechnic University (originally Hebei Institute of Technology), China, in 1991. After teaching for six years at Hebei Polytechnic University, he entered the graduate school of Tsinghua University, China, in 1997, where he received the Master of Science degree in Civil Engineering in the field of Disaster Prevention and Protection in 2000. He received a Master of Science degree in Civil Engineering from The Ohio State University in 2002. He entered the graduate school of The University of Texas at Austin in 2002 for his PhD study.

Permanent address: Lubei Qu, Shan Xi Nan Li (25# Xiao Qu), 6-3-103  
Tangshan, Hebei Province  
China, 063001

This dissertation was typed by the author.